V

Applied Battery Research for Transportation

Introduction

Core Support Facilities

Critical Barrier Focus: Voltage Fade

Materials Optimization

Process Development

V. Applied Battery Research for Transportation

V.A Introduction

The critical technological component in plug-in electric vehicles (PEVs) that enables comparable convenience, affordability, and safety to those found in today's petroleum-powered vehicles continues to be energy storage. To promote the widespread adoption of electric vehicles and enable a strong U.S.-based battery manufacturing sector, the materials discovery and device innovation taking place in national laboratories and at universities must be translated into commercially viable products and processes. Such applied research activities are inherently high risk; coupling the frontier, cutting edge nature of materials discovery with the performance/cost needs of a market-changing new product. A significant portfolio of R&D projects funded through the VTO that meet these criteria are grouped together in the Applied Battery Research (ABR) for transportation program.

The ABR program is and will continue to be comprised of high risk projects investigating issues and advances at the cell level. Success in ABR projects means electric drive vehicle energy storage products that can be realized (manufactured) and that lead to cost reduction; thus, fulfilling the energy storage component of EERE's EV Everywhere Initiative. Such improvements will be accomplished through novel materials, particularly the active components of the cell, but also through innovative cell design and electrode composition. As well, materials production, electrode processing, and cell manufacture are also important thrusts within ABR.

The R&D projects in the 2013 ABR portfolio are divided into four distinct but complementary groups:

- Core Support Facilities,
- In-Depth Study—Voltage Fade in Li-ion Battery Cathode Materials,
- Materials & Diagnostic Studies, and
- Process Improvement Projects.

Core Support Facilities. Across several of the national laboratories, infrastructure has been created and resources grouped into facilities that support complex activities critical to applied battery research. This provides the U.S. energy storage research community a powerful tool to carry out scientific investigations using, for example, state-of-the-art fabricated Li-ion battery electrodes, commercially viable and high purity electrolyte additives, chemical and electrochemical analysis of cycled battery components, and component-level abuse response analysis. The services and products of these six facilities are fully funded through the ABR program and are available hierarchically, with VTO funded projects first, followed by other DOE funded projects (BES, ARPA-E), then other government agencies down the line through to U.S. small businesses. The majority of these facilities came on line with Recovery Act funding in 2009 and have now a significant track record in supporting applied research.

In-Depth Study—Voltage Fade in Li-ion Battery Cathode Materials. ABR programs always contain and can usually be defined by a major barrier, a set of structurally and functionally interrelated problems, that simultaneously appears unsolvable and that absolutely requires a solution in order to achieve a particular technical target. These are complex multi-component phenomena, multi-scale in space, time, and energy. The barrier is not going to be overcome by a single brilliant experiment or by a lone expert. Solutions, if possible, require understanding across the dimensions of the problem, and such understanding requires in-depth science practiced by a multi-disciplinary team—and a lot of data. This is the nature of a deep-dive investigation. Within the ABR program the first such deep-dive has been underway for over two years and has been focused on an issue common to a promising (high energy content) class of active cathode materials: Li-, Mn-rich layered, layered transition metal oxides. With these materials, a continuous decay of the average voltage with cycling is observed and this decrease in energy output with cycling is accompanied by an evolving energy inefficiency. For the FY2013 Annual Progress Report, six reports have been prepared detailing various aspects of this in-depth investigation, from the study of various mitigation strategies to the impact on voltage fade of surface coatings. The work was carried out by twenty-nine scientists and engineers and across three different national labs.

Materials and Diagnostic Studies. Eight projects predominately dealing with electrolyte component development and spectroscopic characterization are legacy projects from the first phase of applied research activities in Li-ion batteries. All of these projects have contributed towards the body of knowledge on Li-ion-related energy storage materials and all have been, or will be in 2014, terminated. All the work is of the highest caliber, but the direction of the overall program has changed to reflect the need for R&D efforts involving full cell chemistries as opposed to material-level investigations.

Process Improvement Projects. The second phase of ABR, initiated in FY2012, contained the first process-R&D projects. The work in 2013 continues some of these projects and expands to include more experimental work on electrode fabrication. Critical to establishing a U.S.-based battery manufacturing industry is the development of process-oriented

intellectual property. The four reports in this section detail work that not only has led to IP creation on its own, the research teams have also leveraged the EERE-funded work to partner with American companies developing their own proprietary processing technologies. As new processing resources are developed, they are also being made available to the U.S. energy storage research community in line with the Core Support Facilities described above.

Via FY2013 funding, a significant part of the ABR FY2014 portfolio is now composed of competitively awarded financial assistance grants made to several teams addressing the need for energy density improvement in electric drive vehicle batteries. These projects will be reported on in the next year's annual progress report. In coming years, there will be a reoccurring FOA soliciting proposals for team-based R&D efforts directed at "Applied Battery Research for Improvements in Cell Chemistry, Composition and Processing."

The remainder of this section provides technical highlights and progress on the Applied Battery Research program for FY 2013. The information provided is representative only and detailed information is available from publications cited in each project overview.

V.B Core Support Facilities

V.B.1 Process Development and Scale up of Advanced Cathode Materials (ANL)

Gregory K. Krumdick

Argonne National Laboratory
9700 South Cass Avenue
Argonne, IL 60439-4837
Phone: (630) 252-3952; Fax: (630) 252-1342
E-mail: gkrumdick@anl.gov

Collaborators:
YoungHo Shin, Argonne National Laboratory
Ozgenur K. Feridun, Argonne National Laboratory
Gerald Jeka, Argonne National Laboratory
Mike Kras, Argonne National Laboratory
Bryant Polzin, Argonne National Laboratory
Wenquan Lu, Argonne National Laboratory
Kumar Bugga, Jet Propulsion Laboratory

Start Date: June, 2010
Projected End Date: September, 2014

Objectives

- Process development, scale-up and producing kilogram quantities of the target bench-scale advanced cathode materials for basic research, market evaluation and high-volume manufacturing.
  - Develop scalable manufacturing process with economic feasibility and provide target materials with high quality and reproducibility.

Technical Barriers

Most advanced cathode materials like lithium and manganese-rich metal oxide (LMR-NMC) materials have been synthesized in small quantity at the bench-scale and lack commercial availability. Sufficient quantity of these high energy materials with high quality is hard to obtain for basic research and industrial evaluation. Each such material needs customized synthesis process and scale-up research and pilot-scale production facilities.

Technical Targets

- Develop a customized synthesis process for target bench-scale cathode material.
- Develop continuous carbonate and hydroxide co-precipitation methods (2-way synthesis approach) for precursor preparation.
- Identify and resolve constraints for the scale-up of target bench-scale material.
- Produce sufficient quantities of materials with equal or better quality than target bench-scale material.
- Evaluate and compare the performance of bench-scale and scaled-up material by coin cell test.

Accomplishments

For 1st candidate material - $Li_{1.14}Mn_{0.57}Ni_{0.29}O_2$

- Successful production of scaled-up carbonate cathode material with equal or better quality than target bench-scale carbonate cathode material by coin cell test.
- Achievement of 10% increased capacity, 20% increased tap density and better cycle life of scaled-up carbonate cathode material compared to target bench-scale carbonate cathode material.
- Preliminary synthesis of scaled-up cathode material via hydroxide process which shows equal or better quality than bench-scale hydroxide cathode material.
- Identification of cracking issue of scaled-up carbonate cathode material.
- Preparation and delivery of 200g pre-crushed scaled-up carbonate cathode material.
- Investigation of particle fracturing effect on rate performance and cycle life.
- Investigation of particle size effect on particle cracking during calendaring process.
- Investigation of relation between particle size, morphology and tap density.
- On-going research of particle cracking and mitigation by increased particle density and decreased particle size (using Nanoindenter analysis).

For 2nd candidate material - $Li_{1.2}Mn_{0.54}Ni_{0.13}Co_{0.13}O_2$

- Process development and scale-up via hydroxide co-precipitation for target material.
- Evaluation and comparison of three Toda HE-5050, JPL bench-scale and ANL scaled-up JPL hydroxide cathode materials.
- Synthesis of scaled cathode material via hydroxide process which shows an initial discharge capacity of 237 mAh/g and tap density of 1.23 g/cc. This did not meet JPL specifications.
- Preparation of ANL scaled-up JPL carbonate cathode material to meet specification.
- Successful achievement of 20% increased initial discharge capacity (292 mAh/g), 20% increased tap density (1.82 g/cc) of ANL scaled-up JPL carbonate cathode material compared to the specification.
- Delivery of ANL scaled-up JPL hydroxide precursor material to ANL CSE for domain size study.
- Delivery of ANL scaled-up JPL carbonate cathode material to ANL Cell Fabrication Facility to evaluate particle cracking strength by Nanoindenter.
- Delivery of ANL scaled-up JPL carbonate cathode material to JPL as an intermediate sample.

✧ ✧ ✧ ✧ ✧

Introduction

There is a strong need to produce advanced cathode materials like lithium and manganese rich metal oxide (LMR-NMC) materials with high quality in the kilogram and tens-of-kilograms quantities for basic R&D purposes and industrial needs. To achieve this goal, process development and scale-up of advanced cathode materials with high quality and reproducibility is a critical step between discovery of advanced battery materials, market evaluation and high-volume manufacturing. The performance measures of cathode material such as capacity, tap density and life are strongly affected by synthesis process and its optimization though it has the same composition. Additionally, development of cathode synthesis process with economic feasibility is important to reduce the cost of the full battery pack.

Until recently, there was no systematic engineering research capability or program across the DOE complex or in industry to identify and resolve constraints to the development of cost-effective process technology for the high-volume manufacture of these advanced cathode materials. Now, Argonne's Materials Engineering Research Facility (MERF) enables a systematic engineering approach to investigate customized synthesis processes and scale-up for each candidate material via carbonate and hydroxide co-precipitation and high energy ball mill synthesis methods. For co-precipitation process, MERF already set up two 4L continuous stirred tank reactor systems and a 20L continuous stirred tank reactor system in FY12. These do not represent a batch process or a semi-continuous process. Significant process improvement for these continuous co-precipitation systems was achieved including several inventions conceived, submitted or filed.

MERF's process engineering research will identify and resolve constraints for the scale-up of the target bench-scale candidate material, from the bench to pre-pilot scale, to complete qualified kilogram production corresponding to the specification of the target material.

MERF also carries out material characterization and electrochemical performance test in coin cell for the scaled-up materials. These results will be validated by ANL's Materials Screening Group to confirm a performance match to the original bench-scale materials.

Approach

The first step for the process development and scale-up of advanced cathode material is to identify candidate cathode materials of interest to the ABR program participants including materials produced by the carbonate, hydroxide or other processes. A database of materials to scale has been developed and maintained and is used to rate and prioritize candidates for scale-up. These candidates are ranked based on electrochemical performance, process complexity and interest level of the researcher and the lithium-ion battery industry.

In FY12, MERF successfully completed the process development, scale-up and kilogram production of the 1st candidate material ($Li_{1.14}Mn_{0.57}N_{i0.29}O_2$) with high quality. Carbonate process was fully developed and hydroxide process set-up was initiated. As a major constraint for the scale-up of the 1st candidate material, particle cracking issue was identified. Many approaches were made to mitigate particle cracking of carbonate cathode material and this work continued in FY13.

In FY13, we started the process development and scale-up of JPL hydroxide ($Li_{1.2}Ni_{0.13}Mn_{0.54}Co_{0.13}O_2$) cathode material as the 2nd candidate and will generate kilogram quantities of this material for evaluation and delivery. We plan to then select and begin the process development and scale-up of the next candidate in the materials queue.

Results

1st candidate material ($Li_{1.14}Mn_{0.57}N_{i0.29}O_2$): completion of process scale-up and kg production with equal or better quality.

The major technical targets for the 1st candidate material were as following:

- Scale-up process development via carbonate co-precipitation method.
- Production of kg quantities of uniform material.
- Achieving equal or better performance than bench-scale material.

We successfully developed the synthesis processes (both carbonate co-precipitation in FY12 and hydroxide co-precipitation in FY13) for this 1st candidate material. Production and delivery of kg quantities of this material was completed in FY12. In FY13, for this cobalt-free composition, the scaled-up carbonate and hydroxide materials were evaluated by coin cell test and compared to its bench-scale materials.

Table V - 1 shows that scaled-up carbonate (optimized) and hydroxide (preliminary) materials has equal or better tap density and initial discharge capacity than bench-scale materials. The morphology and secondary particle size of scaled-up materials are more uniform and spherical compared to bench-scale materials.

Table V - 1: Comparison of bench-scale and scaled-up carbonate and hydroxide cathode materials for 1st candidate

	Manufacturer Lot #	ANL CSE 101217B	ANL MERF ES-120905	ANL CSE 1108102	ANL MERF ES-130110
	Co-precipitation	Carbonate	Carbonate	Hydroxide	Hydroxide
	Scale Status	Bench-scale	Pre-pilot scale Optimized	Bench-scale	Pre-pilot scale Preliminary
Precursor	SEM 3000x	x	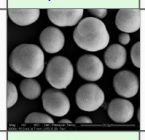	x	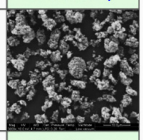
	ICP analysis	x	$Ni_{0.33}Mn_{0.67}(CO_3)_x$	x	$Ni_{0.33}Mn_{0.67}(OH)_x$
	$D_{10}/D_{50}/D_{90}$ [µm]	x	**0.2/11.7/16.4**	x	**1.0/4.0/6.3**
	Tap density [g/cc]	x	**1.40**	x	**0.91**
Cathode	SEM 8000x	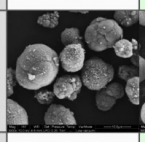	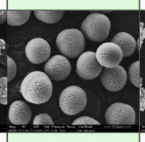	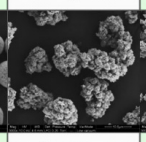	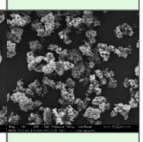
	ICP analysis	$Li_{1.35}Ni_{0.32}Mn_{0.68}O_y$	$Li_{1.37}Ni_{0.33}Mn_{0.67}O_y$	$Li_{1.31}Ni_{0.33}Mn_{0.67}O_y$	$Li_{1.35}Ni_{0.33}Mn_{0.67}O_y$
	$D_{10}/D_{50}/D_{90}$ [µm]	**7.6/12.7/21.0**	**6.9/11.1/18.4**	**7.7/13.2/22.1**	**2.4/4.7/8.9**
	Tap density [g/cc]	**1.41**	**1.70**	**0.98**	**1.02**
	Initial disch. [mAh/g]	**221.7 ***	**251.0 ***	**172.4 ***	**184.2 ***

** 4.75~2.4 V at 25 °C (25 mAh/g)*

As can be seen by the rate (Figure V - 1) and C/3 cycle life (Figure V - 2) comparisons, the optimized, pre-pilot scaled-up carbonate cathode material has the highest capacity at any C-rate and the lowest capacity loss during 160 cycles. The pre-pilot scaled-up hydroxide cathode material shows equal or better properties than bench-scale material. Improvement of hydroxide process was anticipated to get better material density and electrochemical performance.

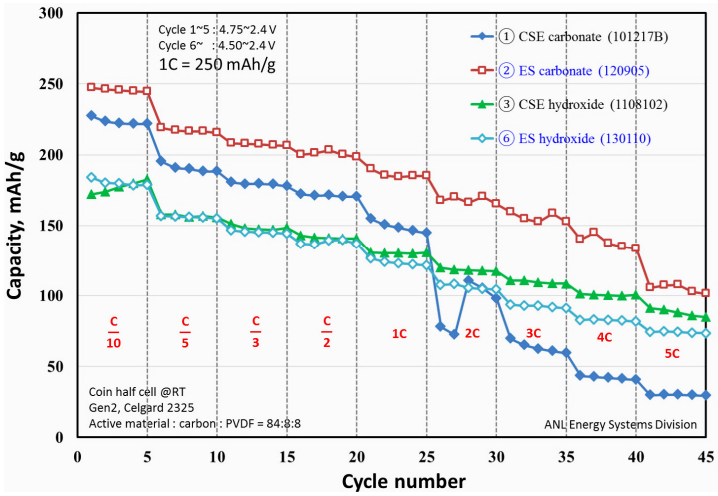

Figure V - 1: Rate performance comparison of scaled-up carbonate and hydroxide to bench-scale materials

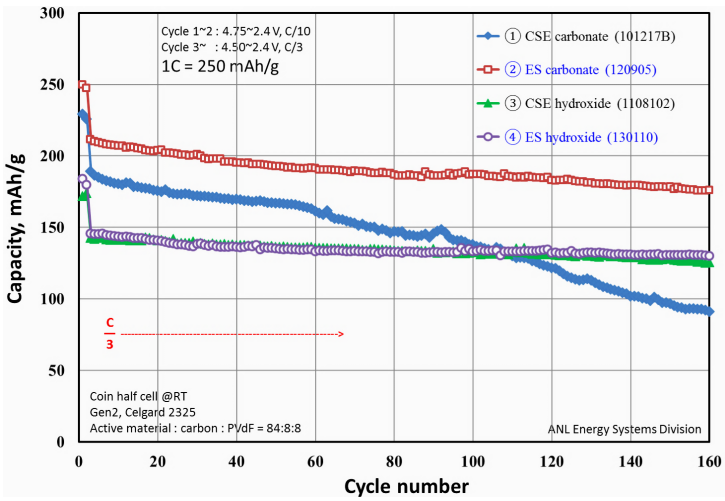

Figure V - 2: C/3 cycle life comparison of scaled-up carbonate and hydroxide to bench-scale materials

1st candidate material ($Li_{1.14}Mn_{0.57}N_{i0.29}O_2$): identify and mitigate particle cracking issue during process development and scale-up.

When the carbonate cathode material was calendared, it cracked, yielding unpredictable results. This particle fracturing issue seems to be an inherent problem with the carbonate process as it has also been reported from bench-scale researchers, which wasn't considered a critical problem at the initial stage. However, in FY12, the ANL Cell Fabrication Facility (CFF) noticed the particle fracture during calendaring process when they evaluated the scaled-up carbonate material (lot # ES-20120222, average secondary particle size of 15.6 µm). To mitigate particle cracking, the

Table V - 1. This scaled-up hydroxide material shows much lower tap density (around 1.0 g/cc) than the scaled-up carbonate product with precise particle-size control technology was evaluated by ANL Cell Fabrication Facility (lot # ES-20120709+11, average secondary particle size of 7.8 µm) in FY12, which also showed particle cracking problem.

In FY13, the second approach to mitigate particle cracking issue was the preparation of pre-crushed carbonate material. Using pulverizer, 200g pre-crushed carbonate material was prepared and delivered to ANL CFF at 02/20/2013, which showed increased surface area, low tap density (1.43 g/cc) and decreased electrochemical performance than un-crushed carbonate material as reported by ANL CFF.

The third approach was to synthesize the same material using the hydroxide process as one can see in tap density of scaled-up carbonate material (around 1.7 g/cc) because of its leaf-like structure of primary

particle. The electrochemical performance of the hydroxide material is not good. These results have prompted us to revisit the carbonate process and to try to minimize the particle fracturing issue by improvement of calendaring process and carbonate co-precipitation. To evaluate the effect of particle cracking, we look at the calendaring process and at the relation between electrode porosity and electrochemical performance.

The effect of particle fracturing on electrode and its porosity on electrochemical performance was investigated. As one can see in Figure V - 3, we prepared four electrodes with different porosities and compared their electrochemical performances.

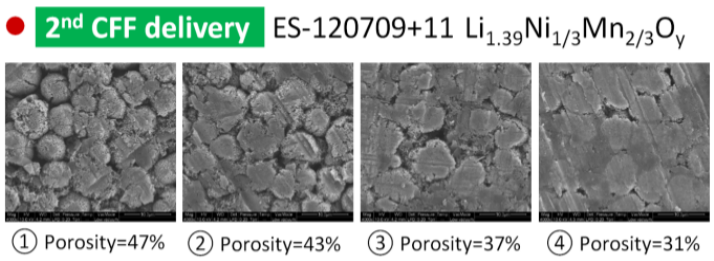

Figure V - 3: Preparation of electrode with different porosity for ES-20120709+11

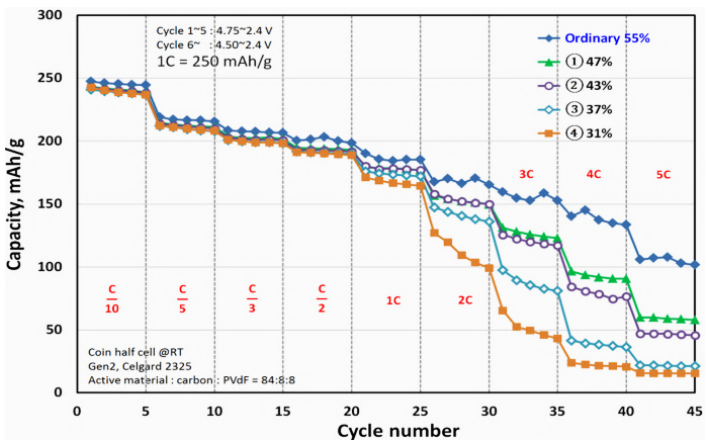

Figure V - 4: Rate performance comparison of electrode with different porosity for ES-20120709+11

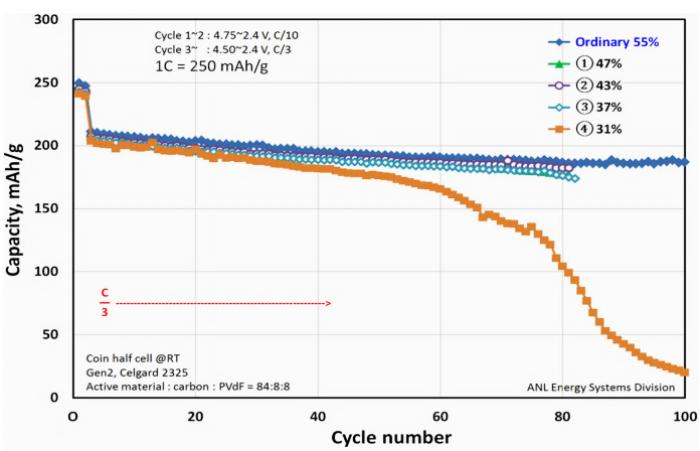

Figure V - 5: C/3 cycle life comparison of electrode with different porosity for ES-20120709+11

The rate performance and cycle life decrease as electrode porosity is reduced (Figure V - 4 and Figure V - 5). It is clear that particle cracking causes these undesirable behaviors.

We tried smaller particles (7.8 µm and 4.0 µm) for calendaring process to see the effect of particle size on cracking and there is a tendency that the smaller particles results in slightly less cracking (Figure V - 6). However, they also resulted in lower tap density.

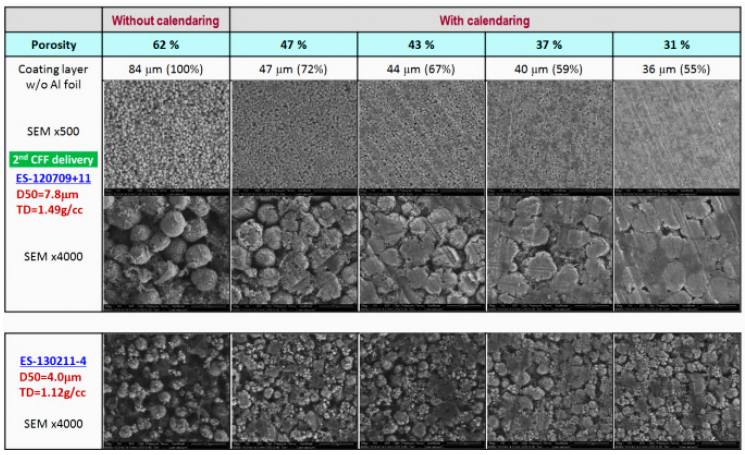

Figure V - 6: Effect of particle size on particle cracking during calendaring process

We then looked at the relation between secondary particle size, morphology and tap density. In Figure V - 7, the 1st, 2nd and 3rd carbonate cathode materials have similar tap densities even though their average secondary particle sizes are quite different because they are spherical. But the SEM images of 4 through 7 of Figure V - 7 clearly show that if the morphology becomes less spherical, the tap density decreases even though the average secondary particle sizes are similar. Therefore, we can say that particle morphology has a greater effect on tap density than secondary particle size. So, if the secondary particle is spherical, we can keep the same tap density of carbonate cathode material even though the secondary particle size is reduced for the purpose of mitigating particle cracking issue.

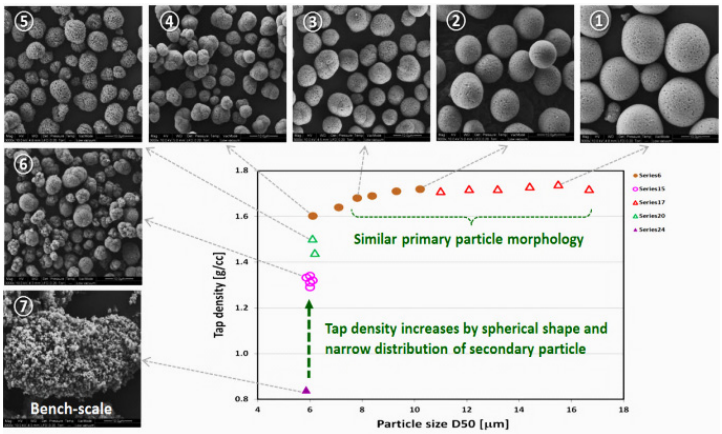

Figure V - 7: Comparison between secondary particle morphology, size and tap density of carbonate cathode material ($Li_{1.39}Ni_{0.33}Mn_{0.67}O_y$)

This relation between secondary particle size and tap density has encouraged us to improve the carbonate process to make small, spherical secondary particles with increased particle density to mitigate the particle fracturing. Also we plan to continue to work on the integrity of both carbonate and hydroxide co-precipitation processes in an attempt to control morphology and increase tap density.

Recently, we synthesized the 2nd candidate material ($Li_{1.2}Mn_{0.54}Ni_{0.13}Co_{0.13}O_2$) with increased tap density of 1.82 g/cc and decreased average secondary particle size of 6.7 µm via an improved carbonate process. For the

analysis of particle cracking for this material, we are collaborating with Bryant Polzin at Argonne who newly developed the Nanoindentor process which will be used to measure stresses required for particle cracking.

2nd candidate material (JPL, $Li_{1.2}Mn_{0.54}Ni_{0.13}Co_{0.13}O_2$): completion of process scale-up with equal or better cathode quality.

An existing high capacity/voltage cathode development project with JPL/NASA had produced a cathode composition ($Li_{1.2}Mn_{0.54}Ni_{0.13}Co_{0.13}O_2$) with high capacity (~230 mAh/g) and high tap density (>1.7 g/cc) at the bench scale, but JPL had difficulties scaling the material to kilogram scale for commercial evaluation. Toda America produced this composition (HE-5050) at high capacity (~250 mAh/g) but at a much lower tap density (~1.0 g/cc). In FY13, Argonne's cathode scale-up program was tasked to scale this composition and produce high capacity, high tap density material for evaluation. The target properties are:

- Composition: $Li_{1.2}Mn_{0.54}Ni_{0.13}Co_{0.13}O_2$
- Tap density: > 1.5 g/cc.
- Capacity: ~ 240 mAh/g (1st discharge)
- Cycle life: ~ 200 cycles

Our first approach was to optimize a hydroxide based process to synthesize the material. We evaluated and compared Toda HE-5050, JPL bench-scale and ANL scaled-up JPL hydroxide materials. The XRD analysis shows that these 3 materials have the same structure (Figure V - 8).

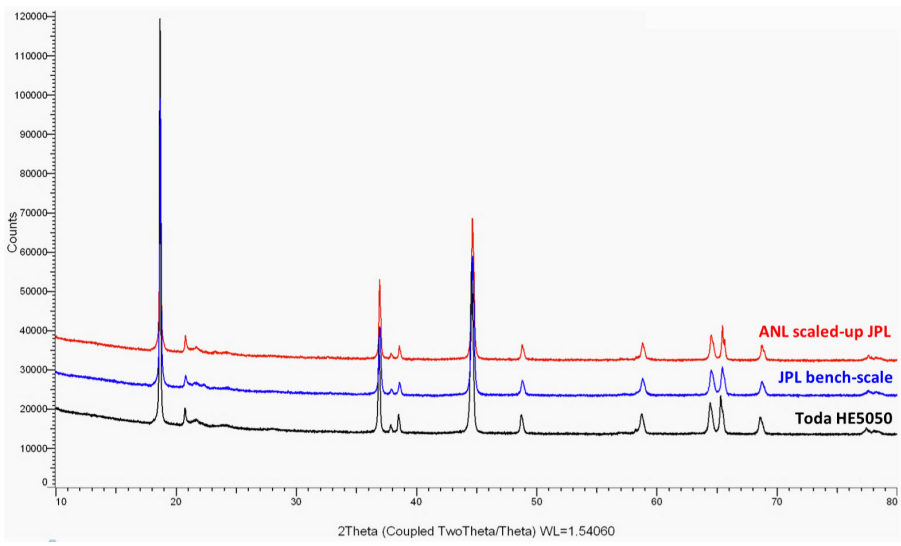

Figure V - 8: XRD comparison between Toda HE5050, JPL bench-scale and ANL scaled-up JPL hydroxide materials

The tap densities of synthesized ANL scaled-up JPL hydroxide materials were between 0.7 ~ 1.3 g/cc depending on the ratios of NaOH and NH_4OH to transition metals. It is difficult to achieve the target tap density (> 1.5 g/cc) via hydroxide process for this composition at the kilogram scale. We then focused on a carbonate based approach based on the scale-up experience of 1st candidate material. Successfully, ANL's scaled-up JPL carbonate material was synthesized and evaluated. Table V - 2 shows the comparison of three HE-5050 samples, JPL bench-scale, ANL scaled-up JPL hydroxide and carbonate materials.

Table V - 2: Comparison of 6 cathode materials with same composition: ① SEM (8000x), ② $D_{10}/D_{50}/D_{90}$ (μm), ③ tap density (g/cc), ④ initial discharge capacity at C/20 (mAh/g)

	Toda-HE5050 B#1 5-P767	Toda-HE5050 B#2 P1407	Toda-HE5050 B#3 P2564	JPL pristine	ANL scaled-up JPL hydroxide ES-20131004	ANL scaled-up JPL carbonate ES-20130924
	Hydroxide co-precipitation			Hydroxide	Hydroxide	Carbonate
	Commercial	Commercial	Commercial	Bench-scale	Pre-pilot	Pre-pilot
①	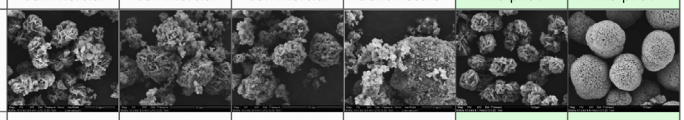					
②	3.1/5.3/9.2	1.1/5.2/11.3	2.0/4.9/10.4	1.2/11.1/29.3	3.0/5.1/9.0	4.0/6.7/11.4
③	1.03	1.16	1.07	1.70	1.23	1.82
④	255.3	261.8	254.5	228.2	237.7 *	292.0 *

** Under optimization*

JPL bench-scale material shows the initial discharge capacity of 228 mAh/g and tap density of 1.7 g/cc. Toda America has produced this composition (HE-5050) at a high initial discharge capacity (~250 mAh/g) but at a much lower tap density (~1.0 g/cc). For ANL scaled-up JPL hydroxide material, the tap density is 1.23 g/cc and the initial discharge capacity is 238 mAh/g which is less than the target specification (Figure V - 9). However, as seen in Figure V - 10, ANL scaled-up JPL carbonate material shows a very high initial discharge capacity of 292 mAh/g with the highest tap density of 1.82 g/cc.

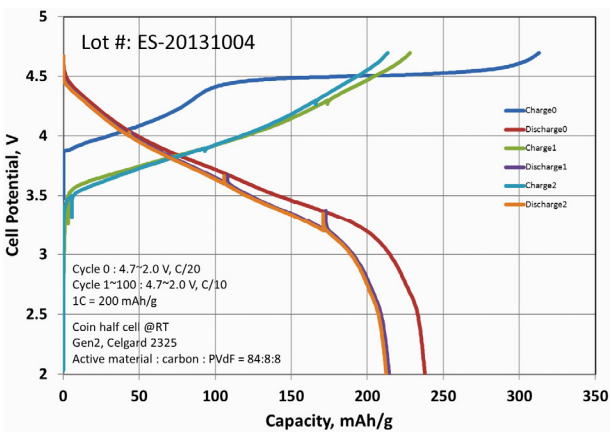

Figure V - 9: Voltage profile of Argonne scaled-up JPL hydroxide material (lot #: ES-20131004)

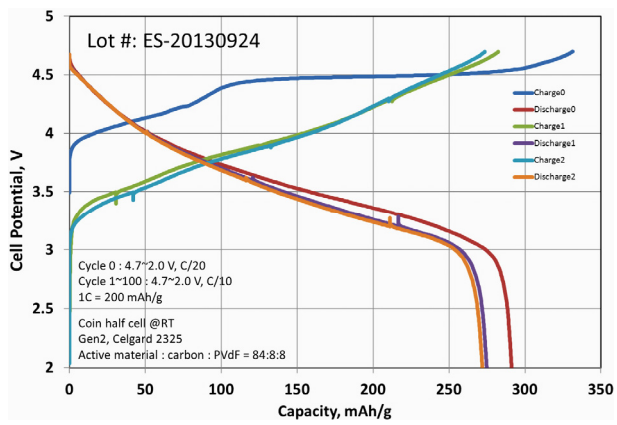

Figure V - 10: Voltage profile of Argonne scaled-up JPL carbonate material (lot #: ES-20130924)

2nd candidate material ($Li_{1.2}Mn_{0.54}Ni_{0.13}Co_{0.13}O_2$): production and delivery of precursor and cathode materials.

The precursor and cathode materials were produced by a reproducible, scalable process and were delivered to Argonne's Materials Screening Group and JPL for evaluation.

- 10/30/2013: 5g JPL hydroxide precursor to ANL CSE.
- 10/31/2013: 100g JPL carbonate cathode to JPL.
- 11/11/2013: 500g JPL hydroxide precursor to ANL CSE (scheduled).
- 12/20/2013: 2~3kg JPL carbonate cathode to JPL (scheduled).

Conclusions and Future Directions

ANL's MERF successfully completed the process development, scale-up and kilogram production of 1st candidate material with equal or better quality. This scaled-up cathode material shows 10% increased capacity, 20% increased tap density and a better cycle life compared to bench-scale material. To identify and mitigate the particle cracking issue of carbonate cathode material, many approaches were investigated. Hydroxide cathode material with same composition was synthesized. Pre-crushed carbonate cathode material was prepared and evaluated. Particle fracturing effect on electrochemical performance and particle size effect on

particle cracking during calendaring process were investigated. Also the relation between secondary particle size, morphology and tap density was studied. These kinds of efforts will open the possibility to mitigate particle cracking of carbonate cathode material. The increased particle density and decreased secondary particle size can be a direction to mitigate the particle cracking of carbonate cathode material which is under on-going investigation using Nanoindenter analysis.

For the 2nd candidate material (JPL, $Li_{1.2}Mn_{0.54}Ni_{0.13}Co_{0.13}O_2$), MERF successfully developed the synthesis processes (both carbonate and hydroxide co-precipitation). To compare the properties of scaled-up materials, three Toda HE-5050, JPL bench-scale and ANL scaled-up JPL hydroxide and carbonate cathode materials were evaluated which have the same composition. ANL scaled-up JPL carbonate cathode material shows excellent properties such as 20% increased initial discharge capacity (292 mAh/g) and 20% increased tap density (1.82 g/cc) compared to the specification.

In FY14, we plan to continue to develop synthesis routes and improve processes to mitigate particle cracking of lithium and manganese rich carbonate cathode material (LMR-NMC) without the trade-off between capacity and density. Kilogram quantities of the 2nd candidate material will be produced and delivered to JPL, ANL Cell Fabrication Facility and ANL Materials Screening Group. The 3rd candidate material will be selected and scaled to kilogram quantities. Additional cathode materials will be synthesized for research purposes as requested.

FY 2013 Publications/Presentations

1. 2013 DOE Annual Peer Review Meeting Presentation.
2. "METHOD FOR PRODUCING SIZE SELECTED PARTICLES," Provisional patent filed – May 14, 2013.

V.B.2 Process Development and Scale up of Advanced Electrolyte Materials (ANL)

Gregory K Krumdick, Program Manager

Argonne National Laboratory
9700 South Cass Avenue
Argonne, IL 60439-4837
Phone: (630) 252-3952; Fax: (630) 252-1342
E-mail: gkrumdick@anl.gov

Collaborators:
Krzysztof (Kris) Pupek, Argonne National Laboratory
Trevor Dzwiniel, Argonne National Laboratory
Daniel Abraham, Argonne National Laboratory
Zhengcheng (John) Zhang, Argonne National Laboratory
Wenquan Lu, Argonne National Laboratory
Gao Liu, Lawrence Berkeley National Laboratory
Dan Scherson, Case Western University
Wesley Henderson, North Carolina State University
Kang Xu, Army Research Laboratory

Start Date: June 2010
Projected End Date: September 2014

Objectives

The objective of this task is to conduct process engineering research for the scale-up of new electrolyte and additive materials. Advanced electrolytes and additives are being developed to stabilize the interface of lithium-ion batteries by forming a very stable passivation film at the carbon anode. Stabilizing the interface has proven to be key in significantly improving the cycle and calendar lives of lithium ion batteries for HEV and PHEV applications. Up to this point, these advanced electrolytes and additives have only been synthesized in small batches. Scaling up the process involves modification of the bench-scale process chemistry to allow for the semi–continuous production of materials, development of a process engineering flow diagram, design of a mini-scale system layout, construction of the experimental system and experimental validation of the optimized process. The mini system will be assembled utilizing an existing synthesis reactor system. Electrolyte materials so produced will be analyzed to confirm material properties and for quality assurance. The electrochemical properties of the material will be validated to confirm a performance match with the original materials.

Technical Barriers

Advanced electrolytes and additives have been synthesized in small batches using 1-5L vessels, which produce approximately 200 mL of the material. The bench-scale processes are labor-intensive and time-consuming. Sufficient quantity of material cannot be generated for prototype testing, which is required prior to scaling the process to the next level. Therefore, pilot-scale facilities are required for battery materials scale-up research and development.

Technical Targets

- Scale-up 4-6 electrolyte materials in FY13.

Accomplishments

- Scale-up work has been completed on the following electrolyte materials:
  - **ANL-RS21 (**6,7-dimethoxy-1,1,4,4-tetramethyl-1,2,3,4-tetrahydronaphthalene).
  - **ARL- LiPFTB (**Lithium perfluoro-tert-butoxide).
  - **ANL-RS5** [(2,5-dimethoxy-1,4-phenylene) bis(diisopropylphosphine oxide)].
  - **ANL-RS51** [(2,5-dimethoxy-1,4-phenylene) bis(diethylphosphine oxide].
- **CWU-FRION (**lithium [(2,5-bis(diethylphosphoryl) catecholato) oxalatoborate]).
- Work has begun on the following materials:
  - **Li-FSI** (electrolyte additive).
  - **Li-TDI** (electrolyte additive).
  - **LBNL-PEFM** (organic binder).
- We are in the process of developing protocol for electrochemical validation of scaled up materials:
  - Redox shuttle RS5 and RS51 are currently tested against baseline electrolyte.
  - Comparison study, RS5 vs. RS51 are in progress.
  - Electrochemical study of in-process materials will be used to develop material specification (minimum required purity and impurity profile).

✧ ✧ ✧ ✧ ✧

Introduction

Researchers in the battery materials programs across the DOE complex refer to scale up as synthesis of battery materials in gram quantities, and with time consuming, multiple small-scale runs. There is a need to develop scale-up processes for battery materials (primarily lithium-ion based batteries) to the kilogram and tens-of-kilograms quantities at DOE labs to support the transition of these technologies to industry. Currently, there is no systematic engineering research capability or program across the DOE complex or in industry to identify and resolve constraints to the development of cost-effective process technology for the high-volume manufacture of these advanced materials.

Approach

A formal approach for the scale-up of electrolyte materials has been defined (see Figure V - 11). This approach starts with the initial discovery of a new electrolyte material and an initial electrochemical evaluation. This determines if the material is to be added to the inventory spreadsheet, ranked and prioritized. At this point, the scale-up process begins with the initial feasibility study, proof of concept testing, 1st stage scale-up and 2nd scale scale-up. Go/No go decisions occur after feasibility determination and electrochemical validation testing.

For each material scaled, we will develop a scalable manufacturing process, analytical methods and quality control procedures. We will also prepare a "technology transfer package" which will include:

- Summary of the original process used by discovery researchers to synthesize the material.
- Summary of the scalable (revised) process suitable for large scale manufacturing.
- Detailed procedure of the revised process for material synthesis.
- Analytical data/Certificate of Analysis for the material (chemical identity and purity).
- The material impurity profile.
- Electrochemical performance test data.
- Preliminary estimates of production cost.
- MSDS for the material.
- Develop material specifications.

We will also make kilogram quantities of the material available for industrial evaluation, which would have been fully characterized chemically and electrochemically.

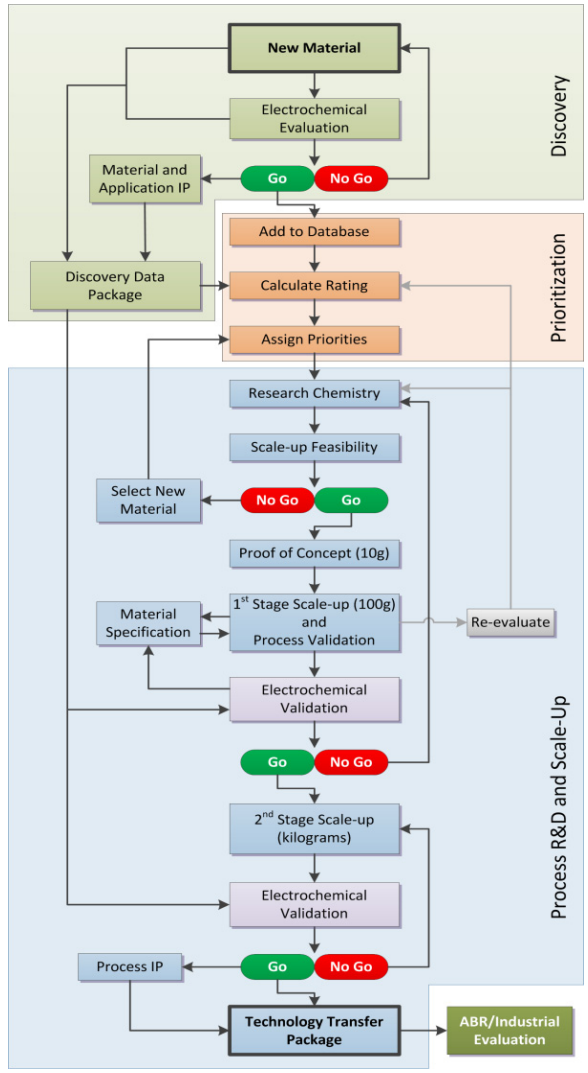

Figure V - 11: Electrolyte Materials Process R&D Workflow

Results

MILESTONE	DATE
ANL-RS21 – Complete	
Assess scalability of disclosed process	9/28/12
WP&C documentation approved	9/28/12
Develop and validate scalable process chemistry (10g scale)	10/30/12
First process scale-up (100g bench scale)	11/30/12
Second process scale-up (1000g pilot scale)	01/10/13
2,320g produced in a single batch, purity >99.5%	
ARL-LiPFTB – Complete	
Assess scalability of disclosed process	11/21/12
WP&C documentation approved	9/28/12
Develop and validate scalable process chemistry (10g scale)	12/21/12
First process scale-up (100g bench scale)	2/28/13
Second process scale-up (1000g pilot scale)	3/15/13
1,200g produced in a single batch, purity >99%	
ANL-RS5 – Complete	
Assess scalability of disclosed process	9/28/12
WP&C documentation approved	9/28/12
Develop and validate scalable process chemistry (10g scale)	7/31/13
First process scale-up (100g bench scale)	10/15/13
115g produced in a single batch, purity >99.9%	
ANL-RS51 – Complete	
Assess scalability of disclosed process	N/A
WP&C documentation approved	9/28/12
Develop and validate scalable process chemistry (10g scale)	7/31/13
First process scale-up (100g bench scale)	8/16/31
96g produced in a single batch, purity >99%	
CWU-FRION – Complete	
Assess scalability of disclosed process	5/21/13
WP&C documentation approved	9/28/12
Develop and validate scalable process chemistry (10g scale)	7/9/13
First process scale-up (100g bench scale)	9/24/13
118g produced in a single batch, purity >97%	

Wenquan Lu in the Materials Screening Group in the CSE division is conducting the electrochemical validation of the materials. RS21, RS5, RS51, and FRION are in the queue to be tested. Technology transfer packages have been prepared for all materials scaled. To date, we have provided 47 electrolyte material samples to interested companies and national labs. (NOTE: RS5, RS51 and FRION were synthesized on 100g scale to provide material for researchers and complete electrochemical evaluations.)

Conclusions and Future Directions

The technology transfer package for CWU-FRION is being written. Initially, scale-up work will continue on Li-FSI, Li-TDI and LBNL-PEFM. Additional materials to scale will be added after discussions with the project sponsor. The scale-up of 4-6 electrolyte materials are targeted for FY14.

Standardized protocols for validation of electrochemical performance for various classes of materials (electrolyte solvents, additives, redox shuttles) will be developed.

Over 24,000 g of battery grade materials have been produced, 47 samples have been provided to industry and various national labs for evaluation and experimentation (total 7,300 g, 4 samples in FY11, 25 samples in FY12 and 18 samples in FY13).

FY 2013 Publications/Presentations

1. 2013 DOE Annual Peer Review Meeting, May 13th-17th 2013, Arlington, VA.
2. T. Dzwiniel, K. Pupek and G. Krumdick: "*From Beaker to Bucket: The Safe Scale-up of Organic Electrolyte Materials,*" 246th ACS National Meeting, American Chemical Society, 2013.
3. Technology transfer packages were written for ANL-RS21, ANL-RS5, ANL-RS51, and ARL-LiPFTB.

V.B.3 Cell Analysis, Modeling, and Prototyping (CAMP) Facility Production and Research Activities (ANL)

Andrew N. Jansen
Argonne National Laboratory

Collaborators:
Daniel P. Abraham, Argonne National Laboratory
Dennis W. Dees, Argonne National Laboratory
Kevin G. Gallagher, Argonne National Laboratory
Wenquan Lu, Argonne National Laboratory
Bryant J. Polzin, Argonne National Laboratory
Stephen E. Trask, Argonne National Laboratory
Martin Bettge, Argonne National Laboratory
Joseph J. Kubal, Argonne National Laboratory
Yan Li, Argonne National Laboratory
Qingliu Wu, Argonne National Laboratory
Ye Zhu, Argonne National Laboratory

Start Date: October 2012
Projected End Date: September 2014

Objectives

- The objective of this core-funded effort is to design, fabricate, and characterize high-quality prototype cells that are based on the latest discoveries involving high-energy anode and cathode battery materials. Using this multi-discipline facility, analytical diagnostic results can be correlated with the electrochemical performance of advanced lithium-ion battery technologies for EV and PHEV applications.
  - Link experimental efforts through electrochemical modeling studies.
  - Identify performance limitations and aging mechanisms.

Technical Barriers

The primary technical barrier is the development of a high energy density battery for EV and PHEV applications that is safe, cost-effective, and has a long cycle life.

- Interpret complex cell electrochemical phenomena.
- Identify cell degradation mechanisms for a variety of novel high energy materials.

Technical Targets

- Obtain a viable supplier of battery grade silicon powder.
- Assess influence of LiDFOB, LiBOB, and HFiP electrolyte additives for HE5050 cathode.
- Evaluate MERF cathodes ($Li_{1.25}Ni_{0.3}Mn_{0.62}O_2$) based on hydroxide and carbonate precursors.
- Validate performance of advanced battery materials and add to Electrode Library as needed.
- Determine sources of impedance rise and capacity fade during extensive cycling of cells containing various electrochemical couples.
- Recommend solutions that can improve the life of high-energy lithium and manganese rich Ni/Mn (LMR-NMC) electrodes and cells.
- Enhance battery design and cost model concentrating on designs for advanced lithium-ion electrochemical couples.
- Advance development of electrochemical models focusing on the impedance of LMR-NMC positive electrodes.

Accomplishments

- The CAMP Facility was successfully organized into a streamlined effort with the task of assessing new battery materials in industrially relevant prototype formats.
- Over 14 cell builds were performed to date with combinations of baseline NCM523, 5V spinel, and high energy composite structure cathode materials (LMR-NMC) from Toda Kogyo, ABR researchers, and the Materials Engineering Research Facility (MERF). Over a thousand deep discharge cycles were achieved with many of these cells.
- Electrolyte additive studies for LMR-NMC suggest that the effect of additives is dependent on formation protocol and/or cell format.
- It was determined that the effective utilization of silicon in the anode will require a tailored silicon-carbon-binder system with limits on the silicon lithiation and use of electrolyte additives (FEC).

- Examined the LMR-NMC positive electrode SEI impedance using the EIS electrochemical model to study the impact of the voltage hysteresis during cycling.

✧ ✧ ✧ ✧ ✧

Introduction

The "valley of death" is a phrase that is often used to describe the path that a new discovery must traverse to become a commercial product. This is especially true for novel battery materials invented in research laboratories around the world. Often researchers are resource-limited and only able to make gram quantities of the new material. A few grams is enough for several coin cells to prove the concept, but never enough for a battery manufacturer to test in a realistic format. Consider that a typical coin cell has a capacity near 4 mAh, while a cell in a PHEV/EV battery has a capacity near 40 Ah – four orders of magnitude larger. An unwarranted amount of resources could be gambled to make the tens of kilograms needed for a full-sized cell for industrial demonstration. Many great materials may have been abandoned on the benchtop because the scale-up risks were deemed too excessive.

This is where the CAMP Facility contributes. The CAMP Facility is appropriately sized to enable the design, fabrication, and characterization of high-quality prototype cells using just a few hundred grams of the latest discoveries involving high-energy battery materials. Prototype cells made in the CAMP Facility generally have near 400-mAh capacity, which straddles the gap between coin cells and full cells nicely – two orders of magnitude from each end point. Thus, a realistic and consistent evaluation of candidate chemistries is enabled in a time-effective manner with practical quantities of novel materials.

The CAMP Facility is more than an arrangement of equipment, it is an integrated team effort designed to support the production of prototype electrodes and cells, and includes activities in materials validation, modeling, and diagnostics. It is not the aim of this facility to become a small battery manufacturer, but instead to be a laboratory research facility with cell production capabilities that adequately evaluate the merits and limitations of mid- to long-term lithium-ion chemistries in a close-to-realistic industrial format.

As new cell chemistries and systems progress, they reach the point where they are considered for further development in larger prototype cells. When this happens, a limited quantity of these materials, along with their preliminary data, are transferred from the lab to the CAMP Facility for materials validation to determine if they warrant further consideration. The source of these materials (anodes, cathodes, electrolytes, additives, separators, and binders) may originate from the ABR and BATT Programs, as well as from other domestic and foreign organizations such as universities, national labs, and industrial vendors. Electrochemical couples with high power and energy density are given extra priority. Lately efforts have focused on silicon-based anodes and LMR-NMC cathodes.

The CAMP Facility has the capability to make two prototype cell formats in a 45 m² dry room: pouch cells (xx3450 format, with capacity around 0.4 Ah) and 18650 cells. Pouch cells are anticipated to be easier to assemble, but they may suffer from bulging if gases are evolved during cell aging and cycling. 18650s, which are rigid containers, may be used if the pouch cell format is deemed unreliable due to gassing, or if higher capacity cells are needed (greater than 1 Ah). Central to this effort is a pilot-scale coating machine that operates with slurry sizes that range from 20 grams to a few kilograms. This is a key feature of the CAMP Facility that enables a professional evaluation of small quantities of novel materials. If needed, the MERF is available for scaling up materials for these prototype cell builds.

In general, two types of modeling are employed within this effort. First, battery design modeling is a spreadsheet based simulation that is used to determine the impedance behavior, available capacity, and thermal effects for general and specific cell, battery module, and battery pack designs. The model is also capable of performing simulations on multiple battery designs for comparison and optimization. In addition, the battery design model includes a module that calculates battery costs by combining materials and components costs with manufacturing expenses based on a plant design. A publicly available version of this work the battery performance and cost (BatPaC) model, is the only public domain model that captures the interplay between design and cost of lithium-ion batteries for transportation applications.

The other type of modeling is electrochemical modeling, which is aimed at associating electrochemical performance measurements with diagnostic studies conducted on lithium-ion cells. The methodology for the electrochemical model is described in detail in literature [1-3]. Essentially, continuum based transport equations are combined with kinetic and thermodynamic expressions to allow the potential, concentration, and current distributions to be determined throughout the cell. Two versions of the cell electrochemical model with the same basis are utilized to fully examine the broad range of electrochemical studies. One version of the electrochemical cell model is used to simulate the cell response from Electrochemical Impedance Spectroscopy (EIS) studies, and the other model version is utilized for examining DC studies, such as controlled

current or power cycling and diagnostic hybrid pulse power characterization (HPPC) tests.

Approach

The general approach used in this effort is to start small and grow large in terms of cell size and amount of resources devoted to each novel battery material. At various points in the development process, decisions are made to either advance, modify, or terminate studies to maximize utilization of available resources.

Coin cells (2032 size) are used for materials validation purposes with initial studies performed at room temperature or 30°C. After formation cycles, the coin cells go through HPPC testing, rate capability testing, and limited cycle life testing. Accelerated aging studies are also performed at 45°C to 55°C for promising materials to give a preliminary indication of life. Where appropriate, the thermal abuse response is studied using a differential scanning calorimeter.

Using the recommendations and results obtained by the materials validation of promising materials, single-sided electrodes are fabricated on the larger dry-room coater for diagnostic study. The new cell chemistries are studied in detail using advanced electrochemical and analytical techniques, including micro-reference electrode cells. Factors are identified that determine cell performance and performance degradation (capacity fade, impedance rise) on storage and on extensive deep-discharge cycling. The results of these tests are used to formulate data-driven recommendations to improve the electrochemical performance/life of materials and electrodes that will be incorporated in the prototype cells that are later fabricated in the dry room. This information also lays the foundation for electrochemical modeling focused on correlating the electrochemical and analytical studies, in order to identify performance limitations and aging mechanisms.

The approach for electrochemical modeling activities is to build on earlier successful characterization and modeling studies in extending efforts to new EV and PHEV technologies. The earlier studies involved developing a model based on the analytical diagnostic studies, establishing the model parameters, and conducting parametric studies with the model. The parametric studies were conducted to gain confidence with the model, examine degradation mechanisms, and analyze cell limitations. Efforts this year included expanding and improving the model's capabilities with the focus on LMR-NMC cathodes.

The approach for the battery design modeling studies is to continue to develop and improve methods to design lithium-ion batteries for electric-drive vehicles based on spreadsheet calculations. In addition, the battery design model is used to determine the impact of advanced materials on the current technology. The performance of the materials within the battery directly affects the energy density and cost of the battery pack. Both modeling efforts complement each other and are specifically aimed at supporting the CAMP facility goals.

If the results from diagnostics and modeling still look promising, full cell builds are conducted using double-sided electrodes. The electrodes are then either punched in the case of pouch cells, or slit in the case of 18650 cells and assembled into full cells in the dry room using the semi-automated cell assembly equipment. Formation procedures are conducted on the cells to encourage electrolyte wetting and solid-electrolyte-interface (SEI) formation. These cells undergo rigorous electrochemical evaluation and aging studies under the combined effort of the CAMP Facility team, and Argonne's Electrochemical Analysis and Diagnostic Laboratory (EADL) and Post-Test Facility. After testing, select cells are destructively examined by the Post-Test Facility to elucidate failure mechanisms. This information is then used to further improve the new chemistry, as well as future electrode and cell builds. The results of these tests are shared with other members of the ABR & BATT Programs and with those associated with the materials' origin, and with battery developers (if appropriate).

Results

Materials Validation.

Silicon-based Anodes. Three commercially available silicon materials have been obtained and are under various stages of testing. The first material is a 1-5 µm silicon powder from Alfa Aesar (Figure V - 12a); while the second is a silicon powder obtained from Nanostructured and Amorphous Materials Incorporated (NanoAmor). This material is a 130 nm silicon powder (spherical with some nanowires mixed in). A third source of silicon materials is from American Elements, which is available in several particle sizes in kg quantities. Particle sizes of 50, 150, and 1,000 microns were selected for validation and are now under test.

Lithium half cells have been made with laminates of various compositions. Currently in this study, the best electrode produced using Alfa Aesar silicon was a nearly pure silicon electrode with a lithiated PAA binder and a citric acid buffer (76 wt.% silicon, 10 wt.% C-45 carbon, and 14 wt.% LiPAA with citric acid buffer) (Figure V - 12b). This electrode was able to maintain high gravimetric capacities even at a 2C rate and has an average columbic efficiency of 99.4% during cycling.

While the morphology (and lack of surface treatment) of the readily available silicon powder from Alfa Aesar is not ideal, it is capable of being cycled and

was used as a temporary baseline for further binder development. Surprisingly, the cycle life was relatively good for initial electrode formulations that used high silicon to graphite content, which was attributed to competing binder functions, i.e., binders developed for silicon may not be ideal for graphite.

Studies were conducted with the silicon powder obtained from NanoAmor using lithiated polyacrylic acid (Li-PAA) as the binder, with graphite and a carbon additive in an aqueous slurry system. The electrode composition consisted of 9 wt% NanoAmor Silicon (130 nm), 80.5 wt% Timcal SFG-6 graphite, 5.5 wt% Li-PAA (450,000 m.w.) and 5 wt% Timcal C-45 carbon

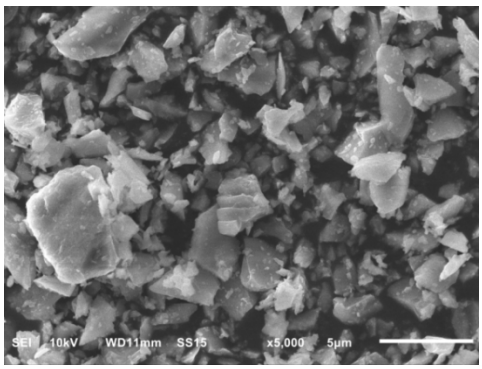

(a)

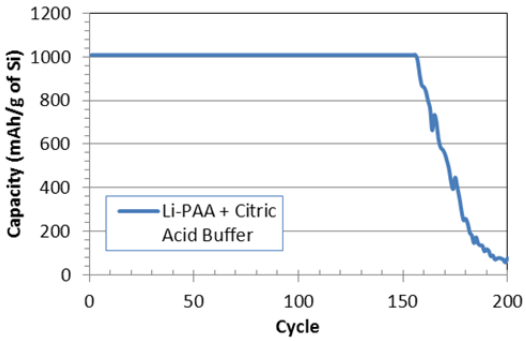

(b)

Figure V - 12: (a) SEM image of silicon powder from Alpha Aesar, and (b) capacity results for a silicon electrode (76 wt.% Alpha Aesar silicon, 10 wt.% C-45, and 14 wt.% LiPAA with citric acid buffer) vs. Li metal in 2032 coin cell (capacity limited cycles)

coated on 10 um copper foil. The slurry was prepared using sonication for the mixing process in de-ionized water. Half-cell coin cells were constructed using 97 wt.% 1.2 M $LiPF_6$ in EC:EMC (3:7 by wt) electrolyte with 3 wt.% fluoroethylene carbonate (FEC) additive. Electrochemical tests cycled the cells from 0.050V to 1.500V at a galvanostatic ~C/2.5 rate (Figure V - 13). It was encouraging to see a capacity that was higher than the graphite alone, but the capacity fade rate is still a problem that must be overcome. While additional validation needs to be performed, this appears to be a possible candidate to use for silicon-based anodes for prototype cell builds; it cycles better than most other silicon powders cycled thus far, and sizable quantities of this material can be obtained at reasonable prices without any limitations on its distribution and data reporting.

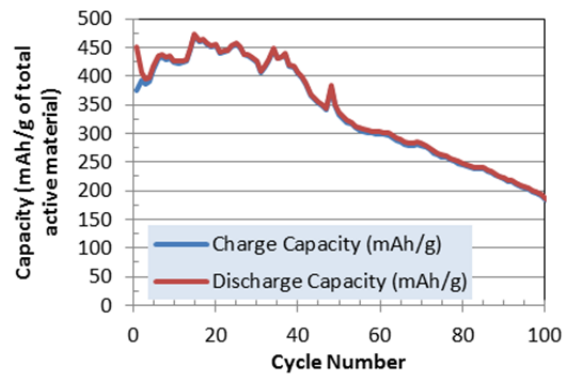

Figure V - 13: Silicon-graphite electrode using NanoAmor silicon powder vs. Li metal in coin cells. These cells were able to maintain capacities over 400 mAh/g for the first 40 cycles

An even more promising open source of silicon is the materials from American Elements, which has a range of particle sizes tailored to lithium-ion battery use. These silicon materials were received near the end of FY13 and are now under test.

In addition to testing commercial silicon materials obtained thus far, collaborations are ongoing with companies to make improved silicon/graphite composite electrodes. Samples of silicon were received from Electrochemical Materials (EM), with their proprietary organic coating on the silicon that allows it to cycle when using PVDF as a binder in a silicon/graphite composite electrode (Figure V - 14). Their improved coating also allows the particles to be coated in aqueous binder systems. A multitude of electrodes have been made with this new batch of powders, altering both the binder and the graphite. Currently, two different graphite powders are being used in conjunction with the EM powder. The first is the standard A12 (high power graphite) along with the less dense but more exfoliated SFG-6. A12 has been shown to underperform when mixed with silicon in aqueous systems, which is believed to be caused by improper binding to the graphite. However, since this silicon material can be made using PVDF (a binder which works well with the A12 graphite), this relationship needs to be further examined. In addition to testing PVDF, CMC (carboxyl methyl cellulose) is being tested as well per recommendation from EM.

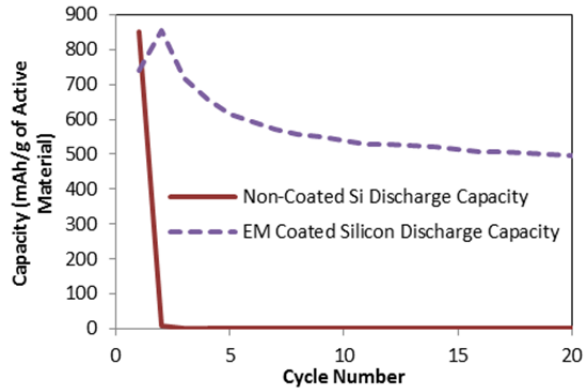

Figure V - 14: Comparison between Electrochemical Materials' (EM) surface-treated silicon against that of a silicon powder that has not been treated, both using PVDF as the binder. The EM electrode is 9 wt.% EM-treated silicon, 51 wt.% graphite, 10 wt.% carbon black, and 30 wt.% PVDF

A silicon-graphene electrode from XG Sciences was also received and tested. The electrode consisted of 70% Si/graphene active material, 20% graphene, and 10% PAA binder. The total loading, including grapheme and binder, is about 1.15 g/cm². 1.2 M $LiPF_6$ in EC/EMC with 10% FEC additive was used as the electrolyte. The Li/Si-C half cell was initially tested between 10mV and 1V at C/10 and 30°C. The test results of two formation cycles are shown in Figure V - 15. The reversible specific capacity was determined to be over 2,400 mAh/g based on the weight of silicon-graphene composite. The first cycle irreversible capacity loss was 17%. Rate performance tests were also conducted on the Li/Si-C half cell. The lithiation rate was fixed to C/5 rate and the delithiation rate varied from C/5 to 2C. Surprisingly, the silicon graphene composite electrode demonstrated excellent rate performance: no capacity drop was observed at even the 2C rate.

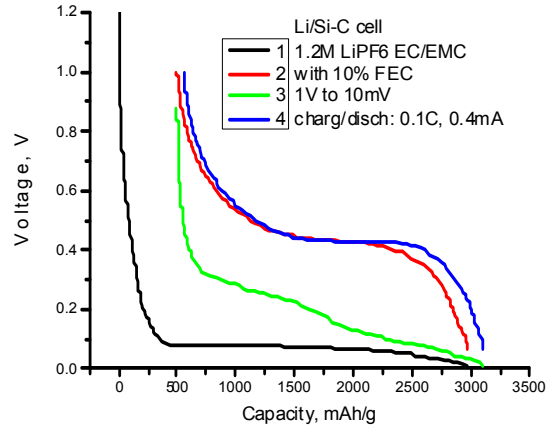

Figure V - 15: Voltage profile of Si-graphene from XG Sciences in a half cell during formation cycles

Since PVDF has been generally shown to be an inferior binder with uncoated silicon-based electrodes, other binders needed to be employed. Silicon undergoes major expansions and contractions during cycling, and when PVDF is used as the binder, electrical contacts between particles are difficult to be maintained. Repeated cycling of the electrode tends to fracture and isolate silicon particles from the conductive network, which diminishes the capacity. Using aqueous binders such as CMC, Alginic Acid or PAA increases cyclability by helping prevent the loss of contacts between particles, but these electrodes tend to be brittle.

The PAA aqueous binder system with graphite and silicon has shown positive performance in coin cell cycling, but there are challenging issues of physical properties during the slurry preparation process that need to be addressed. The PAA-based slurry has a shear thickening action and a time dependency for keeping the particles in suspension, which are not conducive to standard coating procedures. The dried electrodes are brittle as well. Typical PAA slurries have a pH between 2.6 and 3.0. An investigation to resolve these issues has included the use of a base, lithium hydroxide, to titrate the slurry to a higher pH. Several slurries were coated with varying pHs from a range below 3 to above 10. The study found that a slurry pH of 6 to 7 yielded slurries with reasonable fluid dynamics for coating, and dried calendered electrodes with the best cohesion and adhesion. Adjusting the pH to neutral has improved the fluidity of the slurry and electrode integrity, but the issue of particle separation in the slurry state is still prevalent. Future work will include considering thickening agents, such as xanthan gum, to minimize the particle settling issue. Also, supplementing or replacing lithium hydroxide with other bases, such as ammonium hydroxide, will be investigated.

In addition to the binders that have been tested, polyethylene-co-acrylic acid (PEAA) has been

considered a possible binder for silicon based electrodes. While electrodes made with only PEAA for a binder have shown poor electrochemical results, the electrode itself had better mechanical properties than electrodes made only with PAA or CMC, meaning that PEAA could be a useful additive. Electrodes made with xanthan gum have shown some promise as well. It is likely that a multi-component binder system will be needed to make an ideal silicon-composite anode.

Collaboration with binder manufacturer Zeon Chemical has produced useful insights into binder mechanisms. Zeon produces a polystyrene-butadiene rubber (SBR), which has been shown to improve the laminate's physical properties along with increased electrochemical performance. Zeon's binder has been tested in conjuction with mainly CMC upon their recommendations. In addition to supplying their binder, they loaned Argonne a Primix mixer, and with this mixer nine large scale slurries (all over 100 grams of solids) were made. Several graphite/SBR/CMC slurries were successfully coated on the large coater in the CAMP Facility dry room, with these being the first aqueous-based slurries to have been coated in the dry room environment. No adverse effect on the humidity in the dry room was noted. Future work involves creating a procedure that will maximize dispersion of the silicon particles with use of different mixers available along with trying a variety of additives to improve dispersion.

Silicon electrode provided by LBNL. Dr. Gao Liu (LBNL) invented a conductive binder designed to improve the cyclability of silicon electrodes by tailoring the polymer with dual functionality: conducting electricity and binding closely to silicon particles. This conductive binder is referred to as PFFOBM. A silicon electrode with 33% PFFOBM was prepared by Dr. Liu and shipped to Argonne. Upon receipt, the electrode was vacuum dried and then assembled in coin cells with 1.2 M $LiPF_6$ in EC/EMC (3:7 by wt.) electrolyte plus 10 wt.% FEC. Three formation cycles were conducted on these lithium half cells at a C/10 rate between 1 V and 10 mV. After three formation cycles, the half cells underwent various lower cut-off voltages during cycling: 10 mV, 40 mV, and 200 mV. For the cell with the 200 mV cut-off voltage cycling, a capacity rate test was conducted before life cycling. The delithiation capacity for each cell is shown in Figure V - 16.

All the cells showed relatively good cycling performance, regardless of the cut-off voltage, compared to non-conductive binders. It can also be seen from this plot that the cell with the lowest cut-off voltage (10 mV) experienced the fastest capacity fade rate, which is expected due to the excessive volume expansion upon lithiation. When the higher cut-off voltage is used, less lithiation of the silicon particle occurs, leading to less stress and volume expansion in the silicon particle. This will in turn improve the cycle life. In Figure V - 16 (bottom), the coulombic efficiency is plotted as a function of cycle number. Another interesting cut-off voltage effect was observed: the coulombic efficiency increased continuously with cycling when 10 mV and 40 mV were used as cut-off voltages. However, the coulombic efficiency jumped up to almost 100% when the cut-off voltage was changed to 200 mV. It is believed that the coulombic efficiency improvement is related to less stress of the SEI at 200 mV. When a low cut-off voltage is used, the high stress as discussed above will pulverize the particle and expose the new surface for new SEI formation, resulting in low coulombic efficiency.

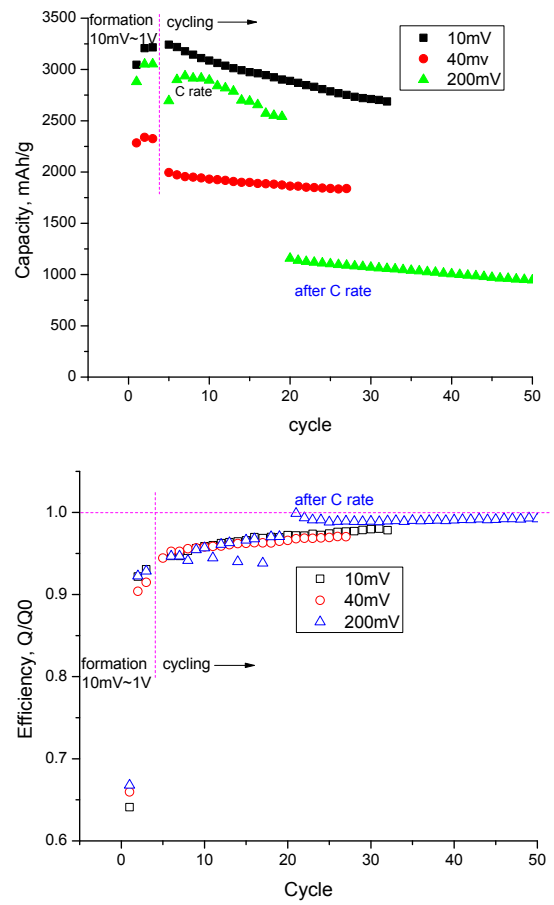

Figure V - 16: Cycling (top) and coulombic efficiency (bottom) of silicon electrode with PFFOBM conductive binder from LBNL. Note that, in the top curve, the lower cutoff was raised from 10 to 200mV at 20 cycles in the green data, resulting in a drop in capacity

Cathodes. Materials are constantly being sought that are of interest to the battery R&D community. If warranted, several of these materials are then added to the Electrode Library. The latest material that is ready to be made into electrodes is $LiCoO_2$. The materials

validation process has been completed on this material and an electrode has been designed for inclusion in the Electrode Library.

$LiCoO_2$ is one of the most used cathode materials in lithium-ion batteries and serves as a valuable baseline for material researchers. An electrode was made with $LiCoO_2$ from BTR (China), which was used as received. The electrode consisted of 94 wt.% $LiCoO_2$, 2 wt.% Super P-Li carbon black, and 4 wt.% PVDF binder. The punched electrode was fabricated into 2032 coin cells after calendaring with 1.2 M $LiPF_6$ in EC/EMC (3:7 by wt.) as the electrolyte. These lithium half cells were cycled between 4.1 V and 3.0 V at C/10 for three cycles. The voltage profile is shown in Figure V - 17. The reversible capacity after three cycles was 125 mAh/g with less than 10% initial irreversible capacity loss during the 1st cycle.

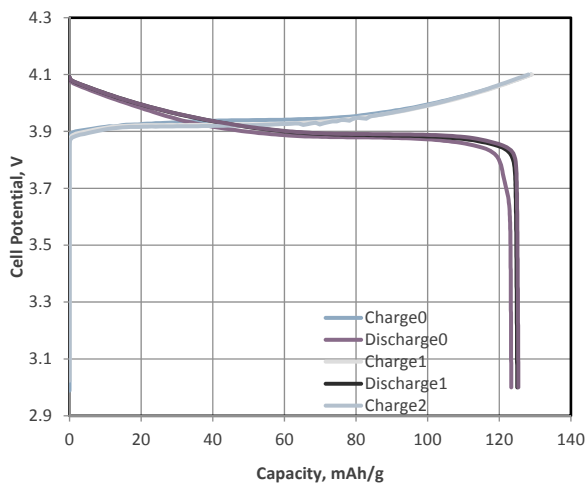

Figure V - 17: Voltage profile of Li/$LiCoO_2$ cell at C/10 rate

After three formation cycles, the cells were subjected to a capacity rate study. Those results are shown in Figure V - 18. It can be seen from the figure that this material can deliver over 110 mAh/g up to the 1C discharge rate. The cells were then cycled at a 0.3 C rate between 4.1 V and 3.0 V. More than 90% capacity retention was obtained after 50 cycles. More capacity can be expected if the voltage is increased to 4.2 V vs. lithium.

Additional materials that are currently going through the materials validation process are as follows: Hanwah $LiFePO_4$, Toda 4V Spinel, Toda NCM 424, and Toda HE5050 (5/13 10-kg batch). Kureha Hard Carbon (J and S(F) grades) and MCMB (G-15) graphite will also be added to the library. The electrochemical performance data on these materials will be used to design electrodes that will match those in the Electrode Library.

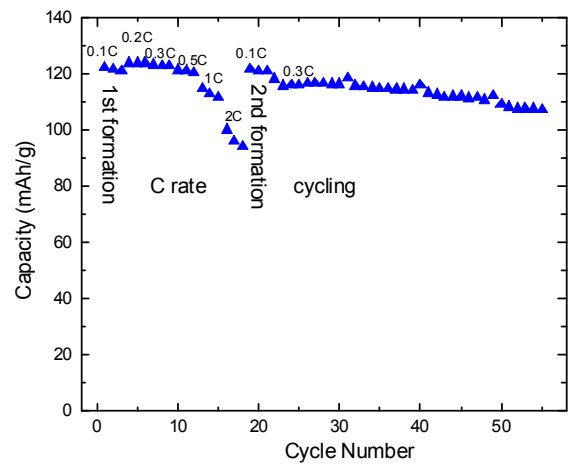

Figure V - 18: Rate study and cycling performance data for Li/$LiCoO_2$ half cell

The electrochemical validation of $LiFePO_4$ powder from Hanwha was completed using lithium metal half cells. The electrode consisted of 84% $LiFePO_4$, 4% SFG-6, 4% carbon black, and 8% PVDF binder. The loading was 9.3 mg/cm². The electrode porosity was calculated to be 30% after calendering. The electrolyte used was 1.2 M $LiPF_6$ in EC/EMC without any additive. According to the formation cycle at a C/10 rate between 2.9 V and 3.8 V, the specific capacity during the 3rd formation cycle was 150 mAh/g (Figure V - 19). The irreversible capacity loss was about 4% during the 1st cycle. The rate performance test was also conducted on the half cells. The capacity delivered at the 2C rate was still more than 82% of the C/10 capacity.

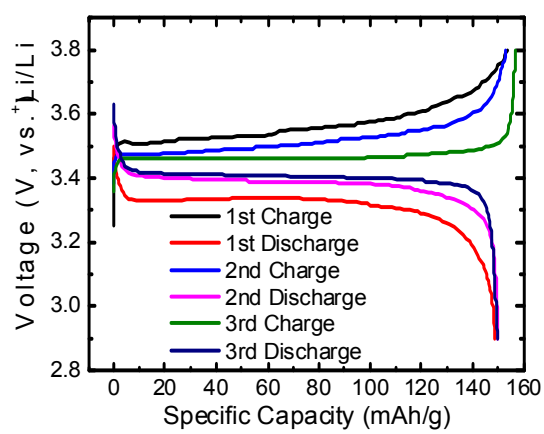

Figure V - 19: Voltage profile of Li/$LiFePO_4$ half cell during formation cycles

JPL Coated Cathode. Two cathode powders were received from Jet Propulsion Lab (JPL). One powder is $Li_{1.2}Mn_{0.54}Ni_{0.13}Co_{0.13}O_2$ and the other one is a similar powder with 1 wt.% $AlPO_4$ coating (Figure V - 20). The brightness of the coated particle is caused by the charge

during SEM measurement, which indicates the insulating feature of the coating.

These powders were made into electrodes using the same formulation: active materials/SFG-6/carbon black/PVDF = 86/4/2/8. Lithium half cells were used to characterize the electrochemical performance of these two active materials. The separator was Celgard 2325 and 1.2 M $LiPF_6$ in EC/EMC solvent was used as the electrolyte.

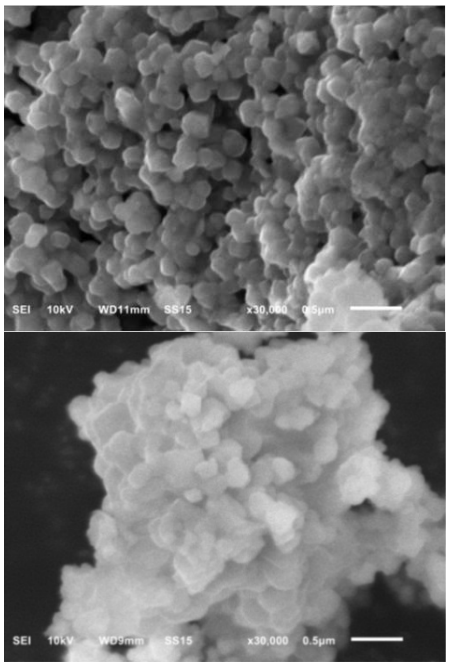

Figure V - 20: SEM images of $Li_{1.2}Mn_{0.54}Ni_{0.13}Co_{0.13}O_2$ (top) and similar material with 1 wt.% $AlPO_4$ coating (bottom). SEM from Argonne's Post Test Facility

It was noticed from the formation cycle that both materials showed a typical activation voltage plateau near 4.5 V, which is similar to other LMR-NMC materials. However, a difference between the two active materials was observed when the differential capacity profile was compared in Figure V - 21. For the coated sample, the reduction peak slightly above 3.0 V shifted to lower potentials. In addition, a new reduction peak was observed near 2.5 V, which suggests that the coating process has an impact on the electrochemical performance of LMR-NMC.

The voltage fade protocol was also applied to these two materials. Basically, a low current of 10 mA/g was used for the 1st formation cycle, followed by cycling at a current of 20 mA/g. The voltage profiles vs. normalized capacity are shown in Figure V - 22a. The black curves correspond to the uncoated sample and the red curves correspond to the coated sample. The lower operational voltage of the coated sample can be clearly seen near the end of discharge. This results in a lower average discharge voltage for the coated sample as shown in Figure V - 22b. It was also noticed that the discharge voltage fade rate of the coated sample is comparable, if not worse, to that of the uncoated sample.

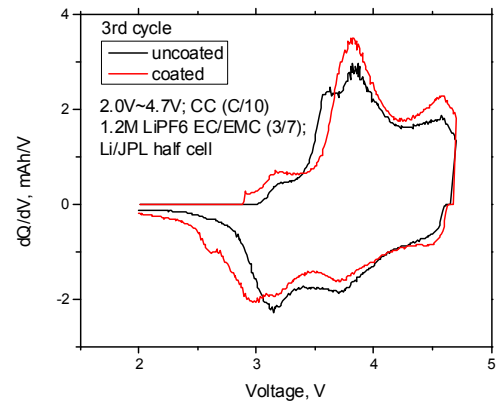

Figure V - 21: Different capacity plot of $Li_{1.2}Mn_{0.54}Ni_{0.13}Co_{0.13}O_2$ with and without $AlPO_4$ coating

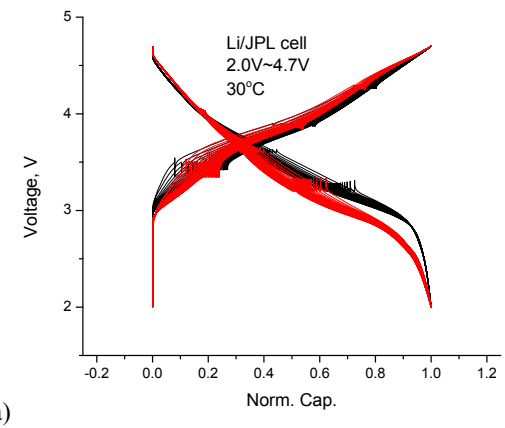

a)

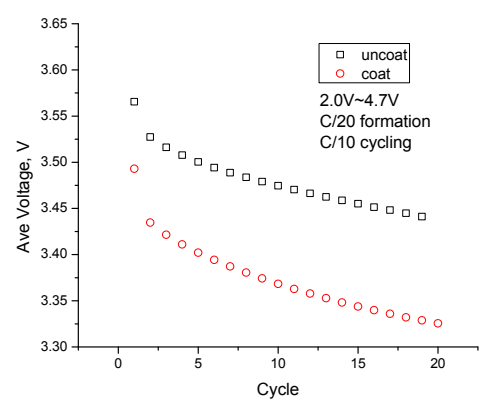

b)

Figure V - 22: a) Voltage profile and b) average voltage as a function of cycling for $Li_{1.2}Mn_{0.54}Ni_{0.13}Co_{0.13}O_2$ with and without $AlPO_4$ coating

Alumina-doped Cathode. It has been reported that addition of alumina powder to the positive electrode coating can improve cell capacity retention. To test this

claim, positive electrodes were prepared by blending 5 wt% Al_2O_3 nanosized powder with the other electrode constituents: $Li_{1.2}Mn_{0.55}Ni_{0.15}Co_{0.1}O_2$ (HE5050), SFG-6 graphite, Super P carbon and PVDF (Solvay 5130) binder. The Al_2O_3 powder had a particle size of ~50 nm and a high surface area (32–40 m^2/g). To ensure adequate dispersion, the Al_2O_3 powder was mixed into NMP at the beginning of the slurry making process.

Figure V - 23 shows cycling data and impedance spectra from full–cells containing the alumina-powder modified positive electrode and an A12 graphite negative electrode. The capacity fade after 50 cycles (~C/3 rate) is ~0.12% per cycle, significantly better than the ~0.48% per cycle for the baseline cell. The improved cell capacity retention probably results from HF- and water- scavenging by the alumina. On the other hand, the impedance rise of the alumina-powder modified cells is similar to that of baseline cells. The data suggest that cell capacity fade is largely independent of impedance rise for this cell couple.

Aqueous Binders. Due to its stronger adhesive ability and environmental friendliness, aqueous based binders have become very popular with graphite/carbon anode materials. Recently, Argonne has investigated the SBR based aqueous binders from JSR Micro for graphite electrodes. The electrochemical performance results obtained look promising.

JSR Micro is also working on an aqueous binder for cathode electrodes. Argonne used their fluorinated acrylic hybrid latex binder (FA) for a cathode using LMR-NMC (Toda HE5050). In this study, three different binder content, 1%, 2% and 4%, were used to make slurries. The carbon content in all the slurries was 5 wt.%. Lithium half cells were used as the test vehicle to investigate the binder impact on the electrochemical performance of LMR-NMC.

Figure V - 24 shows the resulting voltage profile of these Li/LMR-NMC half cells using 1 wt.% aqueous binder during three formation cycles. Compared to previous test results on HE5050 using PVDF-NMP binders, no difference was observed. The lithium half cells with 2% and 4% aqueous binders show similar results. HPPC, rate performance, and cycling tests were also conducted on the half cells. They all show comparable performance to that of cells with PVDF-NMP binders. The next step was to make a full cell that operated solely with aqueous binders.

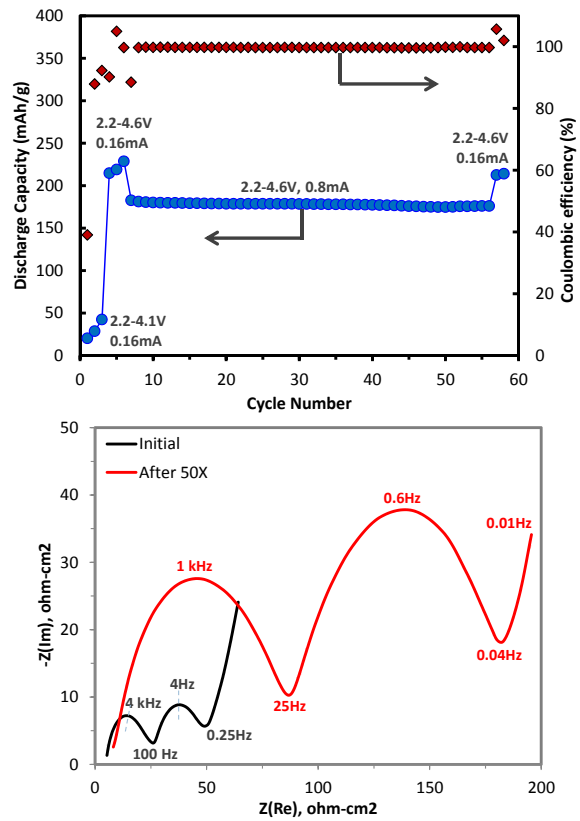

Figure V - 23: Plots for full cells containing the alumina-powder modified positive electrode showing (top) discharge capacity and columbic efficiency changes with cycle number, voltage range, and current, and (bottom) EIS data after initial cycles (black) and after fifty 2-4.6 V cycles (red)

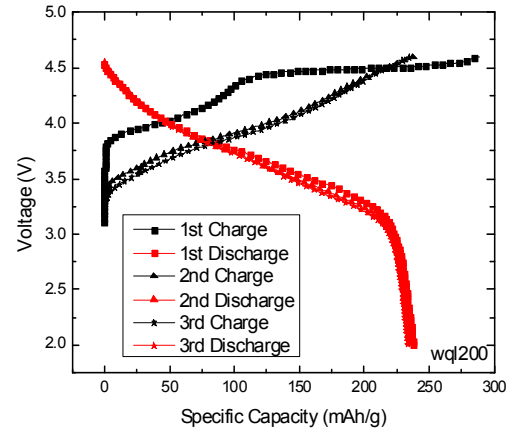

Figure V - 24: Formation cycles of LMR-NMC using aqueous binder from JSR Micro

Full cells were made and tested of graphite/HE5050 in coin cells using SBR and FA as binders, respectively. The electrode composition for the graphite anode was 98 wt.% graphite (A12, Phillips 66), 1 wt.% sodium carboxymethyl cellulose (CMC, MAC350, Nippon Paper Chemicals) and 1 wt.% SBR binder. The cathode

comprised 92 wt.% of HE5050, 5 wt.% of C-45 carbon black, 2 wt.% of CMC, and 1 wt.% of FA binder. The full cells were tested using established protocols from the Voltage Fade project: one cycle at 10 mA/g between 4.5 V and 2.0 V, followed by 20 mA/g with the same voltage window. The voltage profile is shown in Figure V - 25. There is roughly 85% capacity retention after 50 cycles, which is only slightly less than the full cell using PVDF binder. These results, combined with other favorable information from rate test and hybrid pulse power characterization tests (not shown here) highlight the possibility of designing novel battery systems with high energy, long cycle life, low cost, which are environmentally benign.

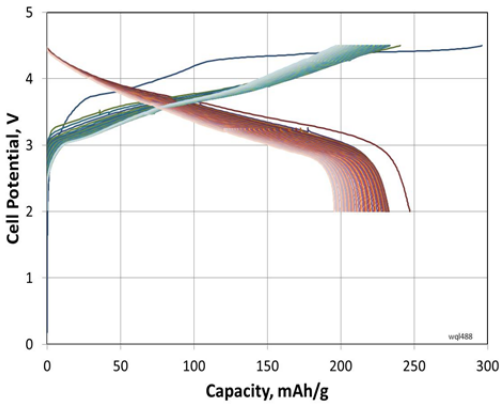

Figure V - 25: Voltage profile of graphite/LMR-NMC cell using aqueous binders from JSR Micro

Electrolyte Additives. Electrolyte additives are known to be an effective and economic approach to improving the stability of electrode surface films. In the past two decades, many organic and inorganic compounds have been identified as effective electrolyte additives: examples include vinylene carbonate (VC), ethylene sulfite (ES), vinyl ethylene carbonate (VEC), and FEC. In recent years, with the emergence of many high-voltage cathode materials, the anodic stability of common electrolytes is recognized as the main bottleneck limiting the calendar- and cycle- life of high-energy lithium-ion cells. Therefore, more attention has been devoted to improving stability of the cathode–electrolyte interface.

Ways are being examined to mitigate performance degradation of cells containing $Li_{1.2}Ni_{0.15}Mn_{0.55}Co_{0.1}O_2$-based positive electrodes that are cycled at voltages beyond 4.5 V versus Li. Studies indicate that common electrolyte additives such as VC, VEC, and FEC are not effective at enhancing long-term cycling performance of these cells, *i.e.,* stable electrode passivation is not achieved with traditional SEI-forming additives. This observation underscores the need for new electrolyte additives that effectively form stable electrode passivation films in high-energy and high-voltage lithium-ion cells.

The synergistic effects of $LiB(C_2O_4)_2$ (LiBOB), $LiF_2B(C_2O_4)$ (LiDFOB), triphenylamine (Ph_3N), and 1,4-benzodiozane-6,7-diol (BDOD) as functional electrolyte additives in cells was examined (see Figure V - 26). The influence of these additives, individually, and in different combinations, was evaluated using galvanostatic cycling of cells containing $Li_{1.2}Ni_{0.15}Mn_{0.55}Co_{0.1}O_2$-based positive electrodes, graphite–based negative electrodes, and a $LiPF_6$–based electrolyte. EIS, linear sweep voltammetry (LSV), and voltage-hold tests were also used. The data showed that cell performance can be significantly improved by choosing additives that separately affect the positive and negative electrodes, thus circumventing the difficulty of finding *one* good bifunctional additive. In addition, the synergistic effects of electrolyte additive combinations can be beneficial to cell performance.

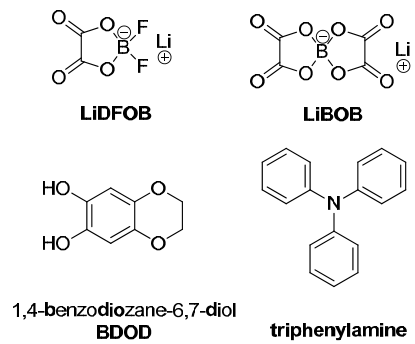

Figure V - 26: Chemical structures of additives used in this work

The following conclusions can be reached from these various tests:

1. All additive-bearing cells show certain performance improvements over cells containing the baseline electrolyte, both at 30° and 55°C.
2. Cells containing only the LiBOB additive show better capacity retention, but higher impedances, than those containing the structurally-similar LiDFOB additive.
3. The aromatic organic compounds Ph_3N and BDOD are oxidized at the positive electrode before the baseline electrolyte; these compounds are also effective at reducing electrolyte oxidation. However, when used individually, these additives do not reduce cell performance degradation on long-term cycling.
4. The addition of LiDFOB, Ph_3N, and BDOD to LiBOB-containing cells further improves capacity retention (see Figure V - 27) and lowers impedance rise on extended cycling. These additives may enhance the passivation characteristics of cathode surface films, reducing electrolyte oxidation and protecting the oxide surface.

5. The SEI films formed with additives examined in this study are not completely stable under the test conditions used. Even the best additive combination only slows down performance degradation and does not completely prevent it.

Polyfluoroalkyl (PFA) compounds are well known for their high chemical stabilities, and exhibit both hydrophobic and lipophobic behaviors. Upon dispersing in organic solvents, solvophobic PFAs tend to aggregate and form micelles in solution. These types of compounds have been extensively used as fluorosurfactants, and are especially valuable as additives in stain repellents. In light of these facts, it can be envisioned that compounds containing PFAs could serve as a new type of electrolyte additive, forming double-layered passivating layers that reduce both electrode surface degradation and electrolyte

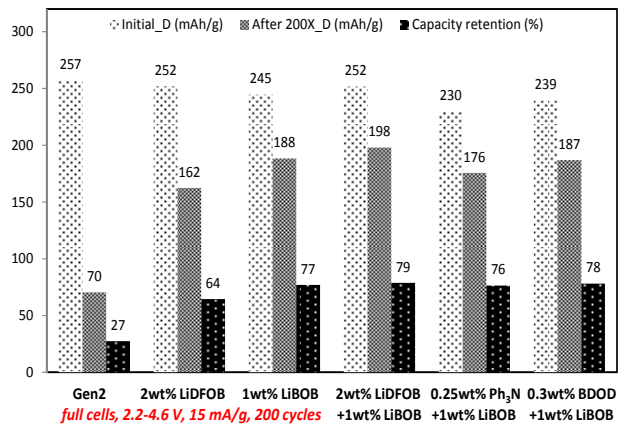

Figure V - 27: Capacity and capacity retention of full cells cycled at 30°C between 2.2 and 4.6 V at a 15 mA/g rate showing the effect of various additives in the Gen2 electrolyte. The capacity values (and cycling current) are based on the $Li_{1.2}Ni_{0.15}Mn_{0.55}Co_{0.1}O_2$ content in the positive electrode

decomposition. In our design, the PFA additive has two components: (i) a reactive headgroup for attachment onto electrode surfaces via either reductive or oxidative decomposition, so that it becomes an integral part of the surface layer (inner layer); (ii) a polyfluoroalkyl chain that self-assembles on this inner layer as a solvophobic layer (outer layer) that is highly stable and impermeable to the electrolyte solvent. To explore this novel idea, we synthesized a series of PFA-substituted ethylene carbonates (polyfluorooctyl-EC or PFO-EC) and studied them as electrolyte additives in our lithium-ion cells.

Figure V - 28 shows capacity-voltage data from $Li_{1.2}Ni_{0.15}Mn_{0.55}Co_{0.1}O_2$//graphite full cells containing the Gen2 electrolyte and Gen2+0.5wt% PFO-EC electrolyte. After 200 cycles, the discharge capacity of cells with 0.5 wt% PFO-EC is 172 mAh/g, which is 66% of its initial discharge capacity (260 mAh/g). In contrast, the discharge capacity of the baseline (Gen2 only) cells is 70 mAh/g, which is 27% of its initial discharge capacity (258 mAh/g). These data indicate that the 0.5 wt% PFO-EC additive enhances capacity retention.

The PFO-EC additive is also effective at inhibiting cell impedance rise during long-term cycling. Figure V - 29a shows that cells with 0.5 wt% PFO-EC have similar impedances as baseline cells after the initial cycling. However, after 200 cycles between 2.2 and 4.6 V (Figure V - 29b), the impedance of the PFO-EC bearing cell is much smaller than that of the Gen2 baseline cell. Previous studies have indicated that cell impedance rise in $Li_{1.2}Ni_{0.15}Mn_{0.55}Co_{0.1}O_2$//graphite full cells occurs primarily at the positive electrode. The reduced full cell impedance for the PFO-EC containing cells suggests that the additive forms effective surface films at this electrode.

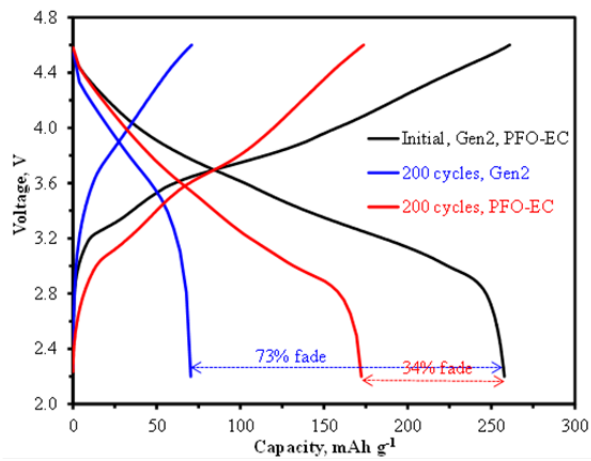

Figure V - 28: Capacity-voltage plots for full cells containing the Gen2 electrolyte and Gen2+0.5wt% PFO-EC electrolyte. The data were acquired with a 15 mA/g(oxide) current in the 2.2-4.6 V voltage window at 30˚C. The initial data are similar for cells with and without the additive

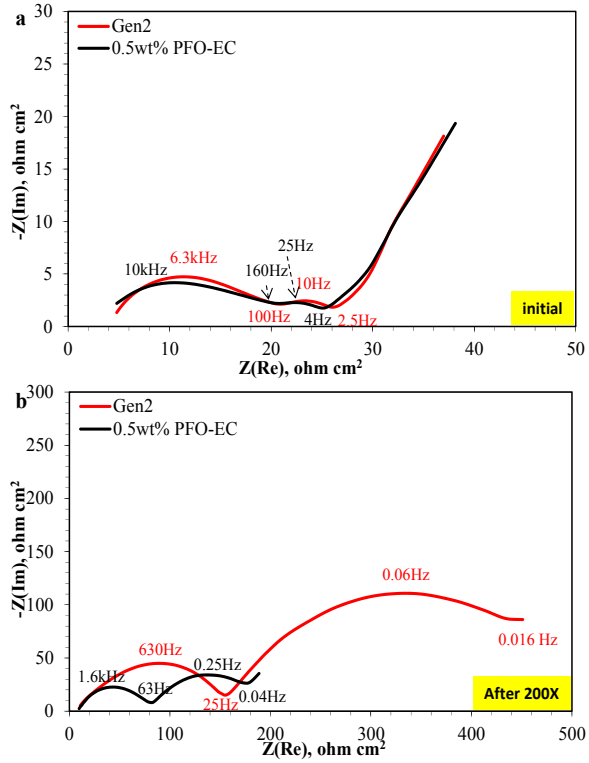

Figure V - 29: AC impedance spectra of $Li_{1.2}Ni_{0.15}Mn_{0.55}Co_{0.1}O_2$/ /graphite full cell after (a) formation cycles, (b) 200 cycles at 30°C with and without 0.5 wt% PFO-EC

Prototype Fabrication.

MERF Cathodes. The MERF has supplied the CAMP Facility with two separate batches of the $Li_{1.25}Ni_{0.3}Mn_{0.62}O_2$ cathode (LMR-NMC) material made via the carbonate process. This is a high-energy material that is of particular interest because it is cobalt free. The first batch (Lot# 2012-02-22) had a particle size distribution at D50 of 15µm, with a tap density of 1.36 g/cc (Figure V - 30). The second batch (Lot# 2012-07-09&11) has a particle size distribution at D50 of 7.8µm, with a tap density of 1.49 g/cc (Figure V - 31). The SEM images show the improved particle morphology from Lot# 2012-02-22 to Lot# 2012-07-09&11. The latter also has both a lower particle size distribution at D50 and higher tap density.

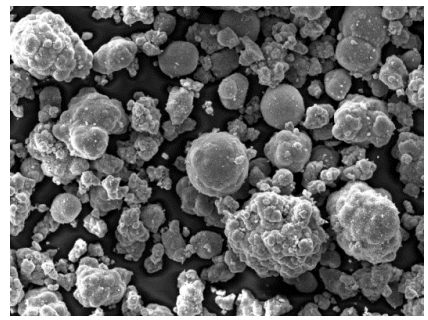

Figure V - 30: SEM images of MERF $Li_{1.25}Ni_{0.3}Mn_{0.62}O_2$ (Lot# 2012-02-22) powder at 1000x. SEM from Argonne's Post Test Facility

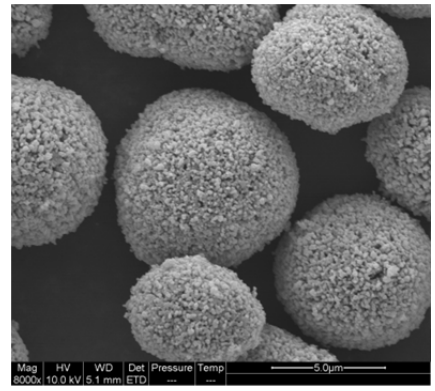

Figure V - 31: SEM images of MERF $Li_{1.25}Ni_{0.3}Mn_{0.62}O_2$ (Lot# 2012-07-09&11) powder. SEM from Argonne's Post Test Facility

Each cathode powder was used to fabricate electrodes for individual pouch cells builds. The Lot# 2012-02-22 was given the build name (CFF-B8), and the Lot# 2012-07-09&11 was given the build name (CFF-B13). Both cathode electrodes were fabricated using 90 wt.% LMR-NMC, 5 wt.% Timcal C-45 carbon black, and 5 wt.% Solvay 5130 PVDF. Both anode electrodes were fabricated using 91.8 wt.% Phillips 66 A12 graphite, 2 wt.% Timcal C-45 carbon black, 6 wt.% Kureha KF-9300 PVDF, and 0.17 wt.% oxalic acid. The coated and calendered cathode SEM images may be found in Figure V - 32 (CFF-B8) and Figure V - 33 (CFF-B13). Both cathode electrodes experienced particle fracturing during the calendering process, as seen in the SEM images, but the CFF-B13 cathode had less particle fracturing than CFF-B8.

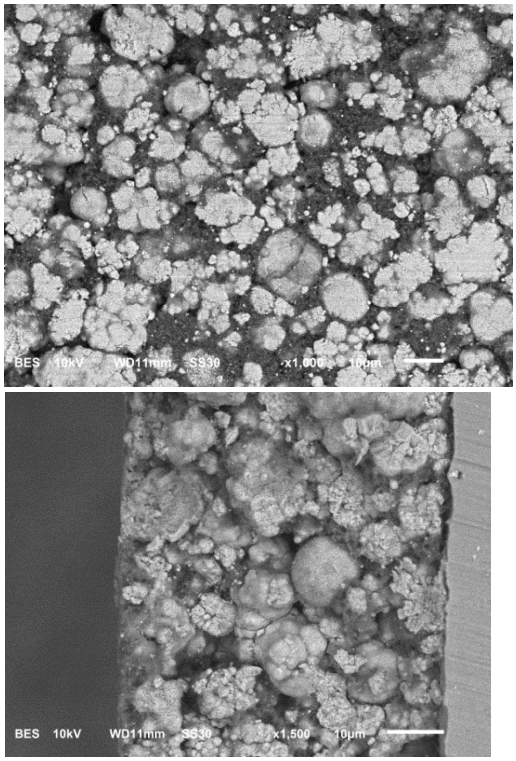

Figure V - 32: SEM images of CFF-B8 for a) Surface and b) Cross section. SEM from Argonne's Post Test Facility

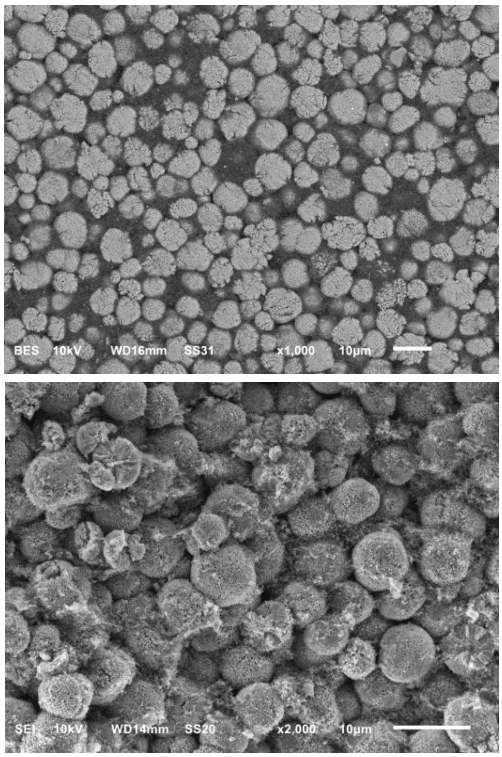

Figure V - 33: SEM images of CFF-B13 for a) surface and b) cross section. SEM from Argonne's Post Test Facility

The rate testing results of the CFF-B8 and CFF-B13 are shown in Figure V - 34a and Figure V - 34b, respectively. CFF-B13's rate performance surpassed that of CFF-B8's. The improved performance is likely due to the minimized particle cracking and fracturing during the calendering process, more uniform particle morphology, and lower particle size distribution. The CFF-B13 performance at lower rates (C/5) is reasonable, but the higher rates quickly degrade as can be observed in the data spread of the 8 cells plotted.

a)

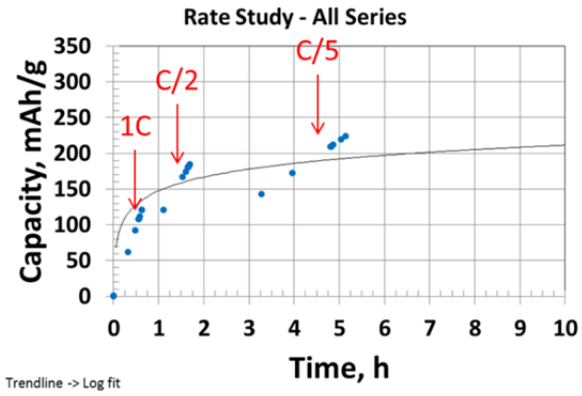

b)

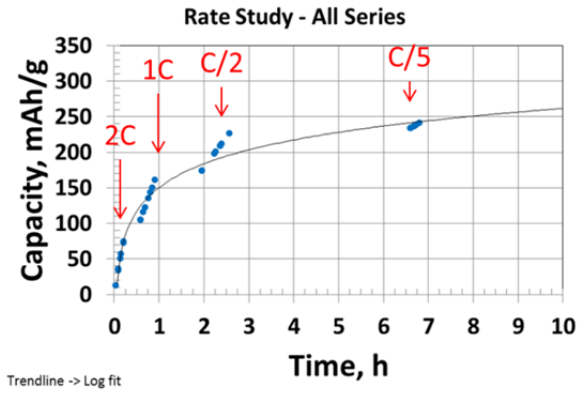

Figure V - 34: a) Rate performance results of 8 identical CFF-B8 cells. b) Rate performance results of 8 identical CFF-B13 cells. Note: testing was performed at 30°C using 1.2 M $LiPF_6$ in EC:EMC (3:7 by wt.). Trend line in both plots is the average log fit for the 8 cell data series

Similar trends were seen during the cycle life testing of CFF-B13 in Figure V - 35, where the cathode electrode is able to transfer charge at lower rates, but significant loss of charge transfer occurs during the C/2 rates. The pouch cell electrochemical results show improved performance of the MERF LMR-NMC Lot# 2012-07-09&11 over the MERF LMR-NMC Lot# 2012-02-22. These results coincide with the SEM and raw powder specification improvements in terms of particle size, morphology, and tap density. Continued efforts by the CAMP Facility will be performed to evaluate future

MERF cathode materials using pouch cells. These include LMR-NMC powders made via the carbonate and hydroxide processes.

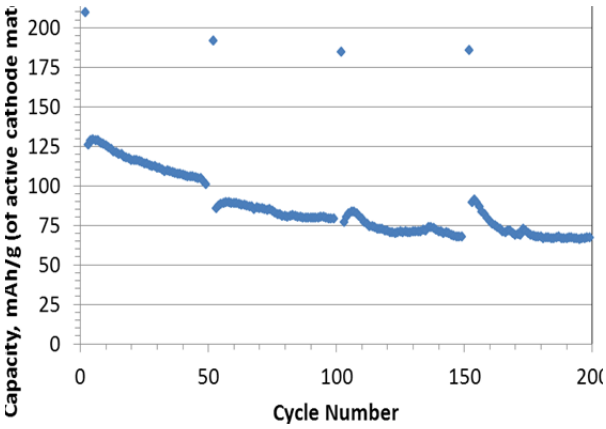

Figure V - 35: Cycle life plot of a CFF-B13 pouch cell with ~400 mAh C/1 capacity and 169 cm² cathode area, at 30°C, and C/2 rate. C/24 rate (data points included in plot) and HPPC (data points not reported in plot) performed every 50 cycles. 4.4 V to 2.5 V voltage window used

In an effort to understand and improve the performance of the MERF-made LMR-NMC ($Li_{1.25}Ni_{0.3}Mn_{0.62}O_2$) material, particle optimization and electrode composition was examined. Previous studies of the MERF-made LMR-NMC powder had shown that particle cracking occurred during the calendering process. The particle cracking has been hypothesized to be a significant factor in the poor performance at high current rates due to the particles having less of an electronic network because the particle fragments had been dislodged and isolated from the network. To troubleshoot the problem, staff at MERF milled the original LMR-NMC powder using the method of ball milling for 72 hours then dried the LMR-NMC material at 95°C for 48 hours. The dried material was then pulverized using a small-scale pulverizer for 3 minutes. The idea was to "pre-crack" the weaker particles before the calendering process to allow the binder and carbon black to coat the newly created particle during the slurry preparation for a thorough covering.

Electrodes were fabricated using both the original (un-milled) LMR-NMC powder and the milled LMR-NMC powder with 84/8/8 composition and 90/5/5 (LMR-NMC/Timcal C45/Solvay PVDF) composition. The results indicated that the milling of the LMR-NMC powder was detrimental to the overall electrochemical performance of the coin cell half-cells, especially at higher discharge rates in the rate study (Figure V - 36).

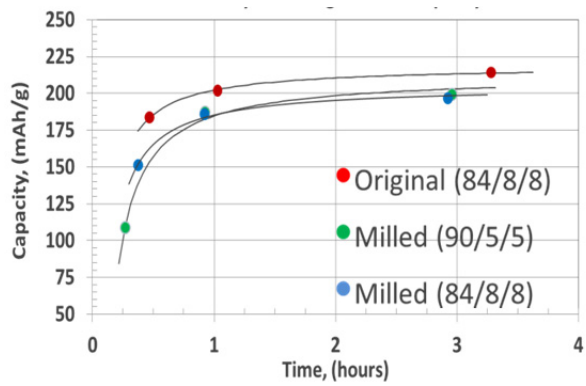

Figure V - 36: Discharge capacities for original (un-milled) and milled LMR-NMC powder from MERF versus lithium as a function of discharge time in 2032 coin cells. Voltage window (2.0 - 4.6 V), charged and discharged at C/3 (11 mA/mg), 1C (33 mA/mg), and 2C (66 mA/mg) rates; 5 cycles at each rate. All electrodes were calendered to ~35% porosity

Electrolyte Additives. Efforts by the CAMP team have shown improved capacity retention over time and cycles using LiDFOB and/or LiBOB additives in the standard 1.2 M $LiPF_6$ in EC:EMC 3:7 by wt (Gen2) in coin cells using graphite/LMR-NMC cells. (The additive validations for LiDFOB and another additive, HFiP, from MERF had been completed previously.) Based on these promising results, two combinations of the additives were chosen to be tested in the xx3450 pouch cell configuration, namely: 1) Gen2 + 2 wt.% LiDFOB and 2) Gen2 + 2 wt.% LiDFOB + 1 wt.% LiBOB. The electrode couple used for the pouch cell testing was Toda HE5050 ($Li_{1.2}Ni_{0.15}Mn_{0.55}Co_{0.1}O_2$) and A12 Graphite from Phillips 66.

The nomenclature shown in Table V - 3 depicts the Build 9 (Toda HE5050 vs. A12) electrode couple with varying suffixes (i.e., "A," "B," "C") for the electrolyte variables. 8 pouch cells were constructed and tested for B9A, 4 for B9B, and 4 for B9C.

Table V - 3: Pouch cell builds for electrolyte additive study using Gen2 electrolyte—1.2 M $LiPF_6$ in EC:EMC (3:7 by wt)

Build ID	Electrode Couple	Electrolyte
CFF-B9A	HE-5050 vs. A12	Gen2
CFF-B9B	HE-5050 vs. A12	Gen2 + 2wt.% LiDFOB
CFF-B9C	HE-5050 vs. A12	Gen2 + 2wt.% LiDFOB + 1wt.% LiBOB

The electrolyte additives were prepared for the B9B and B9C pouch cells on the same day the cells were filled with electrolyte and started formation procedure. Due to the nature of the pouch cell design and increased electrode area to electrolyte volume, the evacuated and sealed cells underwent a 24 h soak in the electrolyte to encourage wetting of the separator and electrodes. Immediately prior to the 24 h soak, a 5 minute C/10 tap

charge was performed on each cell to drive the anode potential down to mitigate corrosion of the anode copper foil. Following the 24 hour soak, formation cycling of the cells began (2.5 V to 4.1 V at C/10, then 4.55 V at C/10, then 4.5 V at C/3). There were slight differences seen in the voltage profile formation data when comparing the "Gen2 only" cells to the additive cells (Figure V - 37). It appears that the additives are being partially activated during the tap charge, and then fully activated during the first charge to 4.1 V (after the 24 hour hold).

Following the formation procedure, the cells were taken to the dry-room, cut open, evacuated, and resealed to remove any generated gas from formation (standard for typical pouch cell testing protocol). Cycling was then continued to determine the rate capability for each set of cells, which is shown in Figure V - 38.

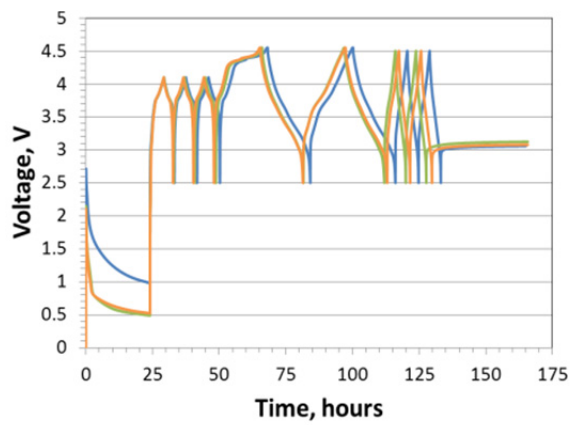

Figure V - 37: Formation profile used for B9A, B9B, and B9C consisting of sequential cycling with voltage window of 2.5 V to 4.1 V at C/10, then 4.55 V at C/10, then 4.5 V at C/3, performed at 30°C

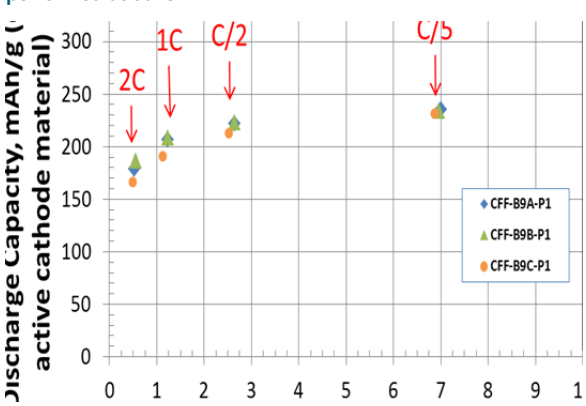

Figure V - 38: Rate Study of B9A, B9B, and B9C. Testing performed at 30°C. Voltage widow of 2.5 V to 4.5 V. Nominal rates of C/5, C/2, 1C and 2C at 3 cycles each were used. The 3rd cycle for each rate is plotted above

Cell builds B9A, B9B, and B9C all resulted in similar rate performance when compared with each other. The ~240 mAh/g for the C/7 rate and ~165 mAh/g for the 2C rate matched well to the coin half-cell data from the earlier materials validation results for HE5050 in Gen2 electrolyte. Following the rate study, HPPC testing was performed on these cell builds. The resulting ASI plots for both discharge and charge pulses are shown in Figure V - 39.

Similar to the rate study results, the initial HPPC results between the three cell builds show strong similarities to one another. Overall, a slight improvement in the discharge and charge ASI can be seen for the cell builds with additives. The coin cell studies also showed improvements in the impedance with the use of the LiDFOB/LiBOB additives.

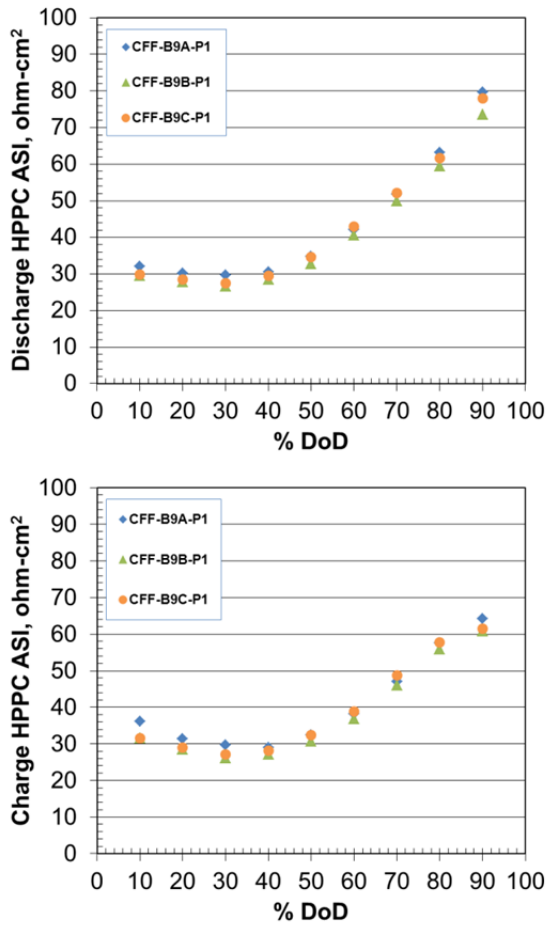

Figure V - 39: HPPC data for B9A, B9B, and B9C pouch cells. Testing performed at 30°C. Voltage window of 2.5 V to 4.4 V with 5C discharge pulse with 3.75 charge pulse at 10 s each

Cycle life testing began after the HPPC testing. General trends can be observed in Figure V - 40. Noticeable differences in cycle life performance are seen between B9A, B9B, and B9C. B9B shows a significant increase of capacity fade when compared to B9A. Whereas, B9C has similar capacity fade to B9A, but lower overall capacity in the cell. The initial cycle

capacities of B9B and B9C are also lower than B9A. It would be expected that all three builds would have the same starting capacity because they have all experienced the same testing conditions, but this was not the case here.

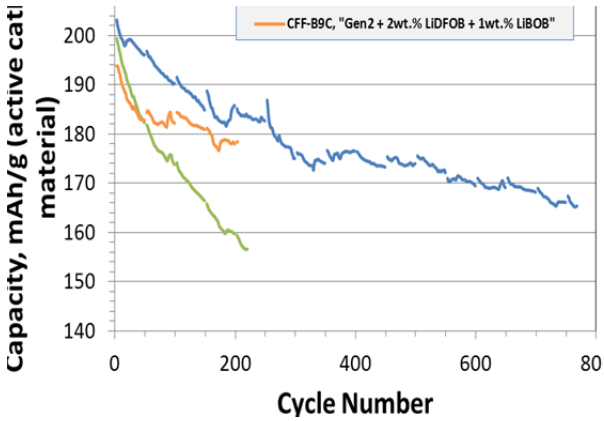

Figure V - 40: Cycle life study of B9A, B9B, B9C cell builds. Plot does not include cycle data from formation, rate study, or HPPC testing. All testing was performed at 30°C. Voltage window of 2.5 V to 4.4 V. Cells cycled at C/2 rate, with interruptions every 50 cycles for RPT/HPPC tests (data not shown in plot above)

In summary, the expected cycle life capacity retention improvements of the additives to the Gen2 electrolyte were not observed in the pouch cells as they were seen in the coin cell results. In these pouch cells, the additives actually poisoned the cells. There are several fundamental differences in cell design formats between coin cells and the larger pouch cells that could be the source of this discrepancy. First, the coin cell format is generally flooded with electrolyte which creates a high electrolyte to electrode area ratio. In a pouch cell format the design limits the amount of electrolyte that can be added. This lower ratio in the pouch cell format also correlates with there being less additive (mole basis) per area of electrode than there is in the coin cell format. The second factor is that in a coin cell, due to the larger electrolyte to electrode area ratio and the lower electrode thickness, the cells do not usually undergo a special formation procedure to ensure that the electrode has been wetted fully. Whereas, the larger format cells have thicker electrode coatings and multiple electrodes that are stacked, which take longer to wet fully.

The general procedure used in pouch cells to encourage proper wetting is to first perform a quick tap charge for five minutes to minimize copper corrosion, and then let the cell rest for 24 hours. This difference in cell formation could have significant implications for these additives and thus, were studied further.

The LiDFOB & LiBOB additives are bifunctional, in that they react on both the cathode and anode. In order to achieve improved cell performance, the additive should ideally form passivation layers that minimize cathode reactions with the electrolyte. The dQ/dV plots show that the additives (LiBOB & LiDFOB) are mainly consumed on the anode during both the tap charge and the 1st cycle charge of the formation procedure. The peak at ~1.8 to 2.0 V is due to the LiBOB additive reduction, and the peak at ~2.0 to 2.4 V is due to the LiDFOB additive reduction at the anode based on results found previously in diagnostic studies. Because of these reduction processes, there may be insufficient additive leftover to form effective passivation layers at the cathode later when the cell voltage is increased.

It is clear from the data shown in Figure V - 41 that the pouch cell formation protocol must be modified when using these additives. Suggested modifications include the following: (i) using elevated temperatures after the electrolyte fill to encourage electrode wetting; (ii) limiting the tap charge to less than 1.5 V before the 24-h hold; (iii) applying a higher C rate (greater than C/10) to pass through the 1.8 V to 2.4 V window more quickly to minimize consumption of additives on the anode; (iv) using a higher additive concentration (3-4 wt.%, instead of 1-2 wt.%) in the Gen2 electrolyte. These modifications and other formation cycling protocols are now being explored.

Initial tests are underway using the A12/HE5050 electrode couple in coin cells that are formed using the pouch cell formation process. A baseline set of data is being established that accounts for the effect of different electrode size configurations (matched 9/16" anode and cathode, or 14 mm cathode and 9/16" (14.3 mm) anode), as well as the ratio of electrolyte/additive to electrode area. Once it is established that the pouch cell conditions and performance can be replicated in coin cells, studies will begin with the targeted additives incorporated in the coin cell electrolyte. The formation process will then be adjusted to maximize the performance of the coin cells in a manner that will be later deployable in a pouch cell environment. After the formation and additive content is optimized, the process will be confirmed in a pouch cell build.

Aqueous Binders. Many of the silicon/graphite/binder systems that are being explored are aqueous based slurries. Initial coating trials of these systems were first performed using the standard bench top small scale coater. Several of the slurries and corresponding coatings that showed good adhesion, cohesion, and homogeneity were scaled up using the A-Pro coater in the dry room.

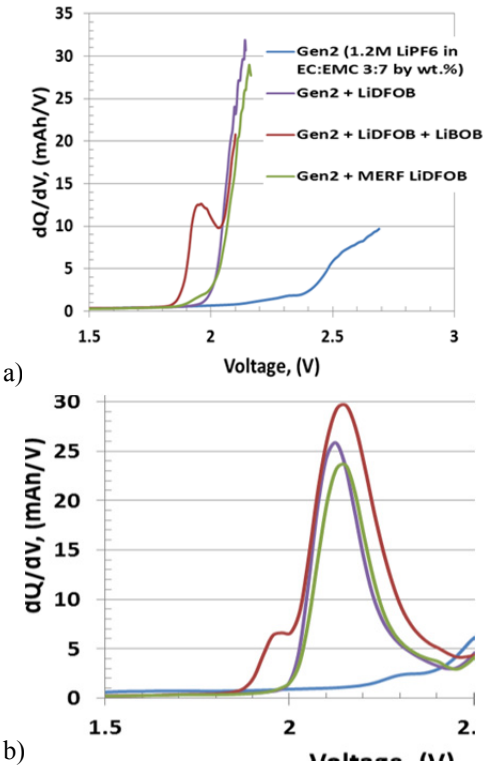

Figure V - 41: Pouch cell data of the initial 5 minute C/10 tap charge (a) and the subsequent C/10 charge of the 1st cycle dQ/dV that occurs after the 24 hour rest step (b) using various additives. (All data above is from CFF-B9 "HE-5050 vs. A12," except for the series "Gen2 + MERF LiDFOB" which is CFF-B12 "NHE5050 vs. A12." "Gen2" electrolyte is 1.2 M $LiPF_6$ in EC:EMC 3:7 by wt.%. "Gen2 + LiDFOB" is Gen2 + 2 wt.% LiDFOB. "Gen2 + LiDFOB + LiBOB" is Gen2 + 2 wt.% LiDFOB + 1wt.% LiBOB. "Gen2 + MERF LiDFOB" is Gen2 + 2 wt.% MERF-made LiDFOB)

There has been initial success in coating Phillips 66 A12 graphite in an aqueous-based binder slurry using the A-Pro coater. The aqueous system coated had the following components: 96 wt.% Phillips 66 A12 graphite, 2 wt.% Timcal C-45 carbon black, 1 wt.% CMC (MAC 350), and 1 wt.% SBR (Zeon X-3). A comparison of the aqueous CMC/SBR A12 electrode coin cell half-cell performance versus a PVDF/NMP-based A12 electrode (A-A002 from the CFF Electrode Library) coin cell half-cell performance is provided in Table V - 4. The CMC/SBR anode had a total coating loading of 4.6 mg/cm^2, coating thickness of 45 µm, and a porosity of 35.0%. The PVDF Electrode Library anode had a total coating loading of 6.0 mg/cm^2, coating thickness of 53 µm, and a porosity of 38.8%.

The data in Table V - 4 demonstrate the improved performance of the A12 graphite (no Si or SiO_x) when using the CMC-SBR aqueous binder system. In addition, a higher capacity was achieved with less total active material present in the CMC-SBR aqueous electrode compared to the PVDF/NMP electrode. As expected, the corresponding voltage plateaus were relatively unchanged. The results of using CMC/SBR for aqueous slurry making, its initial application in the dry room using the A-Pro coater, the homogeneous coating quality, and the good initial electrochemical performance are all a positive step forward. This newly gained information will greatly aid in incorporating Si/SiO_x powders in aqueous slurry systems for coating and ultimately be implemented into pouch cell fabrication.

Table V - 4: Electrochemical performance of CMC/SBR aqueous-based graphite anode compared to PVDF/NMP-based graphite anode in initial characterization cycling tests. Electrodes were made on large A-Pro coater in dry room

CMC/SBR A12 Graphite Electrode		PVDF A12 Graphite Electrode	
Formation		Formation	
1st Cycle Lithiation Capacity	363 mAh/g of A12	1st Cycle Lithiation Capacity	345 mAh/g of A12
1st Cycle Delithiation Capacity	342 mAh/g of A12	1st Cycle Delithiation Capacity	339 mAh/g of A12
1st Cycle Efficiency	94%*	1st Cycle Efficiency	97%
Rate Study		Rate Study	
C/5	358 mAh/g	C/5	330 mAh/g
C/2	355 mAh/g	C/2	326 mAh/g
1C	348 mAh/g	1C	318 mAh/g
2C	330 mAh/g	2C	310 mAh/g
HPPC		HPPC	
ASI at 50% DOD	47	ASI at 50% DOD	49

* A possible wetting issue may be present

Analysis.

Data Handling. Each pouch cell build has consisted of multiple cells, for each variable tested, to provide statistically relevant data. Providing the statistics of multiple cells being tested under the same variables is important. The data is simple to collect, but data processing can quickly become complex and time consuming. Effort has gone into utilizing Excel software to improve the data processing procedure. Excel macros and templates have been created in order to rapidly perform a significant number of consistently accurate automatic calculations for any size cell (i.e., coin cell, pouch cell, 18650, etc.), averaging of multiple data sets with sample standard deviation error bars, and creation of standard tables and plots for simplified data comparison. An Excel macro/template has been created for each of the main characterization tests used by the CAMP Facility, including: formation, rate study, HPPC, and cycle life testing. All the Excel macros/templates are accompanied with detailed instructions.

The formation macro/template automatically plots the voltage profiles, capacity curves, and dQ/dV plots for up to 8 cells, along with a table of the first cycle efficiency and reversible capacity values (Table V - 5). Both the individual cells and average processed data are available in the output.

Table V - 5: Capacity and efficiency values automatically calculated for formation testing (data provided from 8 pouch cells; CFF-B9A, "HE5050 LMR-NMC vs. A12 Graphite")

	Cell #									
mAh/g	1	2	3	4	5	6	7	8	Average	Standard Deviation
1st C cap (mAh/g)	299	298	297	297	297	303	294	297	298	2.5
1st D Cap (mAh/g)	268	267	266	266	267	265	263	267	266	1.4
1st Cycle Eff (%)	90	90	90	89	90	87	90	90	89	0.8
Reversible C Cap (mAh/g)	268	267	268	267	268	273	264	268	268	2.1
Reversible D Cap (mAh/g)	266	265	266	266	266	267	262	266	265	1.2
Irreversible Cap Loss (mAh/g)	33	32	31	31	32	36	31	31	32	1.7
Irreversible Cap Loss (%)	11	11	10	10	11	12	11	11	11	0.5

The rate study is an initial characterization test to determine a cell's rate capability. The rate study macro/template automatically plots the voltage profiles, capacity vs. current, capacity vs. cycle number, averaging plots with trend lines for reasonable forecasting, a table of C-rates based on trend lines, and tables of capacities each cell obtained for each cycle. The macro can process (and average) up to 12 cells at one time. Both the individual cells and average processed data are available in the output. (Table V - 6 and Figure V - 42).

Table V - 6: Expected discharge C-rates determined by the averaging of all the data with corresponding capacity values based on the rate study test results (data provided from 8 pouch cells; CFF-B9A, "HE5050 LMR-NMC vs. A12 Graphite")

C-rate	mAh	mAh/g	mAh/cm²
2C	409	196	2.42
1C	436	209	2.58
C/2	463	222	2.74
C/5	498	239	2.95
C/10	525	252	3.11

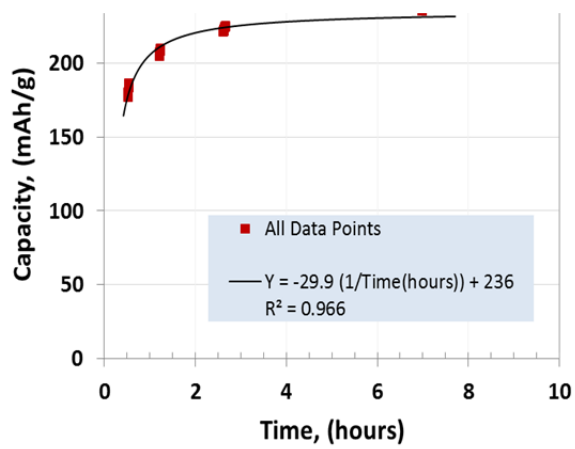

Figure V - 42: Typical discharge capacity plot of data from multiple cells showing an averaged trend line generated to predict an expected C-rate from the rate study test results (data provided from 8 pouch cells; CFF-B9A, "HE5050 LMR-NMC vs. A12 Graphite")

The HPPC test is intended to determine dynamic power capability over the device's usable voltage range using a test profile that incorporates both discharge and regen (charge) pulses. The HPPC macro/template automatically plots the voltage profiles, area specific impedance (ASI) vs. open circuit voltage (OCV), ASI vs. DoD or as a function of pulse number, and ASI vs. time during pulse. The macro can process up to 8 cells at one time. Both the individual cells and

average processed data are available in the output tab (Figure V - 43).

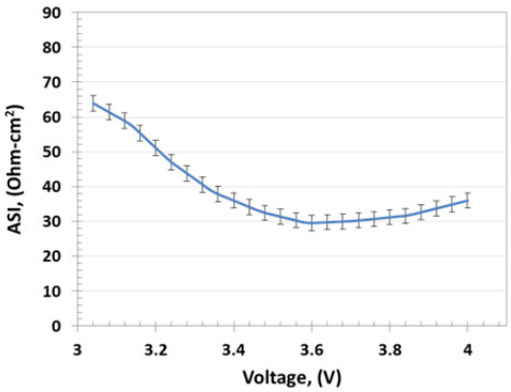

a)

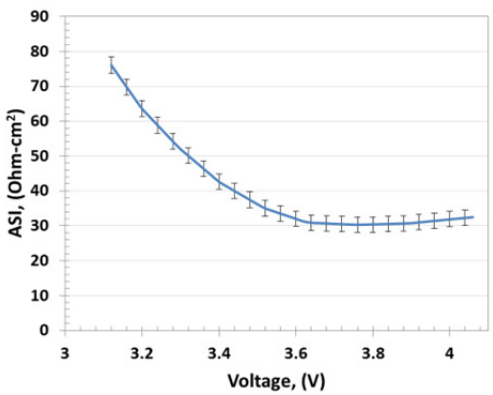

b)

Figure V - 43: Typical HPPC ASI vs. OCV plots of average data with sample standard deviation error bars from multiple cells (data provided from 8 pouch cells; CFF-B9A "HE5050 LMR-NMC vs. A12 Graphite") for a) charge and b) discharge

The cycle life test is used to accelerate the aging of cells by cycling at a C/2 capacity tests while monitoring the capacity fade and impedance rise via scheduled HPPCs and C/24 rates during cycling. The cycle life macro/template automatically creates multiple plots, including: capacity vs. cycle #, efficiency vs. cycle #, capacity retention vs. cycle #, energy and energy density vs. cycle #, energy retention vs. cycle #, ASI vs. DoD and voltage as a function of HPPC's performed throughout the cycle life, ASI vs. cycle # as a function of DoD, voltage vs. SOC as a function of cycle #, and dQ/dV vs. voltage as a function of cycle #. The macro processes only one cell at a time due to the large number of data points to be processed, and averaging of multiple cells takes place in a separate macro/template. The individual cell's processed data is available in the output tab (Figure V - 44 & Figure V - 45). The cycle life macro/template processes the data in a couple of minutes.

Diagnostic Investigations. In-depth investigations were conducted for positive electrodes that contain 86 wt% $Li_{1.2}Mn_{0.55}Ni_{0.15}Co_{0.1}O_2$ (HE5050), 4 wt.% SFG-6 graphite (Timcal), 2 wt.% Super P (Timcal) and 8 wt.% PVDF (Solvay 5130), and for negative electrodes that contain ~90 wt% graphite (Phillips 66 A12), 6 wt% PVDF (Kureha KF-9300) and 4 wt.% Super P (Timcal). In previous reports, we have shown that cell impedance rise is mainly governed by the positive electrode; impedance rise at the negative electrode is relatively small. In AC impedance data, the positive electrode impedance rise appears as an increase in the high-frequency arc width (electronic impedance) and in the mid-frequency arc width (ionic impedance).

XRD and Raman Spectroscopy results indicated structural changes in the positive electrode carbons during cell cycling. In particular, XRD data from a fresh positive electrode indicate a relatively sharp graphite (002) peak at $2\theta = 26.5°$. This peak arises from the SFG-6 graphite, present as an electron conduction additive, in the electrode coating. The peak becomes weak and broadens significantly after only a few 2–4.6V full-cell cycles; however, it does not disappear entirely and shows a small, but measurable, intensity even in electrodes harvested from cells after 300 and 1500 cycles.

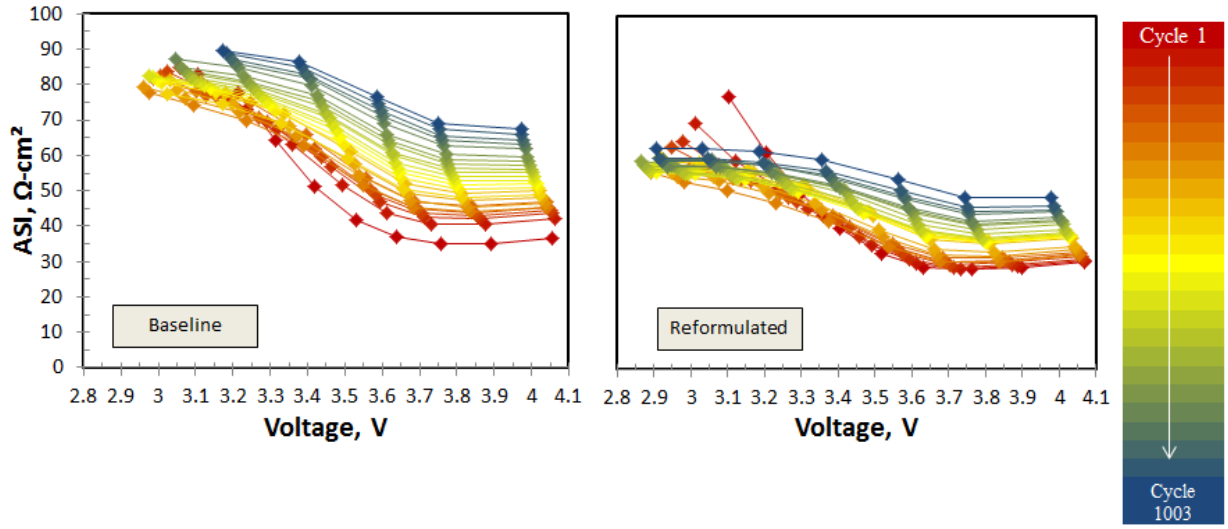

Figure V - 44: Example comparison plots exhibiting the powerful capabilities of the cycle life excel macro/template. The plots show the HPPC area specific impedance versus OCV, as a function of cycle life (color gradient) for "Baseline Cells" and "Reformulated Cells." Note that the impedance is higher at lower voltages for both sets of cells. The impedance rise for the Reformulated cells is lower than that of the Baseline cells for the entire life of the cell (data provided from 1 Baseline pouch cell; CFF-B4A, "HE5050 LMR-NMC vs. A12 Graphite" and from 1 Reformulated pouch cell; CFF-B9A, "HE5050 LMR-NMC vs. A12 Graphite")

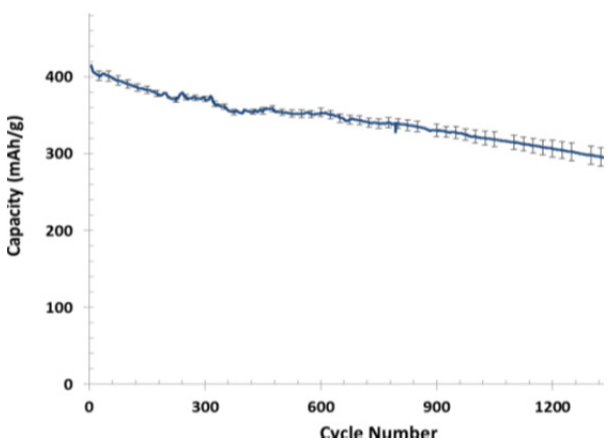

Figure V - 45: Typical discharge capacity vs. cycle number plot of average data with sample standard deviation error bars from multiple cells (data provided from 2 pouch cells; CFF-B9A, "HE5050 LMR-NMC vs. A12 Graphite")

Changes in the positive-electrode graphite behavior on cycling were also evident in data from Raman spectroscopy. Figure V - 46 shows representative Raman spectra from a fresh positive electrode and from electrodes harvested from cycled cells. The G-band observed at ~1,580 cm^{-1} corresponds to the E_{2g} vibrational mode and is commonly attributed to the in-plane stretching of all pairs of sp^2 carbon atoms in both rings and chains. The D-band observed at ~1,350 cm^{-1} and the D'-band observed at ~1,620 cm^{-1} are defect-induced Raman features. The D– to G– band intensity ratio (I_D/I_G) is commonly used to determine the extent of structure disorder in graphite.

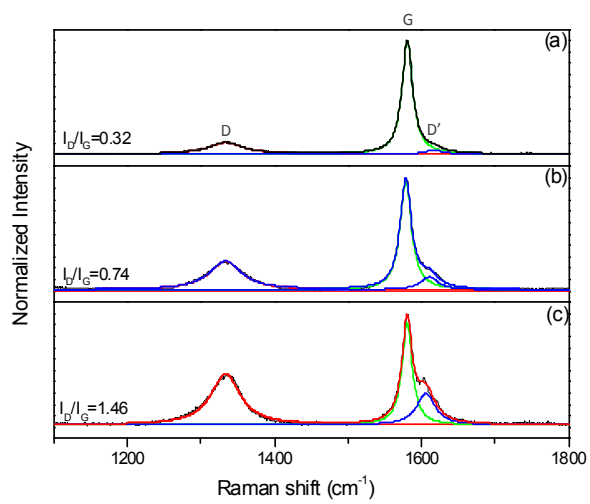

Figure V - 46: Raman spectra from (a) fresh positive electrode, (b), (c) positive electrodes harvested from cells after initial cycles, and after 1500 cycles, respectively. Band intensities are normalized to the G-band

From an analysis of Figure V - 46 the I_D/I_G ratio for the fresh electrode is 0.32. This value is higher than that expected for pure graphite because the electrode also contains Super P carbon, which is disordered and has an I_D/I_G ratio of 2.47. The I_D/I_G value increases to 0.74 for the initial–cycle sample, and to 1.46 for the 1,500–cycle sample. These data indicate that the positive electrode

carbons undergo severe structural disordering upon prolonged cycling. The structural disordering is related to the intercalation of PF_6^- anions into graphitic structures. Separate experiments have shown that significant PF_6^- intercalation into SFG-6 graphite occurs at voltages >4.45 V vs. Li. Anion intercalation into the Super P carbons also occurs, albeit in quantities that are ~2 orders of magnitude smaller than that for the graphite. These changes in the positive electrode carbons are partially responsible for the degradation of the electron conduction network that appears as the high-frequency arc in the AC impedance data. Based on the electrochemistry, diffraction, and spectroscopy data, it is recommended to not use graphite-based electron conductive additives in the preparation of LMR-NMC electrodes that are cycled at voltages >4.4 V vs. Li.

Secondary Ion Mass Spectrometry (SIMS) and Inductively Coupled Plasma–Mass Spectrometry (ICP-MS) were also performed to determine the accumulation of transition metal elements at the graphite electrode during cycling. Figure V - 47 shows SIMS sputter depth profiles for carbon, manganese, nickel, cobalt and lithium from negative electrodes harvested from cells that underwent the initial cycles (a), and the 1,500 aging cycles (b). In Figure V - 47a, the carbon signal increases for the first 200 seconds of sputtering, and then reaches a steady state value. The lower carbon signal near the surface is consistent with a SEI that contains a lower carbon concentration than the bulk electrode. In Figure V - 47b, however, the carbon signal reaches a steady state value indicative of the bulk electrode only after ~8,000 seconds of sputtering. The longer sputtering time indicates that the SEI is significantly thicker for the aged sample.

The Li signal during early sputtering mainly arises from lithium in the electrode's SEI layer near the top surface. At longer sputtering times the signal also includes contributions from lithium remnants deeper inside the electrode. Figure V - 47 shows that the Li count rate (counts per second, cps) of the aged sample is more than an order of magnitude greater than that of the sample after the initial characterization cycles. The data are consistent with lithium trapping in the negative electrode, especially in the SEI, and explain the significant deterioration of cell capacity that results from extended cycling.

In Figure V - 47a, the Mn, Ni and Co signals peak after ~50 s sputter time, then decrease relatively rapidly for Mn and more gradually for Ni and Co; the elements display quasi-steady state cps values after ~2,000 s sputter time. In Figure V - 47b also, the Mn, Ni and Co signals peak after short sputter times and then decrease. However, the cps values measured after ~2,000 s is more than an order of magnitude larger for Ni and more than two orders of magnitude larger for Mn. That is, the total Mn and Ni counts obtained by integration under the curves are significantly higher for the aged sample than for the sample after initial cycles.

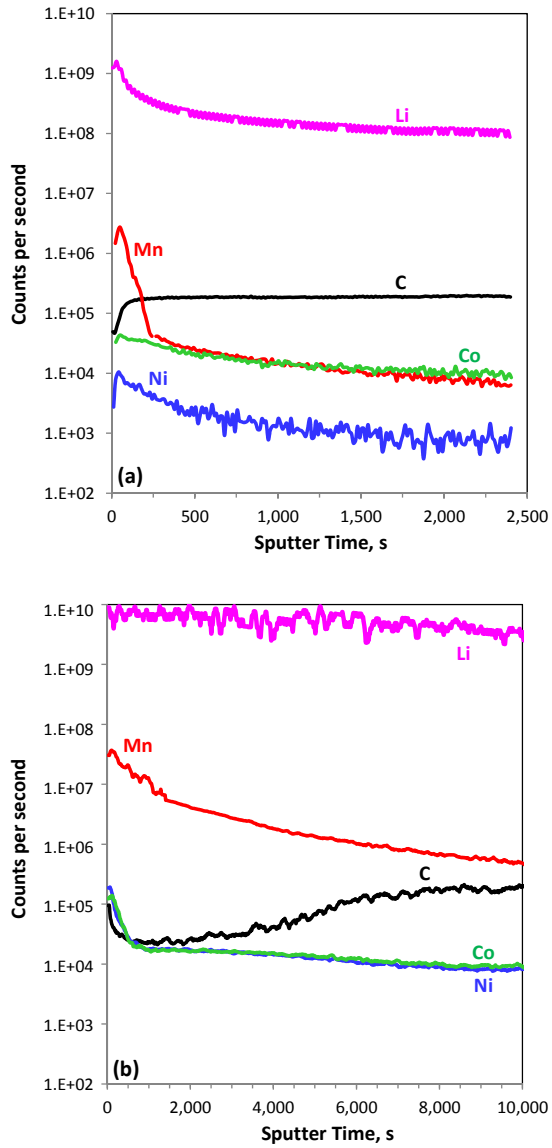

Figure V - 47: SIMS sputter depth profiles from negative electrodes after (a) Initial cycles, and (b) 1500 cycles. Data for carbon, manganese, nickel, cobalt and lithium are shown. The Y-axis scales are the same for (a) and (b), but the X-axis scales are different

The trends in the SIMS data were confirmed by ICP-MS data obtained on the negative electrode coatings, which were scraped off the current collector. The measured data are an average of the element concentrations contained in the samples, which comprises the graphite, SuperP, PVDF, electrolyte residue, and SEI components; the harvested electrodes were rinsed in DMC to minimize electrolyte residue while preserving the SEI. As expected, only trace

quantities of Li, Mn, Ni and Co data were measured in the fresh negative electrode, which serves as a control sample. For the initial–cycle sample, the average Li, Mn, Ni and Co concentrations are 9683, 617, 125 and 63 µg/g-sample, respectively, with a measurement uncertainty of ± 10%; the corresponding values for a 1500–cycle graphite electrode sample are 25936, 1446, 167 and 71 µg/g-sample, respectively. That is, the Li, Mn, Ni and Co content in the 1500–cycle graphite negative electrode are, on an average, 2.7, 2.3, 1.3 and 1.1 times greater than that in the initial–cycle electrode.

The transition metals at the negative electrode originate from the oxide in the positive electrode, and are an obvious example of metal-ion migration between the electrodes. A simple calculation shows that the Mn, Ni, and Co contents in the graphite electrode are 8.1, 0.9, and 0.4 µg/cm^2, respectively, which are several orders of magnitude smaller than the corresponding contents in the positive electrode. These data indicate that cell capacity loss arising from dissolution of these elements, from the positive electrode into the electrolyte, is negligibly small.

In order to elucidate the contribution of the negative electrode to full cell capacity loss, the cycling characteristics of cells containing $Li_{1.2}Ni_{0.15}Mn_{0.55}Co_{0.1}O_2$–based positive and $Li_4Ti_5O_{12}$–based negative electrodes (LTO) were investigated. SEI formation and Li trapping is not expected in the LTO electrodes because the material shows a flat voltage profile about 1.55V vs. Li, much higher than the voltage at which electrolyte reduction occurs (≤0.8V vs. Li/Li$^+$). These cells contained the same positive electrodes described above; the negative electrode comprised a coating of 87 wt% LTO, 5 wt% Timcal C45 carbon, and 8 wt% PVdF (Kureha 9300) binder on a 20 µm thick Al foil.

Representative data from a cell cycled in the 0.75–3.15V (2.3–4.7V for the positive vs. Li/Li$^+$) voltage window are shown in Figure V - 48. This cycling window is wider than a typical cycling window for graphite–based full cells and was selected to accelerate performance degradation. The cycling is mainly conducted at a ~C/2 rate, with periodic capacity measurements at a ~C/10 rate. It is apparent from Figure V - 48 that the cell shows negligible capacity loss even after 600 cycles. Moreover, the measured coulombic efficiency is greater than 99.9%, which also indicates negligible Li loss during cell cycling. These data confirm that capacity loss arises at the negative electrode in the graphite-based cells.

Electrochemical Modeling. The EIS electrochemical cell model was used to examine the impedance characteristics of the hysteresis between charge and discharge in LMR-NMC positive electrodes [4]. The EIS cell model was developed strictly for intercalation active materials. However, the hysteresis and other characteristics indicate that the LMR-NMC bulk material is much more complex. In contrast, the active material/electrolyte interface, commonly referred to as the solid electrolyte interphase or SEI, portion of the EIS electrochemical model should adequately capture the interfacial phenomena.

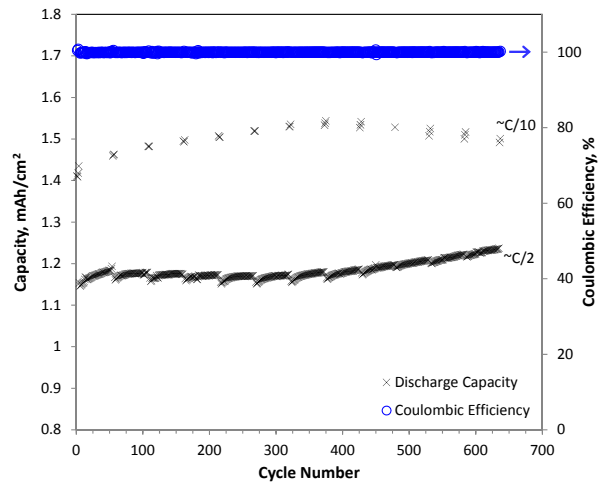

Figure V - 48: Capacity vs. cycle number plot for a full cell containing a $Li_4Ti_5O_{12}$–based negative electrode. The data were acquired at 30°C, with 0.1 mA/cm^2 (~C/10) and 0.5 mA/cm^2 (~C/2) currents, in the 0.75–3.15V cycling window; the corresponding positive electrode cycling window is ~2.3–4.7V vs. Li/Li$^+$. A 1 mAh/cm^2 full cell capacity value roughly equals 150 mAh/g-oxide in the positive electrode

The detailed theoretical description of the SEI is based on post-test analytical diagnostic studies. The SEI region is assumed to be a film on the active material. The film is taken to be an ill-defined mixture of organic and inorganic material through which Li-ions from the electrolyte must diffuse and/or migrate across to react electrochemically at the surface of the active material. The lithium is then assumed to diffuse through the surface layer and into the bulk active material in the particle. Capacitive effects are incorporated into the model at the electrochemical interfaces and a localized electronic resistance between the current carrying carbon and the oxide interface can also be included. The model can also accept multiple particle fractions with unique characteristics.

To accurately model the bulk transport characteristics of the LMR-NMC active materials the EIS electrochemical cell model will need to be modified. The bulk transport electrochemical model is being developed under the Voltage Fade effort (see Section V.C.1). Because this model development is lagging behind the EIS SEI modeling studies in this effort, work under this effort in the latter part of the year was directed towards advancing the electrochemical bulk transport model. As confidence in the bulk

transport model improves, it will be integrated into the EIS electrochemical model.

The EIS electrochemical cell model is applied here to obtain a "snapshot" of the electrode at each SOC. Diagnostic micro-reference electrode lab cell EIS studies were conducted on the baseline HE5050 LMR-NMC electrode at several states-of-charge (SOCs) during the charge and discharge half cycles. In general, over the voltage range where the EIS studies were conducted (between 3.3 and 4.0 volts vs. lithium) within the same half-cycle, either charge or discharge, impedance increases as the SOC and electrode potential decreases. The discussion here will be focused on three EIS sweeps: two taken at 3.74 and 3.36 volts (vs. lithium) during the discharge half cycle and one at 3.74 volts during the charge half cycle. Because of the hysteresis between charge and discharge, the two 3.74 volt sweeps are taken at the same electrode potential, but differing SOCs. While the 3.36 volt discharge sweep and 3.74 volt charge sweep are taken at about the same SOC (i.e., same lithium content).

The EIS data and electrochemical model fit for the LMR-NMC electrode at 3.74 volts is shown in Figure V - 49. The interfacial impedance for a lithium ion positive electrode typically consists of two circular arcs (i.e., a high-frequency arc and a mid-frequency arc) with a diffusional Warburg impedance tail at low frequencies.

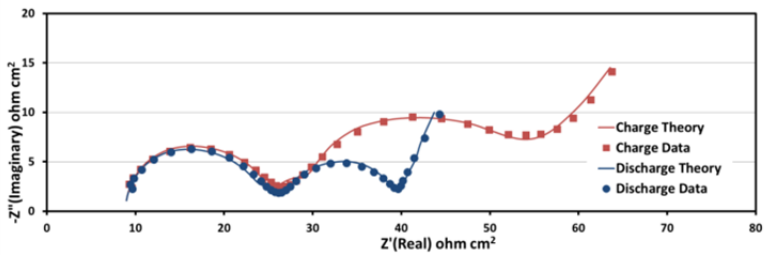

Figure V - 49: LMR-NMC electrode impedance (100kHz-10mHz) at 3.74 volts vs. lithium taken during the charge and discharge half cycles with a micro-reference electrode cell

The initial EIS electrochemical modeling studies on the LMR-NMC electrodes are discussed in the FY2012 annual report. The work focused on comparing the LMR-NMC electrode to earlier studies on other layered cathode materials and examining possible sources of aging effects. It highlighted the susceptibility of LMR-NMC cathodes to increases in the high frequency impedance owing to the lower overall bulk conductivity of the materials. This manifests in a high contact resistance between the particles and the conductive carbon additives that worsens with continued exposure to high potentials (i.e., electrolyte oxidation). Also included in the high frequency impedance arc are ion migration effects through the surface film on the active material. The lithium ion diffusion effects through the surface film can impact either or both the high and mid frequency arcs. These effects are generally less sensitive to SOC. The studies here focus on the changes in the mid-frequency arc and Warburg impedance. The mid frequency arc includes impedance effects from the electrochemical reaction (i.e., Butler Volmer kinetics) and lithium diffusion through active material surface layer. The Warburg impedance is dominated by solid-state diffusion in the oxide particles, but also includes electrolyte salt diffusion. Of all the parameters extracted from the EIS data, changes in the lithium diffusion coefficient (D_{sb}) of the bulk active material are most precisely followed. A general discussion of how the relative time constants for the various phenomena are determined was also discussed in the FY2012 annual report. The size of the impedance for the Butler Volmer kinetics is determined by the exchange current density (i_o). The impact of lithium diffusion through the surface layer is governed by its diffusion coefficient (D_{si}) and the partition coefficient (K_s) for lithium between the bulk material and the surface layer. These parameters are given in Table V - 7 for the indicated electrode potential and half-cycle.

Table V - 7: Selected electrochemical model parameters for LMR-NMC electrode at indicated electrode potential and half-cycle

Positive voltage vs. Li	Half-Cycle	D_{si}	D_{sb}	K_s	i_o
Volts		cm^2/s			mA/cm^2
3.36	Discharge	5.5E-13	2.0E-14	33.0	0.0055
3.74	Charge	6.0E-13	8.5E-14	10.0	0.015
3.74	Discharge	1.4E-12	1.7E-12	10.0	0.035

In general, as one goes down the columns in Table V - 7 the parameters change in the direction of lowering the electrode impedance. Therefore, for the constant SOC data (i.e., first and second lines) the discharge impedance is greater than the charge impedance and the opposite is true for the constant voltage data (i.e., second and third lines), as seen in Figure V - 49. How much of a trend this is over the full voltage range is yet to be determined. In Table V - 7 at an electrode potential of 3.74 volts, both i_o and D_{si} vary by about a factor of

two between the charge and discharge half-cycles. Since it is implicitly assumed that both phenomena contribute about equally to the impedance, the changes account for the doubling of the size of the mid-frequency interfacial arc, as seen in Figure V - 49. Less obvious from examining Figure V - 49 is the change in the bulk lithium diffusion coefficient (D_{sb}) of the active material by about a factor of twenty, suggesting that the bulk material is significantly different between the charge and discharge half-cycles. An even greater change in the discharge D_{sb} is observed between 3.74 and 3.36 volts. While more studies over a wider voltage range need to be conducted, it is clear that both the interface and bulk LMR-NMC material is changing significantly within and between each half-cycle.

Additional activities this year include modifying the open circuit voltage expressions for phase change active materials (i.e., in this case the graphite negative) in the DC electrochemical cell model. This corrects a nagging issue with the model that tended to occasionally drive one of the local lithium active material concentrations negative at high discharge rates. This model has been used extensively to examine performance changes with electrode thickness. Further electrode thickness studies are planned in support of the prototype cell fabrication effort and BatPaC development.

Conclusions and Future Directions

Significant effort this year was devoted to developing a silicon-based anode that could be used in future prototype cell builds and in the Electrode Library. Three sources for commercially available silicon powder were identified that could be used freely, without restrictions on data or material distribution. Traditional binders, which work well for graphite, do not function as well for silicon.

The value of the CAMP Facility was well demonstrated this year, particularly in the study of electrolyte additives. Ideas that work well in simple coin cell studies, may not always work in full size cell systems. Validation and studies using prototype cells can save valuable resources later on.

In FY14, efforts will continue on the analysis, modeling, and prototype cell fabrication of advanced electrochemical energy storage systems with an emphasis on high energy anode and cathode materials. The main goal will be to fabricate pouch cells using a silicon-based anode coupled with a high energy LMR-NMC cathode that is produced by the MERF at ANL.

Additional activities will be pursued to understand the mechanisms taking place in high energy cell systems. These include: determining the negative to positive (n:p) ratio effect on performance; role of the separator material; effect of formation process for prototype cells that use bifunctional electrolyte additives; and effect of electrode thickness.

Failure mechanisms of new energy storage chemistries will be determined, and remedies proposed, using diagnostic techniques within the CAMP Facility coupled with the support of the Post-Test Facility at Argonne.

The battery design modeling effort will continue to support the CAMP facility effort, but funding and reporting will be shifted to the core BatPaC studies. The development of advanced electrochemical models focusing on high energy lithium-ion electrochemical couples (e.g., LMR-NMC positive and silicon/graphite negative electrodes) will continue. As the interfacial impedance studies and bulk transport electrochemical model are developed further for the LMR-NMC positive electrode, they will be integrated into a single electrochemical model.

FY 2013 Publications/Presentations

1. Positive Electrode Passivation by LiDFOB Electrolyte Additive in High-capacity Lithium-ion Cells, by Ye Zhu, Yan Li, Martin Bettge, and Daniel P. Abraham, Journal of The Electrochemical Society 159, A2109-2117 (2012).
2. Overcharge Effect on Morphology and Structure of Carbon Electrodes for Lithium-ion Batteries, Wenquan Lu, Carmen M. Lopez, Nathan Liu, John T. Vaughey, Andrew Jansen, and Dennis W. Dees, Journal of The Electrochemical Society 159(5), A566-A570 (2012).
3. Electrolyte Additive Combinations that Enhance Performance of $Li_{1.2}Ni_{0.15}Mn_{0.55}Co_{0.1}O_2$-Graphite Lithium-ion Cells, by Y. Zhu, Y. Li, M. Bettge, and D.P. Abraham, Electrochimica Acta in press; 10.1016/j.electacta.2013.03.102 (2013).
4. Examining Hysteresis in Composite xLi_2MnO_3•$(1-x)LiMO_2$ Cathode Structures, by J. R. Croy, K. G. Gallagher, M. Balasubramanian, Z. Chen, Y. Ren, D. Kim, S.-H. Kang, D. W. Dees, and M. M. Thackeray, Journal of Physical Chemistry C 117, 6525−6536 (2013).
5. Structure Evolution of $Li_{1-x}VPO_4F$ Studied by *In situ* Synchrotron Probes, by Ying Piao, Yan Qin, Chengjun Sun, Yang Ren, Steve M. Heald, Dehua Zhou, Bryant J. Polzin, Steve E. Trask, Khalil Amine, Yinjin Wei, Gang Chen, Ira Bloom, and Zonghai Chen, under review by Energy & Environmental Science.
6. Understanding Long-Term Cycling Performance of $Li_{1.2}Ni_{0.15}Mn_{0.55}Co_{0.1}O_2$ – Graphite Lithium-Ion Cells, by Y. Li, M. Bettge, B. Polzin, Y. Zhu, M. Balasubramanian and D.P. Abraham, Journal of

The Electrochemical Society 160(5), A3006-A3019 (2013).

7. Perfluoroalkyl-substituted ethylene carbonates: novel electrolyte additives for high-voltage lithium-ion batteries, by Y. Zhu, M.D. Casselman, Y. Li, A. Wei, D.P Abraham, J. Power Sources 246 (2013) 184 –191. 10.1016/j.jpowsour.2013.07.070.
8. Electrochemical Modeling the Impedance of a Lithium-Ion Positive Electrode Single Particle, by D. Dees, K. Gallagher, D. Abraham, *J. Electrochem. Soc.*, **160** (3), A478-A486 (2013).
9. A Volume Averaged Approach to the Numerical Modeling of Phase-Transition Intercalation Electrodes Presented for Li_xC_6, by K. Gallagher, D. Dees, A. Jansen, D. Abraham, and S.-H. Kang, *J. Electrochem. Soc.*, **159** (12), A2029-A2037 (2012).

References

1. D. Dees, E. Gunen, D. Abraham, A. Jansen, and J. Prakash, *J. Electrochem. Soc.*, **152** (7) (2005) A1409.
2. D. Abraham, S. Kawauchi, and D. Dees, *Electrochim. Acta*, **53** (2008) 2121.
3. D. Dees, E. Gunen, D. Abraham, A. Jansen, and J. Prakash, *J. Electrochem. Soc.*, **155** (8) (2008) A603.
4. J. R. Croy, K. G. Gallagher, M. Balasubramanian, Z. Chen, Y. Ren, D. Kim, S.-H. Kang, D. W. Dees, and M. M. Thackeray, *Journal of Physical Chemistry C*, **117**(13), 6525-6536 (2013).

V.B.4 Scale-up of BATT Program Materials for Cell Level Evaluation (LBNL)

Vincent Battaglia, Ph.D.

Lawrence Berkeley National Laboratory
Department of Energy Storage and Distributed Resources
1 Cyclotron Road
Berkeley, CA 94720
Phone: (510) 486-7172; Fax: (510) 486-4260
E-mail: vsbattaglia@lbl.gov

Start Date: October 2009
Projected End Date: September 2013

Objectives

- Identify baseline materials for a high-voltage system.
- Test materials developed in the BATT Program as a result of investigations of the High-voltage Focus Group.

Technical Barriers

With the advent of the *EV Everywhere* Grand Challenge, there is a renewed and heightened interest in high energy-density couples. The BATT Program is focused on finding materials with the capacity to improve cell energy density and the ABR Program is focused on verification and evaluation of these new materials in full cells.

Technical Targets

EV Performance Targets

- 200 Wh/kg at C/3, system level.
- 1000 full charge/discharge cycles.
- 2 to 1 Pulse-power to Energy.

Accomplishments

- Four carbon conductive additives tested in a cathode containing NMO.
- A compilation of data that allows for an explanation of the coulombic inefficiency during the formation cycles.
- Two materials from the BATT Program developed based on analysis performed by the High-voltage Focus Group.
- A new material from NEI evaluated at 30° and 55°C.

✧ ✧ ✧ ✧ ✧

Introduction

To meet the *EV Everywhere* Grand Challenge put forth by the DOE, it is important to find materials capable of functioning with higher capacity for lithium over a large voltage separation. Scientists throughout the world including some supported by the BATT Program are developing such materials. As they make progress it is important that these materials are tested in half- and full-cells in a like manner. Both Argonne and LBNL have materials testing facilities, but the production of new materials is difficult for any one group to stay ahead of. For this reason, the LBNL Group has focused its effort on BATT produced materials and NMO-based materials. In the previous year, one material from NEI was designated as the baseline material for the High-voltage Focus Group in the BATT Program. Materials from Ceder and Manthiram and from certain large suppliers were tested and all of them showed that the biggest problem with cells containing NMO is a large capacity loss in full cells during formation. This is a difficult challenge as it is highly dependent on interactions with the anode. This year, different carbon additives and separators, two new materials from Manthiram, and a new material from NEI were tested.

Approach

To assess materials, electrodes are cast according to our on-line manual. The electrodes loading is typically around 1 mAh/cm^2. This loading allows for the assessment of the material; loadings that are too much greater may result in electrodes that fail due to electrode breakdown as opposed to a chemistry issue. On the other hand, the electrode is thick enough so as to identify coulombic efficiency issues that may not be revealed at lower loadings. Investigators in the BATT Program and large material suppliers to Li-ion battery manufacturers are queried for their most current materials. Electrodes are made of the new materials where only the new material is swapped in. Materials are tested for irreversible capacity loss, reversible capacity, rate capability, and cycleability. Results are provided to the suppliers and reported in Quarterly Reports.

Results

Testing of Conductive Carbon Additives and Polypropylene Separators. Beyond the testing of materials developed in the BATT Program, it is our group's responsibility to test supplier materials for a $LiNi_{1/2}Mn_{3/2}O_4$ high-voltage baseline study for both the ABR and BATT Programs. Through this effort, an active material from NEI was identified last year. This year, three carbons from Timcal, Super C65, Super C45, and Super P-Li; and VCGF, were tested and compared to the present baseline carbon additive material Denka black (ATD Gen 2 baseline conductive additive).

Half-cells were fabricated with a fairly low active material loading of approximately 0.6 mAh/cm^2 with 4% binder and 3% conductive carbon. It has been shown by our lab that for half-cells with Denka black there is an extended amount of side reaction during the C/10 charge when a 4.95 V upper cut-off voltage is employed. Independent of the carbon used, the results shown below were identical except for the Super P-Li (Figure V - 50).

Close inspection of the data shows a highly variable voltage response during the constant-current charge and an extended charge time during the 5th charge cycle. Such an irregular voltage response is not only an indication of a side reaction but also of a side reaction that involves the production of a gas. And, not only is this most likely the result of a gas, but a gas that is reversibly oxidized or reduced to generate a benign shuttle between the two electrodes.

For a cell with a comparable loading but containing Super P-Li, the response is much more favorable, as seen in the lower figure (bottom, Figure V - 50). Consistent with this result, is that the Super P-Li consists of larger particles and a lower surface area. Also consistent with this result, is that at double the loading the half-cell response appears similar to that of the cells with the other carbons at half the loading. All of this data adds up to the conclusion that there is a reversible shuttle in the half cell that involves a gaseous reactant that is oxidized on the cathode and that this reaction is limited by reducing the surface area of the cathode and by the eventual formation of a protective film on one of the electrodes.

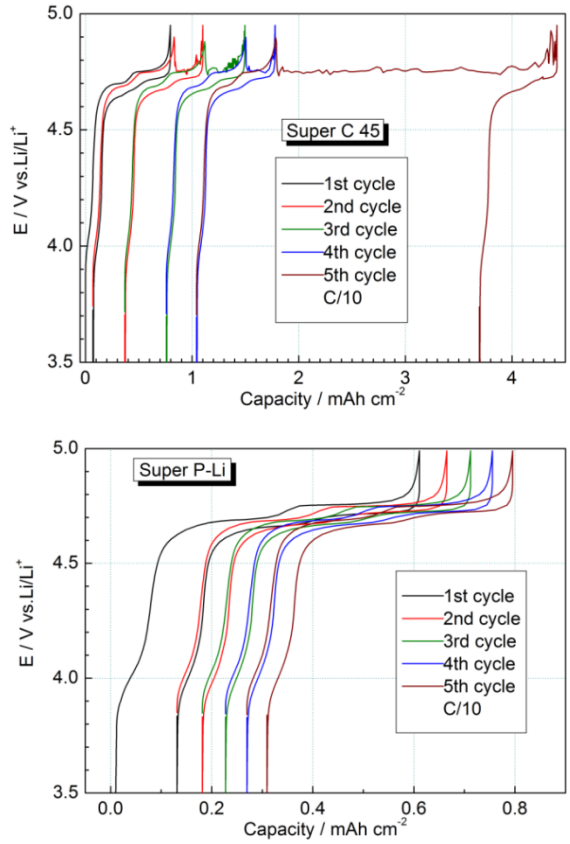

Figure V - 50: The first five cycles of half cells of NMO with, top, C45 conductive additive, and, bottom, Super PLi

Separators from Celgard were also tested: 2400, 2500, and 3501. They were all polypropylene based, however, the 2500 and 3501 are high-power separators with high porosity, and the 3501 also contains a wetting agent. Charging results, not provided here, indicated erratic voltage dependence for the more porous separators and favorable performance for the low-porosity separator. Based on these results, Super P-Li is recommended as the conductive additive and Celgard 2400 the separator for cells with high-voltage $LiNi_{1/2}Mn_{3/2}O_4$ cathodes.

Testing of Two BATT NMO Materials. Amongst the testing of baseline materials for the Ni-spinel high-voltage system and some salts from HQ, two NMO materials from the University of Texas produced by Prof. Manthiram's Group in the BATT Program were evaluated. From the BATT Focus Group on NMO, it was discovered that particle morphology and the level of transition metal disorder of the active material were critical parameters with regard to cathode performance. Specifically, Dr Guoying Chen showed that an octahedron shape demonstrated better performance than platelets, and Dr. Cabana showed that disordered material provides better rate performance than ordered materials. With this in mind, Dr. Manthiram synthesized

two NMO materials with the polyhedron shape and disordered configurations, one with and one without fluorine doping, referred to as NMFO and NMO, respectively. The fluorine is meant to improve cycling stability.

Figure V - 51 shows the SEMS of both materials. The images are nearly identical. The particles are between one half micron to 3 microns in size and polygonal in shape. Electrodes were made of the same active and inactive material fractions, thicknesses, and porosity. The laminates were punched to circular electrodes and tested in coin cells with a standard electrolyte of 1 M $LiPF_6$ in EC:DEC 1:2. The counter electrode was either lithium metal or graphite. As seen for NMO in our lab, cycling against Li is stable. Most of the capacity is available with very little fade over 100 cycles before Li dendrites short the cell. Cycling with a graphite anode is slightly different. In that case, only half of the capacity of the cathode is accessible after formation. However, once formation is completed, the loss of capacity for the next 200 cycles is minimal (see Figure V - 52). This is the same for the baseline chemistry as it is for the materials Prof. Manthiram produced,

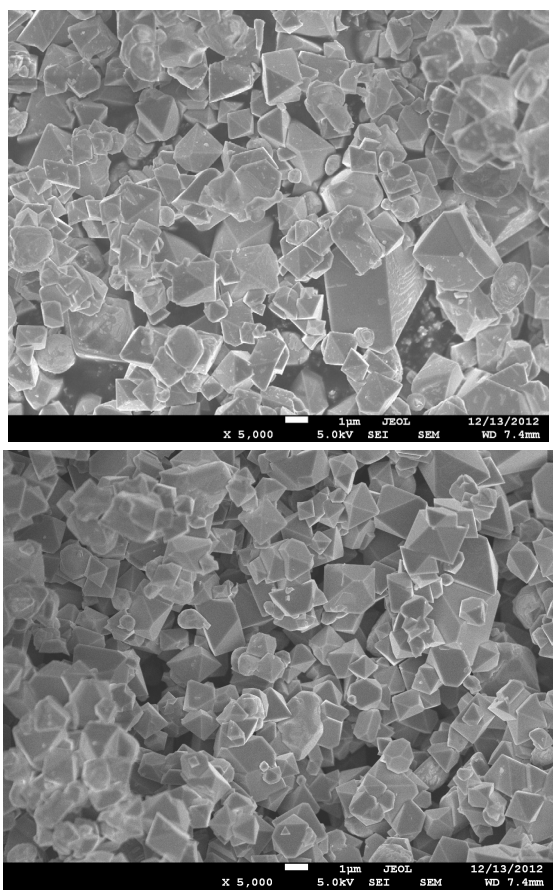

Figure V - 51: Top, SEM of NMO; bottom, SEM of NMFO. Materials appear nearly identical

see Figure V - 52. The source of capacity fade for the first five formation cycles is still under investigation. Half of the loss can be attributed to poor first cycle coulombic efficiency, seen for nearly all chemistries tested. Another 20% of the capacity loss occurs during the first five C/20 formation cycles, and another 15% of the capacity is lost when the cycling current is increased to C/3. Much of the loss can be attributed to SEI formation on the anode and a large impedance established in the first 3 cycles.

New NEI Material. At the 2013 DOE Annual Merit Review Meeting, discussions were held with representatives from NEI, the supplier of the baseline material used in the BATT, High-voltage, Ni-spinel Focus Group. They agreed to send LBNL their latest material. The results of the preliminary analysis of this latest material are reported here.

The physical characterization of this material included SEM, particle size analysis, and a measure of its surface area *via* the BET method. The SEM not only revealed that the particles are on the order of a few microns in diameter and consist of stacked crystal planes, but also provided no indication that these

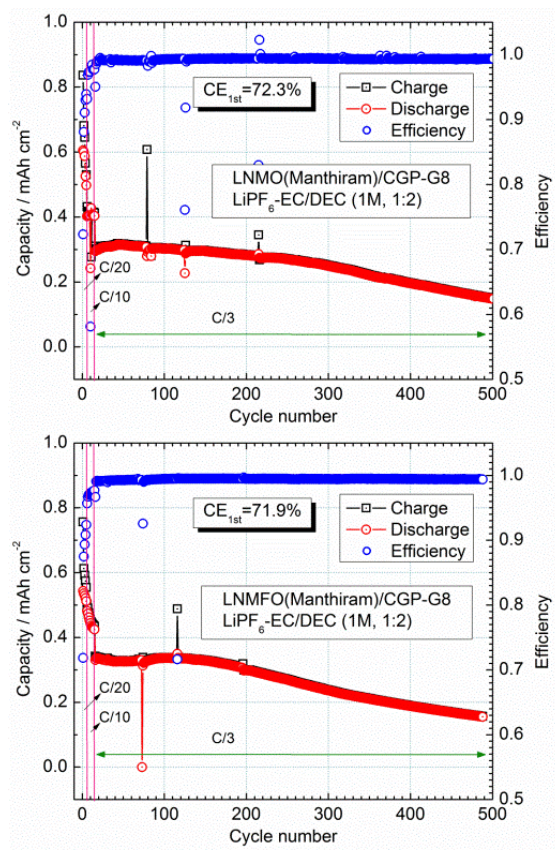

Figure V - 52: Top, capacity *versus* cycle number for a full cell of graphite/NMO; bottom, capacity *versus* cycle number for graphite/NMFO. Note the large capacity decline in the early cycles for both cells

particles consist of smaller primary particles. The particle size analysis indicated a fairly tight particle size distribution: d10 = 4. 2 microns and d90 = 11.8 microns. The mean particle size was measured at 6.6 microns with a standard deviation of 3.5 microns. The surface area was measured at 0.45 m^2/g, which is consistent with a particle diameter of 3.0 microns. It is typically found that the BET-derived diameter is approximately 1/3 the size as indicated by the PSA measurement, and this characteristic is attributed to a rough particle surface.

A cell of relatively low capacity, approximately 0.65 mAh/cm^2, was constructed for electrochemical characterization. The initial tests indicate that the material has a first-cycle coulombic efficiency of 94.1% and a discharge capacity of 133 mAh/g between 4.9 and 3.5 V. Of this capacity, 11.5% was accessible below 4.3 V.

This low specific-area capacity cell demonstrated high rate performance as expected. A modified Peukert plot of cell discharge capability for three different loadings is provided in Figure V - 53. It is clear that a C/2 discharge rate is within the capability of all three of these electrodes where mass transfer limitations are not a factor.

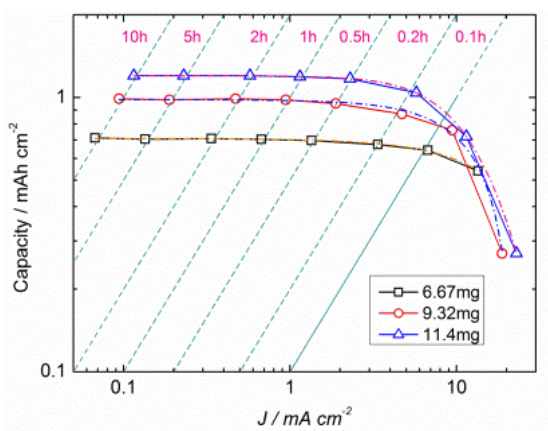

Figure V - 53: Capacity *versus* current density for three loadings

The half-cell capacity between 3.5 and 4.95 V *versus* cycle number is provided in Figure V - 54. With a large operational voltage range, one may not expect much capacity fade, and for this reason the energy of the cell *versus* cycle number is also provided (Figure V - 55.) These data include the impedance rise of both the cathode and lithium counter electrode. Since these data show very little energy decline, it is clear that there is very little impedance rise in this cell for over 150 cycles. All data were acquired from a cell with a standard electrolyte of 1 M $LiPF_6$ in EC:DEC, 1:2. As indicated previously, the problem with this chemistry is not its high-voltage instability but the effects this chemistry has on graphitic anodes.

Half cells of the latest NEI material were built and sealed to prevent leakage at elevated temperatures. The electrolyte was the baseline of 1 M $LiPF_6$ in EC:DEC 1:2. After 5 cycles at C/10 and 30°C, the temperature and cycling rate were both increased. The temperature was raised to 55°C and the C-rate to C/5 for 20 cycles and then increased again to C/2. One can see in Figure V - 56 that the capacity shows no loss after 120 cycles.

To test for impedance rise, the energy density was also tested. In Figure V - 57, the energy per gram of cathode *versus* cycle number is shown. One sees that the energy also does not decline with cycling, indicating that the cell's impedance does not rise with cycling.

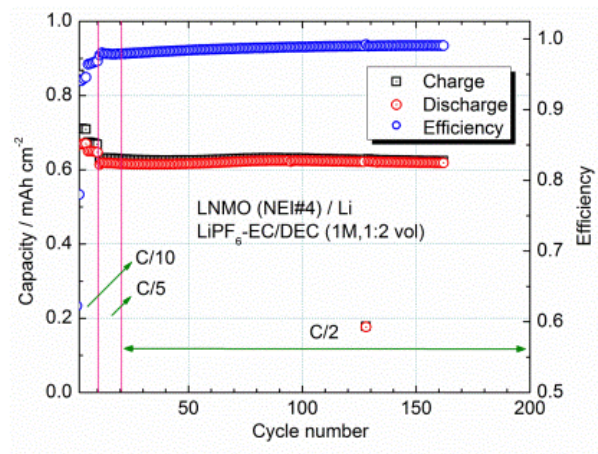

Figure V - 54: Capacity and efficiency *versus* cycle number

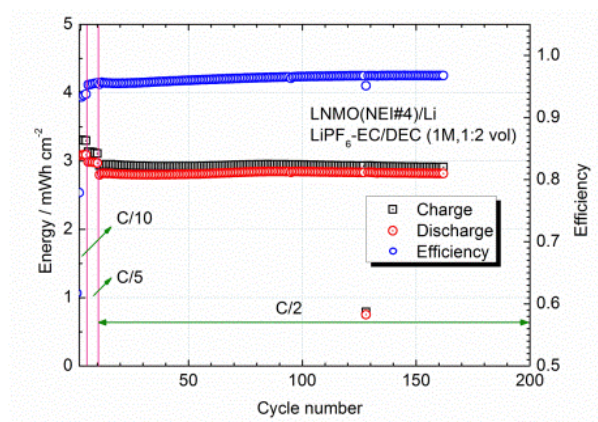

Figure V - 55. Energy and efficiency *versus* cycle number

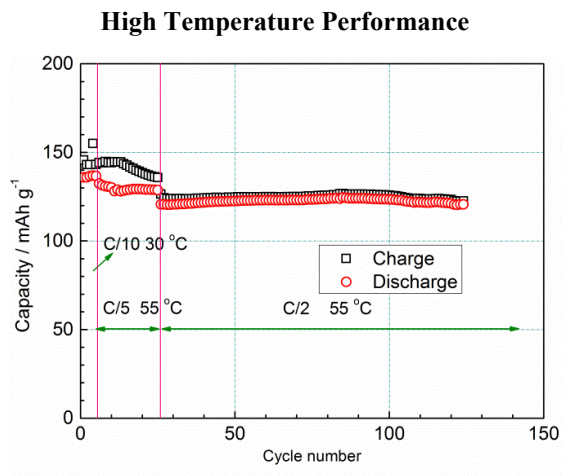

Figure V - 56: Capacity per gram of cathode active material *versus* cycle number at elevated temperature

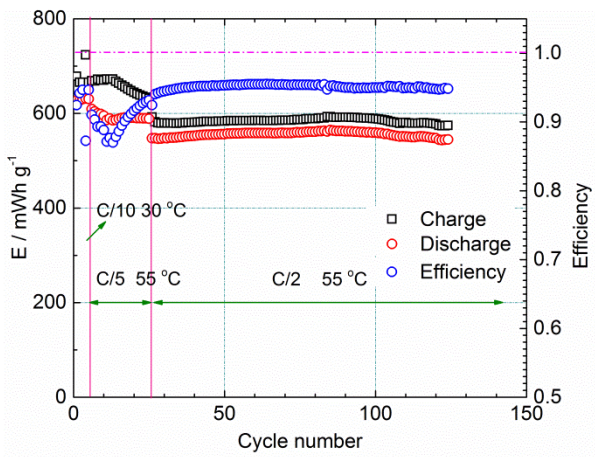

Figure V - 57: Energy per gram of cathode active material *versus* cycle number at elevated temperature

Conclusions and Future Directions

Investigations into the NMO material this year have revealed new information. The large, variable current seen in cells during the first few cycles can be abridged with a change in the conductive carbon and separator. This indicates that the carbon can be a catalyst to the oxidation reactions occurring in cells with this chemistry. It also provided further insight into the source of these reactions and methods on how to reduce them. It was also determined that materials designed based specifically on research that suggested better performance based on the level of disorder and particle morphology did not improve the biggest problem with this cell chemistry – a large capacity loss in full cells as a result of SEI formation. It was also found that the newest materials from NEI cycle very well, even at 55°C, indicating very good stability and no impedance rise up to 80 cycles.

The results obtained for the NMO material are much different than our experience with NMC material. For this reason, it is likely that a new study will soon begin to understand those differences. In particular, the NMC is known to show a great deal of instability and impedance rise when cycled above 4.4 V. It is not clear whether the instability is related to bulk properties of NMC or surface properties. To start, it will be important to identify a stable NMC that is well accepted in industry. We will work with our colleagues at ANL to identify this chemistry.

FY 2013 Publications/Presentations

1. 2013 DOE Annual Peer Review Meeting Presentation.

V.B.5 Impact of Materials on Abuse Response (SNL)

Christopher J. Orendorff, Kyle R. Fenton, Josh Lamb, and Ganesan Nagasubramanian

Sandia National Laboratories
P. O. Box 5800, Mail Stop 0614
Albuquerque, NM 87185-0614
Phone: (505) 844-5879; Fax: (505) 844-6972
E-mail: corendo@sandia.gov

Collaborators:
Prof. Steven George, CU-Boulder
Robert Tenent, NREL
Kevin Gering, INL
Rob Privette, XG Sciences

Start Date: October 2012
Projected End Date: September 2013

Objectives

- Elucidate degradation mechanisms in lithium-ion cells that lead to poor abuse tolerance (runaway thermodynamics, gas evolution, electrolyte combustion).
- Develop and evaluate advanced materials (or material combinations) that will lead to more abuse tolerant lithium-ion cell and battery systems.
- Build 18650 cells in the SNL fabrication facility for cell level evaluation of new materials in support of all ABR thrust areas.

Technical Barriers

There are several technical barriers to achieving the goals stated above including:

- Developing lithium-ion cells that are intrinsically abuse tolerant and do not lead to high order catastrophic failures.
- Mitigating the gas evolution and decomposition of the electrolyte.
- Passivation of cathode runaway reactions and interfacial reactions with electrolyte.
- Limited quantities of advanced materials (and numbers of cells with new materials) to evaluate abuse response.

Technical Targets

- Quantify the thermal runaway response of materials at the cell level (18650).
- Determine the effect of electrolyte salts, solvents and additives on the abuse response of lithium-ion cells.
- Evaluate the thermal response of candidate active materials.
- Identify materials that could be used to reduce gas evolution and the heat and kinetics of runaway reactions.

Accomplishments

- Continued evaluation of candidate electrolytes and salts that minimize the energetics of thermal runaway.
- Evaluated additives, electrode coatings, and new materials to improve abuse response and safety of lithium-ion systems.
- Fabricated electrodes to aid in standardization of ABR materials across national laboratories

✧ ✧ ✧ ✧ ✧

Introduction

As lithium-ion battery technologies mature, the size and energy of these systems continues to increase (> 50 kWh for EVs); making safety and reliability of these high energy systems increasingly important. While most material advances for lithium-ion chemistries are directed toward improving cell performance (capacity, energy, cycle life, etc.), there are a variety of material advancements that can be made to improve lithium-ion battery safety. Issues including energetic thermal runaway, electrolyte decomposition and flammability, anode SEI stability, and cell-level abuse tolerance continue to be critical safety concerns. This report highlights work with our collaborators to develop advanced materials to improve lithium-ion battery safety and abuse tolerance and to perform cell-level characterization of new materials.

Approach

The effect of materials (electrolytes, additives, anodes, and cathodes) on the thermal response of full cells is determined using several techniques. One of the

most useful and quantitative techniques is accelerating rate calorimetry (ARC). The ARCs at SNL are fitted with uniquely designed high pressure fixtures to not only measure quantitative heat flow but also gas generation under ideal adiabatic conditions during full cell runaway. Cells were fabricated using a variety of active materials, electrolytes, and additives in the SNL cell prototyping facility. The in-house prototyping capability gives us the versatility to target candidate materials, perform full cell evaluation, and correlate cell response to fundamental materials properties.

Abuse tolerance tests are performed which evaluate the response to expected abuse conditions and document and evaluate numerous outcomes including 1) failure point of energy storage device 2) conditions that cause failure 3) failure modes and abuse conditions using destructive physical analysis (DPA) 4) quantitate cell or module response to the abuse condition 5) provide feedback to develop new abuse test procedures that more accurately determines cell performance under the most likely abuse conditions.

Possible tests that can be performed cover three main categories of abuse conditions. Mechanical abuse tests include controlled crush, penetration, blunt rod, drop, water immersion, mechanical shock and vibration. Thermal abuse tests include thermal stability, simulated fuel fire, elevated temperature storage, rapid charge/discharge, and thermal shock cycling. Electrical Abuse tests include overcharge/overvoltage, short circuit, overdischarge/voltage reversal, and partial short circuit.

Results

Evaluation of High Energy Materials. One objective of this program is to determine baseline safety performance and thermal stability of the latest advanced high energy lithium-ion materials including lithium-rich layered metal oxide (LMO), Si-composites. The largest barrier to the success of this effort previously was the availability and access to these high energy materials. The first Si-composite anode evaluated at SNL as part of this program is a composite developed at XG Science. Electrodes were coated and cells prepared in the SNL prototyping facility. Performance of the Si-composite in a representative Li ½ cell (1.2 M $LiPF_6$ in EC:EMC (3:7) electrolyte) is shown in Figure V - 58. The specific capacities of all cells evaluated to date are on the order of 750 mAh/g.

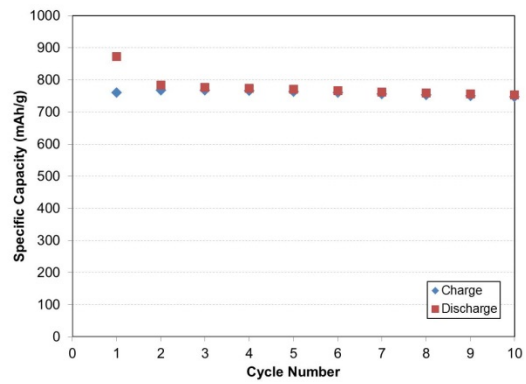

Figure V - 58: Specific capacity (mAh/g) of a representative Si-composite ½ cell vs. lithium

Differential scanning calorimetry (DSC) measurements of this material along with graphite and lithium titanate (LTO) samples for comparison are shown in Figure V - 59. The graphite anode shows the characteristic low heat flow onset at 100°C indicative of SEI decomposition followed by the higher rate decomposition > 200° C. The silicon composite shows a similar response but with an onset temperature of 150°C, but a comparable total specific heat to the graphite anode (3700J/g and 3360 J/g). LTO has a significantly more benign heat flow profile and a specific heat of 670 J/g.

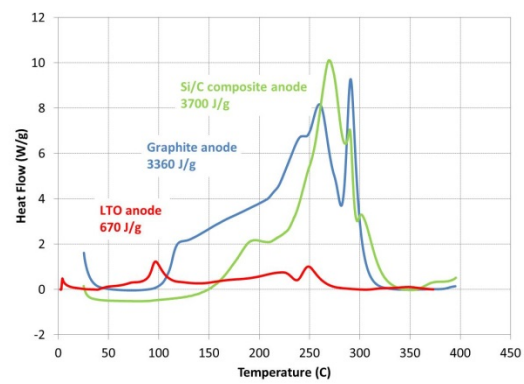

Figure V - 59: DSC profiles for graphite, LTO and Si-composite anodes

Evaluation of a LMR-NMC positive electrode material was also done recently. Initial work has focused on baseline materials characterization of HE5050 (Toda America). Figure V - 60 shows DSC data for HE5050 at 4.6 V and NMC 111 at 4.2 V for comparison. Results show a significantly higher specific heat for HE5050 (2,100 J/g) than NMC 111 (1,470 J/g) and a faster heat release rate. However, it is important to note that the LMR-NMC sample is evaluated at 400 mV higher voltage than NMC in this experiment. Work in FY14 will focus on cell fabrication and characterization of safety performance in 18650 cells.

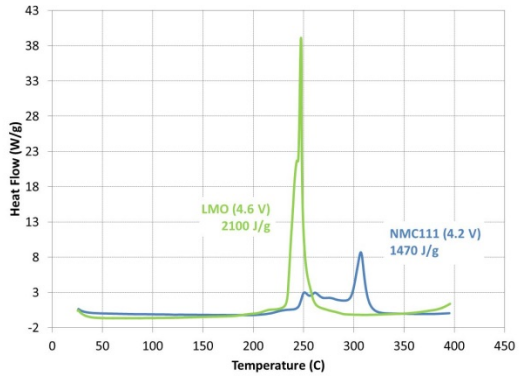

Figure V - 60: DSC profiles for LMR-NMC at 4.6 V and NMC 111 at 4.2 V

Coatings. For a number of years, the ABR program has focused on material coating strategies to improve cell performance and reliability. In earlier work, we have shown that AlF_3-coated NMC improves safety performance, as well. The NREL led coatings programs have focused on Al_2O_3 atomic layer deposition (ALD) coatings and the objective of our contribution is to evaluate the effect of these coatings on thermal stability and safety. NMC 111 (Toda) and graphite (CP A10) electrodes are coated with Al_2O_3 ALD to give ~0.3 nm and 0.8 nm thick coatings on each electrode, respectively. Figure V - 61 (top) shows DSC data for the coated and uncoated graphite electrode. Results show a significant reduction in the heat generation at the onset of SEI decomposition (~100°C). Figure V - 61 (bottom) shows ARC data for 18650 cells with Al_2O_3 ALD and uncoated electrodes. The coated cell shows an increase in the exotherm onset temperature by ~20°C, which is consistent with a stabilized SEI at the anode interface. The high rate cathode decomposition remains unchanged in the coated cell. This is likely due to the fact that the coating is not thick enough (nominally ~0.3 nm) to influence the decomposition of the positive electrode.

Ionic Liquid (IL) Development. Additional efforts to develop intrinsically non-flammable electrolytes with enhanced abuse tolerance performance have focused on ionic liquids as an alternative to the carbonate systems. Figure V - 62 (top) show cyclic voltammetry data of the candidate ILs prepared in FY12 and 13. The newest candidate, IL-3, shows the most promising voltage stability at both high and low potentials. IL-3 is stable to 5V which is comparable to carbonate solvent mixtures (no salt) and near the lithium potential without significant cation reduction. Electrolyte formulations of EC:EMC and IL-3 have been prepared to determine their performance in coin cells (NMC/graphite full cells). Figure V - 62 (bottom) shows specific capacity of for these coin cells with 0-60% IL. Results show that up to 40% IL the specific capacity during formation is identical to the EC:EMC control cell. At 60% IL, the performance begins to decay rapidly. Future work will focus on the optimization of the 40% IL-3 electrolyte formulations over longer cycle life and for safety performance (thermal stability and flammability).

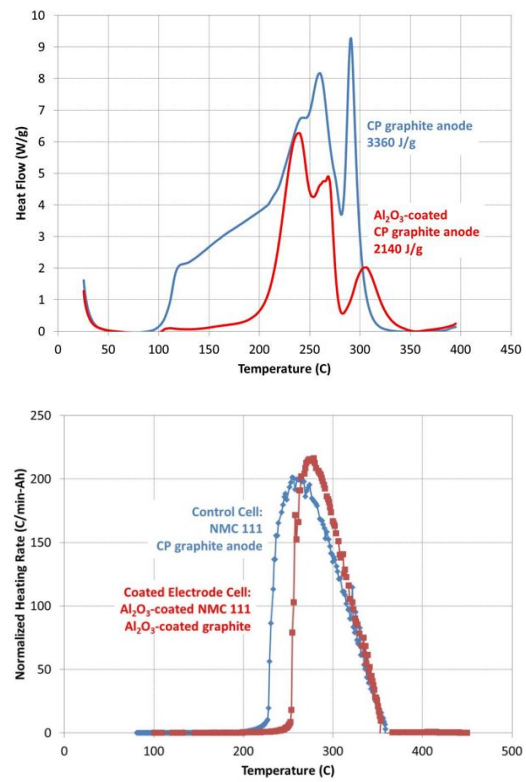

Figure V - 61: (Top) DSC profiles of Al_2O_3 ALD coated graphite and uncoated graphite and (bottom) ARC profiles for Al_2O_3 ALD coated electrodes and uncoated electrodes in an NMC/graphite 18650 cell

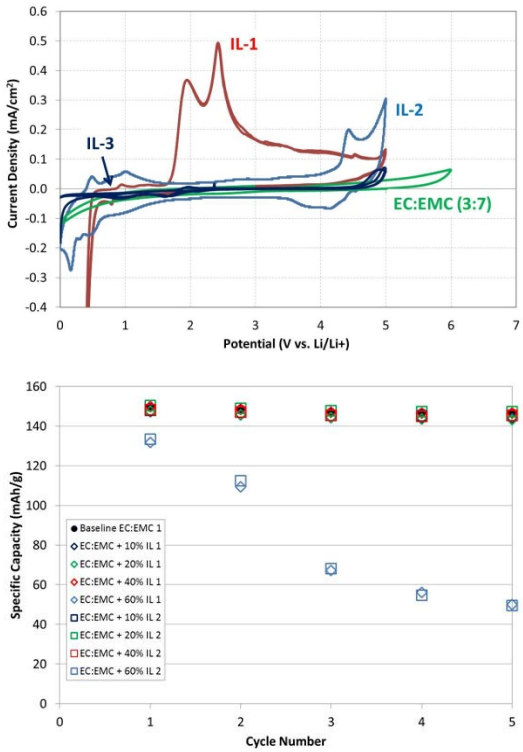

Figure V - 62: (Top) cyclic voltammetry of candidate ILs and (bottom) specific capacity at C/10 of NMC/graphite coin cells with different IL-3 fraction electrolyte formulations

Conclusions and Future Directions

This work demonstrates how specific advances in a variety of materials areas (anode, cathode, and electrolyte) can impact on cell-level safety and thermal characteristics. Work will continue in this area to evaluate cell-level abuse response using Al_2O_3 ALD coated cathodes electrodes to minimize thermal runaway reaction free energy, high energy materials including Si-composite anodes and LMR-NMC cathodes to determine baseline cell response, and IL-based electrolyte formulations for thermal performance and flammability. Future work will focus on the safety performance characterization of new coated materials (Physical Sciences, CU-Boulder, NREL), flame retardant additives (Case Western), and other advanced lithium-ion battery materials.

FY 2013 Publications/Presentations

1. C. J. Orendorff, J. Lamb, K. R. Fenton, and L. A. M. Steele, "Approaches to Evaluating and Improving Lithium-Ion Battery Safety" AABC February 2013.
2. C. J. Orendorff, "Approaches to Evaluating and Improving Lithium-Ion Battery Safety" CU-Boulder, February 2013.
3. 2013 DOE Annual Peer Review Meeting Presentation.
4. J. Lamb et al. J. Power Sources, 247 (2014) 1011-1017. "Thermal and overcharge abuse analysis of a redox shuttle for overcharge protection of $LiFePO_4$."

V.B.6 Post-Test Diagnostic Activities (ANL)

Ira Bloom, Primary Contact,
Nancy Dietz-Rago, Javier Bareño

Argonne National Laboratory
9700 South Cass Avenue
Argonne, IL 60439
Phone: (630) 252-4516; Fax: 630 252 4176
E-mail: ira.bloom@anl.gov

Start Date: April 2010
Projected End Date: September 2010

Objectives

- To accelerate the R&D cycle of DOE and industrial collaborators by developing and conducting standard procedures for post-test characterization of batteries in order to provide insight into physicochemical causes of performance degradation.

Technical Barriers

This project addresses the following technical barriers as described in the USABC goals [1, 2, 3]:

(A) Performance at ambient and sub-ambient temperatures.

(B) Calendar and cycle life.

Technical Targets

- EV: 5-year calendar life; 1,000 80% DOD DST cycles.
- HEV: 15-year calendar life, 300,000 charge-sustaining cycles; EOL performance (min): 25 kW and 300 Wh.
- PHEV: 15-year calendar life, 300,000 charge-sustaining cycles, 5,000 charge-depleting cycles; EOL performance (min): 45 kW and 300 Wh.
- LEESS: 15-year calendar life, 300,000 charge-sustaining cycles; EOL performance (min): 20 kW and 56 Wh.

Accomplishments

- Provided SEM characterization support to CAMP facility to optimize electrode making procedures.
- Characterized structural and physicochemical changes due to cycling of LMR-NMC/graphite and high-energy spinel/graphite cells built at CAMP facility containing standard electrodes from the CAMP electrode library, available to ABR programs. These characterization results provide a baseline for future studies to correlate observed property, structural and physicochemical changes due to cell constitution; e.g., testing a new electrodes or electrolyte additive, while keeping all other cell components standard. (Further cell chemistries pending).
- Collaborations with industrial and academic partners:
  - Argonne CAMP.
  - JCI.
  - Maxwell.
  - Army Research Laboratory (initial discussions).
  - Jet Propulsion Laboratory (initial discussions).
  - University of Hawaii (initial discussions).
  - CIC Energunie (Spain).
  - Dalhoussie University, (Canada).

✧ ✧ ✧ ✧ ✧

Introduction

Post-test characterization of components harvested from aged batteries provides information about physicochemical changes at materials level that, previously, could only be inferred. This information can be correlated to device performance characterization to provide new insights into fundamental causes of device degradation and suggest new design routes to overcome performance limitations.

Approach

We apply a combination of physical, spectroscopic, metallographic, and electrochemical characterization techniques to examine aged cell constituent materials in a systematic fashion. Harvesting and analysis are performed under inert atmosphere conditions to avoid preparation artifacts.

Cells can come either from exploratory DOE programs, such as ABR and BATT, or from pre-competitive R&D programs managed by USABC and

USDRIVE. The Post-Test Facility uses the experience and techniques developed in DOE's ABR program in a standardized fashion.

Figure V - 63: Argonne Post-test facility. The inert-atmosphere glovebox used for sample harvesting and analysis is shown in the background

Results

Initial SEM characterization support was provided to the CAMP facility to assist in optimization of mixing procedures for different electrodes. Test electrodes were examined for homogeneity and structural changes due to slurry mixing and electrode calendering. Once optimized, the CAMP facility used these electrodes to produce several sets (cell builds) of ~ 400 mAh pouch cells of several cathode/graphite cehemistries, using Argonne's standard 1.2 M $LiPF_6$ in EC:EMC (3:7 by weight) electrolyte.

Two sets of cells containing LMR-NMC and high-energy NiMn spinel electrodes were received by the Post-test facility for examination. These cells had been previously cycled by CAMP at C/2 rates to 20-25% initial capacity loss.

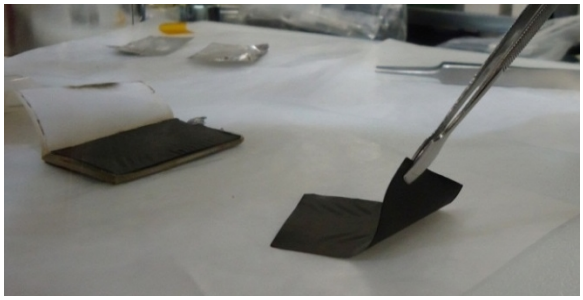

Figure V - 64: NiMn spinel / graphite pouch cell being disassembled from analysis. In this case, the cathode coating delaminated from the Al current-colletor due to adhesion failure

The cells were transferred to an inert-atmosphere glovebox for cell disassembly and sample harvesting, see Figure V - 64. Cells were disassembled by carefully cutting through the cell pouch material to avoid shorting the cell, while monitoring cell temperature in real time to alert the worker of a potential short-circuit or internal reaction. Visual examination of the disassembled cells revealed: (1) a "zebra pattern" of stains in electrodes and separator, probably related to differences in local current density and, hence, electrolyte decomposition rate; and (2) adhesion failure of spinel electrodes resulting in delamination from the current collector resulting in a self-supporting electrode coating layer (see Figure V - 64).

SEM (see Figure V - 65) examination of harvested electrode and separator samples did not reveal appreciable microstructural differences between lighter and darker regions (stripes) of the observed "zebra patters." However, EDS analysis showed F- and P-enrichment at lighter areas in the "zebra patterns," consistent with higher local concentrations of $LiPF_6$ salt decomposition products.

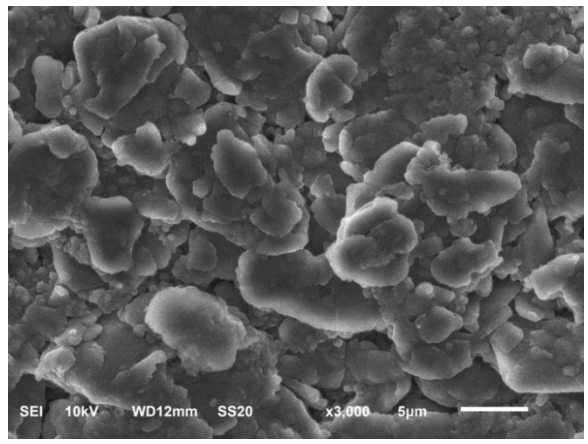

Figure V - 65: SEM micrograph of aged Li-Mn rich NMC electrode. EDS analysis indicates presence of fluorinated electrolyte reaction products

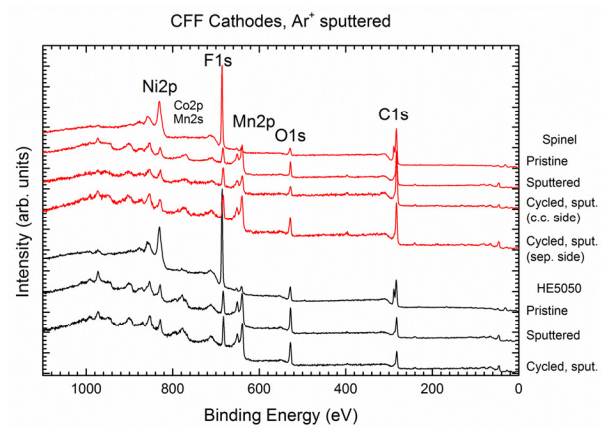

Figure V - 66: XPS comparison of pristine and aged LMR-NMC and NiMn spinel electrodes. Note that sputter cleaning of surface layers (binder, conductive additives) is needed to expose active oxides in pristine material

XPS characterization was used to track changes in surface chemistry of harvested components. Due to the extremely short information depth of XPS it is necessary to sputter away spurious surface films such as electrolyte residue. Figure V - 66 shows an example where oxygen and transition metal films from active oxide particles (LMR- NMC and Li-Ni-Mn-O spinel) are revealed only after Ar^+ sputtering of binder and conductive additives. Sputtering time required to reach underlying oxide can be used as a metric to determine relative thickness of evolved films in a series of samples. Furthermore, ion sputtering allows monitoring differences in chemical composition as a function of depth. Care must be taken to identify and avoid possible artifacts, such as loss of chemical resolution (peak broadening) due to the sputtering process. Well-defined pristine materials are subjected to the same cleaning/sputtering processes as samples of interest to gauge the extent of potential measurement artifacts.

Conclusions and Future Directions

Over FY 2013, Argonne's Post-test Facility has been collaborating with Argonne's CAMP facility and other ABR and USABC programs.

Argonne's CAMP facility is developing a standard library of balanced electrodes for DOE researchers to test new materials in standard cell configurations. Argonne's Post-test facility has started systematic characterization of CAMP's electrodes and physicochemical changes due to aging. In the near future, these tests will provide a characterization baseline to study the effect of new cell components (e.g., active materials, electrolytes, additives) on aging mechanisms of standard cells.

In the future, the Post-test Facility will continue to work with the CAMP facility to expand the library of standard electrodes available to ABR and BATT programs. In particular, we plan on expanding the range of negative electrodes to include Si-based systems.

Additionally, Argonne's Post-test Facility will continue to support ABR, BATT, and USABC development programs through planning, executing and interpreting state-of-the-art *in situ* characterization. Additionally, Post-test Facility workers will step up ongoing outreach efforts to increase our current portfolio of industrial and academic collaborations.

List of Abbreviations

ABR: Advanced Battery Research
BATT: Batteries for Advanced Transportation Technologies
CAMP: Cell Analysis Modeling and Prototyping
DOD: depth of discharge
DST: dynamic stress test (see ref. 3)
EC: ethylene carbonate ($C_3H_4O_3$)
EDS: energy dispersive spectroscopy
EMC: ethyl methyl carbonate ($C_4H_8O_3$)
EOL: end of life
EV: electric vehicle
HEV: hybrid electric vehicle
LEES: low-energy energy storage system
LMR-NMC: Li- and Mn-rich Ni-Mn-Co oxide
NMC: Li-Ni-Mn-Co oxide
PHEV: plug-in hybrid electric vehicle
R&D: research and development
SEI: solid-electrolyte interface
SEM: secondary electron microscopy/microscope
USABC: United States Advanced Battery Consortium (DOE, GM, Chrysler and Ford)
VC: vinylene-carbonate ($C_3H_2O_3$)
XPS: x-ray photoelectron spectroscopy

FY 2013 Publications/Presentations

1. "Compatibility of Lithium Salts with Solvent of the Non-Aqueous Electrolyte in Li-O_2 Batteries." P. Du, J. Lu, K.C. Lau, X. Luo, J. Bareño, X. Zhang, Y. Ren, Z. Zhang, L.A. Curtis, Y-K. Sun, and K. Amine. *Phys. Chem. Chem. Phys.,* 15 (2013) 5572. doi:10.1039/C3CP50500F
2. "Role of Polysulfides in Self-Healing Lithium-Sulfur Batteries." R. Xu, I. Bellharouak, J.C.M. Li, X. Zhang, I. Bloom, and J. Bareño. *Adv. Energy Mat.* 3 (2013) 833. doi:10.1002/aenm.201200990
3. "Improving high-capacity $Li_{1.2}Ni_{0.15}Mn_{0.55}Co_{0.1}O_2$-based lithium-ion cells by modifying the positive electrode with alumina." M. Bettge, Y. Li, B. Sankaran, N. Dietz Rago, T. Spila, R. T. Haasch , I. Petrov, and D.P. Abraham. *J. Power Sources,* 233 (2013) 346. doi:10.1016/j.jpowsour.2013.01.082
4. "A high performance separator with improved thermal stability for Li-ion batteries." J.-J. Woo, Z. Zhang, N. L. Dietz Rago, W. Lu and K. Amine. *J. Mater. Chem. A*, 1 (2013) 8538. doi:10.1039/c3ta12154b
5. (Invited talk) "Post-Test Analysis of Lithium-Ion Battery Materials at Argonne National Laboratory." J. Bareño, N. Dietz-Rago, and I. Bloom. International Battery Association Meeting. Barcelona, Spain. March 10-15, 2013.

6. (Poster) "Cell Fabrication and Post Test Facilities at Argonne National Laboratory ." B. Polzin, W. Lu, A. Janses, D. Dees, S. Trask, J. Bareño, N. Dietz-Rago, and I. Bloom. 30th International Battery Seminar and Exhibit. Fort Lauderdale, FL. March 11-13, 2013.
7. "Cell Fabrication Facility and Post Test Characterization Facility at Argonne National Laboratory." B. Polzin, Z. Chen, J. Bareño, S. Trask, N. Dietz-Rago, A. Jansen, and I. Bloom. 246th American Chemical Society National Meeting & Exposition. Indianapolis, IN. September 11-13, 2013.
8. (Poster) "Post-Test Analysis of Lithium-Ion Battery Materials at Argonne National Laboratory." J. Bareño, N. Dietz-Rago, and I. Bloom. 6th International Conference on Advanced Lithium Batteries for Automotive Applications. Argonne, IL. September 9-11, 2013.

References

1. FreedomCAR Battery Test Manual for Power-Assist Hybrid Electric Vehicles, DOE/ID-11069, October 2003.
2. FreedomCAR Battery Test Manual for Plug-In Hybrid Electric Vehicles, June 2010.

   Electric Vehicle Battery Test Procedures Manual, Revision 2, January 1996.

V.C Critical Barrier Focus: Voltage Fade

V.C.1 Voltage Fade in the LMR-NMC Materials: Background & Project Scope (ANL)

Anthony Burrell

Argonne National Laboratory
9700 South Cass Avenue
Argonne, IL 60439-4837.
Phone: (630) 252-2629
E-mail: Burrell@anl.gov

Collaborators:
Ali Abouimrane, Daniel Abraham, Khalil Amine, Mahalingam Balasubramanian, Javier Bareno Garcia-Ontiveros, Ilias Belharouak, Roy Benedek, Ira Bloom, Zonghai Chen, Dennis Dees, Kevin Gallagher, Hakim Iddir, Brian Ingram, Christopher Johnson, Wenquan Lu, Dean Miller, Yang Ren, Michael Thackeray, Lynn Trahey, and John Vaughey all from Argonne National Laboratory

Claus Daniel, Debasish Mohanty, David Wood III, Jianlin Li (ORNL)

Oak Ridge National Laboratory
One Bethel Valley Road
P.O. Box 2008, MS 6472
Oak Ridge, TN 37831
Phone : (865) 241-9521; Fax: (865) 241-5531
E-mail: danielc@ornl.gov

Start Date: October 2012
Projected End Date: September 2014

Objectives

Voltage fade is one of the major limitations to the commercialization of the LMR_NMC materials. The overarching goal of this project is to eliminate voltage fade in LMR-NMC. To do this in FY13 we proposed to:

- Map out performance and cost space for generic chemistries (complete).
- Make an initial techno economic assessment of LMR-NMC capacity and average voltage to outperform existing materials (complete).
- Finalize LMR-NMC material level properties required to meet DOE PHEV40 and EV goals (Complete).
- Document state-of-the-art performance and barriers still remaining to overcome for LMR-NMC (complete).
- Go-No/go for coatings (complete).

Technical Barriers

The primary technical barriers to the development of a safe cost-effective PHEV battery with a 40 mile all electric range that meets or exceeds all performance goals include:

- Interpreting complex cell electrochemical phenomena.
- Identification of cell degradation mechanisms.

Technical Targets

- Develop a cell to meet the 40-mile PHEV goal.
- Obtain a positive-electrode material that can operate in the high-potential range (4V - 5V vs. Li/Li+) while still achieving approximately 130 mAh/g of capacity.

Accomplishments

- **Go-NO-GO coatings and additives = NO-GO.** Within experimental error, there was little-to-no effect on voltage fade from the coatings and additives, pointing to voltage fade being tied to the intrinsic nature of the cathode material. All coatings work related to voltage fade was halted.
- Established a reliable sol-gel route to the syntheses of LMR-NMC and its variants.
- Evaluated dopants: Al , Fe, V, Ga, and Cr.
- Demonstrated that voltage fade is sensitive to Li-Ni-Mn-Co composition.
- Developed a statistical model relating composition to voltage fade to guide the selection of compositions.
- Developed and deployed a graphically-oriented database to collect and organize the information generated by team members.

- Demonstrated LMR-NMC electrodes display at stable hysteresis - gap exists even after 70 day hold.
- Linked hysteresis and voltage fade phenomena.
- Proposed mechanism for electrochemical behavior based on reversible and irreversible transition metal ion migration.
- Created a new hypothesis on why this class of materials is able to achieve significantly higher capacity than others (i.e., 250 vs 175 mAh/g).

✧ ✧ ✧ ✧ ✧

Introduction

xLi_2MnO_3•$LiMO_2$ (M = Ni, Co, Mn) or LMR-NMC composite cathode materials currently receive world-wide attention as promising candidates for the next generation of high-capacity lithium-ion batteries. This class of materials is capable of delivering 250 mAh/g or more over extended cycling. However, in order to access such capacities these materials must first be 'activated' to high voltages (>4.5 V) to access lithium associated with Li_2MnO_3-like domains. During the activation process oxygen loss and transition metal (TM) migration and rearrangement have both been reported; after which, a continuous decay of the average voltage with cycling is observed. In addition, a large hysteresis in voltage is observed when cycling over the extended windows (~4.6 – 2.0 V) needed to obtain the desired capacities. Therefore, the decrease in energy output with cycling is accompanied by an overall energy-inefficiency. To date, no work, to our knowledge, has been directly aimed at understanding hysteresis in lithium-excess materials. This work begins an initial investigation into the hysteresis phenomenon in order to better understand the structural and chemical properties of composite materials as a function of lithium content and to explore possible correlations, if any, related to voltage fade.

We propose an integrated approach to solving this critical issue which involves a coordinated set of characterization and synthesis experiments designed to both understand the causes of voltage fade and then eliminate the problem. To do this we have formed a team of researchers to maximize the project's abilities in theory, materials development, characterization, cell level modeling, testing, scale-up and characterization.

Approach

Bring together a diverse technical team that will share data and expertise to "fix" voltage fade in the LMR-NMC cathode materials. This will be a single team effort (i.e., not multiple PI's working independently on the same problem).

- Definition of the problem and limitations of the composite cathode materials.
- Data collection and review of compositional variety available using combinatorial methods.
- Modeling and theory.
- Fundamental characterization of the composite cathode materials.
- Understand the connections between electrochemistry and structure.
- Synthesis.
- Post treatment/system level fixes.

Results

We have utilized the team approach to understanding and correcting voltage fade. We have aggressively down-selected projects and different approaches to the research. The results of the research program are broken into different sections and the conclusions are described in the following chapters. One major accomplishment is the inclusion of other research groups in both the characterization of the LMR-NMC materials (BNL, ORNL) and in the down select process (ORNL, NREL, JPL, LBNL). The voltage fade project represents a large volume of research which is covered in the following chapters: IV.C.2- IV.C.6.

Conclusions and Future Directions

The enhanced capacity available in the lithium manganese rich materials us unique in the lithium ion materials. In FY14 we will continue to develop the solution to voltage fade. Specific tasks are:

- Determine effect of "break-in" cycling on voltage fade and the final average voltage.
- Determine the effect that elemental composition has on voltage fade and the final average voltage after "break-in".
- Determine the nature of the synthesis and the dopants that change the rate of voltage fade in the lithium magnesium rich materials.
- Determine the source of the enhanced capacity in the LMR-NMC materials.
- Determine voltage fade phenomenon mechanism.
- Provide a solution to the voltage fade phenomena in the LMR-NMC materials.

V.C.2 Electrochemical Characterization of Voltage Fade in LMR-NMC Cells (ANL)

Daniel Abraham
Argonne National Laboratory

Collaborators:
Martin Bettge, Argonne National Laboratory
Yan Li, Argonne National Laboratory
Ye Zhu, Argonne National Laboratory
Qingliu Wu, Argonne National Laboratory
Kevin Gallagher, Argonne National Laboratory
Wenquan Lu, Argonne National Laboratory
Dennis Dees, Argonne National Laboratory
Ira Bloom, Argonne National Laboratory

Start Date: October 2012
Projected End Date: September 2014

Objectives

- The primary objective of the work is to enable the Argonne high energy composite layered cathode xLi_2MnO_3•$(1-x)LiMO_2$ (M = Ni, Mn, Co), also referred to as lithium and manganese rich NMC material (LMR-NMC), for the 40-mile PHEV (PHEV-40) application.
- Increase understanding of electrochemical behavior of LMR-NMC electrode materials.

Technical Barriers

The primary technical barriers to the development of a high energy density battery for EV and PHEV applications that is safe, cost-effective, and has long cycle life include:

- Interpreting complex cell electrochemical phenomena.
- Identification of cell degradation mechanisms.

Technical Targets

- By 2014, a PHEV battery that can deliver a 40-mile all-electric range and costs $3,400.
- Enabling LMR-NMC materials to a state of commercial adoption.

Accomplishments

- A protocol to measure and quantify voltage fade throughout cycling has been developed and applied to a wide variety of oxide electrode materials.
- Cycling protocols have been shown to impact voltage fade in LMR-NMC electrode materials and their effect has been quantified.
- A probable mechanism for voltage fade has been proposed and examined.

✧ ✧ ✧ ✧ ✧

Introduction

Energy density is an important characteristic of Li-ion batteries. For a given volume or mass, it determines, among other factors, the duration and range of the battery's operational autonomy and the cost of the battery pack. Unfortunately, the deliverable energy of practical Li-ion cells fades when repeatedly charged and discharged. This energy loss can typically be traced back to three major causes: chemical trapping and loss of mobile lithium within the cell, loss of available lithium-hosting sites, and rising cell resistances. Under certain conditions, there exists yet another mechanism which causes the cell's energy output to decrease: a continuous cycle-to-cycle decrease of the cell voltage, during charge and discharge. This decrease is typically associated with the drop in equilibrium voltage of the positive electrode, as observed for many Li-intercalating oxides. This phenomenon, occasionally referred to as "voltage fade" or "voltage decay," reduces the usable energy because the voltage of the cell integrated over the capacity equals the cell's energy. It also complicates state-of-charge (SOC) determination which is crucial to effective battery management.

Although varying degrees of voltage fade have been observed in a range of materials over the past years, several issues remain unaddressed. First, the actual physical mechanisms leading to voltage decay are largely unknown, although theories exist [1, 6]. Second, no comprehensive studies exist which establish structural and experimental conditions for voltage fade to occur. In fact, it is not even clear whether the impact of voltage fade is technologically significant. And last, no formal description of voltage fade and its measurement exists. Especially, the latter one is critically important to successfully address the other issues and to evaluate effectiveness of proposed strategies to mitigate this voltage decay.

Approach

Basic methodology. To track voltage fade, we calculate the average voltage for each charge and discharge. This is possible because the composition-dependent cell voltage *U(q)*, which continuously decreases throughout cycling, affects the measured average voltage $\bar{U}_{meas}$ via $\bar{U}_{meas} = E/Q = (1/Q)\int U(q)dq$, with E and Q being the total energy and capacity of the cell. To correct for the many polarization losses that affect *U(q)* and cause a difference between measured and true (i.e., near equilibrium) average voltages, we use an average cell resistance to obtain a resistance-corrected average voltage, $\bar{U}_{corr} = \bar{U}_{meas} - i\bar{R}$. (Note that a rise in cell resistance forces *U(q)* to increase during charge and to decrease during discharge.) This way, we can compute an average open-circuit electrode potential for the compositional region of interest for each charge and discharge. This is henceforth referred to as "corrected average voltage."

Materials. The material of prime interest in this voltage fade study is a structurally-integrated, Li- and Mn-rich layered metal oxide expressed as $Li_{1.2}Ni_{0.15}Mn_{0.55}Co_{0.1}O_2$, and as $0.5Li_2MnO_3$•$0.5LiMn_{0.375}Ni_{0.375}Co_{0.25}O_2$ in the two-component notation. This material is denoted as "LMR-NMC" throughout the text. The LMR-NMC exhibits high oxide-specific charge- and energy-densities exceeding 250 Ah-kg_{oxide}^{-1} and 900 Wh-kg_{oxide}^{-1} when charged beyond 4.5V vs. Li^+/Li. Details regarding cell chemistry, electrode formulation, and average cell resistances are given in Appendix A1 for a set of standard baseline cells and "modified" cells. The modifications of the latter cells yield improved capacity retention and lower impedance rise in graphite-containing full-cells, as shown elsewhere [2 - 4]. Voltage fade is also studied for other oxide chemistries, such as $LiNi_{0.8}Co_{0.15}Al_{0.05}O_2$ (also known as NCA), $Li_{1.05}(Ni_{1/3}Mn_{1/3}Co_{1/3})_{0.95}O_2$ (also known as NMC), $Li_{1.2}Ni_{0.4}Mn_{0.4}O_2$, $Li_{1.2}Ni_{0.2}Mn_{0.6}O_2$, $Li_{1.2}Co_{0.4}Mn_{0.4}O_2$, and $Li_{1.2}Cr_{0.4}Mn_{0.4}O_2$. The latter five compounds are also structurally-integrated composites and can be expressed in the two component notion as xLi_2MnO_3•$yLi(M_a,Mn_b)O_2$ with M being Ni, Co, or Cr. The LMR-NMC, NCA, and NMC are obtained from commercial sources. The $Li_{1.2}Ni_{0.2}Mn_{0.6}O_2$, $Li_{1.2}Ni_{0.4}Mn_{0.4}O_2$ and $Li_{1.2}Co_{0.4}Mn_{0.4}O_2$ compounds are prepared by a coprecipitation method. The $Li_{1.2}Cr_{0.4}Mn_{0.4}O_2$ compound is prepared by a chemical solution route. Electrodes for electrochemistry experiments are prepared by coating an Al foil with a mixture containing the oxide, SFG-6 graphite, acetylene black, and PVDF binder (84:4:4:8 by weight).

Experimentally measuring and tracking voltage fade. Galvanostatic cycling is conducted in 2032-type coin cells (1.6 cm^2 area electrodes) with Li-metal counter electrodes. All cells contain a 1.2 M $LiPF_6$ in EC:EMC (3:7 by wt.) electrolyte (referred to as "Gen2 electrolyte") and a Celgard 2325 (a polypropylene–polyethylene–polypropylene trilayer) separator. The cells are assembled in an Ar-atmosphere glove box (O_2 < 10 ppm, H_2O < 1 ppm) and cycled at 30°C in an environmental chamber according to a cycling protocol specifically developed to track voltage fade. This protocol uses moderate cycling currents of 10 mA-g_{oxide}^{-1} (0.1 mA, ~C/25 rate) between 2.0 and 4.7V vs. Li^+/Li for the first charge/discharge cycle and 20 mA-g_{oxide}^{-1} (0.2 mA, ~C/12 rate) for subsequent cycles in the same voltage range. The lower current during the first cycle promotes adequate wetting of the electrode and complete electrochemical activation of the active oxide. From the second cycle onwards, the protocol also implements current interrupts to estimate resistances at various cell voltages during charge and discharge. The current is stopped for 10 minutes and the voltages are recorded before and after the stopping period to estimate the cell resistance (i.e., dU/dI). For the LMR-NMC material specifically, resistances are recorded at a total of six different voltages during charge and discharge. The resistance-corrected average voltage is then calculated in three steps:

1. Average charge and discharge voltages are calculated by dividing the total cell's energy by the cell's capacity measured at 4.7V after charging and at 2.0V after discharging.
2. Average charge and discharge resistances are calculated from three interrupts for charge and discharge (at 3.5V, 3.9V, and 4.3V during charge, and at 4.0V, 3.6V, and 3.2V during discharge).
3. Resistance-corrected average voltages are then calculated by subtracting the averaged "$i\bar{R}$" polarization losses from the measured average voltages.

For the other layered oxides, minor adjustments are made to the position of the current interrupts based on their capacity-voltage profiles. Tracking voltage fade in such a manner is reasonably fast and can be carried out during normal cycling. Some limitations of this methodology are discussed later in this report.

Results

Voltage fade of the LMR-NMC baseline material. Figure V - 67 shows charge and discharge profiles for the LMR-NMC baseline material. In Figure V - 67A, a gradual cycle-to-cycle drop of the charge and discharge profiles, along with a relatively small capacity loss, is apparent. In Figure V - 67B, the capacities are normalized for each half-cycle, showing this gradual drop in electrode potential more clearly. Both figures

also show "electrochemical activation" of the material as a ~4.5 V plateau during 1st charge. The mechanistic origin of this plateau is still being debated, but it is typically associated with irreversible structural changes of, and partial oxygen loss from, the active oxide. After activation, charge and discharge profiles become gradually sloped, over nearly the entire compositional region, electrochemically revealing dramatic changes to the local Li environments. The drop in voltage from 1st to 2nd charge is especially striking. Upon continued cycling, the profiles continue to drop to lower voltages. Note that the voltage decay during charge occurs *despite* a rise in average cell resistance that is caused by a degrading positive electrode [2, 4]. Hence, irreversible structural changes of the oxide are the origin of this potential change, and not cell-level charge transport kinetics. The measured cell resistances as a function of the interrupt positions and the corresponding average voltages are shown in the Figure V - 67B (inset table). Although the average resistances increase during cycling, some voltage-specific resistances can decrease (e.g., at 3.2 and 3.5V) because of state-of-charge (oxide-lithium-content) changes with cycling.

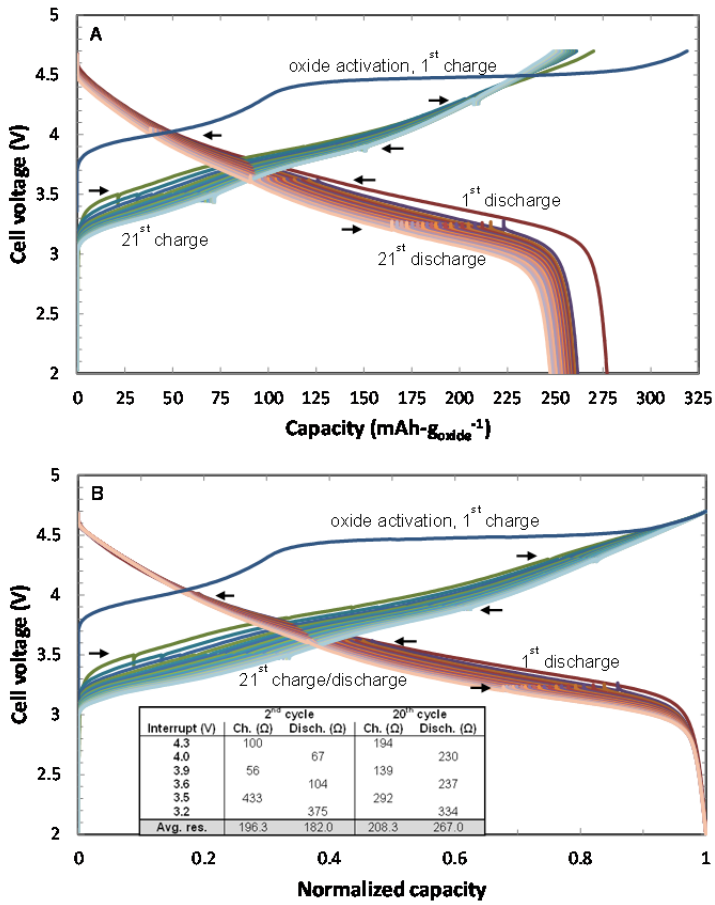

Interrupt (V)	2nd cycle Ch. (Ω)	2nd cycle Disch. (Ω)	20th cycle Ch. (Ω)	20th cycle Disch. (Ω)
4.3	100		194	
4.0		67		230
3.9	56		139	
3.6		104		237
3.5	433		292	
3.2		375		334
Avg. res.	196.3	182.0	208.3	267.0

Figure V - 67: The first 21 galvanostatic charge/discharge cycles for LMR-NMC *vs.* Li in the 2.0-4.7V range at 30°C, as-measured (A) and capacity normalized (B). A depression of the voltage profiles is apparent for charge and discharge curves after capacity normalization. A capacity of unity refers to 319 mAh-g$_{oxide}^{-1}$ (after 1st charge), 277 mAh-g$_{oxide}^{-1}$ (after 1st discharge), and 248 mAh-g$_{oxide}^{-1}$ (after 20th discharge). Black arrows indicate the positions of the six current interrupts used to calculate the average resistances. The inset table in the lower plot shows cell resistances as a function of the interrupt voltage for the 2nd and 20th cycle. fade

Figure V - 68 shows how voltage fade reveals itself in the differential capacity plots for charge and discharge. Here, the 1st cycle with its extensive activation plateau is removed to improve clarity. During the first 20 cycles after activation, the dQ/dV peaks between 3.0V and 3.5V shift down in charge voltage and grow at the expense of the higher voltage peak intensities (between ~3.8V and 4.7V) – a similar behavior is observed during discharge. As a result, the redox-active phase, initially located at ~3.5V (during charge), appears to simultaneously transform and grow into one or more redox-active phase(s). The differential capacity plots reveal also another characteristic of the material: a large hysteresis caused by a major

asymmetry between charge and discharge and by a relatively large voltage relaxation from 4.7V down to ~4.5V at the beginning of discharge. The voltage relaxation is partly caused by sluggish kinetics even at very low cycling currents.

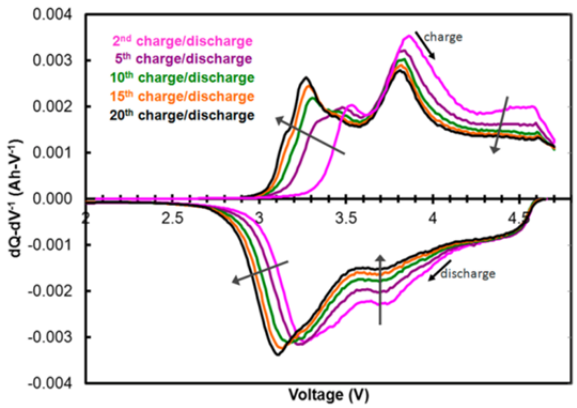

Figure V - 68: Differential capacity plots of the first 20 galvanostatic charge/discharge cycles after the initial activation cycle for LMR-NMC vs. Li over the 2.0-4.7V range at 30°C. The initial activation cycle is removed to highlight the changes that occur after activation. Increasing peak intensities and a shift to lower voltages at around 3.1V reveal voltage fade

Figure V - 69 depicts voltage fade as a drop in uncorrected and resistance-corrected average voltages. The average cell voltages are calculated for charge and discharge as described above. The nonzero average "$i\bar{R}$" polarization causes a difference of 30-70mV (at 0.2mA) between the uncorrected and corrected voltages; this polarization increases as cycling continues and cell resistance rises. A "voltage gap" between the corrected charge and discharge voltages of 240-300mV is the consequence of the material's intrinsic hysteresis. The corrected average voltages are not calculated during the 1st cycle because of uncertainties related to wetting of the electrode and structural changes of the oxide. Nevertheless, the abrupt drop in the uncorrected average voltage from 1st to 2nd charge, along with the difference between 1st charge and discharge, reflect the irreversible changes that occur within the material during its electrochemical activation. Upon continued cycling, a gradual decay in average voltage is clearly visible. For the first 20 cycles, the resistance-corrected average voltage drops by 185mV during charge and by 124mV during discharge which corresponds to a drop by ~3-5%, or, alternatively, to ~6-10mV per cycle. The difference in charge- and discharge-decay rates gradually reduces the initial voltage gap. The rate of decay is more rapid in the early cycles and continues nearly in a linear manner for at least 50 cycles under standard cycling conditions (not shown here).

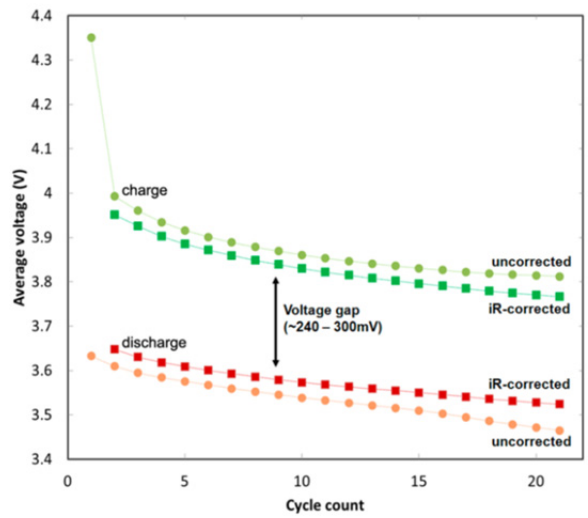

Figure V - 69: Average voltages, corrected and uncorrected, as a function of cycle number for the LMR-NMC *vs.* Li. Average voltages during charge are plotted in light/dark green, and those during discharge are plotted in orange/red. Voltage fade and voltage gap are apparent. Corrected average voltages drop by a total of 185mV during charge and by 124mV during discharge. Thin dotted lines are intended only as a guide to the eye, and are also shown in all subsequent figures

Additional measurements confirm the general voltage decay behavior and the overall effectiveness of the method. Figure V - 70 shows mean and standard deviation of the resistance-corrected average voltages for each cycle, for a total of five cells containing the LMR-NMC material. The standard deviation from the mean is always less than 7mV indicating very reproducible decay behavior with little cell-to-cell variability. On average, the voltage fade is 188mV (±11mV) during charge and 120mV (±1.6mV) during discharge between the 2nd and 20th cycle. Figure V - 70 also compares the corrected average voltages of a baseline cell (squares) to that of the modified baseline cell (diamonds). The modified cell contains the same active LMR-NMC material, but with 2.0 wt.% LiDFOB in the baseline electrolyte and a positive electrode with altered constituent ratios to mitigate the resistance increase of the positive electrode [2 - 4]. The average resistances of the two cell types during the 2nd and 20th cycle are given in Appendix A1; after 20 cycles the difference between the two types is large (~200Ω). Despite this large difference in average cell resistance, which would correspond to ~40mV at 0.2mA, the difference between the corrected average voltages remains small after 20 cycles (less than 14mV). Note also that the baseline cell shows voltage fade *during charge* despite a rise in average resistance; and that the modified cell shows voltage fade *during discharge* despite a decrease in average resistance. This shows that voltage fade and resistance effects can be effectively

decoupled using this approach of correcting the average voltage. Another important point here is that neither electrode formulation nor the addition of LiDFOB (which alters the surface films on the positive electrode) appear to affect the material's voltage fade in any significant manner. Another study, that used the same method to track voltage fade, confirms that surface modifications have no effect on the voltage fade [5].

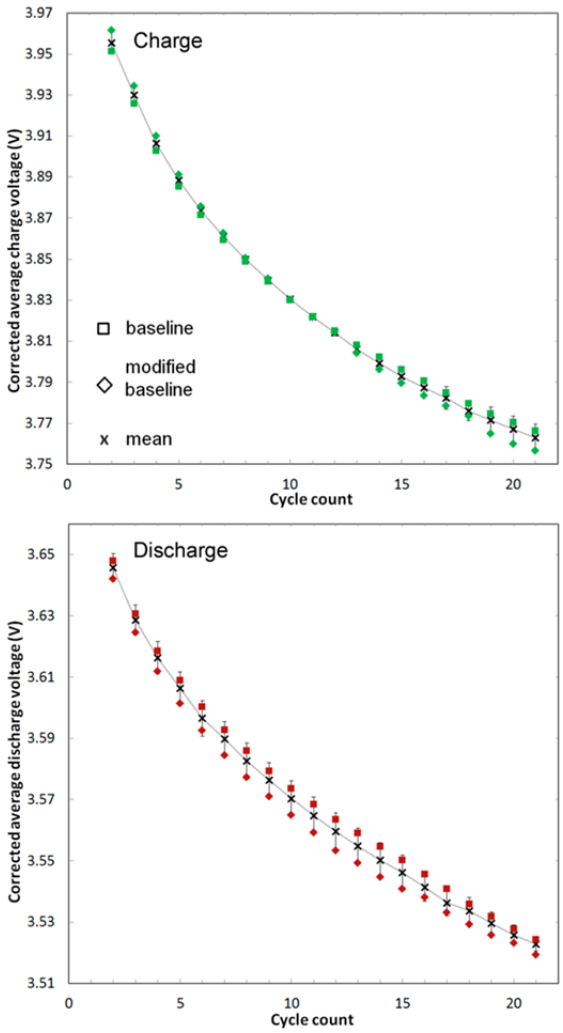

Figure V - 70: Mean and standard deviations, of the resistance-corrected average voltages during cycling, for five cells containing the same LMR-NMC oxide, top during chargem, bottom during discharge. The x-markers indicate the mean. The largest standard deviation from the mean, ±6.6 mV, is found after 21 cycles during charge. For comparison, square- and diamond markers indicate the average voltages for a baseline cell and for an improved baseline cell, respectively. The electrode formulation for the improved baseline cells is changed and LiDFOB is added to the electrolyte. As a result of these modifications, the cell resistance is much lower after 20 cycles

Figure V - 71 demonstrates the effect of voltage fade on energy density of the LMR-NMC cells. The measured discharge energy densities are shown as a function of cycle number for baseline and modified baseline cells. Assuming only a contribution from voltage fade (i.e., no capacity losses and no increase in cell resistance), the energy output continuously decays at a rate proportional to that in Figure V - 69 (as shown by the square red data points).

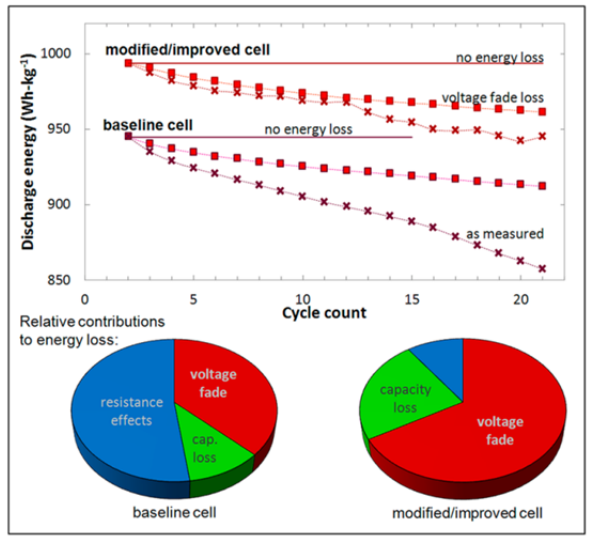

Figure V - 71: Discharge energies as a function of cycle number for the LMR-NMC-based baseline and modified cells. The cycling window is 2.0-4.7V. The measured energy densities for both cells are given by the x-shaped data points. Energy loss comprises contributions from capacity loss, resistance effects, and voltage fade. Energy loss only due to voltage fade is given by the squared data points. The relative contributions of capacity loss (green), resistance effects (blue), and voltage fade (red) after 20 cycles after activation are measured separately and plotted for each cell in the pie charts. Voltage fade is a significant contributor to the overall energy loss

In addition to voltage fade, capacity loss and resistance effects also cause the measured discharge energy to decrease; their physical origins have been identified and discussed elsewhere [2 - 4]. The relative contributions of these three factors leading to the difference between 2nd and 21st discharge energies are shown as pie charts in Figure V - 71. These charts are obtained by calculating the energy of the cell via $E(c) = \bar{U}(c)Q(c)$, with *c* being the cycle count and *E(c)* the released energy upon discharge that decreases continuously throughout cycling. $\bar{U}(c)$ is the measured average cell voltage that decreases due to voltage fade and resistance effects; *Q(c)* is the cell capacity that decreases due to resistance effects and *actual* loss in electrode capacity. This actual capacity loss is typically related to e.g., particle isolation and loss of active Li-hosting sites. The discharge energy after the 2nd

discharge is chosen to be the initial point of reference: it is 945 Wh-kg_{oxide}^{-1} for the baseline cell and 994 Wh-kg_{oxide}^{-1} for the modified baseline cell.

To obtain data for the pie charts, we first calculate the maximum contribution due to capacity loss by using the initial measured (i.e., uncorrected) average voltage, multiplied by the *actual capacity loss* after 21 cycles (i.e., resistance and voltage fade effects are excluded). This actual capacity loss is determined in a separate measurement in which a half-cell containing the oxide electrode is cycled under identical conditions and discharge capacities of the 2nd and 21st cycle are obtained. Here however, the 21st cycle discharge capacity is determined *after* Li counter electrode, separator, and electrolyte are replaced with fresh ones to minimize resistance effects from those components. Second, we calculate the minimum contribution due to voltage fade by using the above, separately determined, 21st cycle discharge capacity, multiplied by the *total drop* of the resistance-corrected average voltage after 21 cycles. Finally, cell resistance effects decrease both, the (uncorrected) average voltage and the measured capacity, and make up the remaining difference between initial and final energy densities.

Clearly, voltage fade is significant. In fact, once the increase in resistance is effectively mitigated through the improved cell design, voltage fade becomes the largest contributor (>65%) to the overall energy fade.

Factors influencing voltage fade of the LMR-NMC oxide. Experimental conditions affect voltage fade; some of these conditions are described below:

Cycling window: Upper and lower cut-off voltages affect the rate of fade. Figure V - 72 shows the corrected average discharge voltages for different upper cut-offs. Clearly, as the cut-off is raised, the voltage fades faster; at voltages less than 4.4V, fade is negligible. The impact of the lower cut-off was recently found to be more complex, as shown over a ~2-4V span by Gallagher et al. [1]. In that article, the largest degree of voltage fade is observed at a lower cut-off around 3.0-3.3V in combination with a 4.7V upper cut-off.

Temperature: Figure V - 73 shows that the corrected average voltages are also affected by temperature. They are ~40-70 mV lower at 55°C than at 30°C. The lower average voltages for charge *and* discharge at the elevated temperature exclude again any cell-level kinetics as a possible reason for this behavior. The cycling data also show that the rate of fade during charge is higher, and that the average voltage gap (between charge and discharge) is larger, at elevated temperatures.

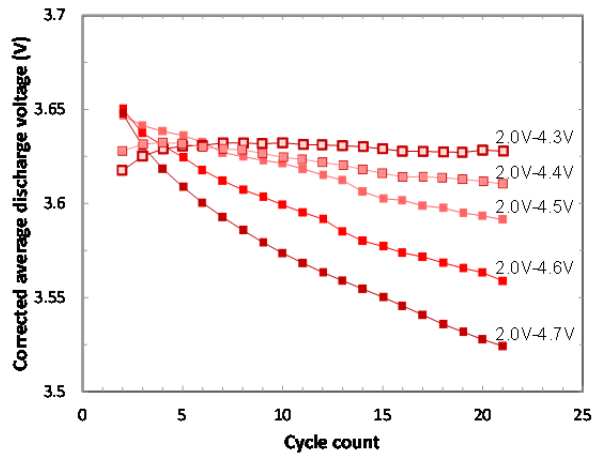

Figure V - 72: Effect of cycling window on the corrected average voltage and its fade during discharge for the LMR-NMC baseline material. For the first activation cycle, the cycling window is kept constant for all samples, i.e., 2.0V – 4.7V. During cycling, only the lower cut-off is kept constant at 2V. The degree of voltage fade increases as the upper cut-off increases. Voltage relaxation at the beginning of discharge down to ~4.5V forces the average voltage after the 2nd discharge to be nearly the same for the data sets with the three highest cut-off voltages

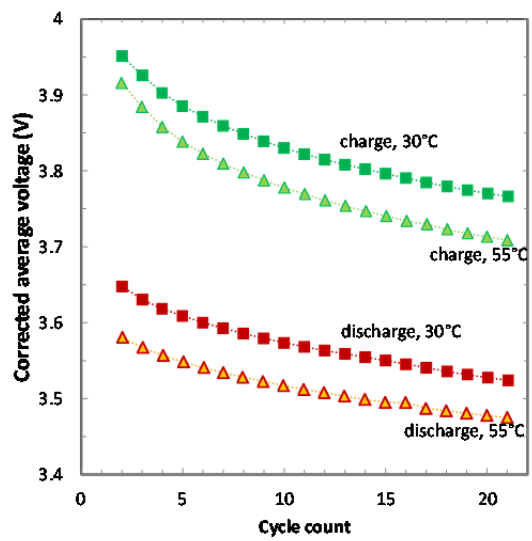

Figure V - 73: Effect of temperature on the corrected average voltages of the LMR-NMC baseline material under otherwise identical cycling conditions

Cycle life and calendar life: Figure V - 69 and Figure V - 70 show that the rate of fade is not constant throughout cycling; the highest rates occur during the initial cycles. Although the rate appears to slow down as cycling continues, ongoing studies have not yet identified a stable, or "final," voltage profile for the LMR-NMC oxide after 50+ cycles following the above protocol. Also, the rate of fade during extended galvanostatic cycling is larger than during potentiostatic

holds for identical time periods (for example, 4.7V *vs.* Li/Li^+) [1].

Voltage fade of selected layered oxides. Another factor influencing voltage fade is the oxide composition. Figure V - 74 and Figure V - 75 extend this study to other layered materials with varying lithium-to-metal ratios, including two which are currently being considered for commercial applications – $Li_{1.05}(Ni_{1/3}Mn_{1/3}Co_{1/3})_{0.95}O_2$ (NMC) and $LiNi_{0.8}Co_{0.15}Al_{0.05}O_2$ (NCA). Several Li-rich chemistries ($Li_{1.2}M_{0.8}O_2$, where "M" refers to any of the transition metals present) are also investigated. The exact cycling conditions for these materials follow the standard protocol given above, unless the material's potential window required adjustments of the current interrupts.

The left hand side of Figure V - 74 provides capacity-voltage profiles of the Li-rich chemistries over the 2.0-4.7V voltage range. The capacities are normalized to highlight the voltage decay. All materials show a 1st charge electrochemical activation near 4.5V, and display signs of voltage fade during subsequent cycles. Noteworthy is that the activation plateau for $Li_{1.2}Cr_{0.4}Mn_{0.4}O_2$ is slightly lower in voltage and more gradually sloped than that for the other materials, which probably results from irreversible structural changes. Note also the presence of a 2V plateau for $Li_{1.2}Ni_{0.4}Mn_{0.4}O_2$ upon 1st discharge, which indicates formation of a Li_2MO_2-like phase. This plateau disappears after the first three cycles, probably due to rising cell resistance on cycling that depress the feature below the lower (2.0V) cutoff voltage.

The right hand side of Figure V - 74 provides the corrected average voltages as a function of charge and discharge number. Again, all materials show voltage fade when cycled to 4.7V. The total drop in charge voltage after 20 cycles lies between 76mV and 191mV for $Ni_{0.4}Mn_{0.4}$ and $Co_{0.4}Mn_{0.4}$, respectively, showing that the rate of fade depends on the materials chemistry. It also depends on the stoichiometry, as seen for e.g., $Ni_{0.4}Mn_{0.4}$ and $Ni_{0.2}Mn_{0.6}$ which show a drop of 76mV and 144mV, respectively. Similar to LMR-NMC, the rate of fade for these materials is on the order of a few millivolts per cycles, ranging from approximately 4mV to 11mV per *charge* cycle. The rate of fade during *discharge* is slightly lower, approximately 1mV to 10mV per *discharge* cycle. Note that the initial average voltage of $Ni_{0.4}Mn_{0.4}$ rises during discharge because of the disappearance of its 2V plateau.

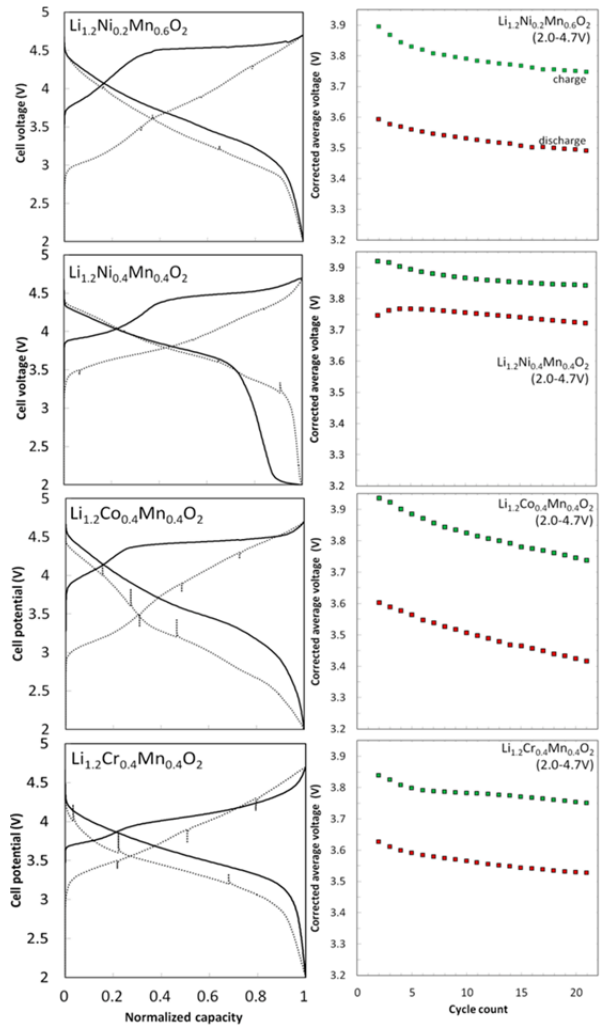

Figure V - 74: Voltage profiles and corrected average voltages as a function of cycle number for selected layered oxides. The cycling window ranges from 2.0V to 4.7V. On the left hand side, all capacities are normalized. The solid line shows the 1st ("activation") cycle; the dotted one the 20th cycle. On the right hand side, the top and bottom curves are the corrected average voltages during charge and discharge, respectively. All materials exhibit some degree of voltage fade if cycled to 4.7V *vs.* Li

Figure V - 75 provides normalized capacity-voltage profiles for NCA and NMC over two different cycling windows, 2.0-4.25V and 2.0-4.7V vs. Li/Li^+. The former range is depicted in the upper two panels of Figure V - 75, the latter one is depicted in the middle panels. To ensure comparable testing conditions, the first cycle is always from 2.0V to 4.7V. Practically, no voltage decay exists, for both materials during the lower voltage (4.25V) cycling, as the 2nd and 20th cycles are nearly identical. Some voltage fade is present at higher voltages (4.7V), although it is less than for the Li-rich chemistries described earlier.

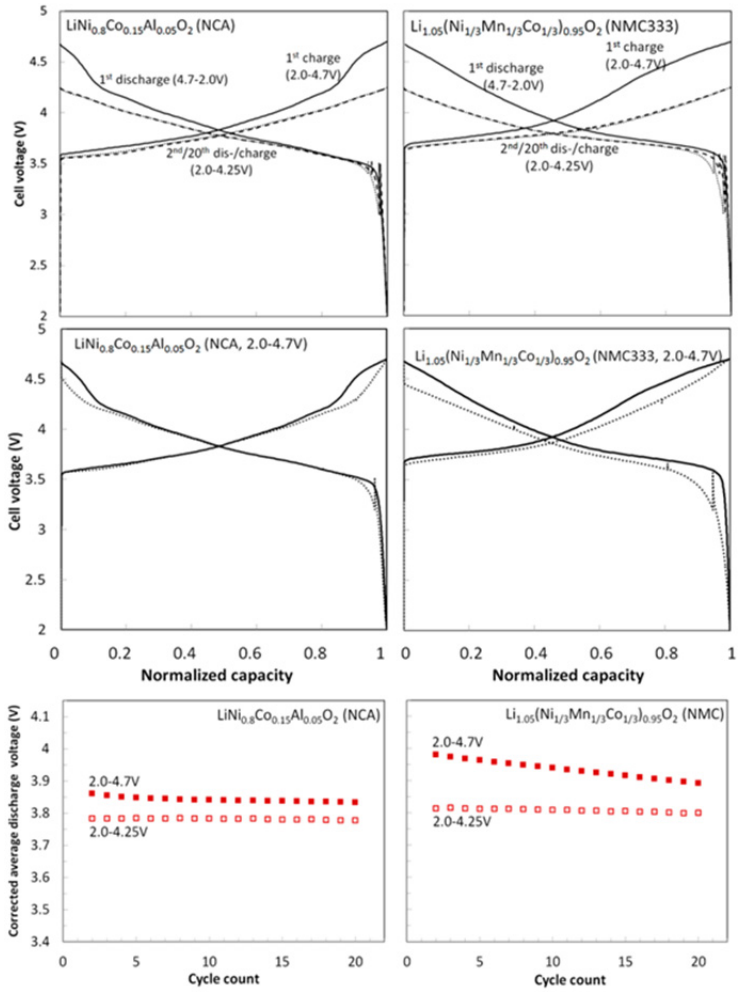

Figure V - 75: Voltage profiles and corrected average voltages as a function of cycle number for NCA and NMC. Both materials are cycled over two different voltage windows, 2.0-4.25V (top panels) and 2.0-4.7V (middle panels), with the first cycle *always* ranging from 2.0V to 4.7V. All capacities are normalized. The solid line shows the 1st cycle; the dashed one the 2nd (only shown for the 2.0-4.25V window); the dotted one the 20th cycle. The lower panels show the corrected average discharge voltages for the two voltage ranges. Both materials exhibit some degree of voltage fade only when cycled up to 4.7V *vs.* Li

The corrected average *discharge* voltages, depicted in the bottom panels, confirm that practically no change in average voltage occurs during the lower voltage (2-4.25V) cycling. When cycled to 4.7V, the *charge* voltage of NCA drops only by 8mV and that of NMC by 46mV; during *discharge* by 27mV and 88mV, respectively. Hence, the voltage gap widens for both materials.

Tracking voltage fade. As described above, a method to track (and quantify) voltage fade throughout cycling is to use a resistance-corrected average voltage. A standard testing protocol is proposed and demonstrated on several layered oxides under different cycling conditions. The advantages of our methodology are as follows: i) it facilitates data comparison through quantification, ii) it is reasonably fast (in comparison to e.g., lengthy galvanostatic intermittent titration technique, GITT, measurements), iii) it records the corrected average voltages for each cycle under the testing conditions of interest, and iv) it tracks simultaneously average and state-of-charge dependent cell resistances.

There are, however, some limitations with this methodology. For instance, voltage fade impacts different compositional regions in a different manner and mechanistic details are simply averaged out, as seen from Figure V - 68. Also, averaging effects, long relaxation times, and changes in the SOC cause a finite deviation from the "true" average resistance, and thus from the true equilibrium average voltage. The current interrupts implemented here are only 10 minutes, but relaxation and equilibration times on the order of hours can exist and have been observed for voltages >4.4V [2, 3]. And as the locations of the current interrupts are

voltage-controlled, state-of-charge changes are unavoidable because of decreasing electrode potentials (Figure V - 67B and table). Ultimately, all these effects can add up and induce a systematic error in the measurement of the corrected average voltage. This error propagates with $\delta\overline{U}_{corr} = i\delta\overline{R}$ and its upper bound can be estimated by taking $\delta\overline{R}$ to be on the order of $(1/2)(R_{max} - R_{min})$. For the LMR-NMC baseline cell, the biggest difference between R_{max} and R_{min} is measured during the first charge after activation, with 433Ω (at 3.5V) and 56Ω (at 3.9V). Such a difference would imply that the error is at most 40mV at 0.2mA. A more accurate prediction of the error is obtained through fitting the cell resistance as a function of capacity; integration and division by the total capacity leads to a capacity-weighted average resistance. Similar to the voltage-dependent resistance (e.g., reference [4]), the capacity-dependent resistance typically shows parabolic behavior for layered oxides. For the LMR-NMC oxide, the difference between this capacity-weighted and measured average resistance is around 50Ω or less, corresponding to an error of <10mV of the corrected average voltage. But regardless of the magnitude of this error, the rate of voltage fade is not, or at most only indirectly, affected by the experimental measurement of the average voltage.

Simply put, the combination of moderate cycling along with the resistance correction allows us to compute near-equilibrium values and voltage fade reproducibly (Figure V - 69 and Figure V - 70). Certainly, special attention to experimental parameters and cell conditions is warranted when data are compared. For instance, identical cells with varying internal resistances can show small differences in voltage fade, as cycling would occur over different SOC ranges, and structural transformations and cell-level kinetics can be very temperature sensitive. In addition, the number, location, and duration of the current interrupts may shift the computed average voltages, depending on material and actual cycling conditions. (Note: measurement accuracy can always be improved e.g., by lowering the current, and by increasing the number of current interrupts and their duration.)

Implications of voltage fade. For the LMR-NMC focused on here, voltage fade clearly worsens as upper cut-off voltages are raised to 4.7V *vs.* Li (Figure V - 72); and as the temperature is raised to 55°C, the initial fade rates and voltage gaps are more severe. Voltage fade will continue at a measureable rate of a few millivolts per cycle for quite some time before an expected stable voltage profile is achieved. And as the other materials share similar decay profiles, it is likely that the trends and behaviors observed for this oxide are in fact common to many other, if not all, layered materials.

Considering the above discussion, an obvious, yet complex, question arises – which oxide material yields the highest energy density during cycling? Among the materials we examined, LMR-NMC, NCA, and NMC exhibit the highest energy densities upon 1st discharge when cycled between 2.0-4.7V, justifying the technological interest in those materials. Of those materials, the LMR-NMC exhibits the highest energy density with more than 1,000 Wh-kg_{oxide}^{-1} on first discharge. Yet, finding the "winning material" is not as straight-forward. Voltage fade significantly lowers the energy density for the LMR-NMC (Figure V - 71), and is also measurably present for NMC at these high voltages. And at cycling voltages below 4.4V, voltage fade effects, along with increasing cell resistances, become negligible during early cycling.

Figure V - 76 provides some guidance in this regard. Here, the oxide-specific energy density of these three materials is examined over 20 cycles and two voltage windows (2.0-4.25V and 2.0-4.7V) after an initial, low current charge to 4.7V to ensure complete activation and comparable testing conditions. LMR-NMC is certainly a high voltage material with a oxide-specific energy density of around 950 Wh-kg_{oxide}^{-1} after 20 cycles for the wider cycling window; its energy drops to ~650 Wh-kg_{oxide}^{-1} when cycled to 4.25V. For NCA, this drop in energy is much less – its 20th cycle energy is lower and around 740 Wh-kg_{oxide}^{-1} when cycled to 4.7V, but it drops only to ~680 Wh-kg_{oxide}^{-1} when cut-off at 4.25V. At 4.7V, all three materials show energy fade; however, NCA and NMC show a more stable performance at 4.25V, with NCA having an energy output of more than 100 Wh-kg_{oxide}^{-1} higher than that of NMC. Therefore, based on an energy consideration alone, LMR-NMC is the material of choice for higher voltages. However, for lower voltage cycling, at which electrolyte oxidation and oxygen loss from the active material are less of an issue, NCA may provide higher energies and more stable performance.

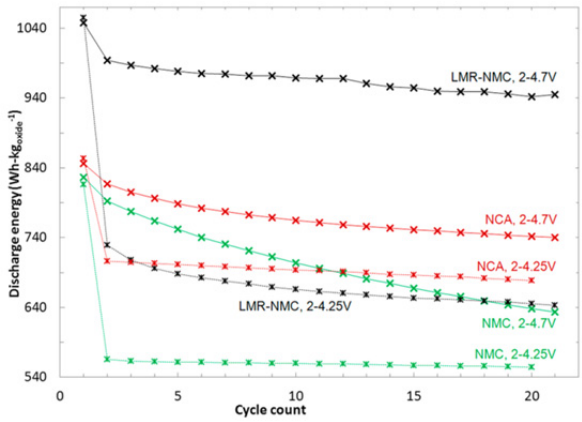

Figure V - 76: Discharge energies for LMR-NMC (embedded in the modified baseline cell), NCA, and NMC for two voltage windows (2.0-4.25V and 2.0-4.7V) as a function of cycle number. Note that all materials are charged to 4.7V *vs.* Li/Li$^+$ at 10 mA-g$_{oxide}^{-1}$ during the first cycle to ensure consistent testing among all materials and to ensure that the higher capacities of the LMR-NMC are accessed

Conclusions and Future Directions

It is clear that voltage fade reduces the energy density for a wide range of layered oxides as they are pushed to higher voltages to improve energy and power densities. A protocol to measure and quantify voltage fade throughout cycling is proposed, and applied to several materials demonstrating that this phenomenon is common for many layered oxides. Voltage fade can be effectively circumvented by choosing lower cut-off voltages and possibly reduced by choosing lower temperatures. Such cycling, however, is undesirable when higher energy and power densities are required. Voltage fade apparently results from irreversible changes that may involve the relocation of transition metals from the metal- into the Li-layer, ultimately leading to the formation of a spinel-like structural framework. To minimize such fade, irreversible transition metal migration needs to be inhibited and the layered structure needs to be stabilized to high voltages. Such stabilization is currently the subject of intense research at Argonne. To move forward, some unresolved questions will need to be addressed: What are the migrating species and what are their migration paths? What makes cation migration irreversible and could it be reversed (or accelerated)? Does the 1st charge cycle electrochemical activation of the oxides affect voltage fade and, if so, how? And, into what structure(s) do the layered oxides eventually transform into?

FY 2013 Publications/Presentations and References

1. K. G. Gallagher, J. R. Croy, M. Balasubramanian, M. Bettge, D. P. Abraham, A. K. Burrell, M. M. Thackeray, *Electrochem. Comm.* DOI: 10.1016/j.elecom.2013.04.022 (2013).
2. M. Bettge, Y. Li, B. Sankaran, N. Dietz Rago, T. Spila, R. T. Haasch, I. Petrov, D. P. Abraham, *J. Power Sources* **233**, 346 (2013).
3. Y. Zhu, Y. Li, M. Bettge, D. P. Abraham, *J. Electrochem. Soc.* **159**, A2109 (2012).
4. Y. Li, M. Bettge, B. Polzin, Y. Zhu, M. Balasubramanian, D. P. Abraham, *J. Electrochem. Soc.* **160**, A3006 (2013).
5. Bloom, L. Trahey, A. Abouimrane, I. Belharouak, H. Wu, Q. Wu, W. Lu, D. P. Abraham, M. Bettge, J. Elam, X. Meng, A. Burrell, C. Ban, R. Tenet, J. Nanda, N. Dudney, *submitted to J. Power Sources* (2013).
6. M. Bettge, Y. Li, K. Gallagher, Y. Zhu, Q.Wu, W. Lu, I. Bloom, D. P. Abraham, J. Electrochem. Soc., 160 (2013) A2046-A2055.

Appendix A1. Electrode chemistry and formulation for baseline cells and modified cells

	Baseline cells	Modified cells
Active positive material	86 wt.% $Li_{1.2}Ni_{0.15}Mn_{0.55}Co_{0.1}O_2$ (Toda HE5050)	92 wt.% $Li_{1.2}Ni_{0.15}Mn_{0.55}Co_{0.1}O_2$ (Toda HE5050)
Binder	8 wt.% PVdF (Solvay 5130)	4 wt.% PVdF (Solvay 5130)
Electrode additives	4 wt.% SFG-6 graphite (Timcal) 2 wt.% SuperP (Timcal)	4 wt.% C45 (Timcal)
Current collector	Al, 15 µm	Al, 20 µm
Active loading density of oxide	6.64 mg-cm^{-2}	5.89 mg-cm^{-2}
Electrode porosity	37%	36%
Laminate thickness	35 µm	26 µm
Negative electrode	Li metal	
Separator	25 µm thick (Celgard 2325)	
Electrolyte	1.2 M $LiPF_6$ in ethylene carbonate (EC) : ethyl methyl carbonate (EMC), 3:7 by wt.	
Electrolyte additive	none	2 wt.% LiDFOB
Avg. cell resistance for all cells; 2nd, 20th discharge cycle	184 Ω, 309 Ω	174 Ω, 120 Ω

V.C.3 Voltage Fade in the LMR-NMC Materials: Mitigation via Doping and Substitution (ANL)

Christopher Johnson

Argonne National Laboratory
9700 South Cass Avenue
Argonne, IL 60439
Phone: (630) 252-4787; Fax: (630) 252-4176
E-mail: cjohnson@anl.gov

VF Synthesis Team:
Abouimrane, Ali; Amine, Khalil; Belharouak, Ilias; Bloom, Ira D.; Chen, Zonghai; Croy, Jason R.; Lee, Eungje; Li, Yan; Lin, Chi-Kai; Long, Brandon R.; Slater, Michael D.; Thackeray, Michael M.; Vu, Anh D.

Collaborators:
ANL VF Characterization Team

Start Date: October 2012
Projected End Date: September 2014

Objectives

In this voltage fade (VF) synthesis project, our objective is to evaluate the structure-function property relationships in the 'layered-layered' composite LMR-NMC or Li-rich & Mn-rich NMC. The project involves conducting synthesis reactions to 1) help understand the mechanism of VF and 2) make new cathode materials that will mitigate VF. We take information from the VF project team and use it to help guide our synthesis efforts. We will also exchange knowledge with the VF team on the development of new materials or concepts that will counteract the VF. We will establish the chemistry occurring in the system which will help us address the mechanism of VF. The syntheses project effort is to make LMR-NMCs with modified compositions, dopants, substitutions and structures that promise low cost, good thermal stability and improved cycling stability.

There are a number of specific objectives of this study that include:

1) Use theory to guide the synthesis efforts.
2) Synthesize materials with variable Li, Ni, Mn, and Co compositions using a combinatorial approach.
3) Conduct doping study in order to evaluate its effect on VF.
4) Determine the effects of oxygen composition in LMR-NMC materials on VF.
5) Design and synthesize Li- and Mn-rich oxides with integrated structures, notably 'layered-spinel' materials, to counter the VF phenomenon.
6) Identify and overcome degradation issues.
7) Exchange information and collaborate closely with others in ABR's 'voltage fade' team.
8) Supply promising high-capacity cathode materials for PHEV cell build.

Technical Barriers

This project addresses the following technical barriers as described in the USABC goals [1, 2]:

- Cycle life
- Performance at ambient temperatures
- Low energy density
- Poor low temperature operation
- Abuse tolerance limitations

Technical Targets

The technical targets to meet at the end of the project are the following:

- PHEV specific energy targets (pack): 3.4 kWh (min) to 11.6 (max) [2].
- EV specific energy targets (pack): 80 (min) to 200 (max) Wh/kg [3].

To accomplish this we must develop a cell to meet the 40-mile PHEV goal (142 Wh/kg, 317 W/kg), a cycle life of 5,000 cycles, and a calendar life of 15 years.

Accomplishments

- Established a reliable sol-gel route to the syntheses of LMR-NMC and its variants.
- Evaluated the following dopants: Al , Fe, V, Ga, and Cr.
- Synthesized $Li_2M'O_3$ (M'=Mn, Sn) model compounds and studied their formation as a function of temperature from starting material compounds.
- Synthesized Li_2RuO_3 and variants to evaluate the electrochemical performance of materials that do not contain pure Mn.
- Determined the electrochemical properties of lithium-manganese-nickel-cobalt-oxide composite electrode structures in three component 'layered-layered-spinel' systems, prepared by lowering the lithium content of

'layered-layered' Li_2MnO_3●$LiMO_2$ materials (M=Mn,Ni,Co).

- Determined the effects of Co and Li_2MnO_3 content on 'layered-layered-spinel' electrode materials.
- Demonstrated that voltage fade is sensitive to Li-Ni-Mn-Co composition.
- Developed a statistical model relating composition to VF to guide the selection of compositions.
- Developed and deployed a graphically-oriented database to collect and organize the information generated by team members.

✧ ✧ ✧ ✧ ✧

Introduction

The LMR-NMC composite electrode structures offers the possibility of producing the highest capacity cathodes in the lithium-ion battery field today (~ 250 mAh/g). Argonne and the international lithium battery community have made considerable progress in understanding and optimizing these materials, their compositions and electrochemical properties. Argonne's deep experience and familiarity with a wide range of materials technologies will enable the team to explore the possibility of identifying and developing advanced cathode materials to meet the demanding performance requirements of transportation applications.

Present limitations of these cathode materials are 1) voltage fade on cycling, 2) a relatively poor rate capability, 3) high impedance, particularly at a low state of charge (SOC), and at low temperatures, and 4) poor cycling stability, notably at high temperatures, due to Mn dissolution. These performance limitations are attributed to poor electronic/ionic conductivity in the oxide bulk, and surface damage from repeated high-voltage cycling. It is now also established that these materials lose energy during cycling manifested by a drop in average discharge voltage. Coined 'voltage fade' or VF, this problem must be understood and corrected. It is likely (1) due to a slow change in phase during prolonged cycling, and (2) massive structural rearrangements on the Li_2MnO_3 component during the activation cycle on the first charge.

Approach

To address the limitations of xLi_2MnO_3•$(1-x)LiMO_2$ electrodes, several approaches were adopted:

1) Use compositional phase diagrams to design integrated 'layered-layered-spinel' structures and to stabilize the electrode to electrochemical cycling.
2) Use combinatorial synthetic methods to identify factors that contribute to voltage fade as part of a team effort. This part of the effort will investigate the effects of Li, Mn, Ni, Co and oxygen stoichiometries on the voltage fade phenomenon. One-hundred, forty-seven compositions (see Table V - 8), spanning the low-cobalt portion of the Li_2MnO_3-$LiCoO_2$-$LiNiO_2$-$LiMnO_2$ phase diagram, were identified for investigation. Selected compositions were made by sol-gel methods for characterization (XRD, elemental analysis and electrochemical performance).
3) Focused on the domain structure of $Li_2M'O_3$, where M' is a tetravalent transition metal & Sn model compound.
4) Developed a sufficient synthesis method to reliably dope the composite xLi_2MnO_3•$(1-x)LiMO_2$ with various ad-cations, and then evaluate the VF response.
5) Elucidated the causes of voltage decay by investigating both bulk and surface effects.

Table V - 8: Group numbers and compositions for the combinatioral type study

Group	Li	Ni	Co	Mn	Group	Li	Ni	Co	Mn
1	1~1.6	0.15	0	0.85	12	1~1.6	0.25	0.2	0.55
2	1~1.6	0.15	0.05	0.85	13	1~1.6	0.3	0	0.7
3	1~1.6	0.15	0.1	0.75	14	1~1.6	0.3	0.05	0.65
4	1~1.6	0.2	0	0.8	15	1~1.6	0.3	0.1	0.6
5	1~1.6	0.2	0.05	0.75	16	1~1.6	0.3	0.15	0.55
6	1~1.6	0.2	0.1	0.7	17	1~1.6	0.35	0	0.65
7	1~1.6	0.2	0.15	0.65	18	1~1.6	0.35	0.05	0.6
8	1~1.6	0.25	0	0.75	19	1~1.6	0.35	0.1	0.55
9	1~1.6	0.25	0.05	0.7	20	1~1.6	0.4	0	0.6
10	1~1.6	0.25	0.1	0.65	21	1~1.6	0.4	0.05	0.55
11	1~1.6	0.25	0.15	0.6					

Results

1. 'Layered-Layered-Spinel' Electrodes. Studies of 'layered-layered-spinel' materials were conducted by synthesizing twelve compositions of $(1-z)[(x)Li_2MnO_3\bullet(1-x)LiMn_yNi_yCo_{1-2y}O_2]\bullet zLiM''_2O_4$ system, where the portion of spinel is LiM''_2O_4. To promote good homogeneity of the transition metals, these samples were synthesized using the oxalate co-precipitation method. By exploring material compositions with a lower Li_2MnO_3 content, this will, in turn, promote growth of the spinel component (less Li/M ratio).

Experiments were done to evaluate the performance of these 'layered-layered-spinel' composite materials. Accordingly, one would expect less capacity on cycling and a lower voltage response due to the spinel character below 3 V in the cell, but the presence of spinel will improve the first-cycle coulombic efficiencies. Capacity versus cycle number from cycling the material between 4.45 and 2.0 V at 15 mA/g, following a formation cycle protocol are shown in Figure V - 77.

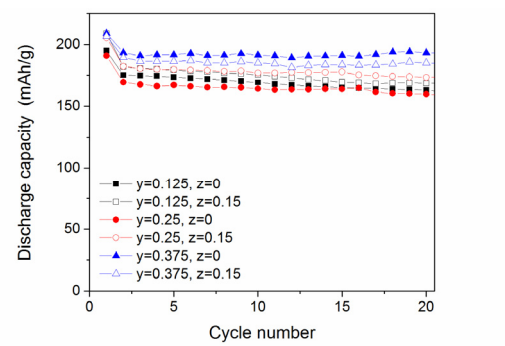

Figure V - 77: Specific capacity as a function of cycle number for the $(1-z)[(x)Li_2MnO_3\bullet(1-x)LiMn_yNi_yCo_{1-2y}O_2]\bullet zLiM''_2O_4$ system. The color markers and different shapes represent the different compositions studied

To follow-up this result, experiments were conducted to evaluate the electrochemical performance of higher xLi_2MnO_3 content compositions. Figure V - 78 shows the specific capacities upon discharge for such compositions studied (4.45 to 2.0 V, 15 mA/g). Increasing the Li_2MnO_3 content increases the capacity for all compositions, but with an apparent slight loss in stability.

Of particular interest are the dQ/dV plots of cells with different Li_2MnO_3 contents and associated spinel contents. Figure V - 79a shows the dQ/dV on the 2nd cycle and Figure V - 79b shows the dQ/dV on the 20th cycle. The dashed lines represent a larger content of Li_2MnO_3 and this result in a significantly larger amount of activity below 3.5 V when compared to the lower content Li_2MnO_3 samples. The tradeoff in capacity attained and average voltage is crucial to energy density and needs to be optimized with consideration of structural stability. Figure V - 79b shows the dQ/dV on the 20th cycle for all samples. The higher Li_2MnO_3 samples show a shift to lower voltages in the 2.5 – 3.5 V region, indicating voltage fade, and thus a loss in energy density. The lower content Li_2MnO_3 samples reach a more stable state with higher voltage activity, which results in a more stable energy density.

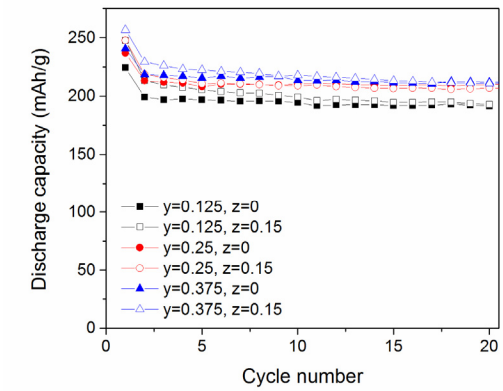

Figure V - 78: Specific capacity as a function of cycle number for the $(1-z)[(x)Li_2MnO_3\bullet(1-x)LiMn_yNi_yCo_{1-2y}O_2]\bullet zLiM''_2O_4$ system. The color markers and different shapes represent the different compositions studied

We can conclude that the addition of spinel into the composite improves the electrochemical performance for all samples, relative to the 'layered-layered' composition.

To obtain a deeper understanding of the composite structure, detailed structural analyses of 'layered-layered-spinel' composite electrodes have been undertaken at ANL's Advanced Photon Source (APS). Peaks that are representative of Li_2MnO_3 (C2/m), $LiMO_2$ (R-3m), and LiM''_2O_4 (Fd3m) structures are seen. The data suggests the formation of a complex structure with all three components integrated, but given the close similarity that can exist in the XRD patterns of cubic-close-packed layered and spinel lithium metal oxides, it is not surprising that low spinel content makes it difficult to distinguish layered and spinel components from one another with this technique. Detailed refinements of the data are underway.

2. Combinatorial Type Work.

Phase Relationships. The XRD patterns of oxides in the Li_2MnO_3-$LiCoO_2$-$LiNiO_2$-$LiMnO_2$ phase diagram are very similar and the phase relationships are complex. For example, Figure V - 80 shows the XRD patterns of $LiMO_2$ (R-3m space group), Li_2MnO_3 (C2/m), and spinel (Fd3m) phases. From the figure, these patterns are very similar, but can be distinguished using high-energy, synchrotron X-rays with their higher spatial resolution.

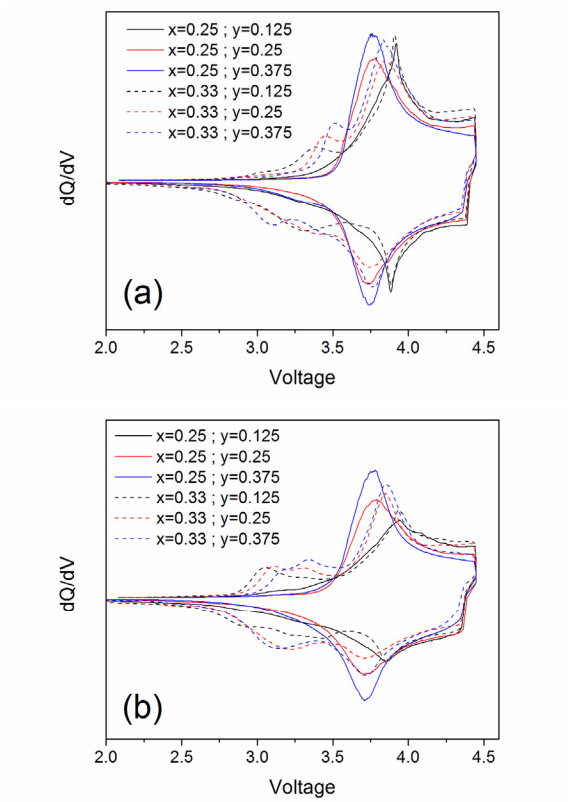

Figure V - 79: Specific capacity as a function of cycle number for the (1-z)[(x)Li_2MnO_3●(1-x)$LiMn_yNi_yCo_{1-2y}O_2$]●zLiM'_2O_4 system. The solid and dashed color lines represent the different compositions studied

The phase distribution was sensitive to lithium concentration. As shown in Figure V - 81, the intensities of the reflections associated with the spinel component were reduced with increasing lithium concentration. Additionally, the reflections due to Li_2MnO_3 (C2/m) and $LiMO_2$ (R-3m) were broadened, shifted, and, eventually, merged into each other. The data may indicate that interphase of domains of Li_2MnO_3 (C2/m) and $LiMO_2$ (R-3m) exist in the composite material as the domain sizes are reduced and become more integrated.

Voltage Fade. All cycling was performed at room temperature. All cells were cycled between 2 V and 4.7 V at 10 mA/g for the first cycle, and then between 2 V and 4.7 V (vs. Li^+/Li) at 20 mA/g for the following cycles. The cells were cycled between 2 and 4.7 V for a minimum of 20 and a maximum of 50 times. While cycling, current interrupt measurements were carried out at 3.5, 3.9, 4.3, and 4.7 V during charge and at 4.0, 3.6, 3.2, and 2.0 V during discharge. This is shown in Figure V - 82.

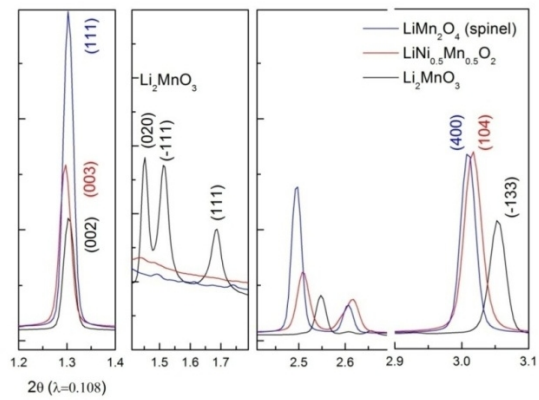

Figure V - 80: Example XRD patterns of the materials indicated in the legend

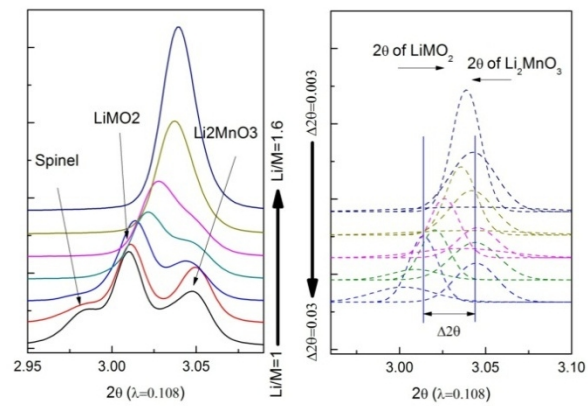

Figure V - 81: XRD patterns showing the effect of lithium:metal ratio. With more lithium, the difference between the peaks decreases

Estimates of cell resistance were calculated from the values of cell voltage and current at times t_0 and t_1 using Eq. 1.

$$R = \left|\frac{v_{t_1} - v_{t_0}}{i_{t_1} - i_{t_0}}\right|, R = \left|\frac{v_{t_1} - v_{t_0}}{i_{t_1} - i_{t_0}}\right|, \qquad \text{Eq. 1.}$$

where v_{t_1} and v_{t_0} are the cell voltages at t_1 and t_0, respectively; i_{t_1} and i_{t_0} are the respective currents.

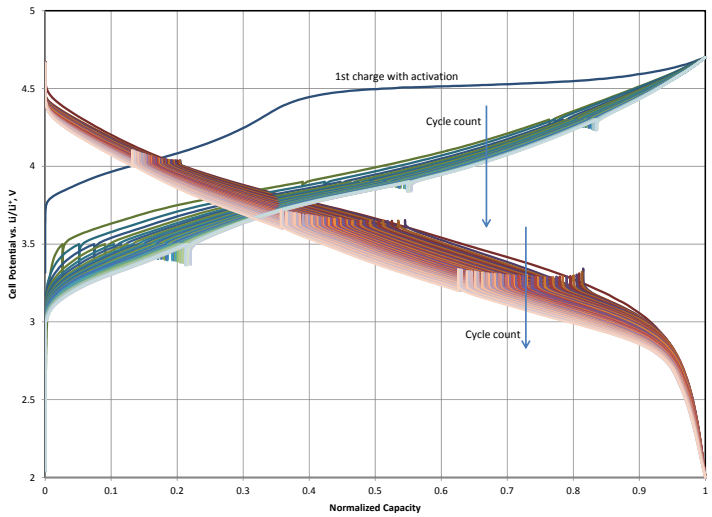

Figure V - 82: Cell potential vs. normalized capacity. The upward (discharge) and downward (charge) ticks in each curve represent the current interrupts

The activation charge subcycle and the discharge immediately following it were omitted from further analysis in this work. After that subcycle, the energy (Wh) and capacity (Ah) values were either extracted directly from the cycling data or were calculated from the raw data using Microsoft Excel®. The average voltage for a given charge or discharge subcycle was calculated as Wh/Ah. The resistance values at the first three voltages were averaged and used to correct the average voltage value for the average resistance of the cell during a given cycle. The relative change in the iR-corrected average voltage was calculated by comparing the value from the first discharge or charge subcycle to the respective value at the 20th discharge or charge subcycle, as shown in Eq. 2.

$$Rel.\,change\ in\ avg.\,voltage = \frac{Avg.voltage_0 - Avg.voltage_{20}}{Avg.voltage_0} \qquad \text{Eq. 2.}$$

These relative average voltage values (hereafter called ΔAvgV) then were used for plotting and subsequent analyses.

Figure V - 83 shows the effect of composition on ΔAvgV. From this figure, composition has a definite impact on the rate of change in ΔAvgV and to its final value. For example, compositions 5-G, 6-G, 7-G, and 8-G, have lower values of ΔAvgV than TODA HE5050. The ΔAvgV value for 5-G is about 85% of that of TODA HE5050.

Simplex Modeling of ΔAvgV. Modeling was limited to those compositions that crystallize in the R-3m space group (layered-layered materials). The ΔAvgV data were treated by multiple linear regression analysis using the cubic simplex equation for four-component mixtures, based on the work of Scheffé [3, 4]. The complete cubic equation is given below.

$Y=a_1x_1 + a_2x_2 + a_3x_3 + a_4x_4 + a_{12}x_1x_2 + a_{13}x_1x_3 + a_{14}x_1x_4 + a_{23}x_2x_3 + a_{24}x_2x_4 + a_{34}x_3x_4 + a_{123}x_1x_2x_3 + a_{124}x_1x_2x_4 + a_{134}x_1x_3x_4 + a_{234}x_2x_3x_4 + b_{12}(x_1 - x_2) + b_{13}(x_1 - x_3) + b_{14}(x_1 - x_4) + b_{23}(x_2 - x_3) + b_{24}(x_2 - x_4) + b_{34}(x_3 - x_4)$, where x_j is the mole fraction of the jth component and a_j are fitting constants.

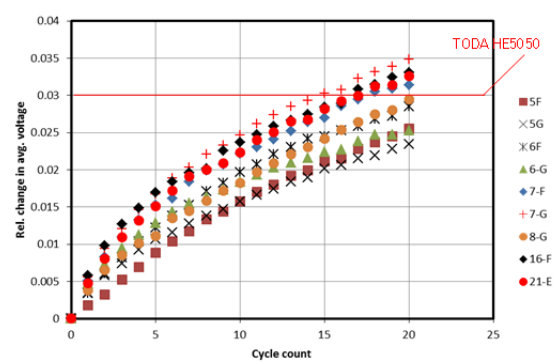

Figure V - 83: Relative change in average voltage vs. cycle count. The abbreviations in the legend reflect different Li, Mn, Ni, and Co stoichiometries. The composition of TODA HE5050 is $0.5Li_2MnO_3 \cdot 0.5LiNi_{0.375}Mn_{0.375}Co_{0.25}O_2$

Of the 26,333 possible solutions, candidate fits of the equation to the data must include the first four terms; use the fewest number of terms; have a high value of r^2, typically greater than 0.98; and have low RMS error. With the current data, a candidate fit was found using just the first four terms. Figure V - 84 shows some of

the result from fitting, plotted as a constant-concentration contour diagram.

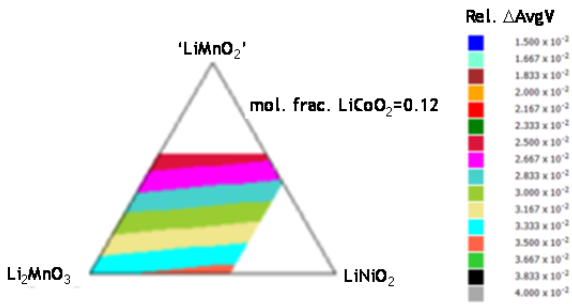

Figure V - 84: Example of some of the results from fitting a four-term polynomial to the ΔAvgV data

This model will be used to help select compositions for further study. As more data are generated, they will be used to refine the model.

3. Synthesis of $Li_2M'O_3$ Model compounds.

It is believed that the structural stability of delithiated Li_2MnO_3 has direct/indirect contribution to the voltage fade of LMR-NMC. In this portion of our work, we attempt to modulate the electrochemical properties of $Li_2M'O_3$ domain (M=transition metal) by doping Mn with Sn, which has more covalent bonding behavior. Figure V - 85(a) and Figure V - 85(b) shows a contour plot of *in situ* high-energy XRD patterns during solid state synthesis of Li_2MnO_3 and Li_2SnO_3, respectively, $Li_2M'O_3$ monoclinic-type structure can be formed for both Mn and Sn. In addition, the super-diffraction peaks for Li_2SnO_3 are much stronger than those for Li_2MnO_3, indicating less stack fault exists in Li_2SnO_3. The challenge for this work is that the *c* value of Li_2SnO_3 is much larger than that of Li_2MnO_3. Hence, we anticipate difficulty in incorporating Li_2SnO_3 directly into the composite materials to form $(1-x)Li_2SnO_3 \cdot xLiMO_2$. Alternatively, we will try to solve this issue by doping Sn into Li_2MnO_3 to (1) modulate the stacking fault in Li_2MO_3 component, and (2) obtain an optima *c* value for integration of Li_2MO_3 in LMR-NMC materials.

Moving forward on $Li_2M'O_3$ model compounds; in the previous annual report we focused on the domain structure of Li_2MnO_3 as the $Li_2M'O_3$ model compound. We used acid-treatment to convert the layer stacking from O3 to P3. It is possible to readily convert P3 to P2 then O2 and thus ultimately we want to synthesize an O2-$[xLi_2M'O_3 \bullet (1-x)LiMO_2]$ composite phase that won't convert to spinel. Recent theory work by Benedek and Iddir (2013) suggests that if the M' in $Li_2M'O_3$ can achieve an oxidation state above 4+, then it may be possible to eliminate the voltage plateau and avoid the massive structural rearrangement of $xLi_2M'O_3 \bullet (1-x)LiMO_2$ to a generic O3- $Li(M_{1-z}M'_z)O_2$ layered phase that is capable of converting to spinel during cycling .

As an electroactive compound, we chose Li_2RuO_3, that has the same crystal structure as Li_2MnO_3 and can achieve oxidation states above Ru(IV). Note that in these Li_2MnO_3 materials the oxidation of Mn(IV) is at a prohibitively high voltage and is not expected to occur. Li_2RuO_3, $Li_2Zr_{0.1}Ru_{0.9}O_3$ and $Li_2Mn_{0.5}Ru_{0.5}O_3$ were synthesized by a combustion method to ensure single phase products. The electrochemistry of these materials is shown in Figure V - 86, along with Li_2MnO_3 as a comparison. Briefly the Li_2RuO_3 compound shows no pronounced flat voltage plateau during Ru oxidation which supports the supposition that redox active M' elements will add capacity but not experience a phase change. It still remains to be seen from XRD analysis if this is the case. The mixed $Li_2Mn_{0.5}Ru_{0.5}O_3$ has a plateau that is shorter and a lower voltage than Li_2MnO_3. Thus, $Li_2Mn_{0.5}Ru_{0.5}O_3$ may be written as a composite: $0.5Li_2MnO_3 \bullet 0.5Li_2RuO_3$. The capacity expected from removal of two lithiums is approximately 340 $mAhg^{-1}$; nearly identical to what is experimentally observed. Finally, the voltage does fade (average discharge voltage change with cycle number; not shown) for $0.5Li_2MnO_3 \bullet 0.5Li_2RuO_3$ but the mechanism of fade appears different than conventional $xLi_2M'O_3 \bullet (1-x)LiMO_2$ (M'=Mn; M= Ni, Mn, and Co), that suggests that electroactive M' plays a role in altering VF. Theory has suggested other electroactive M' elements such as V, Cr, and Mo that have a similar ionic radii and coordination number as Mn, and energetically, prefer to form the monoclinic $Li_2M'O_3$ C2/c instead of $LiMO_2$ rhombohedral R-3m. To this end we have preferentially doped $xLi_2M'O_3 \bullet (1-x)LiMO_2$ (M'=Mn; M= Ni, Mn, and Co; TODAHE5050 based) with V, Cr. Fe, Ga, and Al.

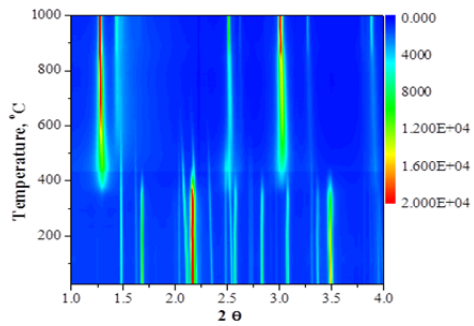

(a)

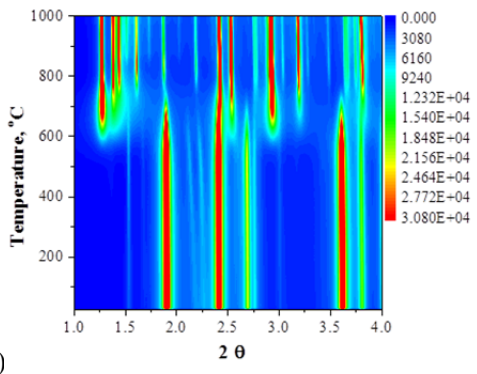

(b)

Figure V - 85: (a) Contour plot of *in situ* high-energy XRD patterns during solid state synthesis of Li_2MnO_3. (b): Contour plot of *in situ* high-energy XRD patterns during solid state synthesis of Li_2SnO_3

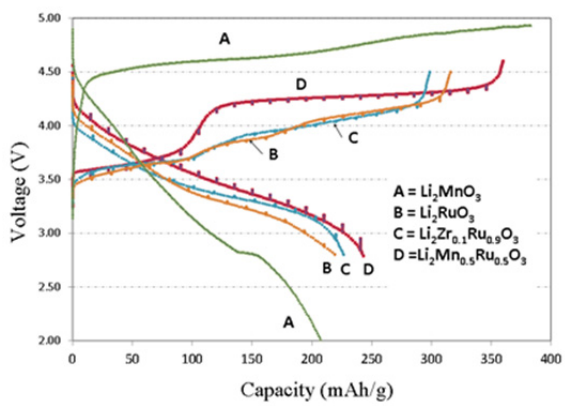

Figure V - 86: Li/$Li_2M'O_3$ cells

4. Doping into $xLi_2M'O_3 \bullet (1-x)LiMO_2$.

As this synthesis project is directed by theory, we are making materials that DFT calculations suggest are useful compositions that can possibly retard VF. Doping may be a way to retard VF if the dopant can alter the path of structural degradation during the first charge in the parent phase. Our hypotheses contain four criteria: (1) strong bonding with oxygen is required, (2) the oxidation state of the dopant can go higher than 4^+ and is stable (mitigate O_2 loss), (3) the dopant can preferentially substitute for Mn in the Li_2MnO_3 domain which will alter the structure or size of the domain, and (4), it should form reversible dumbbell configuration with Li_{tet} during deep charge in order to maintain structural stability. Each dopant tried can fit into one of those classifications. To this end, we have synthesized compositions that contain various dopants using sol-gel methods that create homogeneous distribution of all cations. The dopants evaluated this past year were Fe, Ga, Al, V, and Cr.

First to properly dope into the composite 'layered-layered' material, we need to firmly establish the synthetic method to use. To this end we decided to choose sol-gel methods. We developed a consistent sol-gel synthesis route to make TodaHE5050 composition: $(0.5Li_2MnO_3 \bullet 0.5Li[Ni_{0.375}Mn_{0.375}Co_{0.25}]O_2)$ and that which would facilitate the bulk incorporation of dopant or substitution.

We compared the VF in a carbonate co-precipitated precursor reactant with the target Toda HE5050 product composition to that of the aforementioned sol-gel derived product with the same composition, with the goal being to see if the synthesis route changes the VF. As is shown in Figure V - 87, the synthesis method used did not change the result – VF is about the same with the results similarly fitted to a paralinear function. So, moving forward, we will use the sol-gel method to incorporate dopants and/or substitutions.

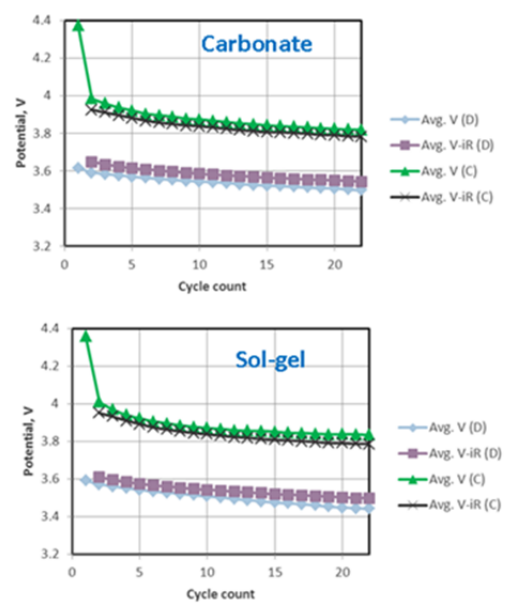

Figure V - 87: Voltage fade of $Li/0.5Li_2MnO_3 \bullet 0.5Li[Ni_{0.375}Mn_{0.375}Co_{0.25}]O_2$ (Toda HE5050 composition) cells

The Fe-doped $Li[(NMC)_{0.87}(Fe)_{0.013})]O_2$, was synthesized. The undoped and a Fe-doped (1.3%) materials show, by XRD, a pure layered phase, and the cycling resulted in approximately 265 mAh/g capacity.

However, the Fe-doping did not change the VF result (Figure V - 88).

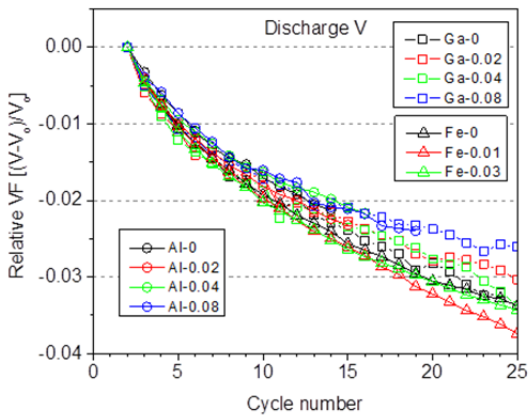

Figure V - 88: Al, Fe, and Ga-dopant VF curves

With increasing Al substitution, the Li-Mn ordering peak becomes broad thus indicating that the Al is doping into the structure, but at the high-end might be distorting or perturbing the Li_2MnO_3 domain. The lattice parameter of Al substituted samples showed almost no change. Also, the VF result as shown in Figure V - 88 is nominally the same as the Al-free sample, therefore indicating no beneficial effect of Al doping despite the chance that Al may sit in T_d sites in the structure.

Typically in the solid state, Gallium (Ga) is known to possess only one oxidation state of three and has been shown to move from O_h to T_d coordination in layered TM oxide phases during cycling. It may immobilize co-bonded cations in the surrounding second-shell T_d coordination sphere of the host phase, and can also act as a pillar effectively co-bonding the Li layer and keeping it intact at high states of charge. As a spectator ion, this could affect the Li_{tet} dumbbell reversibility. Figure V - 89 shows the data results from coin-cell cycling of the Ga-doped LMR-NMC. As is obvious, there is no beneficial effect having Ga in the structure. The VF still occurs. The capacity remains constant for low values of Ga, which is good sign of consistent electrochemical activity in the phase, however.

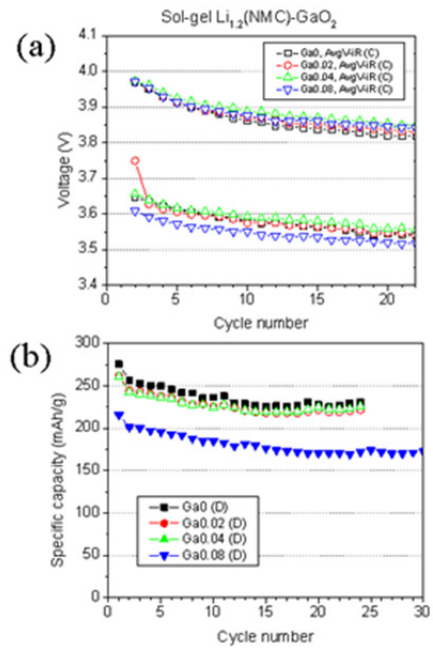

Figure V - 89: (a) Ga-dopant VF curves, and (b) capacity vs. cycle no

Vanadium (V) has a number of stable oxidation states from 2^+ to 5^+. It also can form a short apical bond with oxygen when it is in the 5^+ oxidation state that will actually distort the coordination sphere. Trivalent oxidation state is normally octahedral. Figure V - 90 shows the data from the syntheses of four different dopant levels for $Li_{1.2}Ni_{0.15}Mn_{0.55-x}V_xCo_{0.1}O_2$. As is evident, having V present causes a melting and sintering of the product. The melting is likely due to the formation of a stable lithium vanadium oxide such as LiV_3O_8 in air that creates a flux in the reaction. The product also has poor electrochemical cycling. Future work for doping of V will need to be conducted in inert atmosphere to stabilize the 3^+ V oxidation state. But this is problematic for the parent phase, as oxygen likely will be lost from the sample at high firing temperatures.

(a)

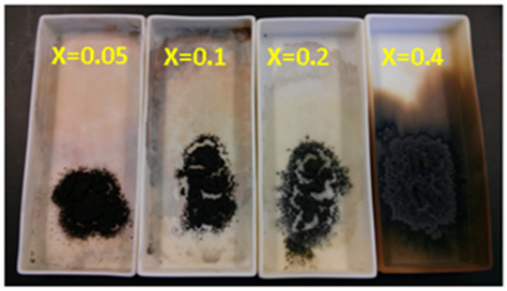

(b)

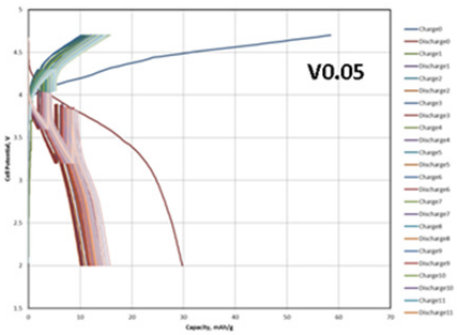

Figure V - 90: (a) Photo of V dopant fired samples. For composition value with x, see text. (b) $Li/Li_{1.2}Ni_{0.15}Mn_{0.50}V_{0.05}Co_{0.1}O_2$ coin cells

Chromium (Cr) doping is an interesting strategy to try since there is a possibility that Cr^{6+} may fill available T_d sites in the phase during first charge which in turn may change the mechanism of movement of other cations, like Mn. First, from the XRD patterns we find that single phases can be readily formed, likely with Cr^{3+}. The XRD peaks shift to lower angle with doping, indicating lattice expansion: the Cr cation radii is larger than the averaged sum of Ni^{2+} and Mn^{4+} radii (i.e., $R[Ni^{+2}_{1/4}Mn^{+4}_{3/4}]$=0.57Å, $R[Cr^{3+}]$=0.615Å). Li-Mn ordering peaks become stronger with a low degree of Cr doping (x = 0.05, 0.1). Figure V - 91 shows the result of cycling the Cr-doped cathodes in the first two cycles. What is interesting is that the first charge (activation) is dramatically altered. As Cr is increased, the plateau is shortened indicative of a change in the degree of oxygen loss in the resultant VF charged material. Cycling of this material continues and more work is needed to understand the role of Cr in the LMR-NMC and its mechanism.

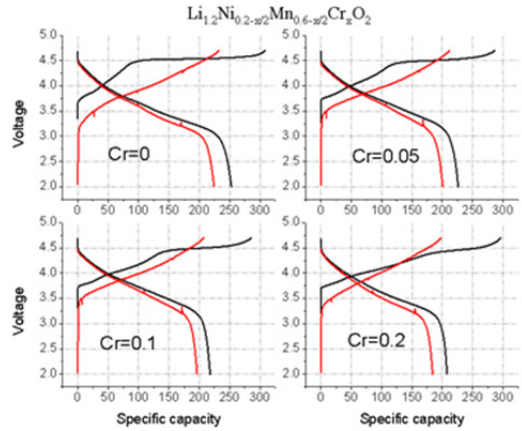

Figure V - 91: (a) Data result of cycling the Cr-doped cathodes. For composition value with x, see text. (b) $Li/Li_{1.2}Ni_{0.2-x/2}Mn_{0.6-x/2}V_{0.05}Cr_xO_2$ coin cells

Conclusions and Future Directions

1. 'Layered-Layered-Spinel' Electrodes.

- Lowering the Li_2MnO_3 content reduces low voltage activity (below 3.5 V) in composite structures, with a reduction in capacity.
- There is a tradeoff in capacity and voltage to optimize energy density that needs to be considered for high capacity lithium metal oxide cathodes.
- Structural analyses of 'layered-layered-spinel' composite electrodes are being conducted at the Advanced Photon Source to provide detailed structural insights before and after cycling.

The results obtained from this study are encouraging; they hold clues that may be used to advance the compositional and structural design of high capacity lithium metal oxide cathodes. This project will continue to further exploit, optimize, and characterize 'layered-layered-spinel' composite electrode structures.

2. Combinatorial Type Synthesis Study.

We have demonstrated that voltage fade, as quantified by ΔAvgV, is sensitive to composition. With a selected composition, we have decreased ΔAvgV to 85% of that of HE5050. A statistical model is being used to help guide the search for new compositions.

3. Synthesis of $Li_2M'O_3$ Model Compounds.

The use of $Li_2M'O_3$ model compounds (Mn, Sn, Ru, Mn-Ru, Zr-Ru) were synthesized with single phase. A comparison is made related to the *c* value axis and the potential ability to substitute into the lattice. An assessment of the electrochemistry of these materials was carried out and high capacities were recorded for Mn-Ru, Ru, and Zr-Ru. We intend to use these materials as a guide in understanding the synthesis of new phases

of 'layered-layered' composites, which ideally have little to no fade. Future work will focus on Zr-based materials, a much less expensive alternate to Ru.

4. Doping into $xLi_2M'O_3 \bullet (1-x)LiMO_2$

A sol-gel method for synthesis of doped and substituted composites was developed and refined. The electrochemical performance of the nominal composition that is the same as the Toda HE5050 formulation is equivalent to materials synthesized using a carbonate co-precipitated reactant.

Cationic dopants including, Fe, Al, Ga, Cr, and V all do not show an alteration in the VF response and have similar VF to the non-doped material. In future, we will terminate the cation doping study in favor of evaluation of anion dopants, such as fluoride or filling of possible oxygen vacancies (oxides O^{2-} anions) through synthesis of materials or annealing of materials strictly in an oxygen atmosphere.

List of Abbreviations

HEV: hybrid electric vehicle

PHEV: plug-in hybrid electric vehicle

EV: electric vehicle

USABC: United States Advanced Battery Consortium (DOE, GM, Chrysler and Ford)

XRD: x-ray diffraction

References

1. Battery Test Manual For Plug-In Hybrid Electric Vehicles, Rev. 1, June 2010, INL/EXT-07-12536.
2. Electric Vehicle Battery Test Procedures Manual, Rev. 2, June 1996.
3. H. Scheffé, J. Royal Statistical Soc. (B) 20 (1958) 344.
4. H. Scheffé, J. Royal Statistical Soc. (B) 25 (1963) 235.

FY 2013 Publications/Presentations

Publications

1. D. Kim, G. Sandi, J. R. Croy, K. G. Gallagher, S.-H. Kang, E. Lee, M. D. Slater, C. S. Johnson and M. M. Thackeray, *Composite 'Layered-Layered-Spinel' Cathode Structures for Lithium-Ion Batteries*. J. Electrochem. Soc. **160(1)**: A31-A38 (2013).
2. D. Kim, J. R. Croy and M. M. Thackeray, *Comments on Stabilizing Layered Manganese Oxide Electrodes for Li Batteries*. Electrochem. Comm. **36(0)**: 103-106 (2013).

Presentations

1. I. Bloom, et al., 2013 DOE Annual Peer Review Meeting Presentation.
2. C. Johnson, et al., 2013 DOE Annual Peer Review Meeting Presentation.
3. B. R. Long, J. R. Croy, D. Kim, K. Gallagher, Z. Chen, P. Chupas, K. Chapman, M. Suchomel, and M. M. Thackeray. *Development of High-Capacity Cathode Materials with Integrated Structures*. Annual Merit Review, Arlington, VA, May 13-17, 2013.
4. M. M. Thackeray, *Recent Developments in Lithium Battery Materials Research*, Presentations to Samsung SDI, LG Chem (Korea); Nissan Research Center, Toda Kogyo (Japan), 30 Aug-2 Sept (2013).
5. B. R. Long, J. R. Croy, and M. M. Thackeray. *'Layered*-Layered-*Spinel' Composite Electrodes for Advanced Lithium-ion Cathodes*. 6th International Conference on Advanced Lithium Batteries for Automobile Applications, Argonne, IL, September 9-11, 2013.

V.C.4 Structure-Activity Relationships for LMR-NMC Materials (ANL, ORNL)

Jack Vaughey, Jason R. Croy, Baris Key, Fulya Dogan, and Mahalingam Balasubramanian

Argonne National Laboratory
9700 South Cass Avenue
Argonne, IL 60439
Phone : (630) 252-9184 ; Fax : (630) 252-4176
E-mail: vaughey@anl.gov

Claus Daniel, Debasish Mohanty, David Wood III, Jianlin Li (ORNL)
Oak Ridge National Laboratory
One Bethel Valley Road
P.O. Box 2008, MS 6472
Oak Ridge, TN 37831
Phone : (865) 241-9521; Fax: (865) 241-5531
E-mail: danielc@ornl.gov

Collaborators:
Andrew Payzant, Ashfia Huq, Athena Sefa-Safat (ORNL)

Start Date: October, 2012
Projected End Date: September 2014

Objectives

- Characterize the local and long-range structure of pristine LMR-NMC materials.
- Understand cation ordering, how it changes with activation and cycling, and identify the associated structure-property relationships related to voltage fade (VF).
- Understand the critical role of lithium and manganese ordering in LMR-NMC with respect to electrochemical performance and voltage fade.
- Identify unknown electrochemical processes associated with the first-cycle activation, excess capacity, and irreversible capacity loss.

Technical Barriers

- Lack of a theoretical understanding of the voltage fade phenomena and its correlation with structural changes.
- Limited spectroscopic sensitivity to unidentified chemical and structural configurations which may occur in low concentrations and/or in disordered environments.
- Incomplete understanding of first-cycle charge compensation mechanisms and the associated structures.

Technical Targets

- Synthesis of LMR-NMC systems fully enriched with lithium-6 (enriched electrolyte, Li-metal and, cathode) for electrochemical characterization and quantitative, high-resolution ^{6}Li MAS NMR experiments.
- Design of novel experiments using synchrotron facilities such as the Advanced Photon Source (APS) at ANL and the spallation neutron source (SNS) at ORNL to gain new information on the atomic-level mechanisms of VF.
- Development of theory elucidating the spectroscopic signatures of defect configurations in LMR-NMC electrodes.

Accomplishments

- Electrochemical characterization of LMR-NMC cathode materials with fully lithium-6 enriched cells (enriched electrolyte, Li-metal and cathode) and quantitative high resolution ^{6}Li MAS NMR experiments on enriched, cycled materials.
- Study of cluster and domain sizes/morphologies with combination of ^{6}Li MAS NMR experimental data and theoretical calculations on paramagnetic NMR shifts and the effects on electrochemical performance
- Installation of a static probe to initiate additional *in situ* solid state NMR studies on related materials.
- Electrochemical characterization of electrochemically active, nano-Li_2MnO_3.
- X-ray absorption spectroscopy (XAS, XANES) of Li_2MnO_3 at various states of charge and discharge, complimentary to NMR studies, revealing the differences of the end-member Li_2MnO_3 relative to the "Li_2MnO_3 component" of LMR-NMC.
- SQUID and TEM investigation showing a direct correlation between cation-ordering and voltage fade in the TODA HE5050 LMR-NMC.

- Combined results from neutron diffraction (ND) and SQUID experiments reveal the structure of pristine TODA HE5050 as a composite between trigonal and monoclinic phase with ~3% inter-layer Li^{+}/Ni^{2+} exchange, providing complete crystallographic information needed to understand the structural changes related to voltage fade.

✧ ✧ ✧ ✧ ✧

Introduction

The ABR program has established a dedicated group to study the causes and propose solutions to the problem of voltage fade in composite lithium-rich cathode materials (LMR-NMC). While these high-capacity, high-energy materials offer attractive advantages over current, state of the art Li-ion chemistries, the issue of voltage fade has been identified as a potentially significant barrier to the success of this class of electrodes. The as-prepared composite materials undergo structural transformations on charge and discharge including changes in the Li-ion local structure and rearrangement of the coordinating cations. This rearrangement is believed to be directly related to the phenomenon of voltage fade. Within the ABR program, diagnostic, materials synthesis, and spectroscopy teams have worked to combine solid-state nuclear magnetic resonance spectroscopy (NMR) XAS, as well as X-ray (XRD), ND, and electron diffraction (SAED) to follow and understand these important and complex structural transitions.

Approach

Materials synthesis and spectroscopy will be combined to design and carry out experiments critical to the understanding of pristine structures, first-cycle processes and extended-cycling structural transformations.

- Characterize domain size in composite materials and how synthesis affects domain size and the subsequent voltage fade.
- Use theory to calculate NMR resonances assigned to domain boundaries.
- Study the critical role in VF of Li and Mn ordering (e.g., $LiMn_6$ units) in end-member Li_2MnO_3 and the integrated counterpart of LMR-NMC.
- Characterize and follow the evolution of cation ordering in pristine and cycled electrodes to gain further insight into structural transformations related to voltage fade.

Results

Characterization of Cathode Materials by Solid State NMR for High Capacity Li-ion Batteries (ANL). Solid state NMR techniques has been used for characterization of Li environments and local order present in Li-rich transition metal oxide cathode materials, correlating the lithium local environments observed with the electrochemical performance. With application of high resolution ^{6}Li MAS NMR spectroscopy we can study the local structural changes for different compositions of pristine and cycled baseline LMR-NMC materials and electrodes before and after activation.

Figure V - 92 highlights high resolution ^{6}Li MAS NMR data for the TODA HE5050 cathode material. Two groups of resonances were observed for the Li species present in the lattice; Li in Li layers around 500-800 ppm region and Li in transition metal layers around 1300-1500 ppm region. The deconvolution of the peaks observed for lithium in Li layers reveals at least five different lithium environments indicating different local ordering/domains and domain boundaries from Fermi-contact shifts of 1st and 2nd coordination shells of Ni, Co and Mn. For the octahedral lithium sites in transition metal layers, two main resonances at 1371 (Li coordinated to 5Mn) and 1475 (Li coordinated to 6Mn) ppm were observed. For the octahedral lithium sites in lithium layers, four ordered Lorentzian resonances and a disordered Gaussian resonance were observed. Apart from well characterized 735 ppm Li_2MnO_3-like domains, specific assignments of all these peaks are complicated. The peaks at 807 ppm, 594 ppm and 551ppm are tentatively assigned to various lithium 2nd coordination to a combination of transition metals and lithium cations. On the other hand, the significantly disordered Gaussian resonance(s) at approximately 600 ppm (green peak in deconvolution, 95 integral units, Figure V - 92) is assigned to domain boundary lithium that exist in the vicinity of two or more locally ordered domains. In order to study the effect of the domains and domain boundary resonances observed by ^{6}Li solid state NMR, a detailed NMR study was initiated on different composite materials synthesized under various reaction conditions.

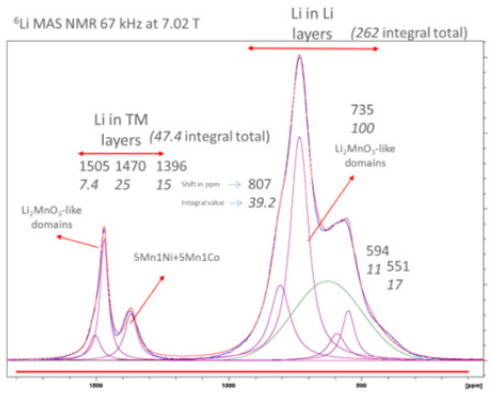

Figure V - 92: ^{6}Li MAS NMR of pristine TODA HE5050 composite $0.5Li_2MnO_3 \cdot 0.5LiMn_{0.375}Ni_{0.375}Co_{0.25}O_2$, or in layered notation, $Li_{1.2}[Ni_{0.15}Mn_{0.55}Co_{0.10}]O_2$

Figure V - 93 shows high resolution ^{6}Li MAS NMR data for the $Li_{1.5}[Mn_{0.5}Co_{0.5}]O_{2.5}$ composition. This composition is selected in order to utilize the calculation data from the theory group and to fundamentally study domain size effects on voltage fade. Two groups of resonances were observed for the Li species present in the lattice; Li in Li layers around 50-1100 ppm region and Li in transition metal layers around 1300-1500 ppm region. The deconvolution of the peaks observed for lithium in Li layers reveals many different lithium environments indicating different local ordering/domains and domain boundaries from Fermi-contact shifts of neighboring Co and Mn. The preliminary assignments for domain boundary lithium were confirmed in this study by varying the synthesis conditions (duration) from 1 hr to 84 hrs which is represented by a broad Gaussian resonance centered at 350 ppm. This resonance is gradually lost (intensity transferred to ordered Lorentzian peaks corresponding to specific Li-O-TM coordination) by increasing synthesis duration which presumably allows the small domains to coagulate, as dendritic branches of the composite structure to grow at high temperature. To be specific, the ratio of Li in domain boundaries to the total amount of Li in the sample is 0.68 for 1hr synthesis, 0.42 for 12hr synthesis and near to 0 for 84 hr synthesis. These deconvoluted Li intensities will be used by the theory group to estimate the average domain sizes/length-scales of the composite materials.

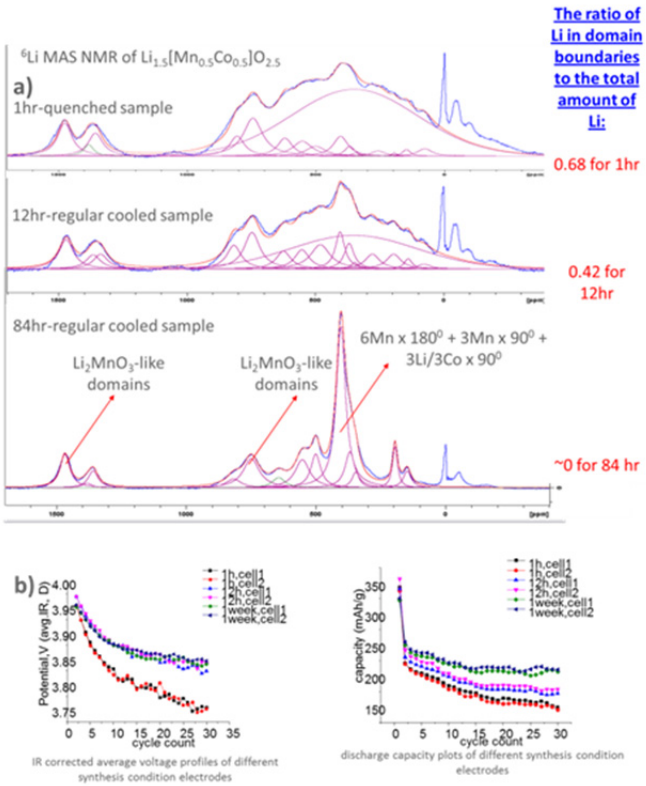

Figure V - 93: (a) Li MAS NMR of pristine $Li_{1.5}[Mn_{0.5}Co_{0.5}]O_{2.5}$ synthesized at 850°C for various annealing times. (b) Electrochemical performance of electrodes synthesized under the different conditions. NMR resonances at 0 ppm and at negative shifts are due to diamagnetic Li in $LiCoO_2$ and spinning sidebands, respectively

The effect of this synthesis parameter and Li occupancy is also correlated to electrochemical performance and voltage fade and can be seen in Figure V - 93b). The voltage fade rate is found to be a minimum but significantly present for the composites with larger domains/less disorder (1 week synthesis duration) and electrochemical discharge capacity and capacity retention values were maximum. The electrochemical performance drops and voltage fade rate increases as more domain boundary lithium are present in the structure and as the domain sizes get relatively smaller (1 and 12 hour synthesis duration).

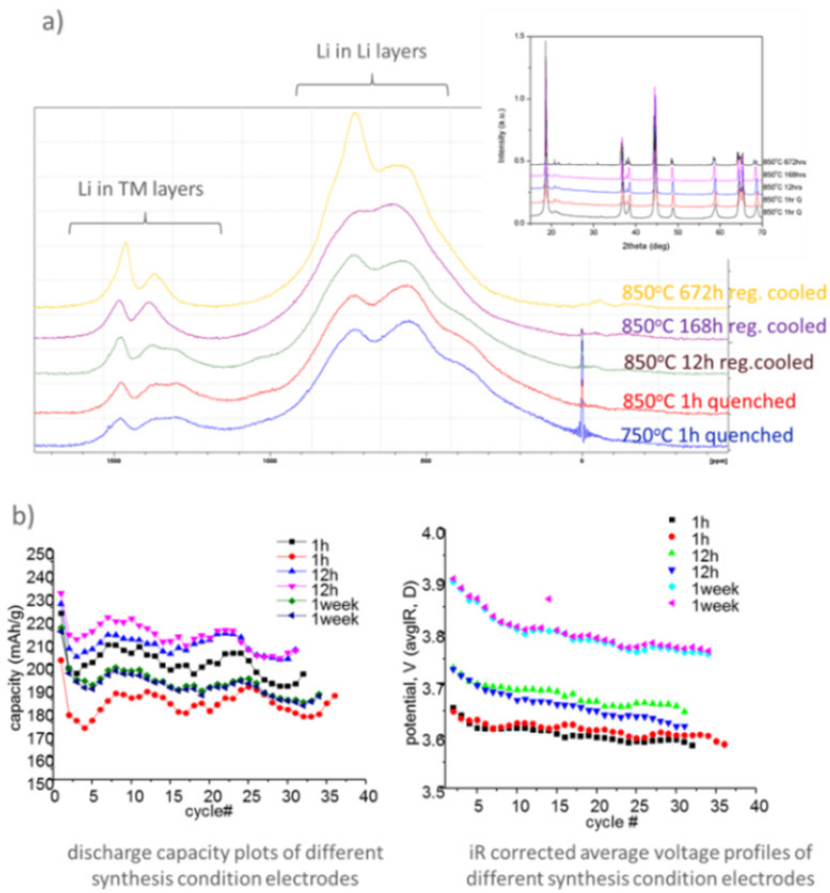

Figure V - 94: (a) Li MAS NMR of pristine $Li_{1.2}[Ni_{0.15}Mn_{0.55}Co_{0.10}]O_2$ compositions synthesized at 850°C for various annealing times, the inset shows X-ray diffraction data for the same samples. (b) Electrochemical performance electrodes synthesized under the different conditions

A new set of samples were synthesized, with ^{6}Li enriched precursors, for a targeted $Li_{1.2}[Ni_{0.15}Mn_{0.55}Co_{0.10}]O_2$ composition to study similar domain size effect with samples prepared at 850°C varying the synthesis duration. Figure V - 94a shows ^{6}Li MAS NMR of the prepared samples. Similar to the previous set of samples, two distinct lithium environments (lithium in lithium layers and lithium in transition metal layers) were observed with a similar, significantly disordered Gaussian resonance overlapping with the Lorentzian resonances. Again, a similar trend was observed with a decrease of the ratio of the intensity of the disordered resonance versus the overall intensity of the ordered resonances with increasing synthesis duration. In order to gain information on the evolution of mid- to long-range order of the composite material, synchrotron XRD patterns were collected for the same samples (Figure V - 94a inset). A typical evolution of increasing crystallinity was observed as samples synthesized at 750 and 850°C for 1 hr showed the lowest crystallinity. Interestingly, the highest crystallinity for a layered hexagonal composite lattice was reached at synthesis durations of 168 hours. Upon further annealing (672 hours) instead of an improvement in crystallinity, formation of a two phase mixture; a monoclinic lattice of Li_2MnO_3 structure and the hexagonal layered lattice of NMC material were observed. This result is consistent with the increase in local order and significant sharpening of the Li_2MnO_3-like resonance observed in ^{6}Li MAS NMR for the same samples. The most likely interpretation of these experimental results is: the well mixed, compatible lattices of the monoclinic Li_2MnO_3 structure and the hexagonal layered lattice of NMC materials, either in the well accepted dendridic domains or other nanodomain morphologies, begin to coagulate and form significant medium- to long-range order. This is the result of significant growth of the domain structure over the nano length-scale and therefore supports the Thackeray explanation (C.S.Johnson *et al.*, Electrochem. Com., 2004) of the composite nature of the Li rich NMC type electrode materials. It should also be noted that electrochemical performance of the sample annealed for 672 hours is very poor (below

150mAh/g discharge capacity, data not shown) which agrees well with the electrochemical inactivity of significant concentrations of crystalline Li_2MnO_3 in an electrode. As for samples which were annealed between 1hr-168hrs, preliminary electrochemical results (see Figure V - 94b) still show significant voltage fade but minimum fade behavior and optimum capacity and capacity retention values can be obtained by fine tuning annealing durations. At this point, it can be concluded that optimum overall electrochemical behavior can be realized for a given composition (for Li rich NMC type materials) not only by a standard 12 hour annealing step during synthesis. However, regardless of domain sizes, shapes, and morphologies of the composite particles, the voltage fade phenomenon persists and further, detailed spectroscopic understanding of the local structures associated with the fade mechanism is required.

In order to study the lithium local environment changes of the composite material upon cycling, we initiated a tedious and expensive preparation of LMR-NMC type cathode materials with fully lithium-6 enriched cells (electrolyte, metal and cathode) and performed a quantitative study with high resolution ^{6}Li MAS NMR spectroscopy on the enriched cycled materials. Figure V - 95a shows the NMR data after one cycle. Comparing with NMR data of the pristine sample (Figure V - 96) a profound loss of order or reordering in the material is observed post activation. It is clearly seen that only 7.1% of the lithium ions go back to the "formal" octahedral sites in the transition metal layers (see loss of Li in TM layers, Figure V - 96. see deconvoluted intensities in Figure V - 92 and Figure V - 95a). This is observed by deconvolution of the lithium resonances with shift values larger than 1,300 ppm (by using integral values in Figure V - 92 and Figure V - 95a). The deconvolution of the majority of the spectrum can be made by keeping a minimum amount of lithium peaks only by introducing a Gaussian and two Lorentzian components. After a dynamic fit of the deconvolution of the peaks the Lorentzian components observed match well with the fit for pristine material octahedral sites in lithium layers (714 and 525 ppm, Figure V - 96a). However a resonance(s) centered at 777 ppm was not observed in the pristine material. This resonance covers 34.5% of the lithium content of the cycled material whereas 58.4% of the lithium ions were found to be in the octahedral sites in the lithium layers. At this point a tentative assignment based on Grey *et al*.'s extensive NMR characterization works is made correlating this Li-occupancy to an extensive Li-Li dumbbell configuration composed of tetrahedral sites which are enabled after removal of octahedral Li from transition metal layers (M. Jiang, B. Key, Y.S. Meng, C. Grey., Chem. Mat., 2009/ Breger *et al.*, Chem. Mat., 2006). After 10 cycles (Figure V - 96b) the deconvoltion of the peaks reveals that the Lorentzian peak intensities and their shifts remain constant whereas there is shift of 122 ppm to lower frequency for the Gaussian component. In order to correlate the effect of the shift with electrochemistry, additional experiments are performed (5 cycles and 40 cycles). It is found that the shift gradually slows down as the voltage fade rate slows down (between cycle 1-10 being fastest, Figure V - 95c and Figure V - 95d red arrow) after 10 cycles the formation of a new lithium resonance at ~260 ppm is observed with solid state ^{6}Li NMR (Figure V - 95c and Figure V - 95d green arrows). The origin of the 122 ppm shift is currently unknown, however such significant and progressive behavior could be explained by significant transition metal migration (presumably Mn since both NM and MC type Li rich materials exhibit fade phenomenon), vacancy formation for both transition metals and/or oxygen.

Comparison of the electrochemical and structural characterization results show a direct correlation between the loss of lithium from the transition metal layers post activation and more importantly transformation/allocation of available lithium sites in lithium layers (presumably tetrahedral crystallographic positions) and electrochemical voltage fade. These changes correlate quantitatively with the amount of voltage fade and require further detailed analyses to narrow down the specific phenomena. In-depth analysis of the data is in progress to investigate the effect of lithium site formation in the lithium layers. Electrochemical performance and optimization of enriched cathode materials is in progress to obtain more reliable data and to reduce systematic errors in the analysis.

X-ray Absorption Spectroscopy of Li_2MnO_3 During First Cycle Charge and Discharge (ANL).

Li_2MnO_3 was prepared via solid state synthesis by mixing and firing the stoichiometrically required amounts of Li_2CO_3 and $MnCO_3$. A final firing temperature of 450°C was used to ensure electrochemically active, nanocrystalline particles (~200 nm). The powders were mixed with Super P carbon and assembled in coin cells with lithium metal anodes. XAS was carried out on the powders after electrochemical insertion/extraction to various states of charge on the first cycle. The element-specific nature of XAS as well as its ability to resolve local structures (~1 nm) allows us an opportunity to follow, at the atomic level, structural changes to specific environments.

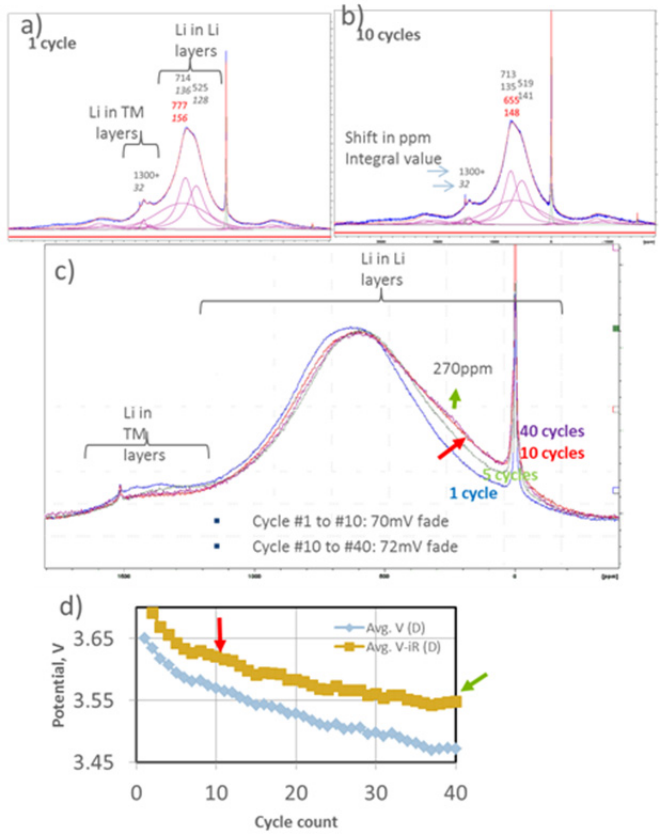

Figure V - 95: (a) and (b) are the deconvoluted 6Li MAS NMR $Li_{1.2}[Ni_{0.15}Mn_{0.55}Co_{0.10}]O_2$ after 1 and 10 cycles, respectively. (c) Comparison of ^{6}Li MAS NMR data for cycled $Li_{1.2}[Ni_{0.15}Mn_{0.55}Co_{0.10}]O_2$ and (d) electrochemical performance

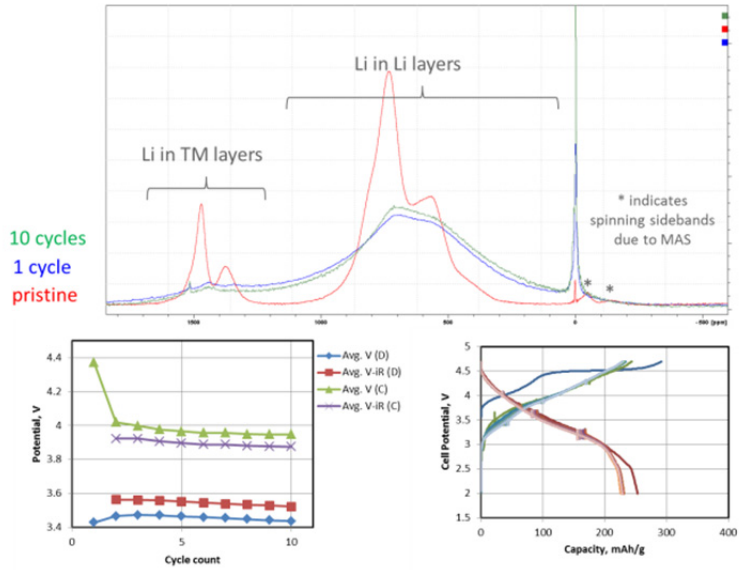

Figure V - 96: ^{6}Li MAS NMR (top) of pristine $Li_{1.2}[Ni_{0.15}Mn_{0.55}Co_{0.10}]O_2$ and after 1 and 10 cycles and plots of electrochemical performance (voltage fade data on the left, electrochemical plots on the right)

Figure V - 97 (a) shows the Mn K-edge data of the as-prepared Li_2MnO_3 powder as well as cells which had been charged to 5.1 V (red) giving ~280 mAh/g and subsequently discharged to obtain capacities of 100 mAh/g (blue), 200 mAh/g (green), and fully discharged to 2.0 V (purple) recovering ~265 mAh/g of the initial charge capacity. Quantitative NMR data (2012 report), however, showed that only ~50% of the lithium removed on charge was reinserted into the Li_2MnO_3 structure. Nevertheless, the overall shift of the NMR resonances toward higher frequency, post activation, revealed a reduction in the average manganese oxidation state below Mn^{4+}.

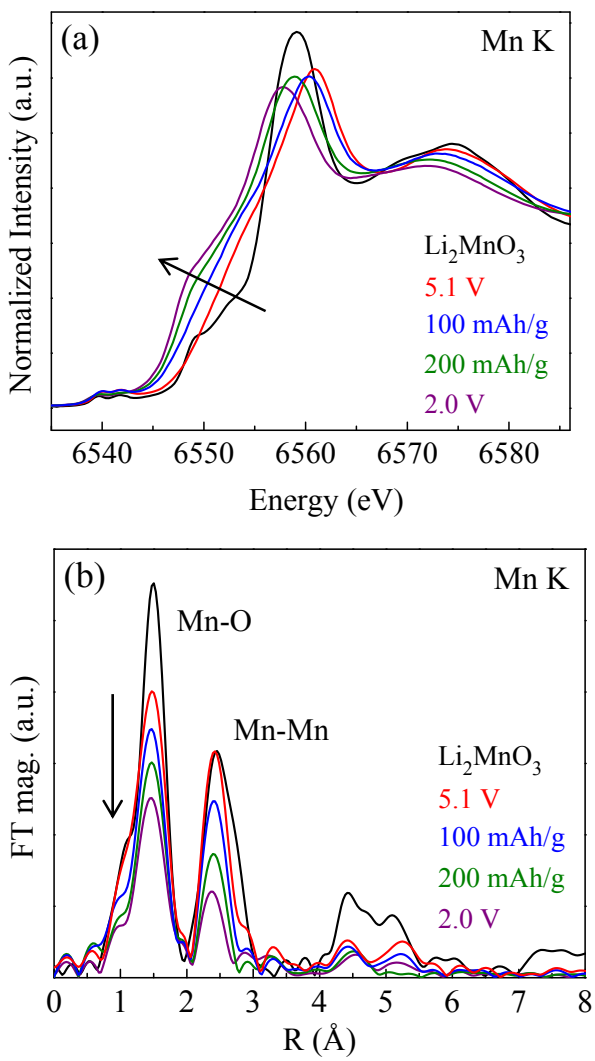

Figure V - 97: (a) Mn K-edge XANES of Li_2MnO_3 powders electrochemically charged and discharged between 5.1 – 2.0 V. (b) Mn K-edge EXAFS of Li_2MnO_3 powders electrochemically charged and discharged between 5.1 – 2.0 V

From Figure V - 97 (a) it can be seen that the charging process up to 5.1 V occurs with a change in shape of the Mn edge rather than any clear or rigid shift of the main edge to indicate oxidation of manganese. This situation is similar to what occurs in LMR-NMC on the first charge where it is generally assumed that manganese retains its 4+ oxidations state throughout the lithium extraction process. The evolution of the Mn K-edge on discharge to 100 mAh/g, 200 mAh/g, and finally to 2.0 V is indicated by the arrow in Figure V - 97(a). The large shift to lower energy and change of shape of the Mn K-edge during the discharge process clearly indicates a continuous reduction of manganese along with distortions in the manganese environment.

Figure V - 97 (b) shows the corresponding EXAF data of the samples in Figure V - 97(a). Upon charge to 5.1 V (red) obvious changes occur for the first shell Mn-O peak at ~1.5 Å (not corrected for photoelectron wave shift) similar to those observed for LMR-NMC materials. Unlike LMR-NMC, however, the Mn-O and Mn-Mn correlations in Li_2MnO_3 decrease continuously on discharge. This drastic decrease in the Mn K-edge EXAFS is in agreement with the continuous reduction of manganese shown in the Figure V - 97(a) XANES and is likely a result of Jahn-Teller distortions (due to Mn^{3+}) and is consistent with the conversion of a significant fraction of the layered structure to spinel. Detailed analysis of the EXAFS data is underway to confirm this hypothesis.

Figure V - 98(a) and Figure V - 98(b) show comparisons of the Mn K-edge XANES and EXAFS, respectively, of Li_2MnO_3 and LMR-NMC after one cycle as well as the as-prepared Li_2MnO_3 of this study; the LMR-NMC delivered ~310 mAh/g on the first cycle charge to 4.7 V and ~260 mAh/g on the subsequent discharge to 2.0 V. The most striking difference is the drastic reduction of manganese in the Li_2MnO_3 to an average oxidation state well below 4+ while the manganese in the LMR-NMC remains very much in line with the pristine Li_2MnO_3 (Mn^{4+}); even after ~75% activation of the "Li_2MnO_3 component" (assuming ~140 mAh/g from $LiMO_2$). According to the oxygen loss model for these materials the average oxidation state after the first cycle discharge should be ~$Mn^{3.5+}$ for the LMR-NMC sample, assuming routine charge compensation on Mn.

Figure V - 98 (b) shows the corresponding EXAFS for the samples in Figure V - 98(a). Again evident from the data is the striking differences between the Li_2MnO_3 and the LMR-NMC sample. The Mn K-edge EXAFS of the LMR-NMC revealed only small changes in the second-shell Mn-Metal correlations (pristine LMR-NMC not shown for clarity) while the first-shell, Mn-O correlations clearly decreased; the pristine material being similar to the Li_2MnO_3 (Mn-O coordination of 6).

In contrast, the pure Li_2MnO_3 sample shows a drastic reduction in the height of the Mn-metal correlation, consistent with the potential formation of a large component of spinel after the first cycle as mentioned earlier. Previous NMR results on these samples (see 2012 annual report) support the above conclusions for reduction of manganese in cycled Li_2MnO_3 as well as structural disorder that is clearly different from LMR-NMC materials.

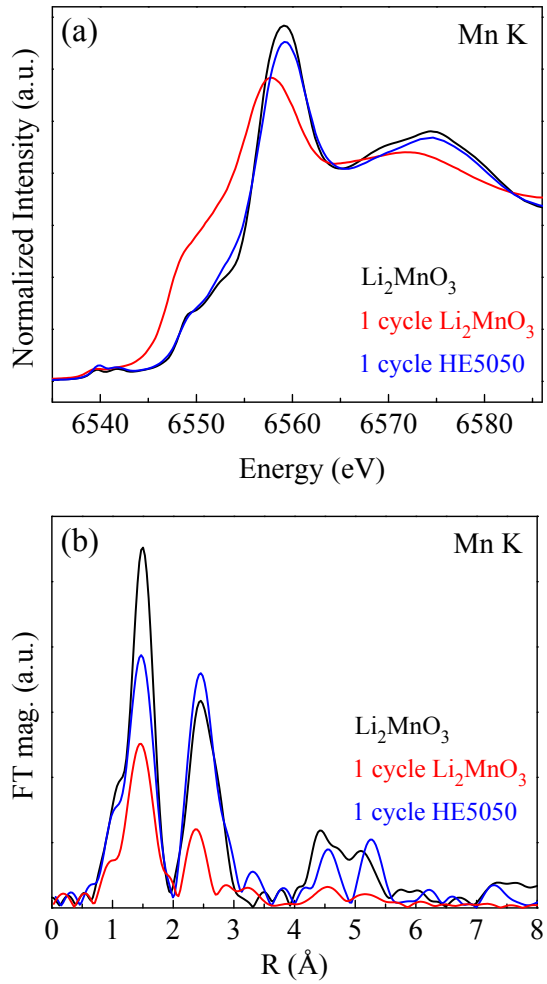

Figure V - 98: (a) Mn K-edge XANES after one cycle for Li_2MnO_3 (5.1 – 2.0 V) and LMR-NMC TODA HE5050 (4.7 – 2.0 V). The as-prepared Li_2MnO_3 is shown for reference. (b) Mn K-edge EXAFS after one cycle for Li_2MnO_3 (5.1 – 2.0 V) and LMR-NMC TODA HE5050 (4.7 – 2.0 V). The as-prepared Li_2MnO_3 is shown for reference

Correlating the voltage fade with the cation ordering in TODA HE5050 high-voltage cathode oxide (ORNL).

The task on determining microstructural changes in ABR developed cathodes during cycling by combined magnetic susceptibility, TEM, selected area electron diffraction (SAED), *in situ* XRD, and ND was carried out at Oak Ridge National Laboratory.

ORNL has implemented advanced diagnostic tools such as temperature dependant magnetic susceptibility and transmission electron microscopy (TEM) techniques to correlate the cation ordering and the voltage fade in the TODA HE5050 oxide cathode to obtain a deeper understanding of the mechanisms of voltage fade.

Two sets of electrochemical experiments were carried out; in one set, the upper-cut off voltage (UCV) was set to 4.2 V (2.4–4.2 V voltage window) and in the other set, the UCV was set to 4.8 V (2.4–4.8 V voltage window). The cells were cycled 125 times. The cycled HE5050 cathodes were harvested, washed with DMC and then dried. The electrochemical data revealed voltage fade from the cell which was cycled at a UCV of 4.8V; however, voltage fade was not observed when the UCV was 4.2V. The SAED, high-resolution TEM and magnetic susceptibility data from the pristine HE5050, after 125 cycles at a UCV of 4.2V and after 125 cycles at a UCV of 4.8V is presented in the Figure V - 99. The SAED collected from the pristine HE5050 material shows the fundamental O3 trigonal reflections (SG 166, $R\bar{3}m$) with faint extra reflections (indicated by arrows) which confirms the presence of cation-ordering arising from the monoclinic phase (SG 12, C2/m). The FFT calculated from the high-resolution TEM also shows the fundamental O3 along with the cation-ordering peaks. The high-resolution TEM shows the O3 phase. The magnetic susceptibility from the pristine HE5050 shows the divergence/splitting of field cooling (FC) and zero field cooling (ZFC) curves at T=50°C (see the highlighted arrow mark) which confirms the cation-ordering in the HE5050 pristine compound. The SAED collected from a particle which was cycled 125 times at a UCV of 4.2V retains the cation-ordering reflections and high-resolution TEM shows the O3 phase. In the magnetic susceptibility data, the divergence of FC and ZFC data is observed which provides further evidence that the cation-ordering is retained in the HE5050 oxides after 125 cycles when cycled at a UCV of 4.2V. After 125 cycles at a UCV of 4.8V, the SAED pattern showed the fundamental O3 reflections, however, it did not show cation-ordering reflections, instead, extra reflections in between two fundamental O3 spots are observed. These extra reflections indicate the presence of a spinel phase. The spinel phase in SAED is also in agreement with the high-resolution-TEM image where spinel-type atomic structure is observed. In the magnetic susceptibility

data, the splitting of FC and ZFC data at T=50°C (which indicates the cation-ordering) was not observed. These observations clearly demonstrate that the cation ordering has been supressed or lost for the HE5050 material which was cycled at a UCV of 4.8V for 125 cycles and the spinel phase has been introduced which lead to the voltage fade at higher UCV (4.8V in this study).

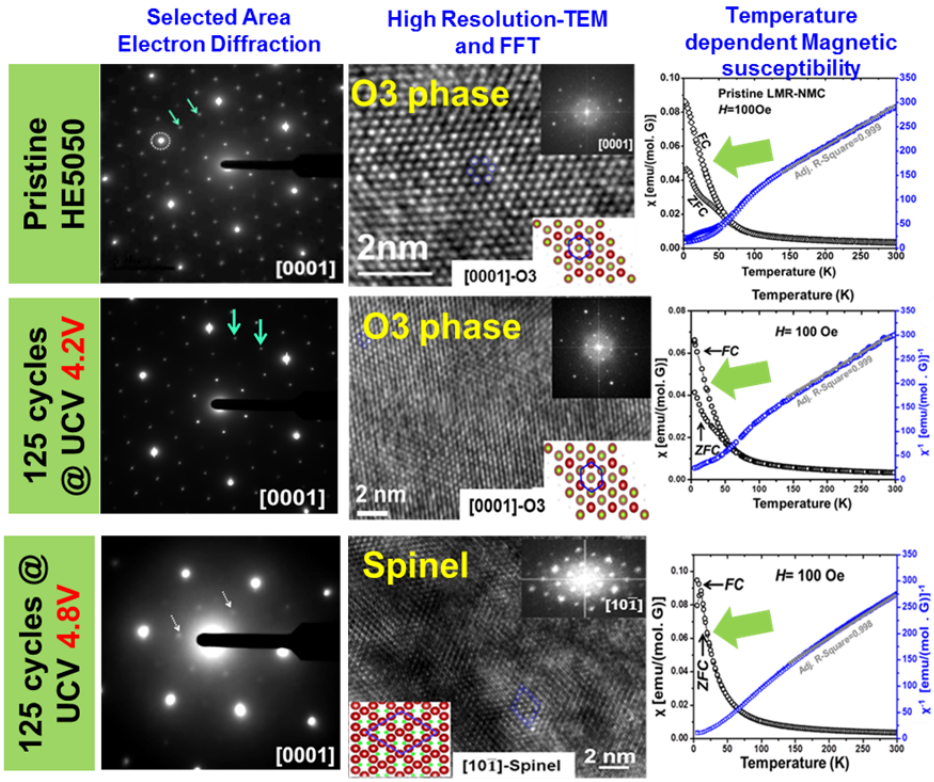

Figure V - 99: SAED, high-resolution TEM, and magnetic susceptibility data from pristine TODA HE5050 and after 125 cycles charged to a UCV of 4.2 V and 4.8 V [*Physical Chemistry Chemical Physics*, 15, 19496, (2013)]

The layered to spinel-type structural rearrangement in HE5050 is believed to occur via formation of an alkali atom in a tetrahedral site during early cycling. When a lithium ion is extracted from an octahedral site in the transition metal (TM) layer, cation-ordering is suppressed and two vacant tetrahedral sites, one in the lithium layer and another in the TM layer, are created. Li or TM ions can then migrate to the empty tetrahedral sites to create a "Li/TM dumbbell" cell, and this structure may be an intermediate between layered and spinel phases. After several cycles at a UCV of 4.8V, (~125 cycles in this study) the nucleation and growth of the spinel phase occurs and the structure may slowly transform to the spinel phase.

ND study to obtain the detailed crystallographic information on HE5050 (ORNL). Collaborating with ANL, ORNL is investigating the mechanisms of voltage fade in HE5050 oxide in order to propose routes to mitigate this adverse effect. ORNL is employing its unique capability of combined ND and magnetic susceptibility diagnostic tools to obtain insights into the atomic structural modifications, phase transformations, and modifications in electronic states of TM ions in the cycled HE5050 oxides to find the cause of voltage fade. Before presenting the data from the cycled materials, detailed crystallographic information of pristine HE5050 was obtained from the ND data. The ND experiment on pristine HE5050 materials was carried out on the POWGEN beam line at the Spallation Neutron Source at ORNL using a frame of neutrons with a centre wavelength of 1.066Å.

The experimental pattern was refined by the Rietveld method using GSAS and the EXPGUI interface. The experimental ND pattern could be refined by considering a composite structure of trigonal and monoclinic phases (Figure V - 100). The complete Crystallographic information is given in Table V - 9. It was observed that in a trigonal phase, a 3% interlayer Li/Ni exchange provided the best fit of the experimental ND pattern (see the inset of Figure V - 100). The crystallographic information along with the site occupancies obtained in the pristine HE5050 will be used to solve the crystal structure of cycled HE5050 in order to investigate the mechanisms of voltage fade.

Table V - 9: The refined crystallographic parameters for pristine HE5050 oxide by taking a composite structure of trigonal and monoclinic phases

Overall Composition: $Li_{1.20}Co_{0.1}Mn_{0.55}Ni_{0.15}O_2$

Agreement parameters: R_{WP}= 5.05% R_p= 8.09 χ^2 =1.50

Phase 2: Crystal System: Monoclinic SG: C2/m
Composition: Li_2MnO_3
Lattice constants: a=4.9464(27), b=8.5624 (5), c= 5.0332(21), β =109.3221 (32), V=201.186 (9), Z= 4, **Phase percentage**: 50% (δ=0.01)

Phase 1: Crystal System: Trigonal $R\bar{3}m$,
Composition: $LiCo_{0.25}Mn_{0.375}Ni_{0.375}O_2$
Lattice constants: a=b= 2.85525(12) 14.2483(10), V= 100.596(7), Z=3
Phase percentage : 5o% (δ=0.01)

Agreement parameters: R_{WP}= 5.05% Rp= 6.69 χ2 =1.50

Site	Atom	x	y	z	SOF	Uiso
3b	Li	0	0	0.5	0.9646(5)	0.0285 (4)
	Ni				0.0354 (5)	
3a	Co	0	0	0	0.25	0.03453 (8)
	Mn				0.375	
	Ni				0.3396	
	Li				0.0354	
6c	O	0	0	0.25941 (8)	1	0.00931 (4)

Site	Atom	X	y	Z	SOF	Uiso
2c	Li	0	0	0.5	1	0.0132(2)
4h	Li	0	0.6606	0.5	1	0.0132(2)
2b	Li	0	0.5	0	1	0.0132(4)
4g	Mn	0	0.1670	0	1	0.0101(4)
4i	O	0.2189 (10)	0	0.2283 (9)	1	0.0027(4)
8j	O	0.2548 (7)	0.3202 (20)	0.2243 (6)	1	0.0048(8)

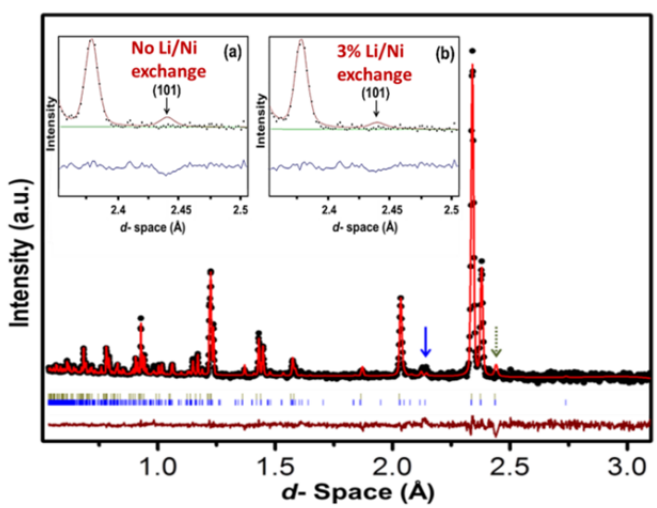

Figure V - 100: Refinement for HE5050 considering a composite monoclinic- Li_2MnO_3 and trigonal $LiMO_2$ (M=Co, Mn, Ni) unit cell. Solid arrow shows the cation-ordering peaks exclusively from monoclinic- Li_2MnO_3 and the dotted arrow marks the (101) reflection in the trigonal phase and (130)/($20\bar{1}$) reflections in the monoclinic phase. The inset shows the trigonal (101) plane intensity (a) before Li/Ni exchange and (b) after 3% Li/Ni exchange

Conclusions

- Monitoring local structural changes via ^{6}Li MAS NMR has revealed that regardless of the domain sizes and/or morphologies, significant voltage fade is observed which indicates the mechanisms for the fade phenomenon must be linked to changes within the first few coordination shells of the cations.
- For the first time, with the application of solid state NMR, quantitative spectroscopic evidence of a specific lithium local structure change is directly correlated to the amount of voltage fade in a lithium rich NMC-type of composite cathode material.
- Future NMR studies will be focused on detailed analyses and assignments of new lithium environments and shift mechanism(s) observed, in collaboration with the theory group.
- Additional solid state NMR experiments are in progress to study the structural causes of electrochemical hysteresis in collaboration with the hysteresis phenomenon team.
- ^{6}Li static *in situ* and ^{6}Li MAS *ex situ* experiments are planned to quantitatively study the correlations of the formation of the new Li-order and understand the irreversible removal of the Li from transition metal octahedral Li sites.
- Obvious reduction of manganese to states well below 4+ occur for activated Li_2MnO_3 while no clear evidence of this for LMR-NMC exists. In addition, the formation of a spinel component can be inferred after just one cycle for Li_2MnO_3 while no such conclusions can be made for LMR-NMC, even on extended cycling for many cases.
- The XAS data indicate that unknown electrochemical processes are responsible for a considerable amount of the capacity obtained from LMR-NMC. Furthermore, structural transformations occurring in pristine Li_2MnO_3 with electrochemical cycling are likely different and much more facile than in the integrated counterpart of composite materials. As such, identifying these unknown electrochemical processes as well as the associated first-cycle structures will be necessary to the advancement of composite cathode technology. This will be a focused milestone in the coming year.
- Magnetic susceptibility and TEM studies on the TODA HE5050 oxide reveals a direct correlation between cation-ordering and voltage fade. Neutron diffraction studies on pristine HE5050 oxide provided detailed crystallographic information with site occupancy factors of lithium and oxygen atoms along with the TM atoms. Rietveld refinements revealed the structure is a composite between layered trigonal and layered monoclinic phases. The refinement showed a ~3% Li/Ni interlayer exchange in the pristine HE5050 oxides.
- Future studies will include the following:
  - Rietveld refinement on neutron diffraction data collected from cycled samples will be performed to propose the mechanism of voltage fade and low first-cycle efficiency.
  - The structure-electrochemical performance correlations leading to voltage fade will be pursued and new and/or modified materials compositions will be synthesized and examined for better electrochemical performance.

FY 2013 Publications/Presentations

1. D. Mohanty, J. Li, L.C. Maxey, R.B. Dinwiddie, C. Daniel, and D.L. Wood, "Improved QC of Slot-Die Coated Lithium Ion Battery Electrodes by IR Thermography and Laser Thickness Techniques," *Analytical Methods*, Revised, 2013.
2. D. Mohanty, A. Huq, E. Andrew Payzant, A. Safa-Sefat, J. Li, D. P Abraham, D.L. Wood, and C. Daniel, "Neutron Diffraction and Magnetic susceptibility studies on a High-voltage $Li_{1.2}Mn_{0.55}Ni_{0.15}Co_{0.10}O_2$ Lithium-ion Battery Cathode; In-sight into the Crystal Structure *Chemistry of Materials,* 25, 4064 (2013).
3. D. Mohanty, A. Sefat, J. Li, R.A. Meisner, R. A. Justine, E. A. Payzant, D.P. Abraham, D.L. Wood, and C. Daniel, "Correlating Cation Ordering and Voltage Fade in a Lithium- and Manganese-Rich Layered-Layered Lithium-ion Battery Cathode Oxide; a Joint Magnetic Susceptibility and TEM study," *Physical Chemistry Chemical Physics*, 15, 19496, (2013).
4. D. Mohanty, S. Kalnaus, R.A. Meisner, K.J. Rhodes, E.A. Payzant, D.L. Wood, and C. Daniel, "Structural Transformation of a Lithium-Rich $Li_{1.2}Co_{0.1}Mn_{0.55}Ni_{0.15}O_2$ Cathode During High Voltage Cycling Resolved by *In situ* X-Ray Diffraction," *Journal of Power Sources*, 229, 239–248 (2013).
5. D. Mohanty, S. Kalnaus, R.A. Meisner, A. Safa-Sefat, J. Li, K.J. Rhodes, E.A. Payzant, D.L. Wood, and C. Daniel "Structural Transformation in a $Li_{1.2}Co_{0.1}Mn_{0.55}Ni_{0.15}O_2$ Lithium-Ion Battery

Cathode During High-Voltage Hold," *RSC Advances*, 3, 7479–7485 (2013).

6. D. Mohanty, A. Safa-Sefat, S. Kalnaus, J. Li, R.A. Meisner, E.A. Payzant, D.P. Abraham, D.L. Wood, and C. Daniel, "Investigating Phase Transformation in $Li_{1.2}Co_{0.1}Mn_{0.55}Ni_{0.15}O_2$ Lithium-Ion Battery Cathode During High-Voltage Hold (4.5 V) via Magnetic, X-ray Diffraction and Electron Microscopy Studies," *Journal of Materials Chemistry A*, 1, 6249–6261 (2013).
7. L. Baggetto, D. Mohanty, R. A. Meisner, C. Daniel, D. L. Wood III, N. J. Dudney, G. M. Veith, "Fabrication and characterization of high capacity lithium rich nickel manganese cobalt oxide cathode thin films," *Journal of Power Sources,* Revised 2013.
8. D. Mohanty, A. Huq, A. Safa-Sefat, J. Li, D. P. Abraham, D.L. Wood, and C. Daniel, "Understanding voltage fade mechanism in a lithium and manganese rich layered-layered high-voltage lithium-ion battery cathode by neutron and magnetic susceptibility studies" In Preparation, 2013.
9. 2013 DOE Annual Peer Review Meeting Presentation.
10. D. Mohanty, J. Li, C. L. Maxey, R. B. Dinwiddie, C. Daniel and D. L. Wood, "In-Line Non-destructive testing of a lithium-ion Battery Electrode by Laser Caliper and Thermography" MRS Fall meeting Boston, Massachusetts, December 1-6, (2013) (accepted).
11. D. Mohanty, A. Huq, A. Safa-Sefat, J. Li, D. P. Abraham, D.L. Wood, and C. Daniel, "Investigating Voltage Fade Pathways in a Lithium and Manganese Rich Layered-Layered High-voltage Lithium-ion Battery Cathode by Neutron Diffraction studies" MRS Fall meeting Boston, Massachusetts, December 1-6, (2013) (accepted).
12. D. Mohanty, A. Safa-Sefat, J. Li, S. Kalnaus, R.A. Meisner, D.L. Wood, and C. Daniel, "Investigating the Cation-Ordering in $0.5Li_2MnO_3 \cdot 0.5LiNi_{0.375}Co_{0.25}Mn_{0.375}O_2$ Cathode by Magnetic and Transmission Electron Microscopy Studies," ACS Spring Meeting, New Orleans, Louisiana, April 7, 2013 (*Accepted as ACS Presentation On Demand)*.
13. D. Mohanty, S. Kalnaus, R. Meisner, A. Safa-Sefat, J. Li, D.L Wood, and C. Daniel, "Structural Evolution in Lithium-Rich $0.5Li_2MnO_3 \cdot 0.5LiNi_{0.375}Co_{0.25}Mn_{0.375}O_2$ Cathode During High Voltage Cycling; an *In situ* X-Ray Diffraction Investigation," MRS 2012, Boston, Massachusetts, November 25, 2012.
14. Croy et al. ECS, 2013.
15. Key et al. ECS, 2013.
16. Gallagher et al. ECS, 2013.
17. Dogan et al. ECS, 2013.
18. Croy et al. ABAA6.
19. Croy et al. USDRIVE.

V.C.5 Hysteresis in Li-ion Battery Active Cathode Materials (ANL)

Kevin Gallagher, Wenquan Lu, & Dennis Dees
Argonne National Laboratory

Collaborators:
Jason Croy, Argonne National Laboratory
Mali Balasubramanian, Argonne National Laboratory
Michael Thackeray, Argonne National Laboratory
Martin Bettge, Argonne National Laboratory
Daniel Abraham, Argonne National Laboratory

Start Date: October 2012
Projected End Date: September 2014

Objectives

- Increase understanding of electrochemical behavior of LMR-NMC electrode materials.
- Determine if hysteresis in LMR-NMC is related to the voltage fade phenomenon.
- Create a physics-based, numerical model of the LMR-NMC electrode materials to improve understanding and forecast long-term electrochemical behavior (e.g., aging of hysteresis and voltage fade phenomena).

Technical Barriers

The primary technical barrier to the development of a safe cost-effective PHEV battery with a 40 mile all electric range that meets or exceeds all performance goals:

- Interpreting complex cell electrochemical phenomena.
- Identification of cell degradation mechanisms.

Technical Targets

- By 2014, a PHEV battery that can deliver a 40-mile all-electric range and costs $3,400
  - Enabling LMR-NMC materials to a state of commercial adoption

Accomplishments

- Demonstrated LMR-NMC electrodes display at stable hysteresis – gap exists even after 70 day hold.
- Linked hysteresis and voltage fade phenomena.
- Proposed mechanism for electrochemical behavior based on reversible and irreversible transition metal ion migration.
- Created new hypothesis on why this class of materials is able to achieve significantly higher capacity than others (i.e., 250 vs 175 mAh/g).

✧ ✧ ✧ ✧ ✧

Introduction

The electrochemical behavior of lithium- and manganese-rich transition metal oxide (LMR-NMC) layered cathode electrode materials is poorly understood even though intense efforts exist attempting to commercialize this material. The hysteresis observed in the open-circuit voltage function between charge and discharge results in energy inefficiency and complicates state-of-charge (SOC) management. More importantly, we have shown this process is directly related to the voltage fade phenomenon that is the primary roadblock to commercialization of this class of materials.[1-5]

A broader implication of this work is the proposed hypothesis for the origin of hysteresis in LMR-NMC. Based on electrochemical and spectroscopic evidence, we propose that transition-metal ions migrate during charge and discharge and may be a key reason why LMR-NMC achieves significantly higher capacity than other materials. As this behavior was not previously widely accepted, our work is shedding light on how charge is stored in these materials and perhaps understand charge storage and decay mechanisms common to layered transition metal oxide materials.

Approach

Our approach combines electrochemical studies with local-structure spectroscopy and physics-based, numerical models. Both industrially provided and laboratory synthesized materials are used to enable a broader study of the LMR-NMC material space. This report examines first the observed electrochemistry and then our attempts to capture the physics responsible for the electrochemistry in a numerical electrochemical model.

Results

Electrochemical Analysis.

Hysteresis and Voltage Fade - Figure V - 101 displays critical electrochemical measurements on lithium half cells using electrodes of $0.5Li_2MnO_3 \bullet 0.5LiMn_{0.375}Ni_{0.375}Co_{0.25}O_2$, or in standard notation $Li_{1.2}N_{i0.15}Mn_{0.55}Co_{0.10}O_2$ (Toda HE5050), that exhibit both the hysteresis and voltage fade phenomena. The galvanostatic cycling curves for the 3rd and 50th cycle show a clear change in both the charge and discharge voltage curves to lower values (i.e., voltage fade). The inset in Figure V - 101 displays the 3rd cycle dQ/dV with scanning curves measured between 2-4.1 V and 3.7-4.7 V. A significant amount of the lithium sites that are emptied above 4.1 V are not refilled until discharging to a potential of ~3.3 V (i.e., a 1 V hysteresis) as communicated by Croy et al.[1]

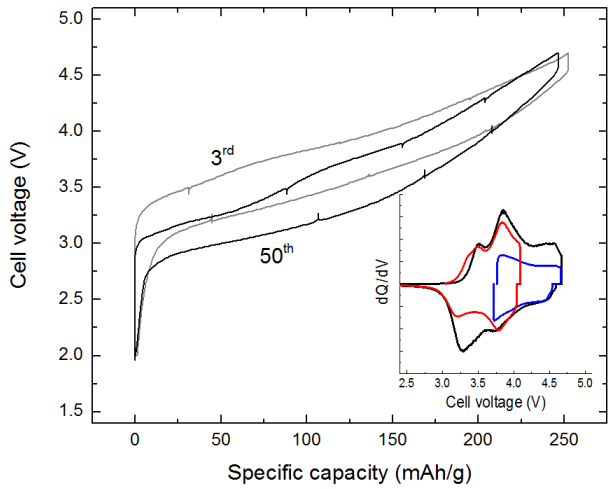

Figure V - 101: Voltage fade and (inset) hysteresis in the electrochemical profiles of a Li/Toda HE5050 half cell

The connection between voltage fade and hysteresis was elucidated in a cycling window study that was undertaken to tease out the accelerating factors related to voltage fade.[2] The testing protocol measured an IR corrected average voltage before and after cycling within a specified voltage window. The cycling windows chosen for the truncated voltage window cycling all included 4.7 V as the high voltage to utilize a large fraction of the total lithium content, thus accelerating voltage fade. The lower voltage window cutoff was varied among different samples to map out the mechanistic space. Figure V - 102 displays the drop in average OCV on discharge between the 2nd and 23rd cycles as a function of lower voltage cutoff during the truncated cycles. The greatest voltage fade occurs when cycling from a high voltage, such as 4.7 V, to a lower voltage, below ~3.4 V. To explore the calendar time dependence, the cycling data was transformed to a calendar time plot and additional data points were measured. The earlier test protocol was repeated on each of the same samples to put up to 65 cycles on the same coin cells. New coin cells were also made and tested with a potentiostatic hold at 4.7 V for 120, 240, 360, or 480 hours rather than continuous cycling in a truncated window.

Figure V - 102 (inset) presents the calendar time (total time on test) behavior of all of the different samples. Once again, it is shown that cycling between 4.7 V and 3.2 V accelerates voltage fade more than any other electrochemical exposure. The calendar time study shows a greater extent of voltage fade for the shortest hold of 120 hours relative to the equivalent 2-4.7 V cycling data; however, holding the electrode material at 4.7 V for longer periods of time only modestly increases the extent of voltage fade. From this observation, we may conclude that while calendar time is important, cycling to low potentials is necessary to significantly accelerate voltage fade. Moreover, the same critical potential, ~ 3.3 V, is observed for the hysteresis and voltage fade phenomena. Bettge et al. have also shown a correlation between the hysteresis in the second cycle and the rate of voltage fade after 20 cycles.[4]

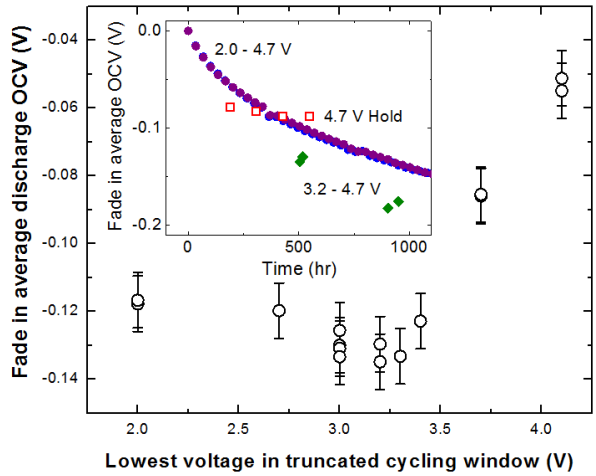

Figure V - 102: Fade in the average OCV on discharge as a function of the lower cut-off voltage between the 2nd and 23rd cycles. (inset) Fade data transformed to calendar time

Recently, Croy et al. further established the connection between voltage fade and hysteresis by carefully tracking the charge passed in different regions of the electrochemical activity.[3] This analysis used the path dependence of the different electrochemically active domains to determine how the capacity grew or shrank over cycling. The amount of capacity lost in the hysteresis region was exactly the same as that gained in the low voltage region, termed voltage fade configuration, around 3.1 V vs Li. This held true for the three stoichiometries analyzed, x=0.1, x=0.3 an d x=0.5, in xLi_2MnO_3•$(1-x)LiMn_{0.5}Ni_{0.5}O_2$. Based on the set of work analyzing the hysteresis and VF phenonmena, a mechanism was proposed, Figure V - 103.

The migration of transition metal ions, sometimes reversible, oftentimes irreversible, occurs in many layered intercalation compounds. This migration has been shown to involve tetrahedral sites in the lithium layer. The presence of a transition metal ion in the lithium layer tetrahedral site, perhaps as a TM--Li dumbbell defect straddling the TM-layer vacancy, directly affects the three nearest neighbor Li-layer octahedral site vacancies and could easily change the energy for lithium site occupancy, thus, resulting in the observed hysteresis. This dumbbell defect would be annihilated when a sufficient driving force for the reduction and migration of the transition metal ion was present, as seems to be the case near 3.3 V when a critical lithium concentration in the electrode structure is reached. With the critical driving force, the transition metal would return to the original octahedral site in the transition metal layer (i.e., hysteresis phenomenon) or it could migrate elsewhere to reside in a different local cubic environment (i.e., voltage fade).

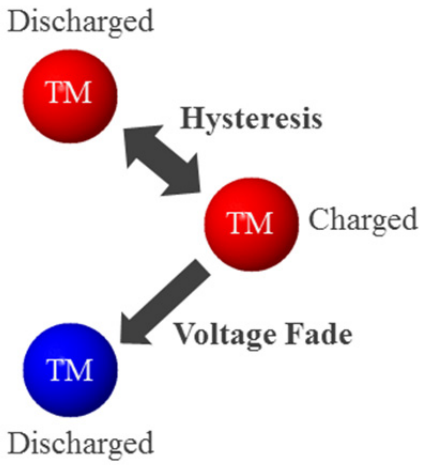

Figure V - 103: Proposed mechanism of transition-metal ion migration that when reversible is the source of hysteresis in LMR-NMC but may irreversibly lead to a lower energy, different cubic environment responsible for the growth of the voltage fade configuration (electrochemically active around 3.1 V)

From these studies we can show three distinct sources of capacity within the LMR-NMC electrode materials, Figure V - 104.[3] The first (white in Figure V - 104) behaves similar to standard intercalation material of layered oxides. The second region (red) is that associated with the hysteresis phenomenon and potentitally results from reversible transition-metal ion migration. Finally, the third region (blue) is the voltage fade configuration that shows electrochemically reversible behavior around 3.1 V. The voltage fade configuration grows at the expense of the hysteresis contribution and may result from irreversible transition metal migration.

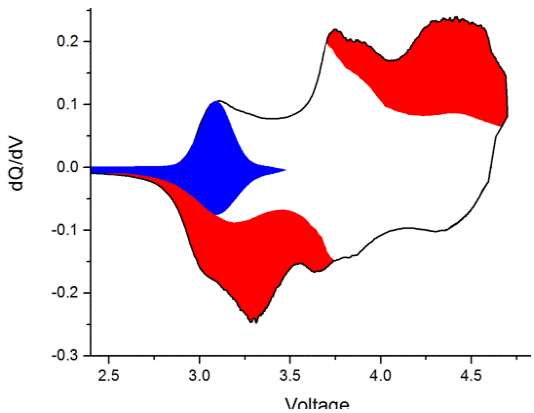

Figure V - 104: Illustration of the three distinct electrochemical contributions to the capacity of LMR-NMC electrode materials

Electrochemical Behavior of the Macro-Components Thought to Compose LMR-NMC on the Nano-Scale- The LMR-NMC electrode materials are often labeled in a composite notation to highlight the importance of the Li_2MnO_3-like structure found within these nano-composite materials. To investigate the relationship of the LMR-NMC materials to what might be considered their parent componds, we analyzed the electrochemistry of bulk (non composite) $LiNi_{1/3}Co_{1/3}Mn_{1/3}O_2$ (NCM) and Li_2MnO_3.[5] Figure V - 105 shows the differential capacity plot of NCM, Li_2MnO_3 and a 50/50 physical blend of powders during their first formation cycle. As expected, the differential capacity plot of the physically-blended electrode preserved the redox preaks of Li_2MnO_3 and NCM, respectively. At about 4.4V, both blend and Li_2MnO_3 start to be activated. Figure V - 106 compares the differential capacity plots of blend and LMR-NMC (HE5050, Toda) during the first cycle. The normalized dQ/dV (dQ/dV*Q) peaks of the Li/blend cell are in the similar potential regions with dQ/dV*Q peaks of Li/LMR-NMC cell. Both the blend and LMR-NMC start to be activated at almost same potential highlighting a signature of Li_2MnO_3; however, important differences exist. A shift was observed for the redox potential related to NCM between the blend and LMR-NMC, which could possibly be attributed the different stoichiometric ratio of Ni, Co, and Mn in NCM (1/1/1) and LMR-NMC (0.37/0.24/0.39). Another likely reason for the NCM redox peak shift is related to the small domain size (nm range) and local environment which is fundamentally different between the bulk NCM material and the nano-composite LMR-NMC material due to transition metal and lithium ordering. Another important distinction is the low voltage peak on discharge. The Li_2MnO_3 shows significant capacity below 3 V whereas the LMR-NMC material shows almost none. We conclude that the LMR-NMC material resembles, but is distinct from, the parent compounds often used to describe the stoichiometry in nano-composite notation.

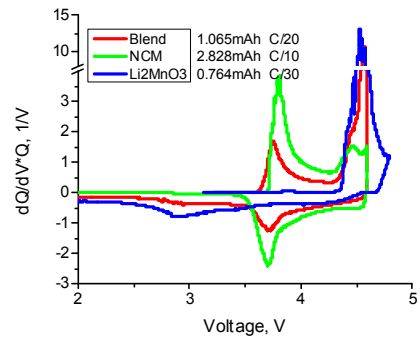

Figure V - 105: differential capacity plot of NCM, Li2MnO3 and their 50/50 blend

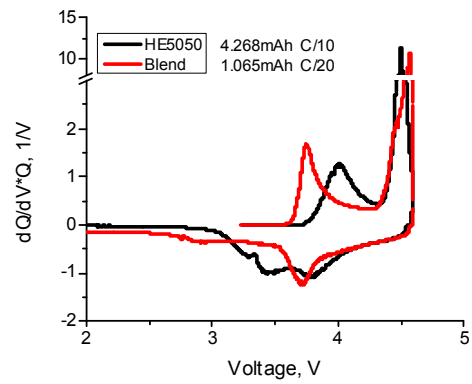

Figure V - 106: Comparision of differential capacity plots of blend and LMR-NMC

Electrochemical Modeling. The general methodology for the electrochemical model follows the work of Newman.[11] Essentially, continuum based transport equations are combined with kinetic and thermodynamic expressions to allow the potential, concentration, and current distributions to be determined throughout the cell. Volume-averaging of the transport equations accounts for the composite electrode geometry. Increasingly complex electrochemical models have been developed for lithium-ion cells that include a detailed model of the transport and reaction in the SEI and phase change active electrode materials [12-14]

The focus of this effort is on the hysteresis that LMR-NMC electrode materials are known to exhibit between their charge and discharge voltage curves, even at very slow cycling rates (e.g., C/200). A number of different models have been examined with varying degrees of success. The model development described below combines and extends some of the earlier work. As discussed below, this model exhibits characteristics that account qualitatively for many of the observed phenomena, but until the model is rigorously compared

and fitted to the experimental data, its true utility cannot be determined.

The activated LMR-NMC cathode material is obviously quite complex and suggested to be composed of nanometer scale sized domains. These domains are highly integrated, but appear to have unique electrochemical properties. The cathode material is assumed to be composed of two types of domains for the initial model development (as mentioned previously, three electrochemically distinct regions exist), where both domains can be electrochemically active. One domain (designated domain number 1) is considered to be relatively stable to changes in lithium concentration, while the other domain goes through a slow reversible structural transition during cycling. At low lithium concentrations, the unstable domain has one lattice structure (designated domain number 2) and at high concentrations, another (designated domain number 3). In other words, domains 2 and 3 are located in the same nanometer spatial regions within the material. Although, the model formulism does account for phase boundaries, domain 2 grows at the expense of the domain 3 in a reversible manner (thus 3 grows at the expense of 2). Each of these domains has an associated open circuit voltage (OCV) curve as a function of lithium concentration in that domain (c_{Si}, i = 1, 2, or 3). Figure V - 107 has the assumed OCV curve for each of the domains, where x_S is the ratio of the lithium concentration in the specific domain divided by its maximum concentration. The actual OCV curve is inevitably more complicated, but this should be adequate for an initial examination of the model. It is important here that the OCV curves are offset by a significant voltage.

Volume-averaged continuum-based diffusion equations are used to describe the transport of lithium through the material. The flux of lithium between two adjacent domains denoted *i* and *j* (N_{ij}) is described by an electrochemical potential (μ_{Li}) driven mass transport expression, Equation 1, where k_{ij} is the mass transfer coefficient. The electrochemical potential can be easily associated with the OCV of the domain.

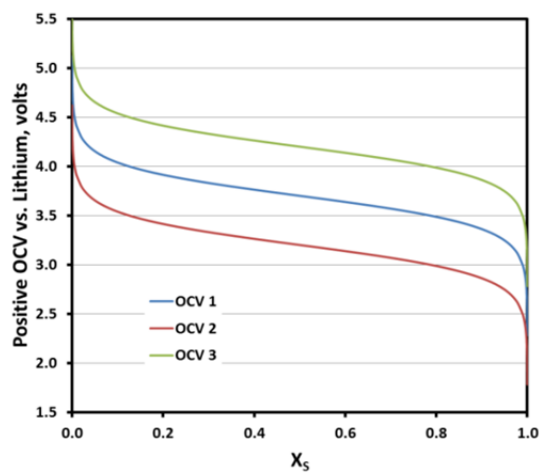

Figure V - 107: Assumed open circuit voltage curve as a function of relative lithium concentration in domain

$$N_{ij} = k_{ij}\left[\mu_{Li}(i) - \mu_{Li}(j)\right] \quad [1]$$

The transitions from domain 2 to 3 and from domain 3 to 2 are assumed to follow the Avrami phase change expression (see Equation 2), where *k* is a lithium concentration driven rate constant and ε_{Si} is the volume fraction of domain *i*.

$$\varepsilon_{Si} = 1 - \exp\left(-kt^n\right) \quad [2]$$

By offsetting the individual domain OCV curves and making the structural transitions and lithium transport between domains extremely slow (i.e., very small rate constant and mass transfer coefficient); the electrochemical model exhibits a hysteresis between charge and discharge, even at a C/200 rate, as seen in Figure V - 108. It should be noted that the model simulations presented here are only for the active material (i.e., single particle calculation), although at very slow rates there is little or no difference between the single particle and the full cell.

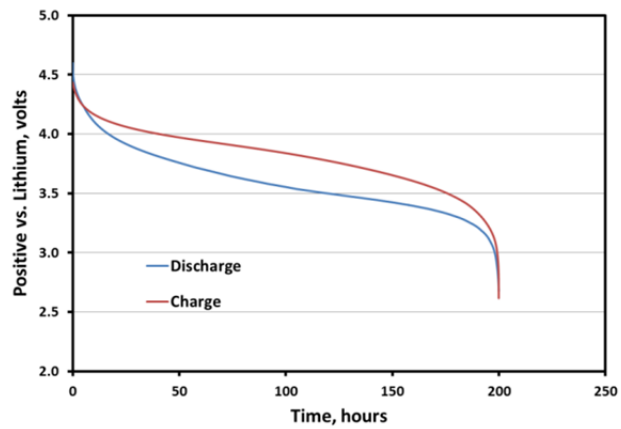

Figure V - 108: Electrochemical model simulation of active material charge and discharge curves at a C/200 rate

The electrochemical model described above will eventually come to equilibrium given enough time. At around a C/5000 rate the charge and discharge simulations collapse to a single curve, which indicates that the material takes months to come to a true equilibrium. This raises the question of whether a material with these poor transport characteristics could ever support high discharge/charge rates. To address this, a series of simulations were conducted over a range of C-rates from about C/5000 to C/1, as shown in Figure V - 109. One can see that there is a significant loss in total capacity over the range studied, but that the material can support these rates.

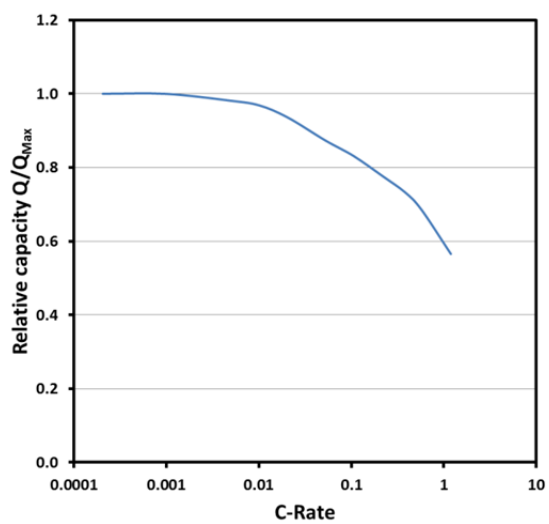

Figure V - 109: Electrochemical model simulation of active material rate behavior

To more rigorously examine the proposed electrochemical model, a specific LMR-NMC material and electrode has been adopted for study. The extensive database of the baseline Toda HE5050 LMR-NMC active material and electrode makes it the best option. While there are a wide variety of electrochemical studies on this material, two types of half-cell (i.e., lithium counter electrode) studies are being utilized for fitting the model parameters. The first type is constant current cycling (C/18) and the second type is relatively slow Galvanic Intermittent Titration Technique (GITT) study, both using the standard electrode. In the GITT study a C/18 current is applied for 10 minutes followed by a 100 minute rest, which is then repeated through a complete cycle. The approximately 30 model parameters associated with the LMR-NMC material makes the parameter fitting a challenge. It is anticipated that multiple fitting iterations of the data will be necessary to generate a full concentration dependent parameter set.

As a starting point, the constant current cycling data was utilized with the particle model described above to develop a working set of parameters. This data is not particularly sensitive to the transport parameters and was used mainly to fit the OCV curves of the three domains and establish average rate constants for the domain transitions, as well as their range of stability. It was clear from the exercise that a perfect fit of data was not possible without allowing the transition rate and transport parameters to be concentration dependent. However, a reasonably good fit of the data could be obtained with average parameters, as shown in Figure V - 110.

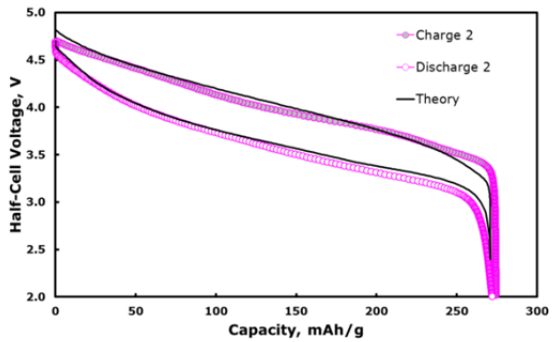

Figure V - 110: Electrochemical model simulation of HE5050 LMR-NMC standard electrode half-cell charge and discharge curves at a C/18 rate

The complex nature of this material that exhibits the hysteresis between charge and discharge curves can be seen by examining the relative amounts of domains 2 and 3 as the material is cycled (see Figure V - 111). As indicated above, domain 2 is stable when fully charged and domain 3 is stable when fully discharged. The data fit indicates that the crossover point for this material is around 3.5 volts. The sluggishness of the transition rates cause the material to never be at equilibrium at any reasonable cycling rate. Further, the slow transition rates result in the changes to appear to be out-of-phase with the cycling. Finally, the differences in the stability ranges and transition rates cause the asymmetry apparent in Figure V - 111.

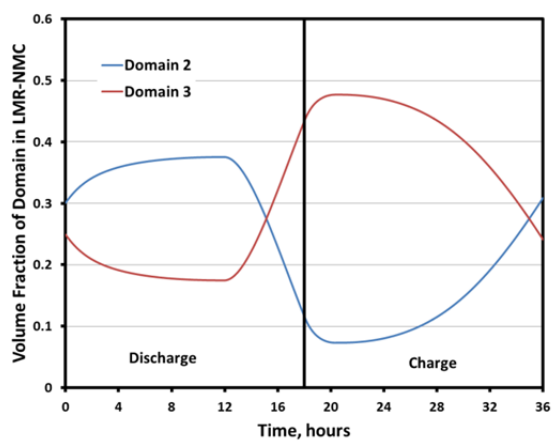

Figure V - 111: Volume fraction of domains 2 and 3 in HE5050 LMR-NMC active material from electrochemical model simulation of charge and discharge at a C/18 rate

The particle model was integrated into the half-cell electrochemical model to use in fitting the GITT half-cell data.[15] Since there is no actual reference electrode in the cell, an estimate of the lithium electrode interfacial area specific impedance (ASI) is important. This is complicated by the high probability that the lithium electrode impedance is likely not stable throughout the full experiment. Nevertheless, an average lithium electrode ASI was estimated by comparing impedance data on reference electrode cells to the approximately one second ASI of the half-cell. The more accurate the lithium ASI the better the LMR-NMC interfacial ASI can be determined. However, this information can best be determined using reference electrode impedance data on LMR-NMC electrodes (see annual report on electrochemical modeling studies in Cell Fabrication Facility Team Production and Research Activities section).

The fitting of GITT data has been initiated using the parameter set from the constant current cycling data. In the initial fitting, the OCV curves and the stability ranges of domains 2 and 3 are not varied. Also, the ratios of the transport parameters and transition rates for each domain are held constant. This reduces the fitted parameters to a reasonable number and these assumptions can be relaxed as the complete parameter set is developed. Even with these assumptions, there is sufficient flexibility to fit the data, as shown in Figure V - 112 for a single charge pulse and relaxation at about 3.8 volts.

Recent experimental studies, Figure V - 113, indicate that the stability range of domains 2 and 3 overlap (i.e., there is a voltage range where both domains are stable). This would create a "true voltage hysteresis" (i.e., a hysteresis that would exist at all cycling rates). Presently, the stability ranges in the model are being adjusted to take the recent observations into account.

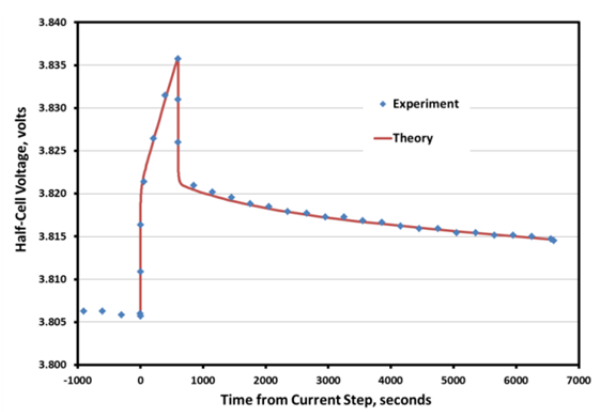

Figure V - 112: Electrochemical model simulation of HE5050 LMR-NMC standard electrode half-cell GITT experiment (600 second C/18 charge pulse and 6000 second relaxation at about 3.8 volts)

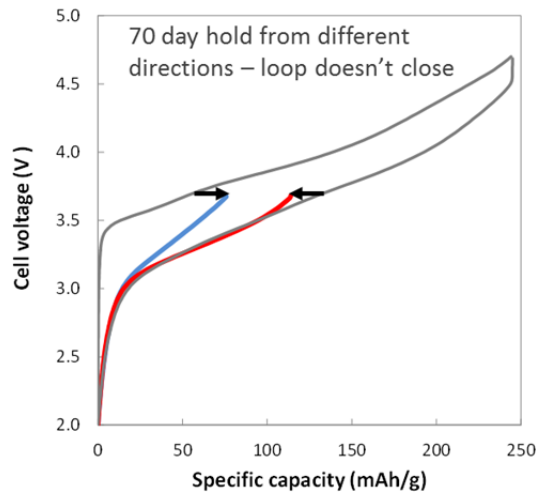

Figure V - 113: Hysteresis loop is not closed at a 70 day hold at 3.7 V from different directions (charge vs discharge). Here shown for the Toda HE5050 material in a lithium half cell

Conclusions and Future Directions

The LMR-NMC material is shown to be composed of three distinct electrochemical contributions: standard layered material intercalation, hysteresis, and voltage fade configuration. The voltage fade phase grows at the expense of the hysteresis contribution. The hysteresis is proposed to result from the migration of transition-metal ions during charge and then back on discharge. This process is postulated to be only semi-reversible. On some frequency, the transition-metal ion would migrate to a different cubic environment and initiate growth of the voltage fade configuration. A domain showing electrochemically reversible activity is found around 3.1 V. The growth of this lower voltage fade thus lowers the average voltage of the LMR-NMC electrode (i.e., Voltage Fade). Future work will support spectroscopic attempts to identify transition-metal ion migration.

An electrochemical model has been proposed that at least qualitatively explains much of the observed experimental behavior of the LMR-NMC electrode. The parameter fitting with the present model will continue. As confidence with the model improves, another domain will be added to the model to account for the voltage fade. Paralleling the voltage fade model modification, the bulk material electrochemical model will be integrated with the complex SEI electrochemical model.

FY 2013 Publications/Presentations

Publications

1. J. R. Croy, K. Gallagher, M. Balasubramanian, Z. Chen, Y. Ren, D. Kim, S.-H. Kang, D. Dees, and M. Thackeray, *Examining Hysteresis in Composite xLi_2MnO_3•(1-x)$LiMO_2$ Cathode Structures*, Phys. Chem. C 117, 6525 (2013).
2. K. Gallagher, J. R. Croy, M. Balasubramanian, M. Bettge, D. Abraham, A. Burrell, and M. Thackeray, *Correlating Hysteresis and Voltage Fade in Lithium- and Manganese-rich Layered Transition-Metal Oxide Electrodes*, Electrochem. Comm. 33, 96 (2013).
3. J. R. Croy, K. Gallagher, M. Balasubramanian, B. Long, and M. Thackeray, Quantifying Hysteresis and Voltage Fade in xLi_2MnO_3•(1-x)$LiMn_{0.5}Ni_{0.5}O_2$ Electrodes as a Function of Li_2MnO_3 Content (submitted).
4. Martin Bettge, Yan Li, Kevin Gallagher, Ye Zhu, Qingliu Wu, Wenquan Lu, Ira Bloom, Daniel P. Abraham, *Voltage fade of layered oxides: its measurement and impact on energy density*, J. Electrochem. Soc., 160 (11) A2046-A2055 (2013).
5. Wenquan Lu, Qingliu Wu, and Dennis W. Dees, Electrochemical Characterization of Lithium and Manganese Rich Composite Material for Lithium Ion Batteries, J. Electrochem. Soc., 160 (6) A950-A954 (2013).

Presentations

1. K. G. Gallagher, J. R. Croy, M. Balasubramanian, and M. M. Thackeray *Hysteresis and Voltage Fade in Lithium- and Manganese-Rich Transition Metal Oxide Electrodes* 224th Meeting of Electrochemical Society, San Francisco, CA USA, October 27-November 1st, 2013, #**958**.
2. K. G. Gallagher, Promises and Challenges of Lithium- and Manganese-Rich Transition-Metal Layered-Oxide Cathodes DOE Merit Review, Washington D.C. USA, May 13 – May 17, 2013.
3. K. G. Gallagher J. R. Croy, M. Balasubramanian, D. W. Dees and M. M. Thackeray, *Examining Hysteresis in Li- and Mn-Rich Composite Cathode Materials* DOE Merit Review, Washington D.C. USA, May 13 – May 17, 2013.
4. W. Lu, *Validation of Electrode Materials and Cell Chemistries* DOE Merit Review, Washington D.C. USA, May 13 – May 17, 2013.
5. K. G. Gallagher, J. Croy, M. Balasubramanian, D. W. Dees, and M. M. Thackeray, *Hysteresis in LMR-NMC Electrodes (xLi2MnO3 •(1-x)LiMO2, M = Ni, Co, Mn)* U.S. Drive Meeting on Cathode Material Development, Argonne National Laboratory, Lemont, IL USA, January 24, 2013.

References

1. J. Newman and K. Thomas-Alyea, *Electrochemical Systems*, John Wiley and Sons, New York (2004).
2. D. Dees, E. Gunen, D. Abraham, A. Jansen, and J. Prakash, *J. Electrochem. Soc.,* **152** (7) A1409 (2005).
3. D. Dees, E. Gunen, D. Abraham, A. Jansen, and J. Prakash, *J. Electrochem. Soc.,* **155** (8) A603 (2008).
4. K. Gallagher, D. Dees, A. Jansen, D. Abraham, and S.-H. Kang, *J. Electrochem. Soc.,* **159** (12), A2029-A2037 (2012).
5. D. W. Dees, S. Kawauchi, D. P. Abraham, and J. Prakash, *J. Power Sources,* **189** (1), 263-268 (2009).

V.C.6 Impact of Coatings on Voltage Fade in the LMR-NMC Materials (ANL, ORNL, NREL)

Coatings Team[11]

Argonne National Laboratory, Argonne, IL
Oak Ridge National Laboratory, Oak Ridge, TN
National Renewal Energy Laboratory, Golden, CO

Start Date: October 2012
Projected End Date: June 2013 (complete)

Objective

- Determine the efficacy of coatings and additives to slow or stop the voltage fade phenomenon

Technical Barriers

This project addresses the following technical barriers as described in the USABC goals [2, 3]:

(A) Performance at ambient temperatures
(B) Cycle life

Technical Targets

- PHEV specific energy targets (pack): 3.4 kWh (min) to 11.6 (max) [2]
- EV specific energy targets (pack): 80 (min) to 200 (max) Wh/kg [3]

[11] The Coatings Team (within the Voltage Fade project) members include: (from ANL) Ira Bloom, Lynn Trahey, Ali Abouimrane, Ilias Belharouak, Xiaofeng Zhang, Qingliu Wu, Wenquan Lu, Daniel P. Abraham, Martin Bettge, Jeffrey W. Elam, Xiangbo Meng, Anthony K. Burrell, (from NREL) Chunmei Ban, Robert Tenent, (from ORNL) Jagjit Nanda and Nancy Dudney.

Accomplishments

The effects of the coatings Al_2O_3, $LiAlO_x$, ZrO_2, TiO_2, $AlPO_4$, and LiPON and of the electrolyte additives 3-hexylthiophene and lithium difluoro (oxalato)borate (LiDFOB) on the voltage fade phenomenon in $0.5Li_2MnO_3 \bullet 0.5LiNi_{0.375}Mn_{0.375}Co_{0.25}O_2$ cathodes were investigated. Cells containing these materials or additives were cycled according to a standard protocol at room temperature between 2.0 and 4.7 V vs. Li^+/Li. As expected, the cells containing either an additive or a coated cathode displayed less capacity loss than cells containing an uncoated cathode and no additive. The voltage fade phenomenon was quantified in terms of changes in the average cell voltage (Wh/Ah). The results indicate that, within experimental error, all of the coatings and additives produced little-to-no effect on voltage fade.

✧ ✧ ✧ ✧ ✧

Introduction

Layered materials in the Li-Mn-rich portion of the Li-Ni-Mn-Co-O phase diagram (LMR-NMC), which are structurally integrated composites of Li_2MnO_3 and $Li(Ni,Mn,Co)O_2$ and are usually written as $aLi_2MnO_3 \bullet (1-a)Li(Ni,Mn,Co)O_2$, are promising cathodes for use in lithium-ion batteries. However, with cycling, the shape of the voltage vs. capacity curve changes. A similar decline is also observed on charging, strongly suggesting that changes to the equilibrium electrochemical potential of the active material cause the voltage fade. In the literature, the continuous change in the shape of the discharge (and charge) curves has been attributed to the formation of a spinel-like phase [4-8]. As a result of the loss in potential, there is a loss in energy, limiting the utility of these materials in energy-demanding applications, such as in electric vehicles.

Approach

Three national laboratories, Argonne National Laboratory, the National Renewable Energy Laboratory and Oak Ridge National Laboratory, are collaborating to devise methods to arrest this voltage fade. The work, described below, approaches this goal by investigating the effects of using cathode coatings and electrolyte

additives. In the literature, coatings, surface modifications, and additives of many descriptions have been used to stabilize the capacity of cathode materials and enhance cycling ability [4-46], enhance the rate capacity of cathode materials [17, 18, 20, 24, 25, 27, 35, 36, 47], lessen their thermal reactivity [16, 48-51], lessen their reactivity towards the organic electrolytes [52], and promote secondary electrolyte interface layer formation on the cathode [50]. The effects of the coatings Al_2O_3, $LiAlO_x$, ZrO_2, TiO_2, $AlPO_4$, and lithium phosphorus oxynitride (LiPON) and of the electrolyte additives 3-hexylthiophene and LiDFOB on voltage fade were investigated. It should be noted that both electrolyte additives are very effective in forming a protective layer on the surface of the positive electrode at high potentials [33, 45].

Results

Coatings. All positive electrodes contained the same commercially available LMR-NMC material, $0.5Li_2MnO_3 \bullet 0.5LiNi_{0.375}Mn_{0.375}Co_{0.25}O_2$ (Toda Kogyo, Japan; referred to as HE5050), which was used to fabricate coated and uncoated cathode laminates. Atomic-layer deposition (ALD) coatings of Al_2O_3 [54, 55-57], TiO_2, ZrO_2, and $LiAlO_x$ [58] were applied to HE5050 laminate sheets. $AlPO_4$ [40-43] and LIPON [18] were applied to HE5050 powders before casting into laminates. The compositions of the cathode materials are given in Table V - 10. All were assembled into coin cells with lithium metal anodes.

Cell cycling. All cycling was performed at room temperature. All cells were cycled between 2 V and 4.7 V at 10 mA/g for the first cycle, and then between 2 V and 4.7 V (vs. Li^+/Li) at 20 mA/g for the following cycles. The cells were cycled between 2 and 4.7 V for a minimum of 20 and a maximum of 50 times. While cycling, current interrupt measurements were carried out at 3.5, 3.9, 4.3, and 4.7 V during charge and at 4.0, 3.6, 3.2, and 2.0 V during discharge. Estimates of cell resistance were calculated from the values of cell voltage and current at times t_0 and t_1 using Eq. 1

$$R = \left|\frac{v_{t_1} - v_{t_0}}{i_{t_1} - i_{t_0}}\right|, R = \left|\frac{v_{t_1} - v_{t_0}}{i_{t_1} - i_{t_0}}\right|, \quad \text{Eq. 1.}$$

where v_{t_1} and v_{t_0} are the cell voltages at t_1 and t_0, respectively; i_{t_1} and i_{t_0} are the respective currents.

Table V - 10: Cathode compositions used in this work

Designation (deposition temperature or time)	Cathode
Baseline	86 wt% HE5050 4 wt% SFG-6 graphite 2 wt% SuperP carbon black 8 wt% PVDF
TiO_2 (100°C) TiO_2 (150°C)	92 wt% active material 4 wt% C45 conductive additive 4 wt% Solvey 5130 binder
ZrO_2 (100°C) ZrO_2 (150°C)	
$LiAlO_x$ (225°C)	
$AlPO_4$	86 wt% active material 4 wt% SFG-6 graphite 2 wt% SuperP carbon black 8 wt% PVDF
5 ALD cycles Al_2O_3 (120°C) 100 ALD cycles Al_2O_3 (120°C)	84 wt% active material 8 wt% PVDF binder 8 wt% Super P carbon black
LiPON (1 h) LiPON (2 h) LiPON (3 h)	85 wt% active material 7.5 wt% SuperP carbon black 7.5 wt% PVDF
LiDFOB, 2.0 wt%	92 wt% active material 4 wt% C45 conductive additive 4 wt% Solvey 5130 binder
3-hexylthiophene, 0.1 wt%	92 wt% active material 4 wt% C45 conductive additive 4 wt% Solvey 5130 binder

The activation charge subcycle and the discharge immediately following it were omitted from further analysis in this work. After that subcycle, the energy (Wh) and capacity (Ah) values were either extracted directly from the cycling data or were calculated from the raw data using Microsoft Excel®. The average voltage for a given charge or discharge subcycle was calculated as Wh/Ah. The resistance values at the first three voltages were averaged and used to correct the average voltage value for the average resistance of the cell during a given cycle. The relative change in the iR-corrected average voltage was calculated by comparing the value from the first discharge or charge subcycle to the respective value at the 20th discharge or charge subcycle, as shown in Eq. 2.

$$Rel.\,change\ in\ avg.\,voltage = \frac{Avg.voltage_{first\ cycle} - Avg.voltage_{last\ cycle}}{Avg.voltage_{first\ cycle}} \quad \text{Eq. 2.}$$

These relative average voltage values then were used for plotting and subsequent analyses.

Capacity fade. As expected, the cell discharge capacity faded with cycling for cells containing the electrolyte additives and the coated or uncoated cathode materials, as shown in Figure V - 114. The baseline showed the greatest amount of capacity fade, which was due to impedance rise and loss of active sites in the

positive electrode when cycled to 4.7 V. Figure V - 114 shows that the capacity fade rate of the coated materials is sensitive to the nature of the coating; some coated materials display greater capacity loss rates than others. It was interesting to note that the loss of capacity in cells containing an electrolyte additive were different, with the cell containing LiDFOB displaying about 25% of the capacity loss of the cell containing 3-hexylthiophene. Of more importance, the data in Figure V - 114 clearly show that the capacity of cells containing coated cathode materials or electrolyte additives fades slower than that of the cell containing either no additive or uncoated materials. This trend is consistent with reports in the literature [15-39, 44-46].

Voltage Fade. In these experiments, the cells containing either coated cathodes or an additive behaved similarly as those that were uncoated or contained no additive. Examples of the aging behavior of cells containing an uncoated cathode and coated cathode are shown in Figure V - 115 and Figure V - 116, respectively. The first charge cycle is believed to activate the Li_2MnO_3 portion of the composite cathode material, a process needed to achieve high capacity density. With continued cycling, the cathode material loses voltage, as indicated by the changes in the voltage vs. normalized capacity curves; this loss of voltage behavior is consistent with that seen by others [4, 9].

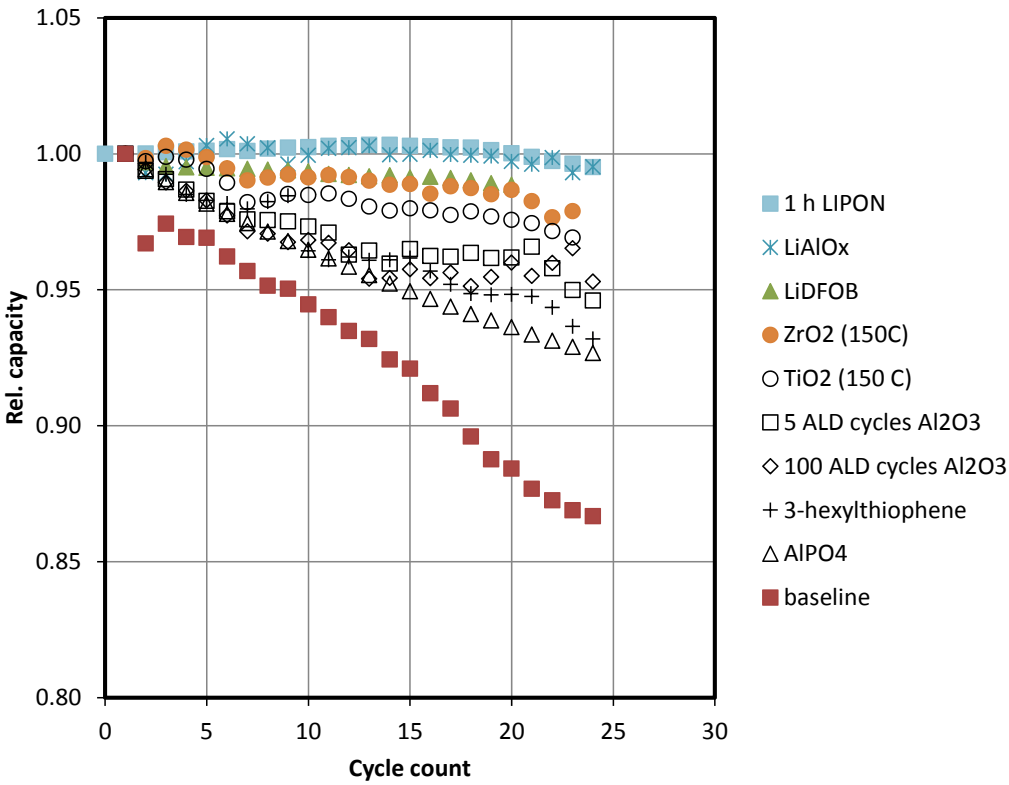

Figure V - 114: Rel. cell capacity vs. cycle count, showing capacity decline with cycle count. The capacity of coated materials tended to decline slower than that of uncoated materials. The relative cell capacity vs. cycle count for the 2- and 3-h LiPON coatings behaved similarly to that seen for the 1-h coating. These data were omitted for the sake of clarity

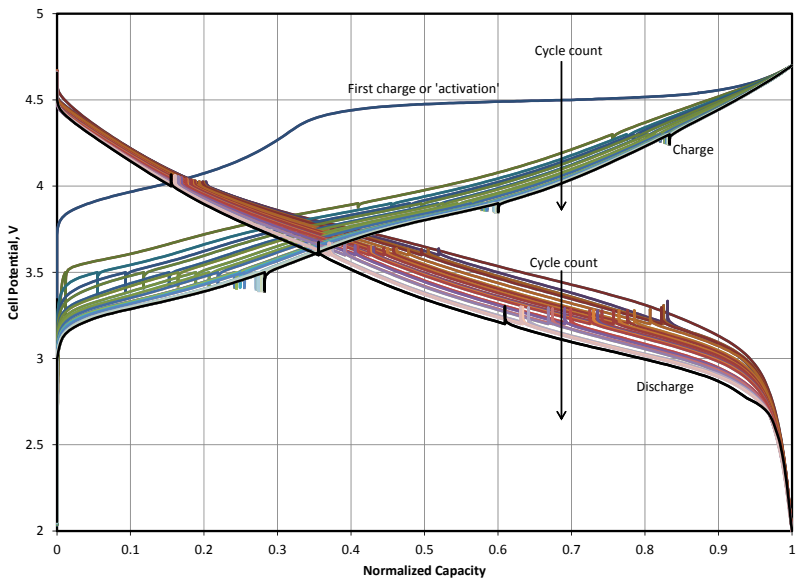

Figure V - 115: Cell potential vs. normalized capacity, representing the typical charge and discharge voltage response of a cell containing an uncoated cathode in these experiments. Selected curves were removed for the sake of clarity. During the first charge, the LMR NMC material was activated. With continued cycling, the voltage response for both the charge and discharge subcycles changed. The downward tick marks on the charge curves and upward tick marks on the discharge curves represent current interrupts

The iR-corrected, average voltage value for a given cycle was calculated using the data shown in Figure V - 116. A typical average voltage vs. cycle count plot is shown in Figure V - 117. The curves shown in Figure V - 117 closely follow the cell voltage behavior shown in Figure V - 116 for both charge and discharge. It should be noted that the shape of the average voltage curve was not sensitive to the presence of a coating or its nature, or to the presence of an electrolyte additive.

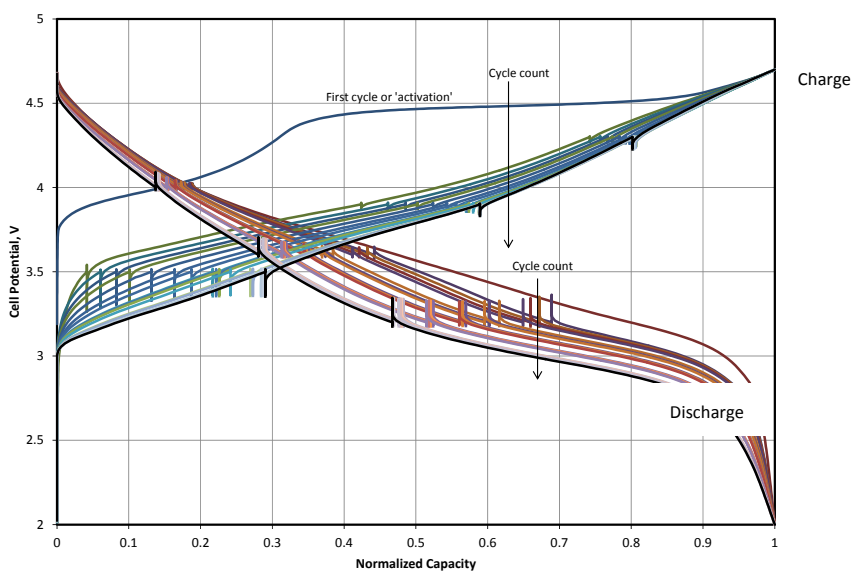

Figure V - 116: Cell potential vs. normalized capacity, representing the typical charge and discharge voltage response of a cell containing a coated cathode in these experiments. This particular cell contained a zirconia-coated cathode (150°C). Selected curves were removed for the sake of clarity. During the first charge, the LMR NMC material was activated. With continued cycling, the voltage response for both the charge and discharge subcycles changed. The downward tick marks on the charge curves and upward tick marks on the discharge curves represent current interrupts

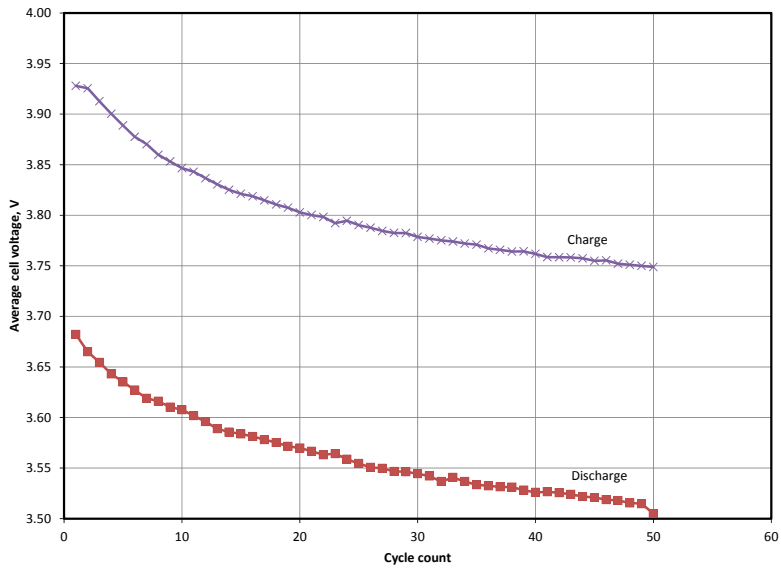

Figure V - 117: Typical plot of iR-corrected average cell voltage (Wh/Ah) vs. cycle count from a baseline cell, showing that, during both charge and discharge subcycles, the average cell voltage decreases with cycling. The first cycle was omitted from this plot

The relative change in average voltage for the cells is given in Table V - 11. In some cases, there was more than one cell for a given coating. This is indicated by the presence of a value for standard error (s.e.). Examining the values for the discharge subcycle shows that, after 20 cycles, most were within about 17% of the value given for the baseline material, and the value for LiPON (3 h) was almost twice that given for the baseline. The values given for the relative change in average voltage during the charge subcycle show a similar pattern after 20 cycles. Most values were within about 30% of the value given for the baseline, and that for LiPON(3 h) was twice that given for the baseline.

It is interesting to note that neither the thickness of the Al_2O_3 layer nor the deposition temperature of the TiO_2 and ZrO_2 layers had a significant effect on the relative change in the average voltage. The voltage loss from cathodes containing $LiAlO_x$ was approximately the same as those containing TiO_2 or ZrO_2 layers.

The data in Table V - 11 show that the values given for the 1-h and 2-h LiPON layers were outside the statistical range for the discharge subcycles and within the statistical range for the charge subcycles. The additional hour of sputtering time did not markedly change the voltage fade response characteristic. However, at 3 h, voltage fade increased by about a factor of 2 for both the charge and discharge subcycles, which was due to the increase in electronic resistance of the LiPON film surrounding the cathode particles [27, 28].

After 20 cycles, the values given for the $AlPO_4$ layer and the electrolyte additives are also outside the statistical range. The values for the electrolyte additives indicate that the average voltage decreased slightly less than the baseline. The value for $AlPO_4$ indicates that the average voltage decreased slightly more than the baseline. After 50 cycles, the values indicate a greater loss.

The central question underlying this work concerned the origin of voltage fade. That is, is the voltage fade phenomenon controlled by a reaction at the cathode-electrolyte interface? Theoretically, if voltage fade were caused by the loss of oxygen (e.g., during electrochemical activation [53]) or the loss of a soluble constituent, such as Mn^{2+}, changing the nature of the exposed cathode surface should change the rate at which the reaction proceeds by a significant amount.

In the literature [15-39, 44-46] and in this work, coatings and electrolyte additives were shown to be very effective in controlling capacity loss. The rates of these reactions displayed significant changes in the presence of an interface-modifying organic or inorganic material. However, the results in the present work indicate that using interface-modifying materials or additives had little-to-no effect on voltage fade. Under the cycling conditions used in these experiments, voltage fade appears to derive from an intrinsic property of the LMR-NMC materials, such as thermodynamic instability, and proceeds at a rate of a few millivolts per cycle [59]. Adjusting the cycling window was found to be one practical approach to reduce voltage fade [59, 60].

Table V - 11: Relative change in average voltage in baseline cells and in cells containing an electrolyte additive or a coated cathode

Coating/Additive	100 × Rel. Change in Average Voltage after 20 Cycles (100 × s.e.)	100 × Rel. Change in Average Voltage after 50 Cycles (100 × s.e.)
Discharge		
Baseline	3.14 (0.10)	4.81
3-hexylthiophene	2.88	4.52
LiDFOB	3.38	
Al_2O_3 (5 ALD cycles)	3.40	5.30
Al_2O_3 (100 ALD cycles)	3.22	5.47
$AlPO_4$	3.68	5.48
$LiAlO_x$	3.32 (0.07)	
TiO_2 (100°C)	3.14 (0.04)	
TiO_2 (150°C)	3.20 (0.07)	
ZrO_2 (100°C)	3.17 (0.01)	
ZrO_2 (150°C)	3.26 (0.03)	
LiPON (1 h)	2.69	
LiPON (2 h)	2.60	
LiPON (3 h)	5.20	
Charge		
Baseline	3.97 (0.49)	4.52
3-hexylthiophene	3.16	4.20
LiDFOB	4.89	
Al_2O_3 (5 ALD cycles)	3.52	5.15
Al_2O_3 (100 ALD cycles)	3.14	4.70
$AlPO_4$	3.66	5.03
$LiAlO_x$	5.21 (0.05)	
TiO_2 (100°C)	4.39 (0.01)	
TiO_2 (150°C)	4.60 (0.01)	
ZrO_2 (100°C)	4.62 (0.02)	
ZrO_2 (150°C)	4.85 (0.03)	
LiPON (1h)	3.67	
LiPON (2 h)	3.75	
LiPON (3 h)	7.97	

Conclusions and Future Directions

The effects of the coatings Al_2O_3, $LiAlO_x$, ZrO_2, TiO_2, $AlPO_4$, and LiPON and of the electrolyte additives 3-hexylthiophene and LiDFOB on the voltage fade phenomenon in $0.5Li_2MnO_3 \bullet 0.5LiNi_{0.375}Mn_{0375}Co_{0.25}O_2$ cathodes were investigated. Cells containing these materials were cycled according to a standard protocol at room temperature. As expected, the cells containing either an additive or a coated cathode displayed less capacity loss than cells containing an uncoated cathode and no additive. The voltage fade phenomenon was quantified in terms of the change in a resistance-corrected average cell voltage. The results indicate that, within experimental error, there was little-to-no effect on voltage fade from the coatings and additives, pointing to voltage fade being tied to the intrinsic nature of the cathode material. Thus, methods, other than coatings and additives, to control voltage should be tried.

FY 2013 Publications/Presentations

1. Ira Bloom, Lynn Trahey, Ali Abouimrane, Ilias Belharouak, Xiaofeng Zhang, Qingliu Wu, Wenquan Lu, Daniel P. Abraham, Martin Bettge, Jeffrey W. Elam, Xiangbo Meng, Anthony K. Burrell, Chunmei Ban , Robert Tenent, Jagjit Nanda and Nancy Dudney, J. Power Sources, *in press.*

References

1. Coatings team members: Ira Bloom, Lynn Trahey, Ali Abouimrane, Ilias Belharouak, Xiaofeng Zhang, Qingliu Wu, Wenquan Lu, Daniel P. Abraham, Martin Bettge, Jeffrey W. Elam, Xiangbo Meng, Anthony K. Burrell, Chunmei Ban, Robert Tenent, Jagjit Nanda and Nancy Dudney.
2. Battery Test Manual For Plug-In Hybrid Electric Vehicles, Rev. 1, June 2010, INL/EXT-07-12536.
3. Electric Vehicle Battery Test Procedures Manual,Rev. 2, June 1996.
4. B. Xu, D. Qian, Z. Wang, and Y. S. Meng, Mater. Sci. Eng. R, 73 (2012) 51–65.
5. J. Croy, K. Gallagher, M. Balasubramanian, Z. Chen, Y. Ren, S.-H. Kang, D. W. Dees, and M. M. Thackeray, J. Phys. Chem. C, DOI: 10.1021/jp312658q.
6. M. M. Thackeray, S.-H. Kang, C. S. Johnson, J. T. Vaughey, R. Benedek, and S. A. Hackney, J. Mater. Chem., 17 (2007) 3112–3125.
7. B. Xu, C. R. Fell, M. Chic, and Y. S. Meng, Energy Environ. Sci., 4 (2011) 2223.

8. A. R. Armstrong, N. Dupre, A. J. Paterson, C. P. Grey, and P. G. Bruce, Chem. Mater., 16 (2004) 3106–3118.
9. D. Mohanty, S. Kalnaus, R. A. Meisner , K. J. Rhodes, J. Li, E. A. Payzant, D. L. Wood III, and C. Daniel, J. Power Sources, 229 (2013) 239–248.
10. M. Gu, I. Belharouak, J. Zheng, H. Wu, J. Xiao, A. Genc, K. Amine, and C. Wang, ACS Nano, 7 (2012) 760–767.
11. B. Xu, C. R. Fell, M. Chic, and Y. S. Meng, Energy Environ. Sci., 4 (2011) 2223.
12. A. R. Armstrong, N. Dupre, A. J. Paterson, C. P. Grey, and P. G. Bruce, Chem. Mater., 16 (2004) 3106–3118.
13. D. Mohanty, S. Kalnaus, R. A. Meisner , K. J. Rhodes, J. Li, E. A. Payzant, D. L. Wood III, and C. Daniel, J. Power Sources, 229 (2013) 239–248.
14. M. Gu, I. Belharouak, J. Zheng, H. Wu, J. Xiao, A. Genc, K. Amine, and C. Wang, ACS Nano, 7 (2012) 760–767.
15. J. Liu, Z. Chen, S. Busking, I. Belharouak, and K. Amine, J. Power Sources, 174 (2007) 852–855.
16. S. S. Zhang, J. Power Sources, 162 (2006) 1379–1394.
17. Y. Kim, N. J. Dudney, M. Chi, S. K. Martha, J. Nanda, G. M. Veith, and C. Liang, J. Electrochem. Soc., 160 (2013) A3113–A3125.
18. S. K. Martha, J. Nanda, Y. Kim, R. R. Unocic, S. Pannala, and N. J. Dudney, J. Mater. Chem. A, DOI: 10.1039/c3ta10586e.
19. D. Guan and Y. Wang, Ionics, 19 (2013) 1–8.
20. J.-H. Kim, M.-S. Park, J.-H. Song, D.-J. Byun, Y.-J. Kim, and J.-S. Kim, J. Alloys and Compounds, 517 (2012) 20–25.
21. H.-J. Kweon, S. J. Kim, and D. G. Park, J. Power Sources, 88 (2000) 255–261.
22. M. Mladenov, R. Stoyanova, E. Zhecheva, and S. Vassilev, Electrochem. Comm., 3 (2001) 410–416.
23. L. A. Riley, S. Van Atta, A. S. Cavanagh, Y. Yan, S. M. George, P. Liu, A. C. Dillon, and S.-H. Lee, J. Power Sources, 196 (2011) 3317–3324.
24. E.-G. Shim, T.-H. Nam, J.-G. Kim, H.-S. Kim, and S.-I. Moon, J. Power Sources, 172 (2007) 901–907.
25. W. C. West, J. Soler, M. C. Smart, B. V. Ratnakumar, S. Firdosy, V. Ravi, M. S. Anderson, J. Hrbacek, E. S. Lee, and A. Manthiram, J. Electrochem. Soc., 158 (2011) A883–A889.
26. F. Wu, M. Wang, Y. Su, S. Chen, and B. Xu, J. Power Sources, 191 (2009) 628–632.
27. R. Guo, P. Shi, X. Cheng, and L. Sun, Electrochimica Acta, 54 (2009) 5796–5803.
28. J. Liu and A. Manthiram, J. Mater. Chem., 20 (2010) 3961–3967.
29. J. Ni, L. Gao, and L. Lu, J. Power Sources, 221 (2013) 35–41.
30. F. Wu, M. Wang, Y. Su, L. Bao, and S. Chen, Electrochimica Acta, 54 (2009) 6803–6807.
31. L. Yang and B. L. Lucht, Electrochem. Sol. State Letters, 12 (2009) A229–A231.
32. H. Zhao, L. Gao,W. Qiu, and X. Zhang, J. Power Sources, 132 (2004) 195–200.
33. A. Abouimrane, S. A. Odom, H. Tavassol, M. V. Schulmerich, H. Wu, R. Bhargava, A. A. Gewirth, J. S. Moore, and K. Amine, J. Electrochem. Soc., 160 (2013) A268–A271.
34. J. C. Burns, N. N. Sinha, D. J. Coyle, G. Jain, C. M. VanElzen, W. M. Lamanna, A. Xiao, E. Scott, J. P. Gardner, and J. R. Dahn, J. Electrochem. Soc., 159 (2012) A85–A90.
35. Z. Chen and J. R. Dahn, Electrochem. Sol. State Letters, 5 (2002) A213–A216.
36. S.-K. Hu, G.-H. Cheng, M.-Y. Cheng, B.-J. Hwang, and R. Santhanam, J. Power Sources, 188 (2009) 564–569.
37. A. M. Kannan and A. Manthiram, Electrochem. Sol. State Letters, 5 (2002) A167–A169.
38. T. Liu, S.-X. Zhao, K. Wang, and C.-W. Nan, Electrochimica Acta, 85 (2012) 605–611.
39. Q. Wu, W. Lu, M. Miranda, T. K. Honaker-Schroeder, K. Y. Lakhsassi, and D. Dees, Electrochem. Comm., 24 (2012) 78–81.
40. J. Cho, T. G. Kim, C. Kim, J.-G. Lee, Y.-W. Kim, and B. Park, J. Power Sources, 146 (2004) 58–64.
41. Y. Wu, A.V. Murugan, and A. Manthiram, J. Electrochem Soc., 155 (2008) A635–A641.
42. E. Jung and Y.-J. Park, Nanoscale Research Letters, 7 (2012) 1–4.
43. J. Wang., Y. Wang, Y. Guo, Z. Ren, and C. Liu, J. Mater. Chem. A, 1 (2013) 4879–4884.
44. M. Bettge, Y. Li, B. Sankaran, N. Dietz Rago, T. Spila, R. T. Haasch, I. Petrov, and D. P. Abraham, J. Power Sources, 233 (2013) 346–357.
45. Y. Zhu, Y. Li, M. Bettge, and D. P. Abraham, J. Electrochem. Soc., 159 (2012) A2109–A2117.
46. Y. Zhu, Y. Li, M. Bettge, and D. P. Abraham, Electrochim. Acta – in press, http://dx.doi.org/10.1016/j.electacta.2013.03.102.
47. A. Abouimrane, O. C. Compton, H. Deng, I. Belharouak, D. A. Dikin, S-B. T. Nguyen, and K. Amine, Electrochemical and Solid-State Letters, 14(9) (2011) 126.

48. Y.-H. Cho, K. Kim, S. Ahn, H. K. Liu, J. Power Sources, 196 (2011) 1483–1487.
49. C.-C. Chang, K.-Y. Lee, H.-Y. Lee, Y.-H. Su, and L.-J. Her, J. Power Sources, 217 (2012) 524–529.
50. C. Li, H. P. Zhang, L. J. Fu, H. Liu, Y. P. Wu, E. Rahm, R. Holze, and H. Q. Wu, Electrochimica Acta, 51 (2006) 3872–3883.
51. S. Santee, A. Xiao, L. Yang, J. Gnanaraj, and B. L. Lucht, J. Power Sources, 194 (2009) 1053–1060.
52. Y. Iriyama, H. Kurita, I. Yamada, T. Abe, and Z. Ogumi, J. Power Sources, 137 (2004) 111–116.
53. C. Li, H. P. Zhang, L. J. Fu, H. Liu, Y. P. Wu, E. Rahm, R. Holze, and H. Q. Wu, Electrochimica Acta, 51 (2006) 3872–3883.
54. M. Bettge, Y. Li, B. Sankaran, N. Dietz Rago, T. Spila, R. T. Haasch, I. Petrov, and D. P. Abraham, J. Power Sources, 233 (2013) 346–357.
55. S. M. George, O. Sneh, A. C. Dillon, M. L. Wise, A. W. Ott, L. A. Okada, and J. D. Way, Appl. Surf. Sci., 82-3 (1994) 460.
56. Y. S. Jung, A. S. Cavanagh, A. C. Dillon, M. D. Groner, S. M. George, and S. H. Lee, J. Electrochem. Soc., 157 (2010) A75.
57. Y. S. Jung, A. S. Cavanagh, L. A. Riley, S. H. Kang, A. C. Dillon, M. D. Groner, S. M. George, and S. H. Lee, Adv. Mater., 22 (2010) 2172.
58. A. Rahtu and M. Ritala, Chemical Vapor Deposition, 8 (2002) 21.
59. M. Bettge, Y. Li, K. Gallagher, Y. Zhu, Q.Wu, W. Lu, I. Bloom, and D. P. Abraham, J. Electrochem. Soc., 160 (2013) A2046-A2055 .
60. K. G. Gallagher, J. R. Croy, M. Balasubramanian, M. Bettge, D. P. Abraham, A. K. Burrell, and M. M. Thackeray, Electrochem. Comm. 33 (2013) 96–98

V.D Materials Optimization

V.D.1 High Voltage Electrolytes for Li-ion Batteries (ARL)

Arthur von Wald Cresce, Kang Xu
Jan Allen, Oleg Borodin, Samuel Delp,
Joshua Allen, Richard Jow

Point of Contact:
T. Richard Jow / Kang Xu
U.S. Army Research Laboratory
2800 Powder Mill Road
Adelphi, MD 20783
Phone: (301) 394-0340 / (301) 394-0321
Fax: (301) 394-0273
E-mail: t.r.jow.civ@mail.mil / conrad.k.xu.civ@mail.mil

Start Date: March 2009
Projected End Date: September 2013

Objectives

- Develop high voltage electrolytes that enable the operation of 5 V Li-ion batteries.
  - Understand the surface chemistry at the high voltage cathode and electrolyte interface.

Technical Barriers

This project addresses the following technical barriers of today's Li-ion batteries:

- SOA electrolytes do not support chemistries beyond 4.5 V.
- Although new electrolyte solvents, such as sulfones and nitriles, remain stable at high voltages on the cathode, they fail to simultaneously cater to the anode SEI formation.
- Replacing SOA carbonates with highly fluorinated solvents drives up the overall cost.
- Lack of reliable 5 V cathodes as testing vehicles for electrolyte development.

Technical Targets

- Design and synthesize new electrolyte additives that target the interphasial chemistry on high voltage cathode surfaces.
- Understand the mechanism of interphase formation on high voltage cathode surfaces.
- Evaluate the additives containing electrolytes using 4.7 V $LiNi_{0.5}Mn_{1.5}O_4$ (LNMO) and 4.8 V $LiCoPO_4$ (LCP) as testing vehicles.

Accomplishments

- Designed, synthesized and scaled-up lithium perfluorinated butoxide (LiPFBO) additive. The effectiveness of LiPFBO has been demonstrated in LNMO/graphite cells.
- Identified additive A2 that is effective in enabling the cycling of LNMO/graphite cells at 55°C with high coulombic efficiency and capacity retention.
- Successfully improved capacity utilization, rate performance and coulombic efficiency of LFCP through new generation of substitution without relying high voltage electrolytes.
- Calculated how oxidative stability of electrolyte solvents changed with the presence of anion, other solvent molecules and their combinations using DFT.
- Studied SEI components and SEI-electrolyte interactions using MD simulations.

✧ ✧ ✧ ✧ ✧

Introduction

In order for 5 V class cathode chemistries such as LMNO and LCP to be used for HEV/PHEV/EV applications, electrolytes must maintain kinetic stability beyond 4.5 V. Despite the developments of new electrolyte solvents that were claimed to be able to support the above chemistries, the accompanying intrinsic weaknesses often make the effort impractical, such as the instability of sulfone and nitriles on graphitic anode, or the high cost of highly-fluorinated co-solvents FEC or FPC. We believe that by using properly-designed electrolyte additives the above intrinsic weaknesses could be circumvented, as our previous work on tris(hexafluoro-iso-propyl)phosphate (HFiP) demonstrated.

This year's work focused on further confirmation of HFiP on different cathode chemistries, surface analysis of these cathodes for understanding the HFiP

breakdown mechanism, as well as design and synthesis of new additives with perfected structures. Computational assistance was also employed to understand the thermodynamic oxidation of these new additives.

Approach

Design new additives and identify additives enabling the 5 V operations of Li-ion batteries using an understanding of the interfacial reactions at the cathode/electrolyte interfaces. – Electrochemical methods, surface analysis including XPS, and computational methods are used to understand the interfacial reactions and develop effective electrolyte additives.

Develop structurally stabilized with less reactive surfaces high voltage cathodes. – The approach of partially substituting the transition metal in high voltage cathodes with other elements is adopted. This development is in concert with the electrolyte additives development.

Results

Design, synthesis and evaluation of new additives (Arthur v. Cresce, Kang Xu).

The new additive, *lithium perfluoro-t-butoxide* (LiPFBO),whose structure is seen in Figure V - 118, was successfully scaled-up utilizing the Argonne National Laboratory's facilities. This was a key step in using the compound as an additive. Perfluoro-t-butoxide is an additive for high-voltage Li-ion electrolytes that effectively improves Coulombic cycling efficiency, as confirmed by Jeff Dahn at Dalhousie University, and shows promise as a low and high temperature additive as well. We are in the process of synthesizing several additives that contain the perfluoro-t-butyl and hexafluoroisopropyl moieties to expand upon work already performed on phosphate-based versions of these compounds. The goal is twofold: to react with the oxidizing cathode surface with the goal of stabilizing the electrolyte-cathode interface, and to improve SEI properties on the graphite anode by limiting the excess growth of SEI material. Current work is therefore focusing on the directed development of new additives that either can deliver fluorinated moieties to the electrode surfaces, or can perform similar functions.

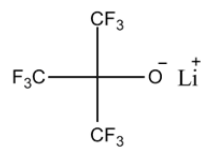

Figure V - 118: Lithium perfluoro-t-butoxide (LiPFBO) structure

The performance of the butoxide additive was noted by Jeff Dahn of Dalhousie University using high-precision coulometry, as seen in Figure V - 119, compared to other ARL additives and a control:

What the Dalhousie results indicate is that the butoxide (blue dots) effectively increases the retention of discharge capacity (although without a large number of cycles). Evolution of high CE is slow compared to a standard electrolyte control but ultimately exceeds the control. Low temperature tests have been performed but have not yet been disclosed.

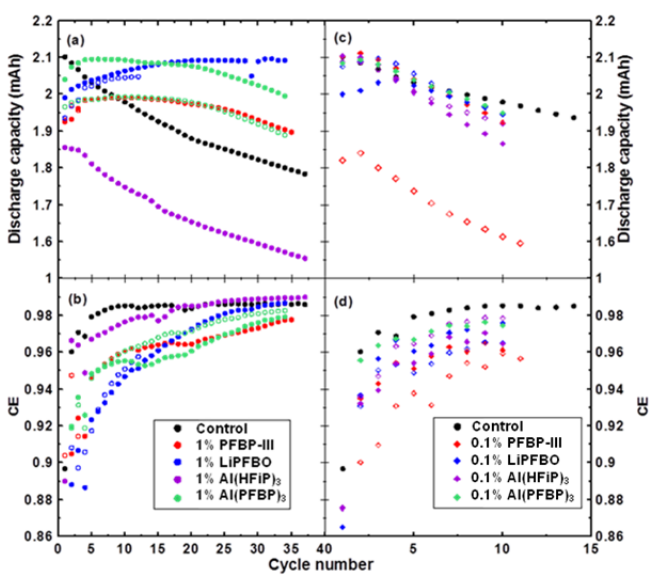

Figure V - 119: Discharge capacity and CE of LNMO / graphite cells cycled in control electrolyte (or Gen 2 electrolytes) with and without additives at 25°C

Impact of Additives on Cycling of LNMO/A12 at 55°C (Samuel Delp, Jan Allen, Richard Jow).

The cycling of LNMO at 55°C remains challenging. The LNMO/A12 full cells were tested at 25°C and 55°C to study the effectiveness of various additives including HFiP, VC and A2 on capacity retention. Both LNMO and A12 (graphite) were provided by ANL. The baseline electrolyte (or Gen 2 electrolyte) is 1.2 M $LiPF_6$ in EC:EMC (3:7).

As shown in Figure V - 120, the effectiveness of A2 additive has been demonstrated in capacity retention, CE, and capacity utilization for the LNMO/graphite full cells.

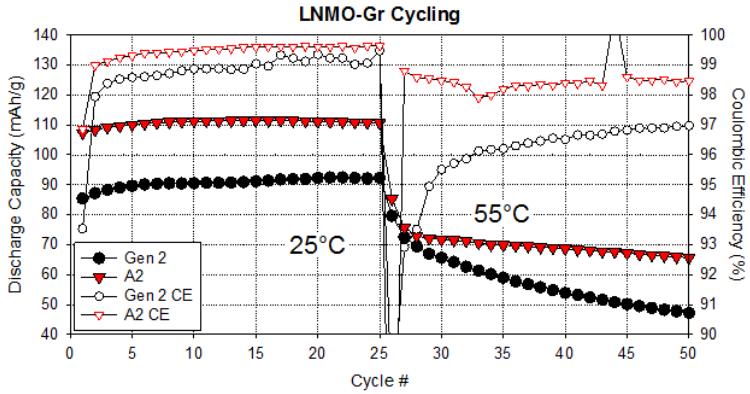

Figure V - 120: C/3 cycling data with capacity retention and CE for Gen 2 electrolyte without and with A2 additive. The first 25 cycles are at 25°C and the next 25 cycles are at 55°C

The effectiveness of A2 additive can also be demonstrated through the dQ/dV vs. V plots as shown in Figure V - 121. The plots were acquired using a C/3 cycling rate. The red line is for the 25th cycle at 25°C. The orange line is the next cycle (cycle 26) but the cells were moved to 55°C before this cycle. The yellow-green line is for the 25th cycle at 55°C (50th overall cycle). The electrolyte with A2 additive retains the overall peak shapes better than the baseline (Gen 2) electrolyte, specifically having a higher voltage on the discharge (bottom portion of curve) indicating faster kinetics/less resistance in the cells.

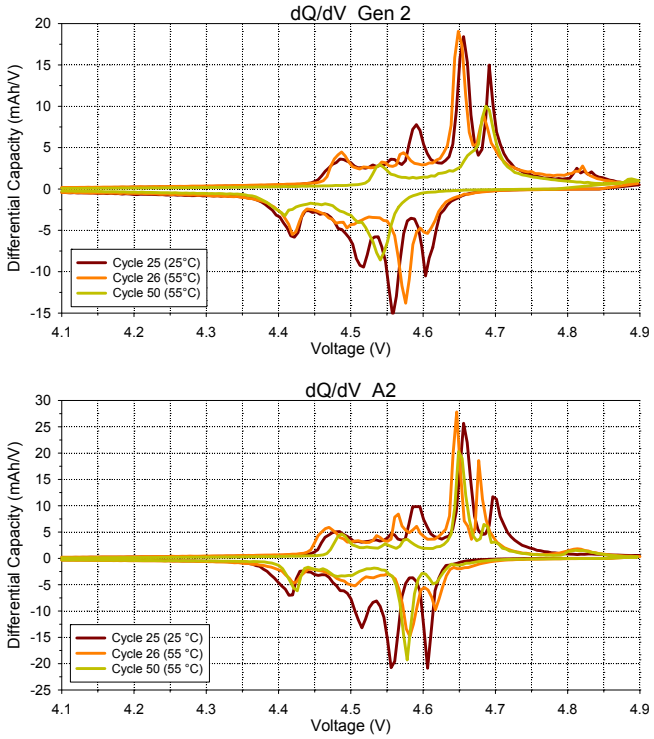

Figure V - 121: dQ/dV versus V plots for LNMO/graphite cells at 25°C and 55°C in Gen 2 electrolyte with and without A2 additive

Cycling of Modified LCP High Voltage Cathode (Jan Allen, Joshua Allen, Samuel Delp, Richard Jow).

Doping LCP has been demonstrated by our lab as a viable means for improving the cathode performance. Most notably, Fe-doping has been shown to greatly improve the cycle life of LCP and yielded half cells able to cycle in excess of 500 cycles when paired with a high voltage additive. Standard LFCP (mixed lithium iron and cobalt phosphate material), however, yields only ~110 mAh g^{-1} discharge capacity and a poor efficiency when cycled with the standard electrolyte (e.g., 1m $LiPF_6$ in EC:EMC, 3:7 w/w). Rather than modifying the electrolyte composition to stabilize the cathode surface, the cathode composition itself was modified to improve the overall cathode stability. By modifying the LCP-based cathode, a significant capacity increase was observed and an efficiency of >99.45% was observed after 100 cycles (see Figure V - 122 and Figure V - 123). This chemistry is being further tuned, as well as the electrolyte composition, to yield an optimized system.

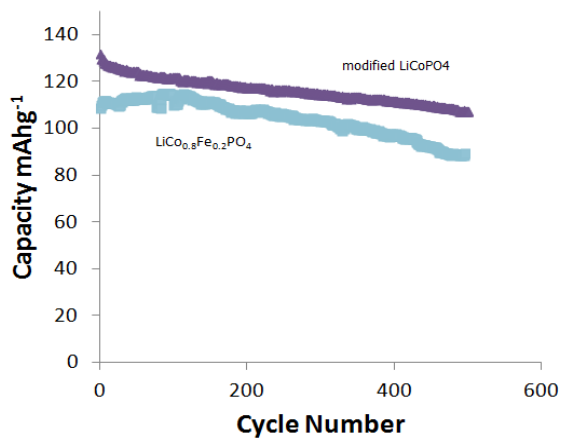

Figure V - 122: Capacity retention of standard LFCP and modified LCP cathodes cycled against Li in standard Gen 2 electrolyte at 25°C

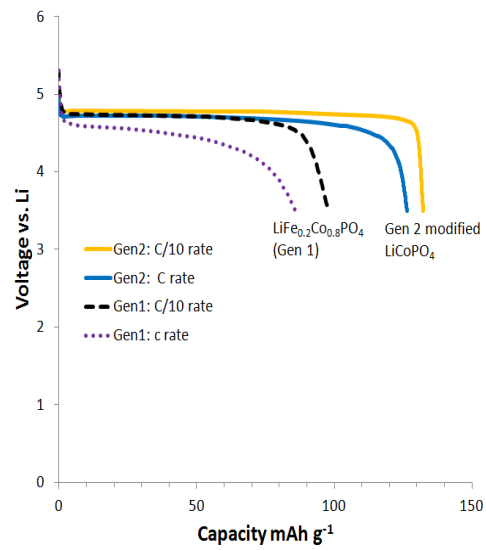

Figure V - 123: Comparisons of rate performance of Gen 1 LFCP cathode and Gen 2 modified LCP electrode in the standard electrolyte

Quantum Chemistry Studies of Electrolyte Oxidation Stability and Decomposition Reactions (Oleg Borodin, Richard Jow).

Oxidation stability and initial decomposition reactions were studied for a wide range of solvent/anion and solvent dimer complexes (carbonates, sulfones, phosphates). The quantum chemistry (QC) predictions [1] of the exothermic proton abstraction occurring in linear and cyclic carbonates such as DMC and EC were subsequently confirmed by radiolytic ionization experiments performed at ANL [2]. Our QC studies indicated that the cluster approach to understanding electrolyte oxidation stability yields a distribution of oxidation stabilities associated with the cluster composition [1, 3]. For example, the oxidation stability of model electrolyte complexes follows the order: $EC_4/BF_4^- < EC_n$ (n=2,3,4) < $EC/BF_4^- < EC/PF_6^-$ < isolated EC [1]. The oxidation stability was found to be rate dependent. At low rates (high barriers) oxidation stability of theEC_n/BF_4^- and EC_n/PF_6^- complexes was predicted around 5 V vs. Li^+/Li, thus, indicating that the oxidation stability of dilute EC-$LiPF_6$ and EC-$LiBF_4$ electrolytes is predicted to be around 5 V even for non-active electrodes. The oxidation-induced electrolyte decomposition reactions were predicted using DFT calculations.[1] The predicted decomposition products were found in good agreement with experimental data.

The influence of salt concentration on the EC-LiTFSI electrolyte oxidation stability was investigated using DFT and compared with experimental data performed by collaborators from NCSU [4]. Only a slight (<0.4 V) increase of the electrolyte oxidation stability was observed when nearly all solvents/anions were complexed by a Li^+ cation at high salt

concentration. MD simulations combined with experiments (NCSU) also provided insight into the salt concentration dependence of the mechanism of Al current collector corrosion by EC/LiTFSI electrolyte [4].

Modeling the SEI and SEI-Electrolyte Interface (Oleg Borodin, Kang Xu).

Initial molecular dynamics (MD) simulations of dilithium ethylene carbonate (Li_2EDC) SEI component [5] were extended to the Li_2EDC-LiF melts and Li_2EDC – carbonate electrolyte interfaces. A snapshot of the simulated system is shown in Figure V - 124. The smectic-like ordered Li_2EDC was used in these simulations.

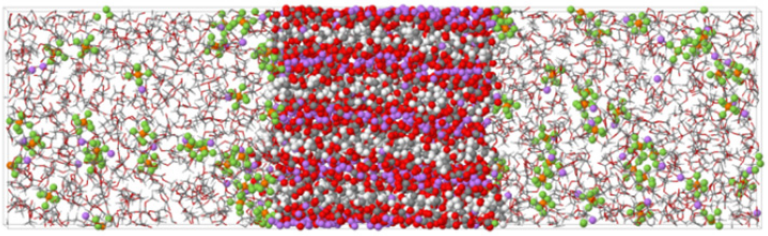

Figure V - 124: A simulation snapshot showing ordered Li_2EDC in contact with the electrolyte. Solvent molecules are shown as wireframe, while Li_2EDC and $LiPF_6$ are highlighted using a ball and stick model

Many-body polarizable force field APPLE&P was used in simulations. Examination of the SEI-electrolyte interface revealed an enrichment of EC and PF_6^- at the SEI surface and depletion of DMC compared to bulk electrolyte concentrations. The process of the Li^+ desolvation from electrolyte was examined with more than 80 of desolvation events occurring at the simulation timescale 300 ns for Li_2EDC-electrolyte at 393 K. During the initial desolvation step, a Li^+ cation showed a preference to shed DMC in a significantly faster rate than losing EC or PF_6^-. The rate of the Li^+ desolvation reaction was estimated from these preliminary simulations. The activation energy for the Li^+ desolvation process was predicted to be ~50 kJ/mol assuming the Arrhenius process. The activation energy for the desolvation reaction is lower than the activation energy for the Li^+ conduction in bulk Li_2EDC (64 kJ/mol) likely due to plasticizing effect of electrolyte on the dynamics of the interfacial SEI layer. The activation energy is, however, similar to the previously experimentally determined activation energy for the Li^+ desolvation from the EC:DMC-based electrolytes into lithiated spinel titanate ($Li_4Ti_5O_{12}$) of 50-52 kJ/mol, but lower than the previously reported activation energy for the desolvation into SEI covered graphite of 60-70 kJ/mol.

Conclusions and Future Directions

ARL has synthesized new additive LiPFBO that improves the capacity retention and coulombic efficiency (CE) of the LNMO high voltage cathode. ARL has also identified an additive A2 that is effective in enabling the cycling of LNMO/graphite cells at 55°C with high CE and capacity retention. With standard electrolyte, LCP based cathode can be cycled with improved capacity, rate and CE through new generation of modified LCP. This suggests that thedevelopment of high voltage Li-ion batteries will rely on improvements to both the electrolytes and the cathodes. Further understanding of the stability and reactivity between these components are critical for future development. Quantum chemistry methodologies will be utilized for high-throughput screening of oxidation stability and initial decomposition reactions occurring in electrolyte components assisting in the design of electrolytes.

References

1. Borodin, O.; Behl, W.; Jow, T. R., Oxidative Stability and Initial Decomposition Reactions of Carbonate, Sulfone, and Alkyl Phosphate-Based Electrolytes. *J. Phys. Chem. C*, 2013, 117, 8661-8682.
2. Shkrob, I. A.; Zhu, Y.; Marin, T. W.; Abraham, D. P., Reduction of Carbonate Electrolytes and the Formation of Solid-Electrolyte Interface (SEI) in Lithium Ion Batteries. 1. Spectroscopic Observations of Radical Intermediates Generated in One-Electron Reduction of Carbonates. *J. Phys. Chem. C*, 2013, 10.1021/jp406274e.
3. Borodin, O.; Jow, T. R., Quantum Chemistry Study of the Oxidation-Induced Decomposition of Tetramethylene Sulfone (TMS) Dimer and TMS/BF4–. *ECS Transactions*, 2013, 50, 391-398.
4. McOwen, D. W.; Seo, D. M.; Borodin, O.; Vatamanu, J.; Boyle, P. D.; Henderson, W. A., Concentrated Electrolytes: Decrypting Electrolyte Properties and Reassessing Al Corrosion Mechanisms. *Energy & Environmental Science* 2014, 7, 410-426.

5. Borodin, O.; Zhuang, G. V.; Ross, P. N.; Xu, K., Molecular Dynamics Simulations and Experimental Study of Lithium Ion Transport in Dilithium Ethylene Dicarbonate. *J. Phys. Chem. C* 2013, 117, 7433-7444.

FY 2013 Publications

1. Understanding Li+ - solvent interaction in nonaqueous carbonate electrolytes with 17O NMR. Xavier Bogle, Rafael Vazquez, Steven Greenbaum, Arthur Cresce, Kang Xu, *J. Phys. Chem. Lett.*, 2013, 4, 1664-1668.
2. Analysis of the thickness and composition of the solid electrolyte interphase layer formed on lithium-ion battery graphite anodes. Arthur Cresce, Selena Russell, David Baker, Karen Gaskell, Kang Xu, *ACS Nano Letters*, submitted, December 2013.
3. Dual-graphite chemistry enabled by a high-voltage electrolyte. Jeffrey Read, Matthew Ervin, Kang Xu, Arthur Cresce. *Energy & Environmental Science*, accepted 19 November 2013.
4. Oxidative Stability and Initial Decomposition Reactions of Carbonate, Sulfone and Alkyl Phospate-Based Electrolytes, Borodin*, O.; Behl, W.; Jow. T. R. *J. Phys. Chem. C.* 2013, 117, 8661–8682.
5. Molecular Dynamics Simulations and Experimental Study of Lithium Transport in Dilithium Ethylene Dicarbonate, Borodin*, O.; Zhuang, V.; Ross, P. N.; Xu, K., *J. Phys. Chem. C* 2013, 117, 7433-7444.
6. Concentrated electrolytes: Decrypting electrolyte properties and reassessing Al corrosion mechanisms, McOwen, D. W.; Seo, D. M.; Borodin, O.; Vatamanu, J. ; Boyle, P. D.; Henderson, W. A., *Energy and Env. Sci.* 2014, 7, 410-426.
7. Quantum Chemistry Study of the Oxidation-Induced Stability and Decomposition of Propylene Carbonate-Containing Complexes, Wang, Y., Xing, L.; Borodin, O.; Huang, W.; Xu, M.; Li, X.; Li, W., *Phys. Chem. Chem. Phys*. (in press)
8. Lithium Battery Electrolyte Stability and Performance from Molecular Modeling and Simulations. Smith, G.; Borodin, O., in *Batteries for Sustainability*, Brodd, R. J., Ed. Springer New York: 2013; pp 195-23. ISBN 978-0-387-89469-0.
9. Quantum Chemistry Study of the Oxidation-Induced Decomposition of Tetramethylene Sulfone (TMS) Dimer and TMS/BF4-, Borodin, O.; Jow, T. R. (invited) , *ECS Transactions*, 2013, 50, 391-398.
10. Transport Properties of $LiCoPO_4$ and Fe-substituted $LiCoPO_4$, Jan L. Allen, Travis Thompson, Jeff Sakamoto, Collin R. Becker, T. Richard Jow and Jeff Wolfenstine*, J. Power Sources*, submitted.

FY 2013 Presentations

1. Interphases on Graphitic Anodes in Li-Ion Battery. Selena Russell, David Baker, Arthur Cresce, Kang Xu. Pacific Rim American Chemical Society Meeting, June 5, 2013.
2. Effect of anion-solvent interaction on the anodic stability of electrolytes in batteries. Selena Russell, Emily Wikner, Arthur Cresce, Kang Xu. The Electrochemical Society Fall 2013 meeting, Oct. 29, 2013.
3. *In situ* analyses on solid electrolyte interphases in Li-ion batteries. Selena Russell, Arthur Cresce, David Baker, Kang Xu. *The Electrochemical Society Fall 2013 meeting*, Oct. 29, 2013.
4. Effect of electrolyte additives on SEI properties in Li-ion batteries as analyzed by *in situ* AFM. *American Chemical Society Meeting*, 28 September 2013.
5. Investigation of Electrolyte Interaction with High Voltage Li-Ion Battery Cathodes, Samuel A Delp, Jan L Allen, T Richard Jow, *224th Meeting of the Electrochem. Soc.* San Francisco, California, October 27-31, 2013.
6. Substituted LiCoPO4 as Li-ion Cathode, Jan L Allen, Samuel A Delp, *224th Meeting of the Electrochem. Soc*. San Francisco, California, October 27-31, 2013.
7. Oxidation-Induced Decomposition of Electrolytes and Additives From Quantum Chemistry calculations, Oleg Borodin, Samuel A Delp, T Richard Jow , *224th Meeting of the Electrochem. Soc.* San Francisco, California, October 27-31, 2013.

FY 2013 Patent Applications

1. High Voltage Lithium Ion Positive Electrode Compositions, Jan L. Allen, Joshua L. Allen, Samuel A. Delp III, Jeff Wolfenstine, T. Richard Jow, *Provisional Patent 61911700* filed.

V.D.2 Development of Novel Electrolytes for Use in High Energy Li-ion Batteries with Wide Operating Temperature Range (JPL)

Marshall C. Smart

Electrochemical Technologies Group
Power and Sensor Systems Section
Jet Propulsion Laboratory
California Institute of Technology
4800 Oak Grove Drive, M/S 277-207
Pasadena, CA 91109-8099
Phone: (818) 354-9374; Fax: (818) 393-6951
E-mail: Marshall.C.Smart@jpl.nasa.gov

Start Date: October 1, 2009
Projected End Date: September 30, 2014

Objectives

- Develop a number of advanced Li-ion battery electrolytes with improved performance over a wide range of temperatures (-30° to +60°C) with projected long-life characteristics (5,000 cycles over 10-yr life span).
- Improve the high voltage stability of these candidate electrolyte systems to enable operation up to 5V with high specific energy cathode materials.
- Define the performance limitations at low and high temperature extremes, as well as life-limiting processes.
- Demonstrate the performance of advanced electrolytes in large capacity prototype cells.

Technical Barriers

This project addresses the following technical barriers associated with the development of PHEVs:

- 750 W/kg (10 mile) and 316 W/kg (40 mile).
- Cold cranking capability to -30°C.
- Cycle life: 5,000 cycles (10 and 40 mile PHEVs).
- Calendar life: 15 years (at 35°C).

Technical Targets

- Demonstrate improved performance of experimental and prototype cells with next generation electrolytes over a wide temperature range (-30° to +60°C) compared with baseline electrolytes.

Prepare and characterize experimental laboratory cells containing advanced electrolytes, which are designed to operate over a wide temperature range and in high-voltage systems (i.e., $LiNiMnCoO_2$), and identify performance-limiting characteristics.

Accomplishments

- Demonstrated good preservation of the low temperature performance (down to -50°C) of prototype 12 Ah cells (manufactured by Quallion) containing JPL-developed methyl propionate-based electrolytes that have been subjected to life testing. The use of mono-fluoroethylene carbonate (FEC) was observed to impede the capacity degradation.
- A methyl propionate-based electrolyte was observed to result in a five-fold improvement in the discharge capacity delivered with prototype NCA-based cells at very high discharge rates (20C) at low temperature (-20°C) compared with a baseline all carbonate-based electrolyte.
- Excellent cycle life performance has been demonstrated with methyl propionate-based wide operating temperature range electrolytes in NCA-based cells at 20°C, with an electrolyte consisting of 1.2M $LiPF_6$ in FEC+EMC+MP providing the best performance, outperforming the DOE baseline electrolyte.
- Demonstrated excellent cycle life performance (over 9,500 full depth-of-discharge cycles) with wide operating temperature electrolytes containing methyl butyrate in A123 $LiFePO_4$-based prototype (26650) cells. These cells have previously been demonstrated to have operational capability over a wide temperature range (-60° to +60°C), including the ability to support high rate discharge at low temperatures (i.e., >11C discharge rates at -30°C).
- Investigated the use of methyl butyrate-based electrolytes containing various additives in the graphite/high voltage NMC system in experimental and coin cells. An electrolyte consisting of $LiPF_6$ in EC+EMC+MB possessing LiDFOB as an electrolyte additive has been observed to provide the best low temperature performance of the electrolytes investigated.

✧ ✧ ✧ ✧ ✧

Introduction

JPL is working to develop electrolytes that enable the operation of Li-ion cells over a wide temperature range, while still providing the desired life characteristics and resilience to high temperature (and voltage). To meet the objectives, the electrolyte development includes the following general approaches: (1) optimization of carbonate solvent blends, (2) use of low viscosity, low melting ester-based co-solvents, (3) use of fluorinated esters and fluorinated carbonates as co-solvents, (4) use of "SEI promoting" and thermal stabilizing additives, and the (5) use of novel non-fluorine based salts. Many of these approaches will be used in conjunction in multi-component electrolyte formulations (i.e., such as the use of low viscosity solvents and novel additives and salts), which will be targeted at improved operating temperature ranges while still providing good life characteristics.

Approach

In the process of developing improved electrolyte formulations, they are characterized using a number of approaches, including performing ionic conductivity and cyclic voltammetry measurements, and evaluating their performance in coin cells as well as larger ~ 400 mAh three-electrode cells equipped with reference electrodes. Initial characterization is typically performed using state-of-art electrode couples, such as (a) MCMB /$LiNi_{0.8}Co_{0.2}O_2$ (a) MCMB /$LiNi_{0.8}Co_{0.15}Al_{0.05}O_2$, or (c) graphite/$LiNi_{1/3}Co_{1/3}Mn_{1/3}O_2$. More recent work has been extended to the high capacity, lithium excess mixed NMC-based cathode materials. In addition to performing charge/discharge characterization over a wide range of temperatures and rates on these cells, a number of electrochemical characterization techniques are employed, including: (1) Electrochemical Impedance Spectroscopy (EIS), (2) DC linear (micro) polarization, and (3) Tafel polarization measurements. The electrochemical evaluation in three-electrode test cells enables the electrochemical characterization of each electrode (and interface) and the identification of performance-limiting mechanisms. Electrodes are easily harvested from these test cells and samples are delivered to collaborators (i.e., URI and Hunter College). In addition to evaluating candidate electrolytes in spirally wound experimental cells, initial screening studies are also performed in coin cells, most notably in conjunction with high voltage cathode materials.

Results

Electrolytes Demonstrated in NCA-Based Systems. During the past year, we continued to evaluate the performance of large capacity prototype cells containing candidate wide operating temperature range electrolytes developed under this program. We continue to evaluate 12 Ah cells (MCMB Carbon/$LiNiCoAlO_2$) manufactured by Quallion, LCC that possess JPL methyl propionate (MP)-based wide operating temperature range electrolytes. We are currently evaluating their life characteristics and the degree to which the low-temperature capability degrades with time. These cells contain electrolytes previously shown to have excellent low temperature capabilities (supporting 2C rates even as low as -50°C), namely (i) 1.20M $LiPF_6$ in EC+EMC+MP (20:20:60 v/v %) and (ii) 1.20M $LiPF_6$ in EC+EMC+MP (20:20:60 v/v %) + 4% FEC. In addition to JPL-developed electrolytes, the group of cells contain a Quallion-developed wide operating temperature range electrolyte, as well as the DOE baseline electrolyte (i.e., 1.2M $LiPF_6$ in EC+EMC (30:70 v/v %)). The cycle life testing consists of partial DOD cycling (approximately 50% DOD), where one cycle is performed each day using variable load profile with low to moderate rates, as illustrated in Figure V - 125. After completing increments of 100 cycles (i.e., 100 days of testing), the cells are re-characterized to determine capacity, impedance, and low-temperature discharge rate capability. The cells recently completed 400 cycles, representing 400 days of life testing, and have been re-characterized at low temperature (down to -50°C). In total, the cells have been tested for ~2.5 years, including the initial rate characterization over the range of temperatures. In summary, of the wide operating temperature electrolytes, the best capacity retention, (as shown in Figure V - 126), was observed with the cell containing the MP-based electrolyte that contains FEC as an additive (4%), suggesting that the additive has produced a desirable, protective SEI layer. In addition, good retention of low temperature capability is observed at -40° and -50°C, at 2C and C/5 rates, after completing the cycling testing, with the MP-based cells delivering the highest capacity. For example, as illustrated in Figure V - 127, the cells containing the MP-based electrolytes were observed to deliver the highest capacity at -40°C using a C/2 discharge rate, with the cell containing the FEC as an electrolyte additive displaying the least amount of performance degradation as a result of life cycling. Excellent performance is also exhibited throughout the life of the cells at -50°C, as illustrated in Figure V - 128, with the best result being obtained with the cell containing the 1.20M $LiPF_6$ in EC+EMC+MP (20:20:60 v/v %) + 4% FEC, which displayed good preservation of the low temperature capability.

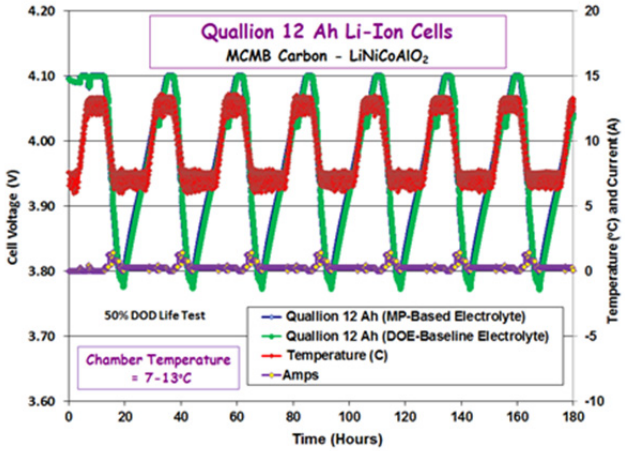

Figure V - 125: Profile of cycle life performance testing (50% DOD) being performing on Quallion 12 Ah cells containing various low temperature electrolytes

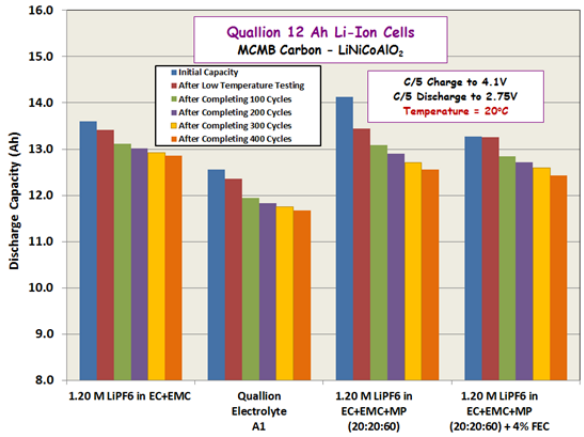

Figure V - 126: Discharge capacity (Ah) of Quallion 12 Ah cells containing various low temperature electrolytes at 20°C during the course of life testing

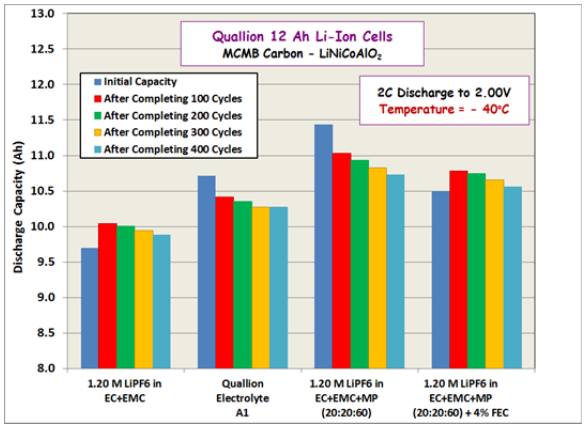

Figure V - 127: Discharge capacity (Ah) of Quallion 12 Ah cells containing various low temperature electrolytes at – 40°C with a 2C discharge rate during the course of life testing

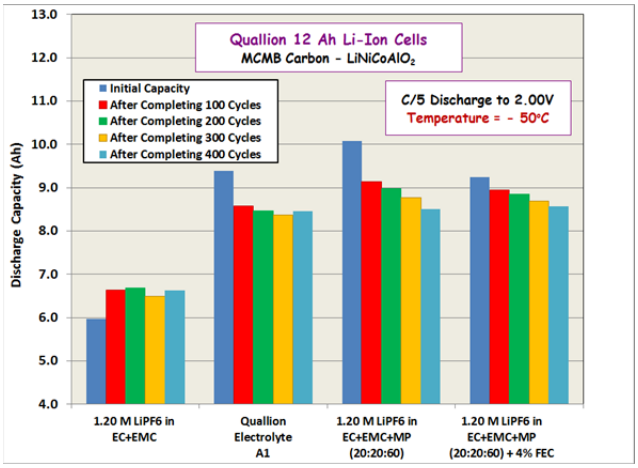

Figure V - 128: Discharge capacity (Ah) of Quallion 12 Ah cells containing various low temperature electrolytes at - 50°C with a C/5 discharge rate during the course of life testing

We also continue to investigate the performance characteristics of additional MP-based electrolytes in smaller hermetically sealed prototype 0.25Ah MCMB/$LiNiCoAlO_2$ cells (manufactured by Quallion, LCC). The electrolytes investigated are permutations of the previous approach described which consist of MP with varying amounts of FEC (4, 10, and 20%). In one case, we have entirely replaced the EC with FEC. Prior to evaluation in prototype cells, these electrolytes were investigated in experimental three-electrode cells, which enabled us to determine the impact of the additives upon the electrode kinetics as a function of temperature. Cells possessing 1.20M $LiPF_6$ in EC+EMC+MP (20:20:60 vol %) + 0.10M LiBOB were also fabricated, since the use of LiBOB as an additive has been previously identified to result in improved low temperature performance and improved cathode kinetics. These electrolytes were envisioned to have improved high temperature resilience compared to the baseline MP-containing electrolyte. A number of performance tests have been performed, including discharge rate characterization as a function of temperature, charge rate characterization, and cycle life performance under various conditions (including high temperatures). Recently, we have focused upon characterizing the cells with very high discharge rates at low temperature (i.e., 20C discharge rate at -20°C). As illustrated in Figure V - 129, the cells containing the 1.20M $LiPF_6$ in EC+EMC+MP (20:20:60 vol %) + 0.10M LiBOB electrolyte displayed the best performance (providing over 60 Wh/kg), delivering over 5 times the capacity obtained with the baseline formulations. This electrolyte was also previously reported to deliver the best performance at lower temperatures, being able to support 5C discharge rates at -40°C and 4C discharger rates at -50°C.

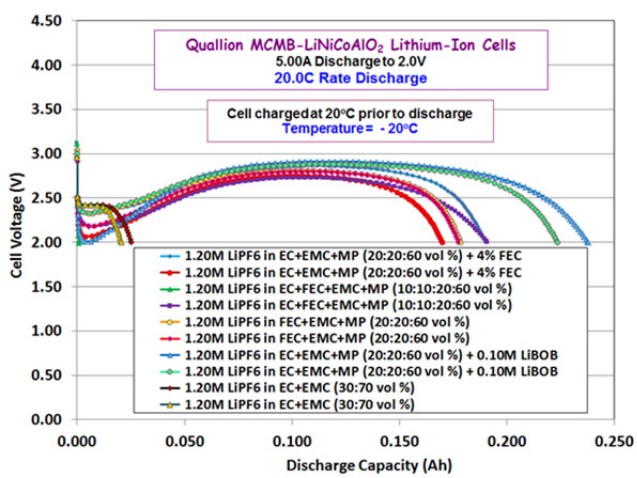

Figure V - 129: Discharge capacity (Ah) of Quallion 0.25 Ah cells containing various low temperature electrolytes at – 20°C with a 20.0 C discharge rate (5A)

We have also continued full DOD cycle life characterization on these prototype cells containing various MP-based electrolytes, including at 20°, 40°, and 50°C, as well under variable temperature conditions in a manner similar to that described previously. As illustrated in Figure V - 130, we continue to observe excellent performance with the cells when subjected to 100% DOD cycle life testing at 20°C, with over 2,600 cycles completed to-date on some of the cells. A trend of lower capacity fade is observed with increasing FEC content in the electrolyte, although high FEC content was observed to lead to somewhat lower initial capacity. As illustrated, the cell containing $LiPF_6$ in FEC+EMC+MP was observed to deliver > 88% of the initial capacity after completing 2,900 cycles, outperforming the baseline. In addition, excellent retention of the watt-hour efficiency was observed with the cell containing $LiPF_6$ in FEC+EMC+MP when subjected to cycling at +20°C, suggesting minimal impedance growth, as illustrated in Figure V - 131. In terms of the capacity fade observed, the cell containing the electrolyte with 10% FEC and 10% EC also outperforms the all carbonate baseline. Although the electrolyte with LiBOB resulted in cells with the best low temperature discharge rate capability, the cycle life performance was inferior to that of the baseline and the cells containing FEC in high proportion.

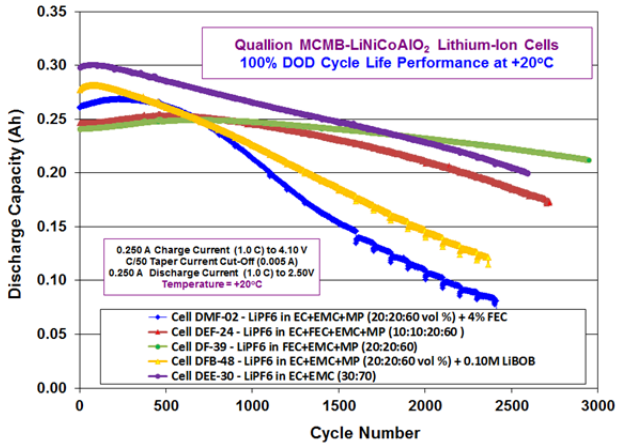

Figure V - 130: Cycle life (Ah) performance of 0.25Ah MCMB-LiNiCoAlO2 cells (Quallion, LCC) containing various electrolytes at 20°C, using C rate charge and discharge over a voltage range of 2.50V to 4.10V

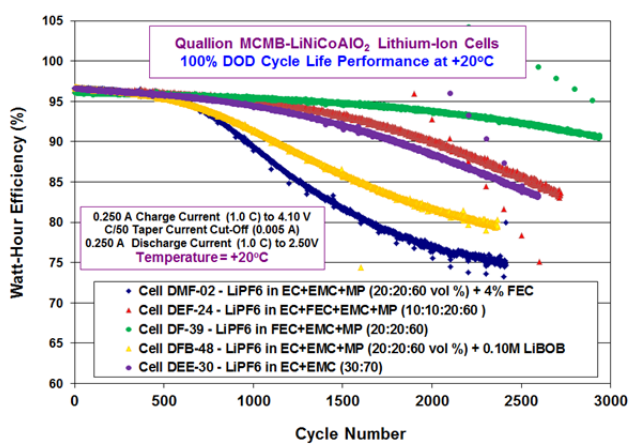

Figure V - 131: Cycle life (Wh) performance of 0.25Ah MCMB-LiNiCoAlO2 cells (Quallion, LCC) containing various electrolytes at 20°C (using C rate charge and discharge)

Electrolytes Demonstrated in LFP-Based Systems. We also continued to evaluate the life characteristics of a number of lithium iron phosphate-based cells (i.e., A123 Systems cells) that possess methyl butyrate (MB)-based electrolytes developed under this program (i.e., specifically 1.20M $LiPF_6$ in EC+EMC+MB (20:20:60 vol %) + 4% FEC and 1.20M $LiPF_6$ in EC+EMC+MB (20:20:60 vol %) + 2% VC). As reported previously, these cells have been demonstrated to have excellent rate capability over a wide temperature range (-60 to +20°C), being able to support up to 10C rates at temperatures as low as -50°C

and C rates at -60°C. As illustrated in Figure V - 132, we continue to obtain excellent full DOD cycle life performance on these cells containing these MB-based electrolytes, exhibiting over 9,500 cycles to-date and displaying comparable performance to the baseline electrolyte (i.e., delivering over 81% of the initial capacity). As noted previously, these cells also have displayed good tolerance to high temperature cycling. These results are notable given the demonstrated low temperature performance capability of these systems.

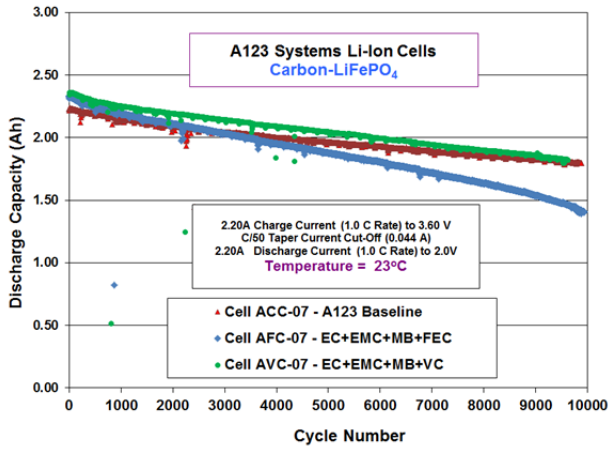

Figure V - 132: Cycle life performance of $LiFePO_4$-based A123 cells containing various electrolytes at +23°C

Electrolytes Developed for NMC-Based Systems. Recently, we have focused upon developing wide operating temperature range electrolytes for the graphite/high voltage NMC system (i.e., Conoco graphite anodes and Li_2MnO_3-$LiMO_2$ (M=Mn, Co, Ni) cathodes (Toda HE5050) supplied by ANL. To accomplish this goal, we have investigated MB-based formulations containing various additives, both coin cells as well as larger three-electrode cells equipped with lithium reference electrodes. The primary objective of utilizing electrolyte additives is to improve the high voltage stability, high temperature resilience, and in some cases improve the low temperature performance due to improved lithium kinetics at the interfaces. A number of electrolyte additives have been investigated, including (i) LiBOB, (ii) lithium difluoro(oxalato)borate (LiDFOB), (iii) lithium tetrafluoroborate ($LiBF_4$), (iv) lithium 4,5-dicyano-2-(trifluoromethyl) imidazole (LiTDI), (v) vinylene carbonate (VC), and (vi) lithium oxalate. The LiDFOB and LiTDI were synthesized and provided by Prof. Wesley Henderson's group at North Carolina State University (NCSU). Using three-electrode cells, we performed electrochemical measurements at a number of temperatures (23°, 0°, -20°, -30°, and -40°C), including EIS, Tafel polarization, and linear micro-polarization measure-ments. The most favorable kinetics at the anode was observed with the cells containing lithium oxalate and VC. Whereas, the most facile kinetics observed at the cathode was observed with the cell containing LiBOB as an additive, suggesting that it participates beneficially in the formation of the cathode electrolyte interface (CEI). Also, at -20°C, the kinetics of the cathode are much poorer than that of the anode for all of the samples (by nearly an order of magnitude), suggesting that the low temperature rate capability will be dictated by the cathode kinetics. We are currently evaluating the discharge performance of these systems as a function of temperature in both three-electrode cells and coin cells.

To complement the three-electrode cell study described above, a number of MB based electrolytes were also evaluated in coin cells consisting of the graphite anodes and Toda HE 5050 cathodes. The electrolytes investigated include: (1)1.20M $LiPF_6$ in EC+EMC +MB (20:20:60 v/v %) + 0.10M $LiBF_4$, (2) 1.20M $LiPF_6$ in EC+EMC+MB (20:20:60 v/v %) + 0.10M LiDFOB, (3) 1.20M $LiPF_6$ in EC+EMC+MB (20:20:60 v/v %) + 0.10M LiBOB, (4) 1.20M $LiPF_6$ in EC+EMC+MB (20:20:60 v/v %) + 0.10M LiTDI, and (5) 1.20M $LiPF_6$ in EC+EMC+MB (20:20:60 v/v %) + 2% DBPC (where DBPC= di-*t*-butyl pyrocarbonate). They were compared to the baseline electrolyte (i.e., 1.20M $LiPF_6$ in EC+EMC (30:70 v/v %).

After performing the formation cycling, a number of cells were subjected to systematic discharge rate characterization testing over a wide temperature range. In summary, the cell containing the MB-based electrolyte with LiDFOB delivered superior performance, approximately twice the capacity for the baseline electrolyte discharged at a C/10 rate at -20°C, and roughly four times the capacity at a C/2 rate at -20°C, as illustrated in Figure V - 133 and Figure V - 134. The beneficial attributes of LiDFOB appear to be associated with desirable film formation on both electrodes. In contrast, although LiBOB has been observed to have beneficial interactions at the cathode interface, it generally results in poorer kinetics at the anode, due to the formation of resistive films.

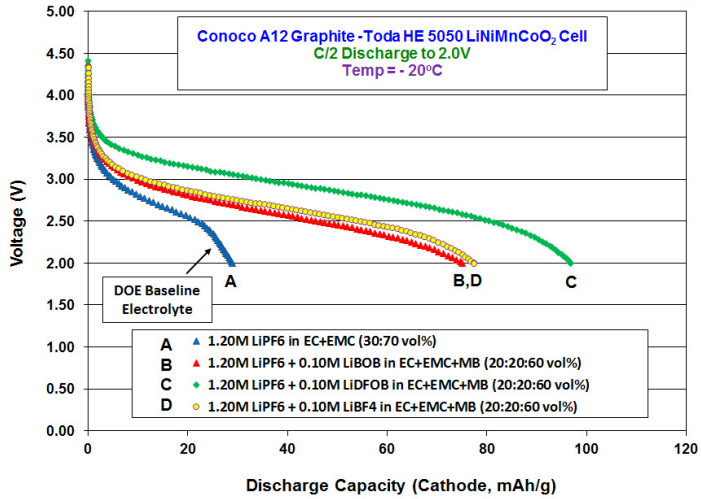

Figure V - 133: Discharge performance of graphite-NMC coin cells containing various electrolytes at -20°C (using a C/2 discharge rate). The cells were charged at room temperature prior to discharge

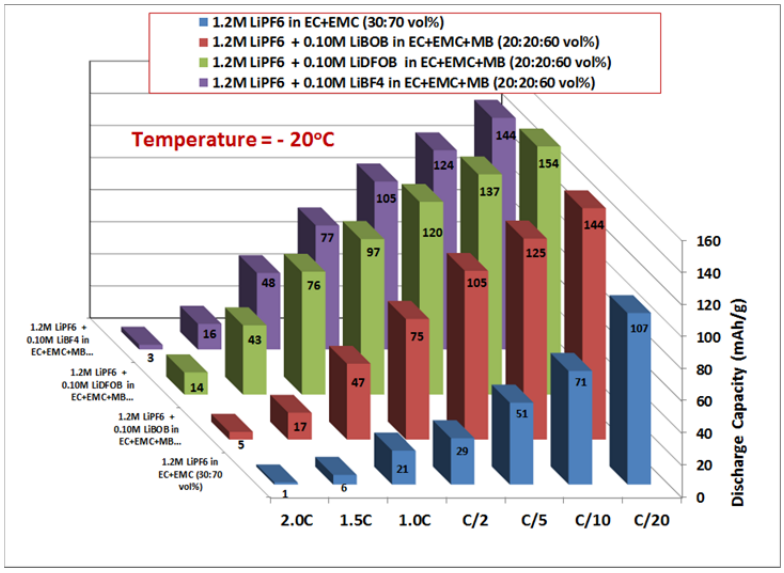

Figure V - 134: Discharge performance of graphite-NMC coin cells containing various electrolytes at -20°C using a range of discharge rates (C/20 to 2.0C). The cells were charged at room temperature prior to discharge

Future work will be focused upon further evaluating the low temperature performance characteristics of ester-containing electrolytes containing the various additives. This will consist of evaluating the discharge characteristics in various systems, as well as determine the electrode kinetics as a function of temperature with the benefit of three electrode cells. In addition, future work will also be focused upon characterizing the high temperature stability and cycle life performance of these electrolytes in the various systems.

Collaborations

During the course of this program, we have collaborated with a number of institutions, including: (a) Univ. Rhode Island (Brett Lucht: analysis of harvested electrodes, on-going collaborator), (b) Argonne Nat. Lab (Khalil Amine: source of electrodes, on-going collaborator), (c) LBNL (John Kerr) (evaluation of novel salt), (d) A123 Systems, Inc. (electrolyte development, on-going collaborator), (e) Quallion, LCC. (electrolyte development, on-going collaborator), (f) Yardney Technical Products (electrolyte development, on-going collaborator), (g) Saft America,

Inc. (industrial partner under NASA program), (h) NREL (Smith/Pesaran) (supporting NREL in model development by supplying data), (i) the Univ. of Southern California (Prof. Prakash, electrolyte salt development), (j) Sandia National Laboratory (Safety testing of low flammability electrolyte and supplier of electrode materials), (k) Hunter College (Prof. Greenbaum, *ex situ* NMR measurements), and (l) NCSU (Prof. Wesley Henderson, Evaluation of novel salts). Some of the work described here was carried out at the Jet Propulsion Laboratory, California Institute of Technology, under contract with the National Aeronautics and Space Administration.

FY 2013 Publications/Presentations

1. M. C. Smart, B. L. Lucht, S. Dalavi, F. C. Krause, and B. V. Ratnakumar, "The Effect of Additives upon the Performance of MCMB/$LiNi_xCo_{1-x}O_2$ Li-ion Cells Containing Methyl Butyrate-Based Wide Operating Temperature Range Electrolytes," *J. Electrochem. Soc*., **159 (6)**, A739-A751 (2012).
2. S. DeSilvan, V. Udinwe, P. Sideris, S. G. Greenbaum, M. C. Smart, F. C. Krause, K. A. Smith and C. Hwang, "Multinuclear NMR Studies of Electrolyte Breakdown Products in the SEI of Lithium-Ion Batteries," *ECS Trans.* ***41 (41),*** *207 (2012).*
3. M. C. Smart, Ratnakumar V. Bugga, and L. D. Whitcanack, "Development of Low Temperature Electrolytes for Lithium-Ion Batteries," Advanced Automotive Batteries Conference, Pasadena, CA, February 5, 2013 (Invited Talk).
4. M. C. Smart, C. Hwang, F. C. Krause, J. Soler, W. C. West, B. V. Ratnakumar, and K. Amine, "Wide Operating Temperature Range Electrolytes for High Voltage and High Specific Energy Li-Ion Cells," ECS Transactions, submitted.
5. M. C. Smart, M. R. Tomcsi, L. D. Whitcanack, B. V. Ratnakumar, M. Nagata, and V. Visco, "The Use of Methyl Propionate-Based Electrolytes with Additives to Improve the Low Temperature Performance of $LiNiCoAlO_2$-Based Li-Ion Cells, 224th Meeting of the Electrochemical Society, San Francisco, October 2013.
6. F. C. Krause, C. Hwang, B. V. Ratnakumar, M. C. Smart, D. W. McOwen and W. A. Henderson, "The Use of Methyl Butyrate-Based Electrolytes with Additives to Enable the Operation of Li-Ion Cells with High Voltage Cathodes over a Wide Temperature Range," 224th Meeting of the Electrochemical Society, San Francisco, October 2013.

V.D.3 Novel Phosphazene-based Compounds to Enhance Safety and Stability of Cell Chemistries for High Voltage Applications (INL)

Kevin L. Gering, PhD

Idaho National Laboratory
2525 N. Fremont Avenue
Idaho Falls, ID 83415-2209
Phone: (208) 526-4173; Fax: (208) 526-0690
E-mail: kevin.gering@inl.gov

Collaborators (INL):
Eric J. Dufek, Mason K. Harrup, David K. Jamison, Harry W. Rollins, Sergiy V. Sazhin, Fred F. Stewart

(External to INL):
John Burba, Princess Energy Systems

Contract No. DE-AC07-05ID14517

Start Date: January, 2009
Projected End Date: Sept. 2013

Objectives

Our focus is producing electrolyte and electrode compounds resilient in both temperature and voltage regimes, while meeting a competitive baseline performance in transport properties and SEI characteristics. In meeting these goals we aim to reduce the presence of carbon in Li-ion cells to produce a more robust inorganic-based cell chemistry. We seek compounds that will:

- enable prolonged usage of advanced higher-voltage electrode couples,
- promote better safety performance under abusive thermal conditions,
- enhance cell life.

Another objective is to gain fundamental understanding of molecular-scale interactions between phosphazenes and other electrolyte species and cell components.

Technical Barriers

Safety and longevity of Li-ion batteries continues to be an issue for future vehicular applications. This is complicated by the drive toward higher voltage cells (5V+) and some usage patterns and conditions that would cause batteries to operate at higher temperatures. A viable alternative electrolyte for Li-ion batteries must simultaneously meet multiple criteria regarding transport properties, SEI film formation, voltage stability, flammability, aging mechanisms, chemical compatibility, performance at high and low temperatures, etc. A fundamental challenge remains to produce electrolyte components that will provide noteworthy levels of flame retardance while reducing viscosity to competitive levels to maintain attractive transport properties, and some success has been had at the INL toward that goal in 2013 within our overall ES materials program.

Technical Targets

Our targets are defined by primary categories:

- *Phosphazenes as primary solvents* (>40%) to greatly reduce electrolyte flammability. Our requirements for the pure phosphazene (with lithium salt) to be viable as a primary solvent: room temperature viscosity less than 5 cP, conductivity greater than 4 mS/cm, and lithium salt ($LiPF_6$) solubility at least 0.6 M.
- *Phosphazenes as cosolvents* (10-40%) to provide mixed benefits of reduced electrolyte flammability and prolonged cell life. Properties for the pure salted phosphazene to be defined as a cosolvent: room temperature viscosity within 5-40 cP, conductivity 0.2-4 mS/cm, and lithium salt solubility within 0.2-0.6 M.
- *Phosphazenes as additive solvents* (≤10%) to enhance chemical/thermal stability of the bulk electrolyte and improve SEI properties in terms of thermal runaway and stability over life. Viable additive candidates are defined as follows: room temperature viscosity exceeds 40 cP, conductivity ≤ 0.2 mS/cm, and lithium salt solubility < 0.2 M.
- Abuse testing at SNL of INL electrolytes looks squarely at how these compounds provide benefit to cell operation and safety at extreme conditions of temperature and voltage. Improvement over a baseline is sought.
- We have worked with ANL and DOE toward scale-up of the best INL phosphazene candidates. One of our compounds in now in the scale-up queue.
- Replace the typical carbon anode with a highly nonflammable polymer-based host that also adds benefit toward chemical compatibility across the cell.

Accomplishments

- Various forms of heterocyclic phosphazene solvent compounds have been synthesized, characterized, and tested in coin cells. More efficient and economical synthesis routes have been found for some classes of compounds to decrease manufacturing costs. Of note for 2013 are newer FM and PhIL (ionic liquid) series compounds.
- Cell testing completed for using INL electrolytes with the NCA (Toda)/Carbon couple, covering characterization of capacity and impedance attributes. Overall results show good compatibility of phosphazenes with the various cell environments, promoting stability at elevated temperatures.
- Completed prolonged thermolysis experiments at 60°C using FM and SM series additives with two markedly different baseline electrolytes.
- Investigation of Phase 3 polymeric alternative anode materials with improved electronic conductivity, porosity, crosslinking, and capacity.
- NMR evaluation of electrolyte fate at elevated temperatures (with Washington State Univ.)
- Further refined and expanded our methods for voltammetric electrolyte and interface characterization, which has the potential of being an important new tool for materials selection.
- Success of INL phosphazene-based electrolyte additives resulted in priority of scale-up of INL electrolyte compounds at ANL; one INL compound is in the scale-up queue.
- DFT modeling results published for trends between molecular configuration and phosphazene solvent-to-lithium binding energy.

✧ ✧ ✧ ✧ ✧

Introduction

Electrolytes play a central role in performance and aging in most electrochemical systems. As automotive and grid applications increasingly rely on electrochemical stored energy, it becomes more urgent to have electrolyte components that enable optimal battery performance while promoting battery safety and longevity. Safety remains a foremost concern for widespread utilization of Li-ion technology in electric-drive vehicles, especially as the focus turns to higher voltage systems (5V). This work capitalizes on the long established INL expertise regarding phosphazene chemistry, aimed at battery-viable compounds that are highly tolerant to abuse. Various references document/relate to the FY13 work [1-5].

Approach

The general heterocyclic phosphazene structure is shown in Figure V - 135.

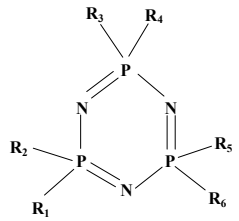

Heterocyclic Phosphazene Ring Structure

MWT: 400-600

Figure V - 135: General heterocyclic phosphazene structure

A change of chemical structure in the ring pendant arms has a strong influence on electrolyte properties, performance, and longevity in a higher-voltage system (5V+) and at higher temperatures. By customizing the pendant structures (R groups) we seek to improve transport properties while increasing flash point and having acceptable SEI characteristics and cell aging. Benefits include inherent stability and non-flammability, very low vapor pressure, good lithium salt dissolution. Challenges would include high viscosity and the need to attenuate N:Li+ attraction that occurs due to electron doublet transfer. To date our numerous compounds derive from the following four groups:

SM: ether groups attached to the phosphorus centers

AL: unsaturated analogues of the SM series

FM: fluorinated analogues of the SM series

PhIL: based on an ionic liquid structure.

The ionic liquid series helps to mitigate some of the limitations seen with traditional cyclic phosphazenic solvents, such as N:Li^+ association that can adversely affect conductivity. Non-cyclic phosphazene compounds are also being targeted through the INL internal R&D program (with success), and salts other than $LiPF_6$ are being considered.

We employ a number of diverse testing and characterization methods to determine viability of candidate compounds, including advanced voltammetry techniques, coupled viscosity and conductivity analysis, flash point, EIS, cell testing, as well as chemical physics and DFT modeling. Coin cells (type 2032) are used to test candidate electrolytes in an actual cell environment, covering crucial issues of formation, interfacial impedance, polarization testing, and aging.

Results

Summarized below are salient results from 2013 research. For brevity, only representative summaries are given. The baseline (BL) electrolyte is 1.2M $LiPF_6$ in EC-EMC (1:4, wt.), unless otherwise defined.

Figure V - 136 shows the result of prolonged thermolysis conditions at 60°C for electrolyte systems with and without (baseline) FM and SM phosphazene additives at 10% levels within each baseline. The baseline samples are the two left-most vials in each row. It is readily seen that the presence of the phosphazenes mitigates degradation of the baseline and have a preservation role at elevated temperatures. Benefits are longer cell life under higher-temperature conditions, and the opportunity to scale-back battery thermal management to balance with the resilient electrolyte.

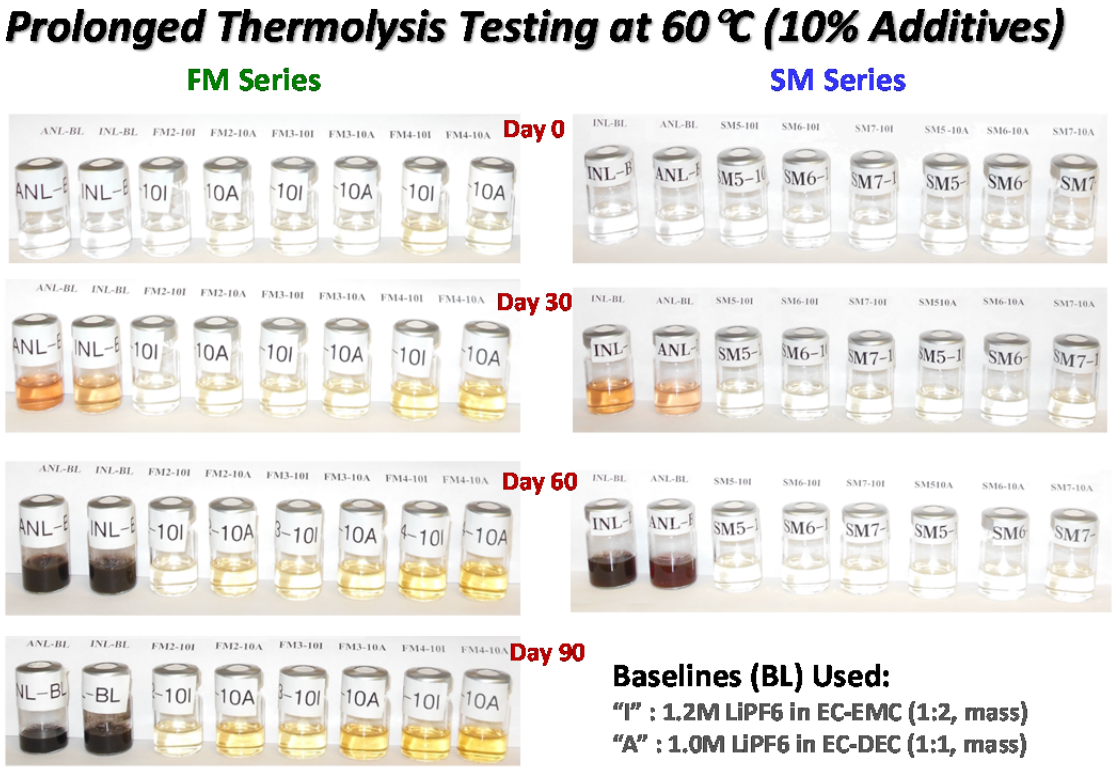

Figure V - 136: INL prolonged thermolysis testing results

Figure V - 137 attests that INL FM-series phosphazene additives extend the electrochemical window (EW) past what is achievable with the BL electrolyte. Presence of the phosphazene more than doubles the EW past the BL value. These additives act to moderate the oxidative processes at the positive electrode, and hence enhance stability at higher voltages. This attribute is also observed for other INL phosphazene compounds (SM, AL, etc.). Figure V - 138 shows the clear benefit of having 3% PhIL-2 in the baseline electrolyte, where the flame duration was dropped by an order of magnitude below the baseline. This adds greatly to the safety of the cell chemistry.

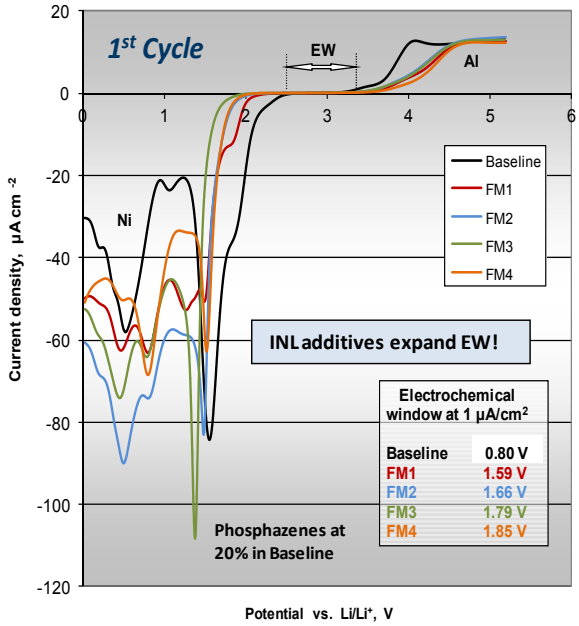

Figure V - 137: Electrochemical window enhancement with INL FTI-series phosphazene additives

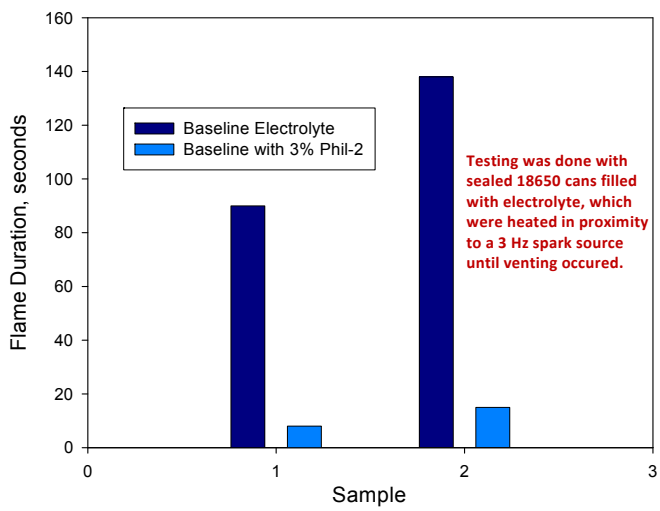

Figure V - 138: INL demonstration of reduced flame duration

Cell testing was performed using 2032-type coin cells to judge performance of the electrolytes with ABR electrode couples. Figure V - 139**(a,b)** summarize the early life capacity performance of coin cells using NCA/graphite, having FM series compounds at various amounts in the baseline. In Figure V - 139a improvement over baseline performance is seen in particular for FM-2 cases. In Figure V - 139b, systems with FM2 levels of at least 12.4 percent show good viability for rates up to C/1.

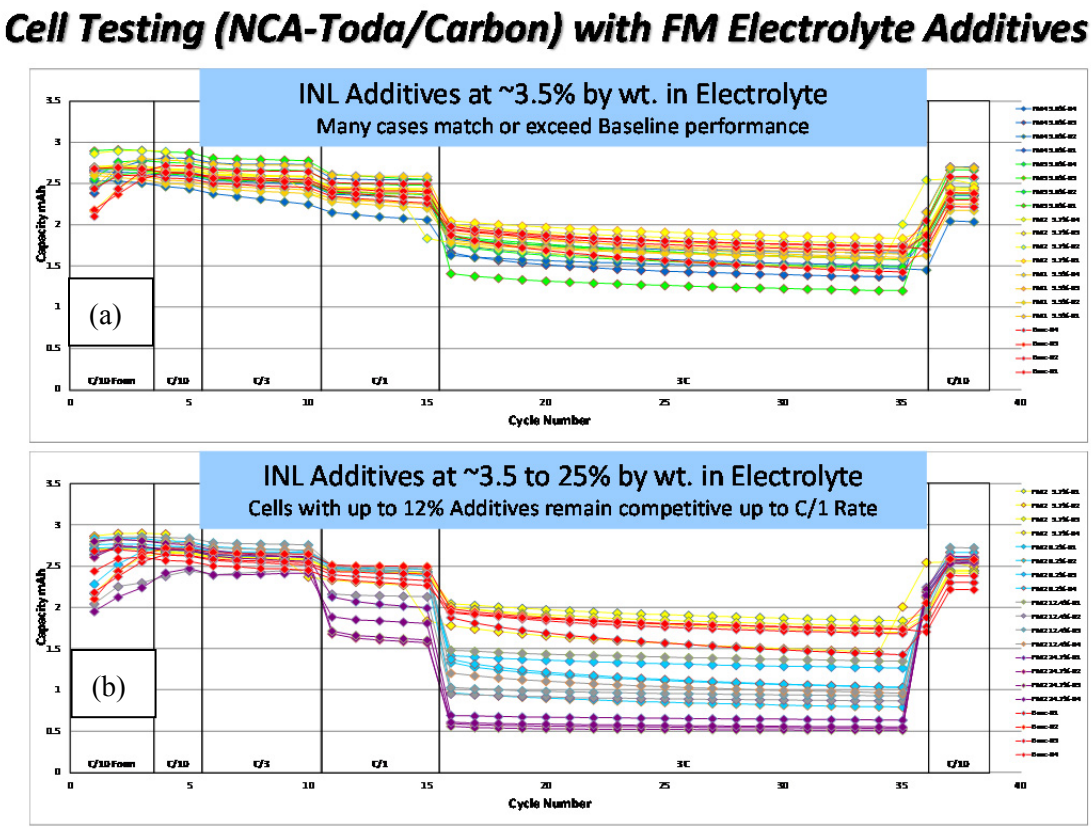

Figure V - 139: INL additive-included electrolyte performance with ABR electrode couples

From initial WSU findings, the BL sample formed a gel at the bottom of the sealed tube over time at 60˚C. This sample became much more viscous overall than Sample 1 (having the protective cyclic phosphazene additive). The evidence of phosphorus-proton coupling in the reaction products of the BL sample suggests that phosphorus is interacting with the solvent mixture. These NMR-observable product species may be intermediates in polymerization of the carbonates, leading to a polycarbonate formation (this might explain the apparent increase in viscosity).

Figure V - 140 contains post-formation capacities for representative cells containing phosphazene-based polymer anodes and thicker HE5050-type cathodes. The capacity range observed is competitive with that of graphitic anodes. Figure V - 141 demonstrates that cells with early-generation phosphazene anodes have reasonably low self-discharging behavior at elevated voltage; this behavior can be improved by modification of polymer attributes optimized over voltage. Better capacities were observed as we increased effective surface area within the polymer matrix (Figure V - 142). The mode of lithium insertion into the polymer host is facilitated in part by the by the electrostatic attributes of the phosphazene moiety, overall exhibiting a dual or hybrid mode of lithium residency surmised in Figure V - 143 (atomistic + micro-clustering) that is a function of voltage, and is highly reversible. The anode in Figure V - 143 was comprised mostly of INL polymer and A12-type graphitic carbon. These anode materials are a breakthrough – a highly “engineerable” option for anodes in Li-ion systems.

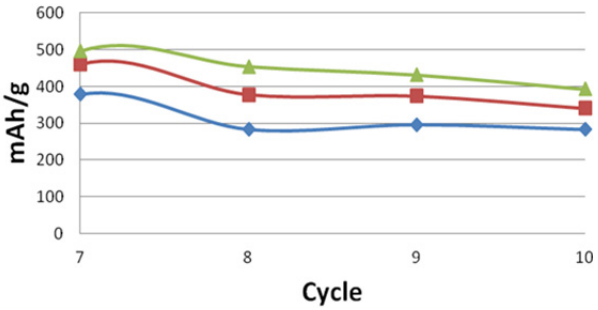

Figure V - 140: Post-formation capacities for representative cells containing phosphazene-based polymer anode and thicker HE5050-type cathodes

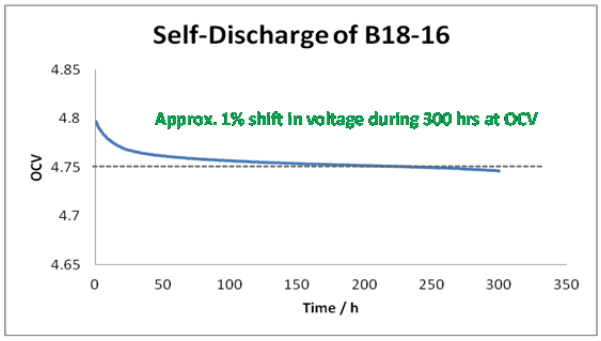

Figure V - 141: Demonstration of low self-discharging behavior at elevated voltage for cells with early generation phosphazene anodes

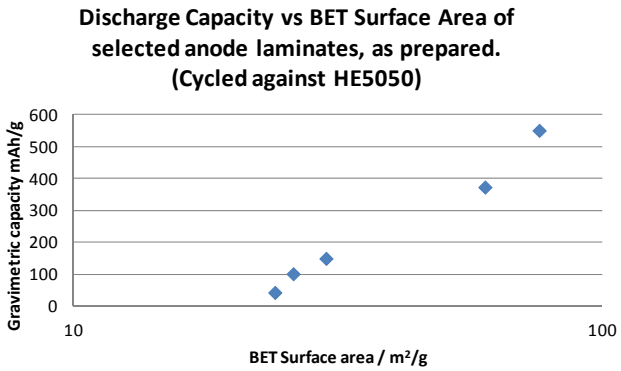

Figure V - 142: Capacity improvement with increased effective surface area within polymer matrix

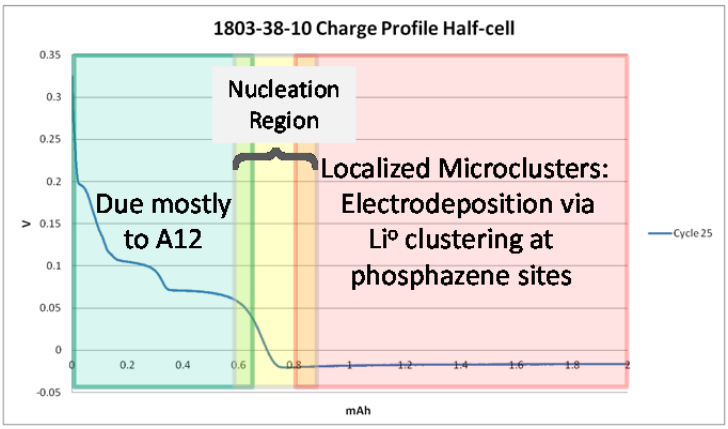

Figure V - 143: Dual/hybrid (atomistic and micro-clustering) mode of lithium residency

Conclusions and Future Directions

INL phosphazene materials improve electrolyte stability at higher voltage and elevated temperatures. The choice of the pendant R groups allows customization of the molecules to fine tune electrolyte properties tied to fate and performance in Li-ion cells. Ionic liquid phosphazenes drastically reduce the inherent association between nitrogen and Li^+, and have shown superior performance in abuse testing at SNL. In FY 13 we explored electrolytes having higher amounts of phosphazene solvents to exploit their low flammability, wherein amounts of at least 12.4% additives appear feasible for cells requiring modest rates. Newer compounds within the FM and PhIL series support optimization of these compound classes. NMR studies revealed mechanistic information regarding molecular fate and why/how our additives provide resilience to the baseline system.

Good progress was had on developing alternative anodes for Li-ion systems, wherein a phosphazene polymer basis was employed as the core host material, with modifications undertaken to modify crosslinking, porosity, and electronic conductivity. Cell capacities (vs HE5050-type thicker cathode) were often on the order of 300-500 mAh/g for these new materials.

FY 2013 Publications/Presentations (Selected)

1. M. T. Benson*, M. K. Harrup, K. L. Gering, "Lithium binding in fluorinated cyclic triphosphazenes," Computational and Theoretical Chemistry 1005 (2013) 25–34.
2. S. V. Sazhin*, K. L. Gering, M. K. Harrup, H. W. Rollins, "Highly Quantitative Electrochemical Characterization of Non-Aqueous Electrolytes & Solid Electrolyte Interphases," submitted to the Journal of the Electrochemical Society, manuscript tracking number JES-13-2932.
3. K. L. Gering* et al., "Advances Toward Inorganic Li-ion Cell Chemistries," Next Generation Batteries (April 30, 2013, Boston, MA).
4. K. L. Gering*, "The Influence of Molecular Interactions on Battery Electrolyte Properties and Processes," 222nd Meeting of the Electrochemical Society (October 11, 2012, Honolulu, HI).

** Lead author or presenter.*

V.D.4 Evaluate Impact of ALD Coating on Li/Mn-rich Cathodes (NREL)

Shriram Santhanagopalan and Ahmad Pesaran

National Renewable Energy Laboratory
15013 Denver West Parkway
Golden, CO 80401
Phone: (303) 275-3944
E-mail: Shriram.Santhanagopalan@nrel.gov

Collaborators:
Chunmei Ban, National Renewable Energy Laboratory
Mohamed Alamgir, LG Chem Power, Inc., Troy MI
David King, ALD Nanosolutions, Broomfield CO
Karen Buechler, ALD Nanosolutions, Broomfield CO

Start Date: June 2012
Projected End Date: Projected September 2013

Objectives

- To assess the technical viability of the Atomic Layer Deposition (ALD) technique on commercial battery active material such and Li/Mn-rich cathode materials.
- To mitigate durability and abuse tolerance issues associated with high capacity Li manganese-rich cathodes.

Technical Barriers

- Rapid fade in capacity of the high voltage Li - manganese rich cathode, particularly at high temperatures (45°C).
- Lack of uniformity in data from large batches of commercial active material treated with the ALD technique to overcome durability issues.
- Ineffectiveness in coating sheets of electrodes directly with ALD to achieve results similar to coating powders of active material.

Technical Targets

- Demonstrate capacity loss of less than 20% at C/2 rate over 500 cycles at 45°C for the high-voltage manganese-rich cathode.
- Demonstrate scalability of the ALD process by coating batches up to 500g, of the Mn-rich cathodes with alumina, to reproduce cell level performance observed at the lab-scale.
- Build capabilities to directly coat electrode sheets up to 6” x 6” in size.

Accomplishments

- In FY12, NREL initiated a collaborative work with LG Chem Power Inc. (LGCPI) and obtained commercial samples of Mn-rich cathode materials.
- These samples were coated with alumina using the ALD technique, in collaboration with ALD NanoSolutions, a leading company for coating ALD on battery materials.
- FY13 accomplishments include:
  - coating of large batches of cathod material powders (several tens of kg).
  - coating of sheet electrode samples in the modified reactor built in the previous year.
  - demonstration of cell performance using pouch cells.

Introduction

Extending the driving range of PHEVs requires the use of high-voltage cathodes that offer consistent performance over 5,000 cycles and 15 years of battery life without compromising safety. The Mn-rich cathode is an excellent material for these specifications and has been shown to have the potential to be stable over a wide voltage window between 4.5 and 2.7 V. Preliminary work at the lab-scale, between NREL and LGCPI indicated that while ALD coating of the cathode improved its cycling performance, no enhancements were observed on coating carbon-based anodes. This effort was initiated in June of 2012. In this report, we show findings from the preliminary study, using large format pouch cells.

Approach

Powders

- Coat 200-500g batches of Mn-rich cathode powders in pilot-scale reactors at a sub-contractor’s facility.
- Optimize the coating conditions to minimize rate-capability losses, if any, by building cells using several batches of ALD-coated cathode material and testing them at NREL.
- Evaluate optimized coatings by building and testing pouch cells at LGCPI.

Electrodes

- Modify ALD-reactors to hold sheet-electrodes.

- Develop a processs to coat electrodes uniformly across the thickness of the sample.
- Characterize and test samples at NREL and LGCPI.
- Refine coating process based on initial evaluation results.

Results

In FY13, the focus was on evaluating the cycling performance of the cells fabricated using the ALD coated powders. The cathode powder samples were subjected to different ALD coating profiles to assess the uniformity of the coating and the resistance as a function of the number of cycles last year. Based on these results, the samples with the coating that best suited the requirements of cycling and resistance build-up were used to build pouch format cells and cycled at different temperatures. The coating procedure was the same as adopted last year.

ALD Coating.

The pre-processing step included drying at overnight. No unusual off-gassing or decomposition reactions were observed. The coating process involved the following steps:

i) loading the bed of powders into the fluidized bed reactor (shown in Figure V - 144),

ii) fluidizing the powders at the coating temperature and pressure, and

iii) introducing the ALD precursors sequentially. Each cycle comprised of the routine A-purge-B-purge – and the process was repeated for the desired number of cycles.

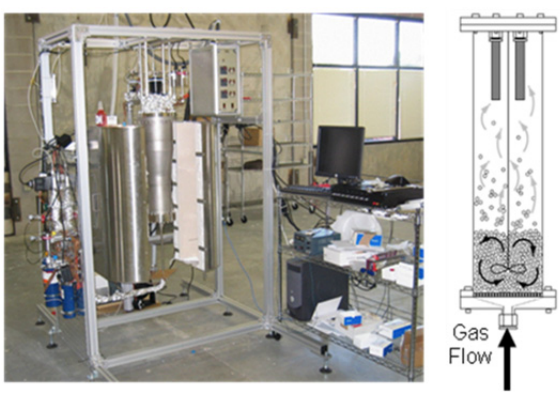

Figure V - 144: Fluidized Bed Reactor to coat powders with ALD cycles: the existing reactor at ALD Nanosolutions can process up to 8L of powder per batch

The coating was carried out at ALD Nanosolutions' facility in Broomfield, CO. ALD Nanosolutions has been doing ALD coating of battery materials and has the capability to process multiple batch sizes from tenss of grams to tens of kilograms. The samples were fluidized at 10 cm^3 per minute after the initial drying. The coating time per batch was about 2.5 hours. The initial trials focused on alumina coatings, since we had demonstrated the proof-of-concept with alumina on the Mn-rich cathode material.

Cell-Evaluation.

Sample results from cycling at 25 and 45°C are shown in Figure V - 145.

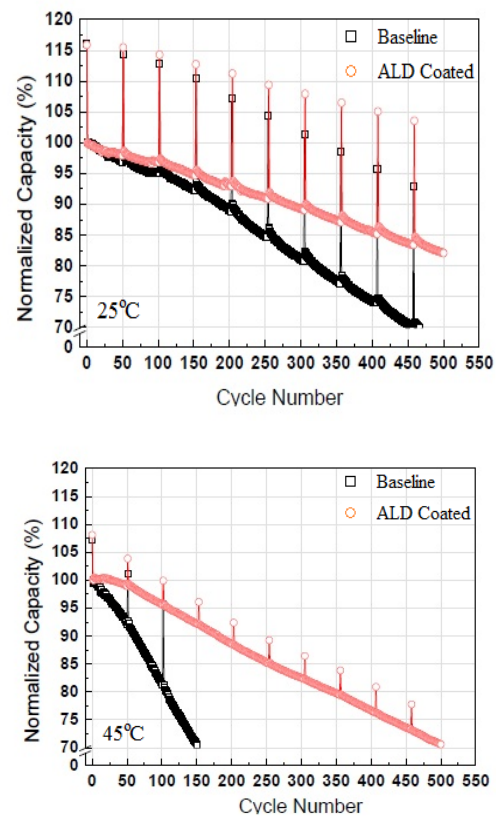

Figure V - 145: Cycling performance of ALD Coated Mn-rich Cathodes

The cell evaluation results indicate that the cycling performance at 25°C show a fade of less than 20%. At 45°C, the cycle life is considerably improved with the coating built under the present effort – however, the performance mark of less than 20% fade was reached around cycle 350.

Conclusions and Future Directions

The scalability of the ALD technique for coating battery materials is attractive – in fact, this technique has now become popular with several materials vendors, who are actively pursuing coating of cathodes to improve high-temperature performance. A roll-to-roll coating

option has also been explored separately, for large scale manufacturing. Future work will consider tailoring the composition of the coatings to improve functionality. For example, the coatings can be used to improve the processing ability of the cathode particles during the cell fabrication process by expanding the range of temperatures over which the performance of the mtaerial is stable.

FY 2013 Publications/Presentations

1. Shriram Santhanagopalan, Mohamed Alamgir, Karen Buechler, David King and Ahmad Pesaran, "Evaluate ALD Coatings of LGCPI Cathode Materials or Electrodes," Milestone Report # 55894, Submitted September 2012.
2. Shriram Santhanagopalan – AMR presentation.

V.D.5 Strategies to Enable the Use of High-Voltage Cathodes and Diagnostic Evaluation of ABR Program Lithium Battery Chemistries (LBNL)

Robert Kostecki

Lawrence Berkeley National Laboratory
Environmental Energy Technologies DIvision
1 Cyclotron Rd. MS 90-3026D
Berkeley, CA 94720
Phone: (510) 486-6002; Fax: (510) 486-5454
E-mail: r_kostecki@lbl.gov

Start Date: October 2012
Projected End Date: September 2013

Objectives

- Increase specific energy at the cell level by addressing the impact of elevated potentials on carbon black additives
  - Explore structural and chemical changes of carbon black additives associated with elevated potentials and investigate methods to reduce side reactions that occur.
  - Explore surface-modification methods to improve stability of carbon black additives in high-energy Li-ion systems.
- Study degradation mechanism(s) in the PHEV test cells and at the system and cell components level.
- Investigate the mechanism of chemical cross-talk between electrodes and its implication for electrochemical performance and lifetime of high-energy Li-ion systems.

Technical Barriers

This project addresses the following technical barriers related to the battery technology development effort of the DOE Office of Vehicle Technologies:

- Inadequate EV and PHEV battery energy, durability and safety, as well as the need for efficent cell-formation processes, are the major barriers addressed by LBNL diagnostic work.
- The primary LBNL role in the ABR Program is to carry out specific diagnostic evaluations to determine the changes in cell components that accompany Li-ion cell power fade, capacity fade and/or failure.
- LBNL also seeks to identify electrode and electrolyte processes that are significantly influenced by various cell-formation protocols.

Technical Targets

- Cycle life: 5,000 (deep) and 300,000 (shallow) cycles.
- Available energy: 200 Wh/kg.
- Calendar life: 15 years.

Accomplishments

- An improved carbon black additive was synthesized and tested in selected composite high-voltage positive electrodes. Enhanced lifetime and reversibility of modified electrodes have been demonstrated.
  - Invention disclosure/patent application filled by LBNL.
  - LBNL Technology Transfer grant obtained to commercialize the technology.
- The mechanism of chemical cross-talk in high-energy Li-ion cells has been determined and possible implications for cell electrochemical performance evaluated.

✧ ✧ ✧ ✧ ✧

Introduction

A primary aim of this project is to develop and use advanced diagnostic techniques to characterize basic physico-chemical properties of electrode active and passive components in ABR Program cells that are being developed for use in PHEV and EV applications. The focus of this task is to correlate fundamental processes that occur in Li-ion batteries with electrochemical performance. The diagnostic results are used to determine cell failure mechanisms, anticipate the system lifetime, and suggest new approaches to design more-stable materials, composites, and electrodes.

Approach

The goal of these studies is to unveil phenomena that determine battery performance and failure modes. A better understanding of the underlying principles that

govern these proesses is inextricably linked with successful implementation of high-energy-density materials such as Si and high-voltage cathodes in Li-ion cells for PHEVs and EVs. The proposed methodologies include:

- Strategies to minimize irreversible capacity losses
  - Determine the mechanism of carbon additive degradation and migration at high potentials and in high-voltage composite electrodes.
  - Improve carbon black stability at high potentials *via* surface treatment.
- Diagnostic evaluation of ABR Program lithium-ion cell chemistries
  - Carry out post-test diagnostic evaluation of components from ABR test cells and model cells (no test cells were sent to LBNL in FY2012 or FY2013.

Results

The focus of our work in FY13 included comprehensive analysis of the irreversible capacity losses (ICL) in high-energy composite positive electrodes, examination of the positive effect of the oxidative heat treatment of carbon black conductive additives, and fundamental investigations of the mechanism of chemical cross-talk in lithium-ion battery cells using fluorescence spectroscopy and imaging.

A new experimental approach has ben designed and created to quantify the extent of electrolyte oxidation at the Toda He5050/Super-P/PVdF positive Li-ion composite electrodes at potentials exceeding 4.2 V *vs*. Li/Li^+. The potential response of the 10th galvanostatic charge-discharge cycle of the Toda He5050 electrode was used used to carry out voltage profile simulation (VPS) measurements on pure carbon black/PVdF electrodes with no active material present. These measurements provided direct quantitative information about the charge consumed by electrolyte decomposition at the carbon black additive alone during a typical charge-discharge process.

The electrolyte oxidation current at the pristine carbon black/PVdF electrode is substantially higher than for the CO_2 heat-treated carbon black/PVdF electrode for both the anodic and cathodic scans during the first cycle. The magnitude of the anodic current tends to decrease significantly in the following scans. However, the current density for untreated CB electrode still remains three time times higher at 4.7 V than that for the CO_2 heat-treated electrode. The calculated charge (mAh/g of carbon) consumed during the model "charge-discharge" cycles of the CB electrodes is shown in Figure V - 146.

This charge profile represents the faradaic component of the current. The significant charge consumed by the electrolyte oxidation processes at the unmodified carbon black electrode during the first anodic scan indicates that irreversible processes must have led to partial passivation of carbon black. The subsequent scans added to the total charge used in these irreversible processes to reach an equivalent of 163 mAh/g of carbon. This is ~5 time higher than the charge consumed during similar "charge-discharge" scans of the CO_2 heat-treated CB electrode. Interestingly, the electrochemical behavior of both samples becomes very similar after 8 cycles suggesting that an effective surface passive layer eventually forms at carbon black.

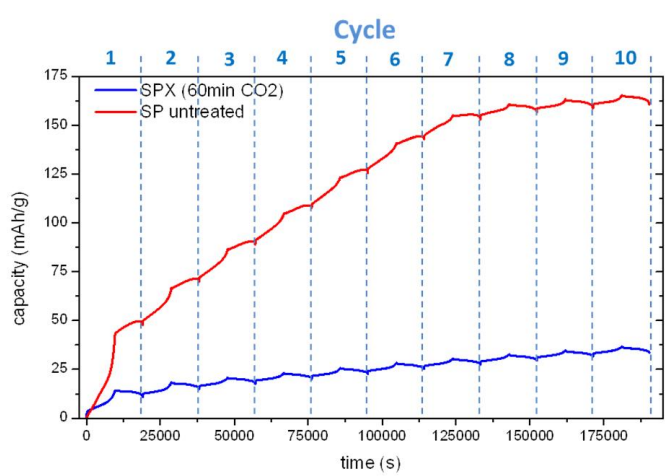

Figure V - 146: Charge consumed in the electrolyte oxidation side reactions during model "charge-discharge" scans of untreated (red), and CO_2 heat-treated Super-P/PVdF electrodes (blue) during the first ten cycles

A typical positive Li-ion composite electrode consists of ~7% carbon black conductive additive. Considering a reversible capacity of NMC-based positive electrode at 170 mAh/g, these results indicate that ~6.7% of the overall electrode charge capacity is consumed in the reversible processes on the carbon black during the first ten cycles. The use of CO_2 heat-treated carbon black additives can help reduce these irreversible losses to ~1.3%. These investigations provide more evidence of the importance of interfacial effects on passive electrode components for the overall performance and lifetime of Li-ion batteries.

In collaboration with the Battaglia group at LBNL, $LiNi_{0.33}Co_{0.33}Mn_{0.33}O_2$ composite electrodes (NMC, Umicore) with the baseline carbon black or the CO_2 heat-treated carbon black, have been manufactured and cycled between 2.5 and 4.6 V *vs* Li/Li^+ in coin cells with metallic lithium as counter and reference electrodes (Figure V - 147). The cells with baseline and modified cathodes perform similarly during the initial cycles. However, the cell with the modified CB cathode displays better capacity retention over the first 60 cycles, and the sudden decline in cell capacity occurs 30 cycles later than for the cell with the standard carbon black additive. This clearly indicates the beneficial effect the CO_2 heat-treatment on the interfacial stability of the carbon black and composite electrode, and on the lifetime of the full Li-ion cell.

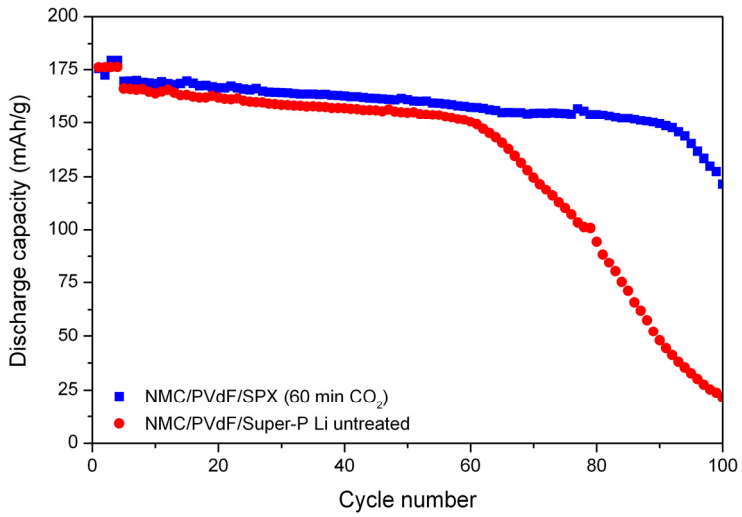

Figure V - 147: Discharge capacity *vs.* cycle number of coin cells utilizing $LiNi_{0.33}Co_{0.33}Mn_{0.33}O_2$ (NMC) and pristine (red) or heat treated (blue) carbon black in EC:DEC 1:2 1M $LiPF_6$

To investigate the mechanism of chemical cross talk in high-energy lithium-ion cells, a novel spectro-electrochemical cell was designed and constructed. The ABR baseline cell chemistry *i.e.*, Toda He5050 cathode, CPG A12 graphite anode and EC:DEC 1:2 1M $LIPF_6$ electrolyte was reproduced in a full cell setup. The composite electrodes provided by ANL were used, and the cell was cycled galvanostatically following ABR Program protocols. The charge cut-off voltage was set at 4.55 V, whereas the discharge cut-off cell voltage was 2.8 V. Figure V - 148 shows the voltage profile of the cell versus time (plotted in blue on the right side), and the corresponding fluorescence intensity across the electrolyte gap between the electrodes (middle image). The x-axis of the image represents the distance between cathode and anode whereas the y-axis shows time. The color of each pixel corresponds to the integrated intensity of the fluorescence spectra at this spot (1 micrometer diameter) at the particular time and cell state of charge (see legend on the left side).

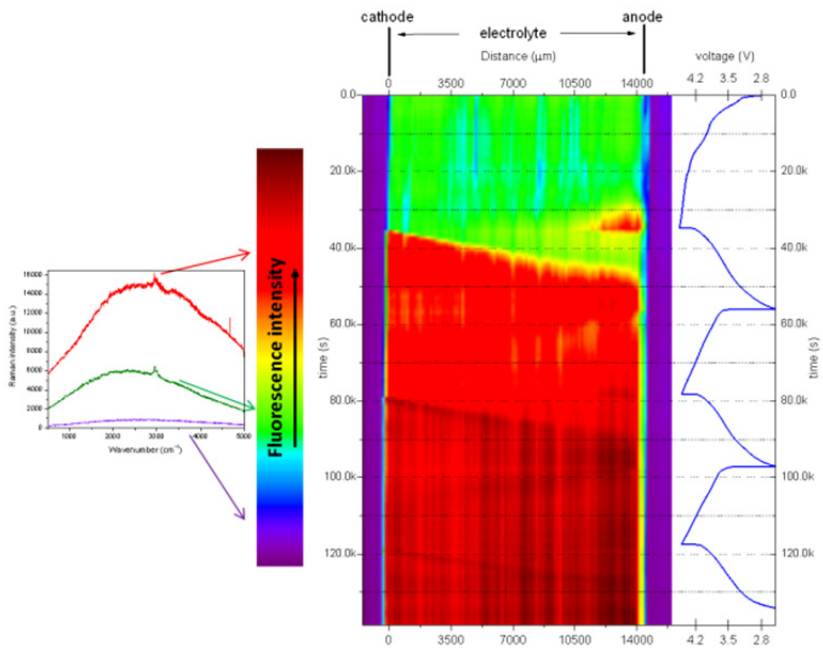

Figure V - 148: Cross-talk visualization by the means of fluorescence spectroscopy (distance between anode and cathode 14 mm, electrolyte EC:DEC 1:2 1M $LIPF_6$) and corresponding voltage profile for the A12-He5050 full cell cycled galvanostatically between 4.55 and 2.5 V vs. Li/Li^+).

At the end of the first charge, the graphitic anode releases fluorescent species into the electrolyte, which slowly migrate into the electrolyte toward the cathode. Interestingly, no photoluminescence active species were released from the He5050 cathode during the phase transformation. However, upon reversing the current from the beginning of the cell discharge, the composite cathode starts releasing fluorescent species into the electrolyte, which migrate across the electrolyte gap in the opposite direction of the lithium ions and reach the anode before the end of the first discharge. These species are most likely consumed by interfacial reactions at the anode because no accumulation effect is visible in the following cycles.

A similar process was observed on the $LiNi_{0.5}Mn_{1.5}O_4$ cathode, where some fluorescent species generated by oxidation of the electrolyte precipitated at the surface of the electrode and some dissolved and diffused away into the electrolyte. Further investigations are needed to determine the composition and origins of these soluble fluorescent species and assess their effect on the composition and stability of the SEI and Li^+ interacalation/deintercalation in graphite.

Conclusions and Future Directions

- Evaluated electrochemical behavior of carbon black additives in composite positive Li-ion electrode.
- The HT CO_2 activation of commercial carbon black additives process effectively suppresses unwanted side reactions in organic carbonate electrolytes.
- Carbon black as conductive additive in the cathode is responsible for 6.7% of the capacity loss in ABR baseline cells during the first 10 cycles
  - CO_2 heat treatment reduces such irreversible losses to 1.3%.
- Preliminary tests of CB-modified Toda He 5050 composite electrodes in full Li-ion cells demonstrated extended lifetime and a higher reversibility.
- Determined that inorganic and organic fluorescent electrolyte decomposition products form at the cathode and anode
  - Phase transformation in the lithium-rich NMC leads to formation of soluble fluorescent species, which diffuse toward the anode and interfere with the anode (SEI Mn poisoning?)
  - Mn and/or Ni dissolution is the root cause of fluorescence compound formation on positive electrode.
- Insoluble electrolyte decomposition products form electronic and ionic barriers in composite cathodes

  - These species contribute to the impedance rise in Li-ion cells.
  - Electrolyte additives and surface coatings could be effective strategies to reduce the surface reactivity of high-voltage cathodes.
- Work directly with Envia Systems and LBNL cell manufacturing/testing facilities on the development of high-energy Li-ion systems in the next phase of the ABR Program.
- Carry out post-test characterization of components from ABR model cells.
- Continue studies of degradation modes of high-voltage systems. Extend diagnostic studies to LMR-LMO.
- Continue search for remedies that decrease irreversible capacity losses and stabilize material during long-term cycling
  - Reduce irreversible charge losses from surface reactions.
  - Investigate pretreatment regimens to reduce side reactions.
  - Understand factors that can enhance the stability of SEI layers.
- Continue migration studies and assess the influence of this migration on cell internal resistance.
- Investigate the surface-treated carbon black in combination with different cathode materials, *e.g.*, NMC and LMNO (funded by received Technology Transfer grant from LBNL).

FY 2013 Publications/Presentations

1. Xiaobo Chen, Can Li, Michaël Grätzel, Robert Kostecki, Samuel S. Mao, "Nanomaterials for Renewable Energy Production and Storage," Chemical Reviews, accepted.
2. Chunjoong Kim, Nick S. Norberg, Caleb T. Alexander, Robert Kostecki, Jordi Cabana, "Mechanism of phase propagation during lithiation in carbon-free Li4Ti5O12 Battery Electrodes", Advanced Functional Materials, 23(9), pp 1214–1222, March 6, 2013.
3. S.F. Lux, I.T. Lucas, E. Pollak, S. Passerini, M. Winter and R. Kostecki, "The mechanism of HF formation in $LiPF_6$ based organic carbonate electrolytes," Electrochemistry Communications, 14, 47–50, 2012.
4. Robert Kostecki, Thomas Richardson, Ulrike Boesenberg, Elad Pollak, Simon Lux, "Modified carbon black materials for lithium-ion batteries," LBNL Invention Disclosure IB-3193 (patent filing planned May 2013).
5. N. Norberg, S. Lux, I. Lucas, J. Syzdek, and R. Kostecki, "*In situ* Fluorescence Spectroscopy of Interfacial Processes in High-Energy Li-ion Batteries," PRiME 2012 in Honolulu, Hawaii, October 7-12, 2012.
6. Kim, C. Alexander, N. Norberg, R. Kostecki, and J. Cabana, "Study of the Factors that Enable Carbon-Free Insulating Li-Ion Battery Electrodes," PRiME 2012 in Honolulu, Hawaii, October 7-12, 2012
7. R. Kostecki, I. Lucas, N. Norberg, and J. Syzdek, "Materials and Interfaces Degradation in High-Energy Cathodes for Li-ion Batteries," PRiME 2012 in Honolulu, Hawaii, October 7-12, 2012 (invited lecture).
8. Robert Kostecki, "Local Probe Studies of Interfacial Phenomena in Li-ion Batteries," Materials Research Society Spring 2012 Meeting, San Francisco, abstract ID: 1284582, (invited lecture).
9. Nick Norberg, Ivan T. Lucas, Robert Kostecki, "Interfacial Phenomena of Li-ion battery electrodes as probed by *in situ* spectroscopy and microscopy techniques," 1st Gordon Research Conference "Batteries, Advanced Characterization, Theory and Mechanisms of Processes in Rechargeable Batteries Across Length Scales, March 4-9, 2012, Four Points Sheraton / Holiday Inn Express, Ventura, CA.

V.D.6 Life and Abuse Tolerance Diagnostic Studies for High Energy Density PHEV Batteries (BNL)

Kyung-Wan Nam

Chemistry Department
Bldg. 555, Brookhaven National Laboratory
Upton, NY 11973
Phone: (631) 344-3202; Fax: (631) 344-5815
E-mail: knam@bnl.gov

Xiao-Qing Yang
Chemistry Department
Bldg. 555, Brookhaven National Laboratory
Upton, NY 11973
Phone: (631) 344-3663; Fax: (631) 344-5815
E-mail: xyang@bnl.gov

Start Date: October 2012
Projected End Date: September 2013

Objectives

- To establish and investigate the structural origin of thermal instability of various cathode materials.
- To search for new approaches on how to improve the thermal stability of cathode materials including surface modification and their effectiveness.
- To provide information on designing thermally stable cathode materials for HEV and PHEV applications.
- To develop new *in situ* diagnostic techniques with surface and bulk sensitivity for studying the thermal stability of various cathode materials.
- To develop *in situ* diagnostic techniques with surface and bulk sensitivity for studying the capacity, voltage, and power fading mechanisms of Li-ion battery.
- To establish and investigate the capacity, voltage and power fading mechanisms of various cathode materials, especially for the high energy density Li-rich Li_2MnO_3-$LiMO_2$ type cathode materials.

Technical Barriers

- Li-ion and Li-metal batteries with long calendar and cycle life.
- Li-ion and Li-metal batteries with superior abuse tolerance.
- To reduce the production cost of a PHEV batteries.

Technical Targets

- Complete the studies of thermal decomposition of charged $Li_{1.2}Ni_{0.15}Mn_{0.55}Co_{0.1}O_2$ (Toda HE5050) cathode materials during heating using combined Time-Resolved XRD (TR-XRD) and Mass Spectroscopy (MS).
- Complete the thermal stability studies of $Li_xNi_{1-2y}Mn_yCo_yO_2$ charged cathode materials with different values of "y" using *in situ* TR-XRD coupled with MS during heating.
- Complete the *in situ* hard XAS studies of Toda HE5050 cathode material for the voltage fading mechanism and limiting factors of their relatively poor rate capability.

Accomplishments

- Developed new *in situ* technique by combining the TR-XRD with MS and applied it to study the Toda HE5050 high energy density cathode material during heating. The co-relation between the structural changes and the oxygen release of this material was obtained.
- Through collaboration with Johnson Control, carried out the thermal stability studies of $Li_xNi_{1-2y}Mn_yCo_yO_2$ charged cathode materials using *in situ* TR-XRD coupled with MS during heating.
- Through collaboration with Argonne National Lab., R&D Center of GM, and other collaborators, carried out time resolved x-ray absorption spectroscopy (TR-XAS) diagnostic studies of Toda HE5050 cathode materials during constant voltage charge. The major limiting factor for the relatively poor rate capability of this type of materials was determined as the Li_2MnO_3 component in the composite material.

✧ ✧ ✧ ✧ ✧

Introduction

The high energy density composite cathode materials, or so called layered-layered

$xLi_2MnO_3 \cdot (1-x)LiMO_2$ (e.g., M=Mn, Ni, and Co) materials, are currently receiving worldwide attention because of their ability to deliver capacities of 250 mAh/g or more. One serious problem is, after the high voltage activation, these composite electrode materials show a continuous voltage fading during charge-discharge cycling. The integrated advanced *in situ* diagnostic studies are crucial in resolving these problems. We have developed a set of synchrotron based *in situ* diagnostic tools, such as TR-XRD and *in situ* XAS during heating. Recently we have further developed integrated simultaneous TR-XRD and MS at beamline X7B of the National Synchrotron Light Source (NSLS), and combined XAS and high-resolution transmission electron microscopy (HR-TEM) during heating. These *in situ* techniques were applied to study the same batch of samples with similar electrochemical histories and heating conditions. With the penetrating power and bulk averaging nature, the XRD results represent a road map of the average structural changes for the phase transitions. The MS is used to monitor the oxygen-releasing behavior during heating or high voltage charge. The XAS provides information about changes in local structure and oxidation states in an elemental selective way. The HRTEM results offer detailed pictures about where the nucleation of the new phases occurs and how the new phases propagate during phase transitions. The integration of these different *in situ* techniques provides a unique way to study the microscopic structural origin of the structural and thermal instability of the materials during cycling and heating. Another very important issue from the application point of view is how to improve the relatively poor rate capability of the Li-rich layered materials. In this regard, we have also developed *in situ* TR-XAS to investigate the dynamic local structure changes of Li-rich layered materials in an elemental selective way during high-rate charging. Therefore, the in-depth understanding with elemental selectivity for the delithiation kinetics distinguishing the $LiMO_2$ and Li_2MnO_3 components in bulk will provide valuable guidance for the optimization of Li-rich layered materials with improved rate capability.

Approach

A combination of TR-XRD and MS, together with *in situ* XAS, and *in situ* TEM techniques were used during heating to study the thermal stability of the electrode materials.

Using *in situ* XRD, soft and hard XAS to study the voltage and capacity fading mechanism of high energy density Li and Mn rich layer structured NCM (LMR-NCM) during charge-discharge cycling.

Results

Thermal stability studies of HE5050. Using combined TR-XRD and MS, the thermal decomposition of charged Toda HE5050 cathode materials during heating has been studied. The results of the $Li_{1.2}Ni_{0.15}Mn_{0.55}Co_{0.1}O_2$ cathode material charged to $Li_{0.3}Ni_{0.15}Mn_{0.55}Co_{0.1}O_2$ during heating from 25° to 550°C are plotted in Figure V - 149 (left and middle panel). The crystal structure evolution is illustrated in the right panel. It can be seen that the crystal structural changes of charged $Li_{0.3}Ni_{0.15}Mn_{0.55}Co_{0.1}O_2$ layered cathode material follow the similar path as the regular layered materials such as $Li_{0.33}Ni_{1/3}Mn_{1/3}Co_{1/3}O_2$ during heating: at about 220°C, the layered structure starts converting into disordered spinel structure. After completing this transition about 400°C, it starts the second phase transition at about 450°C from the disordered spinel to the rock-salt structure. Both of these two phase transitions are accompanied by the release of oxygen.

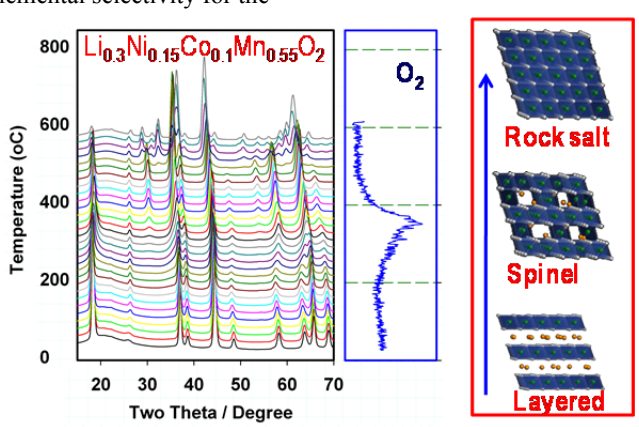

Figure V - 149: *In situ* TR-XRD patterns and simultaneously measured MS for O_2 released from $Li_{0.3}Ni_{0.15}Mn_{0.55}Co_{0.1}O_2$ during heating to 550°C. The right panel shows the models of ideal crystals with rhombohedral (layered), spinel, and rock-salt structures

Thermal stability studies of $Li_xNi_{1-2y}Mn_yCo_yO_2$ samples (y=0.3, 0.2, 0.1) from Johnson Control. Through collaboration with Johnson Control, the thermal stability of charged (4.3V) $Li_xNi_{1-2y}Mn_yCo_yO_2$ cathode materials (with y=0.3, 0.2 and 0.1) were studied using *in situ* technique by combining the TR-XRD with MS during heating. The results are shown in Figure V - 150 and Figure V - 151. It can be seen that the higher the Ni content, the poor the thermal stability, reflected by the lower temperatures of phase transitions and oxygen release. Comparison of phase transition temperatures for the series of charged $Li_xNi_{1-2y}Mn_yCo_yO_2$ samples (with y=0.3, 0.2 and 0.1) together with $Li_xNi_{1/3}Mn_{1/3}Co_{1/3}O_2$ and $Li_xNi_{0.5}Mn_{0.3}Co_{0.2}O_2$ (Figure V - 151, right panel) suggested that the $Li_xNi_{0.5}Mn_{0.3}Co_{0.2}O_2$ would be the ideal composition among the NMC chemistry to ensure the high capacity without compromising the thermal stability.

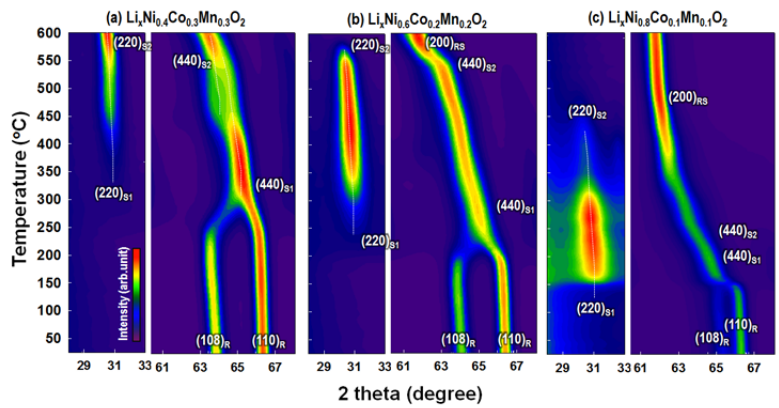

Figure V - 150: Time resolved XRD pattern combined with simultaneously measured mass spectroscopy (MS see the results in Figure V - 151) during heating up to 600°C for three charged (4.3V) $Li_xNi_{1-2y}Co_yMn_yO_2$ samples with y=0.3, y=0.2, and y=0.1

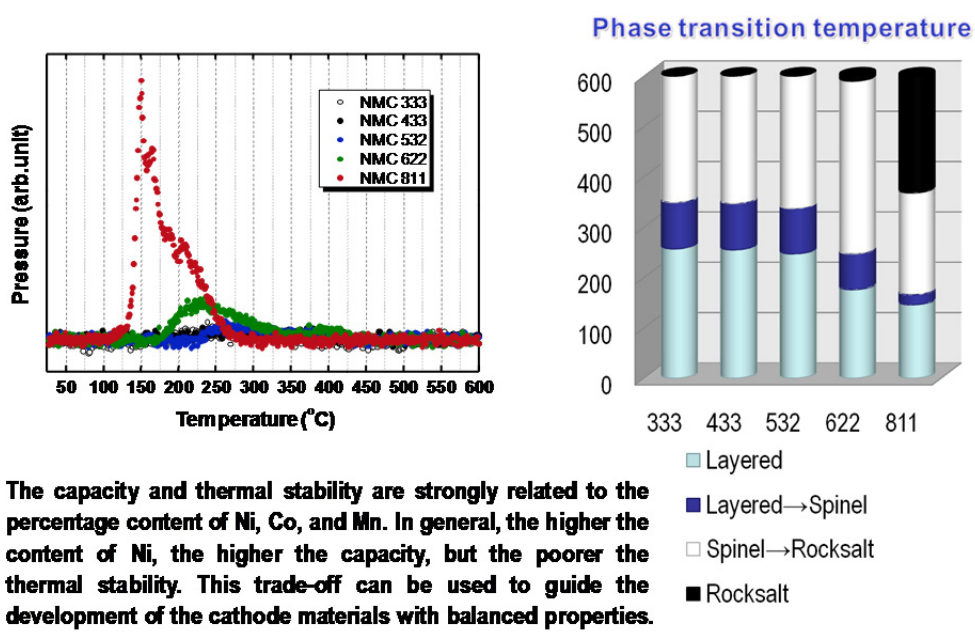

The capacity and thermal stability are strongly related to the percentage content of Ni, Co, and Mn. In general, the higher the content of Ni, the higher the capacity, but the poorer the thermal stability. This trade-off can be used to guide the development of the cathode materials with balanced properties.

Figure V - 151: Simultaneously measured MS data that trace oxygen gas release of charged (4.3V) $Li_xNi_{1-2y}Mn_yCo_yO_2$ samples (with y=0.3, 0.2, and 0.1) in comparison with charged(4.3V) $Li_xNi_{1/3}Mn_{1/3}Co_{1/3}O_2$ and $Li_xNi_{0.5}Mn_{0.3}Co_{0.2}O_2$ during heating up to 600°C

Rate capability studies of HE5050 using TR-XAS during constant voltage charge. The comparative Fourier transformed magnitude of the corresponding Ni, Co, Mn K-edge EXAFS spectra during constant voltage charge at 4.8V for a total time of 900 seconds are plotted in a two-dimensional view in Figure V - 152 by using color scale for the spectrum intensity. For Ni, the first coordination peaks (Ni-O) show dramatic changes in both position and intensity within the first 100 seconds, which represents the charge compensation occurring at the Ni sites. The EXAFS features remain unchanged after 160 seconds, indicating the oxidation of

Ni^{2+} to Ni^{4+} was almost completed within the first three minutes. Compared to Ni, the evolutions of the local structure around Co and Mn sites caused by Li^{+} extraction are more straightforward: the first coordination shell peak (Co-O and Mn-O) intensities show a continuous decrease. No obvious Co-O peak intensity changes can be observed after 200 seconds at 4.8V charge while Mn-O peak intensities continued to decrease in the whole observation time scale (900 second), indicating a much slower delithiation kinetics around Mn sites. The delithiation kinetic features revealed by this TR-XAS technique indicate a much poorer delithiation kinetic in Mn related process (mostly in Li_2MnO_3 component), comparing to the faster reaction kinetics for Ni and Co, which are not much negatively affected by the irreversible structure change of the Li_2MnO_3 component after initial delithiation process. New guidance for designing and improving Li-rich layered cathode materials with better reaction kinetics might be provided in term of tailoring the content of Li_2MnO_3 component as one of the approaches.

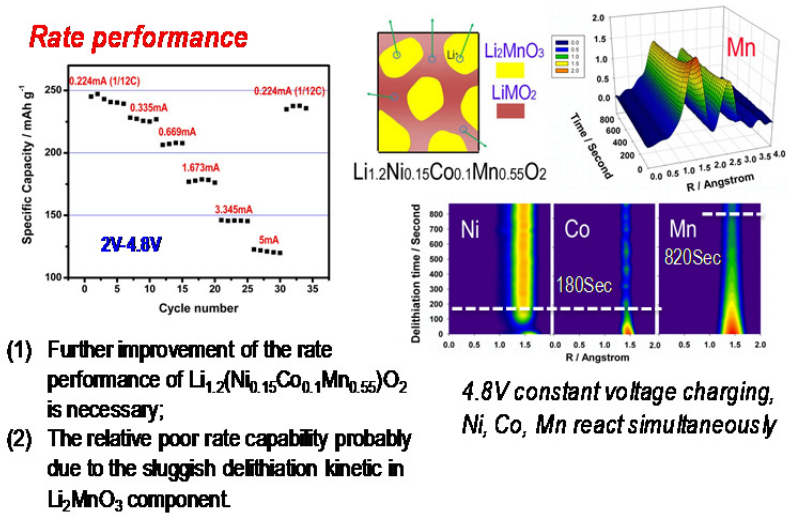

Figure V - 152: During constant voltage charge at 4.8V for a $Li_{1.2}Ni_{0.15}Mn_{0.55}Co_{0.1}O_2$ electrode, Ni, Co, Mn reacted simultaneously which was recorded by a time-resolved XAS technique. Magnitude of Fourier transformed Mn K-edge spectra of $Li_{1.2}Ni_{0.15}Mn_{0.55}Co_{0.1}O_2$ collected during 4.8V constant voltage charging and projection view of corresponding Ni-O, Co-O, Mn-O peak magnitudes of the Fourier transformed K-edge spectra as functions of charging time

Conclusions and Future Directions

The crystal structure evolution of charged high energy density layered cathode material $Li_{0.3}Ni_{0.15}Mn_{0.55}Co_{0.1}O_2$ follows a similar path to the regular layered materials such as $Li_{0.33}Ni_{1/3}Mn_{1/3}Co_{1/3}O_2$ during heating: at about 220°C, the layered structure starts converting into disordered spinel structure. After completing this transition about 400°C, it starts a second phase transition at about 450°C from the disordered spinel to the rock-salt structure. Both of these two phase transitions are accompanied with the release of oxygen.

For the series of $Li_xNi_{1-2y}Mn_yCo_yO_2$ samples with y= 0.3, 0.2, and 0.1, it was found that the thermal stability is poorer with higher Ni content, as the expense for the increased capacity. Comparison of phase transition temperatures for the series of charged $Li_xNi_{1-2y}Mn_yCo_yO_2$ samples together with $Li_xNi_{1/3}Mn_{1/3}Co_{1/3}O_2$ and $Li_xNi_{0.5}Mn_{0.3}Co_{0.2}O_2$ demonstrated that the $Li_xNi_{0.5}Mn_{0.3}Co_{0.2}O_2$ would be the ideal composition among the NMC chemistries for high capacity without compromising the thermal stability.

The TR-XAS studies of HE5050 during constant charge showed that the major source for slow reaction kinetics is the Li_2MnO_3 component. New guidance for designing and improving Li-rich layered cathode materials with better reaction kinetics might be provided by tailoring the Li_2MnO_3 component as one of the approaches. In addition, this novel TR-XAS diagnostic tool can also be applied to investigate the reaction kinetics of other lithium-ion battery materials as well as other battery systems.

In the future, new high energy density cathode materials such as layered NMC with Ni, Mn, and Co concentration gradient will be studied using time resolved XRD and XAS as well as other synchrotron based *in situ* x-ray techniques during heating and cycling.

FY 2013 Publications/Presentations

1. Seong-Min Bak, Kyung-Wan Nam, Won-Young Chang, Xiqian Yu, Enyuan Hu, Soo-Yeon Hwang, Eric A. Stach, Kwang Bum Kim, Kyung Yoon Chung and Xiao Qing Yang, "Correlating

Structural Changes and Gas Evolution during the Thermal Decomposition of Charged $Li_xNi_{0.8}Co_{0.15}Al_{0.05}O_2$ Cathode Materials," *Chemistry of Materials*, Vol. 25 (3), pp. 337–351, (2013).

2. Yong-Hun Cho, Donghyuk Jang, Jeongbae Yoon, Hyunchul Kim, Tae Kyu Ahn, Kyung-Wan Nam, Yung-Eun Sung, Woo-Seong Kim, Yun-Sung Lee, Xiao-Qing Yang, Won-Sub Yoon, "Thermal stability of charged $LiNi_{0.5}Co_{0.2}Mn_{0.3}O_2$ cathode for Li-ion batteries investigated by synchrotron based *in situ* X-ray diffraction," *Journal of Alloys and Compounds*, Vol. 562, pp 219 - 223 (2013).
3. K. Karthikeyan, S. Amaresh, V. Aravindan, W.S. Kim, K.W. Nam, X.Q. Yang, Y.S. Lee, "$Li(Mn_{1/3}Ni_{1/3}Fe_{1/3})O_2$-Polyaniline hybrids as cathode active material with ultra-fast charge-discharge capability for lithium batteries," *Journal of Power Sources*, Vol. 232, pp 240-245 (2013).
4. Jinping Dong, Xiqian Yu, Yang Sun, Lei Liu, Xiaoqing Yang, Xuejie Huang, "Triplite $LiFeSO_4F$ as cathode material for Li-ion batteries," Journal of Power Sources, Vol. 244, pp 716-720 (2013).
5. Xiqian Yu, Yingchun Lyu, Lin Gu, Huiming Wu, Seong-Min Bak, Yongning Zhou, Khalil Amine, Steven N. Ehrlich, Hong Li, Kyung-Wan Nam, Xiao-Qing Yang, "Understanding the rate capability of the high energy density Li-rich layered $Li_{1.2}Ni_{0.15}Co_{0.1}Mn_{0.55}O_2$ cathode material," *Advanced Energy Materials*, accepted.
6. Xiqian Yu, Kyung-Wan Nam, Enyuan Hu, Daniel Abraham, and Xiao-Qing Yang, "Structure Evolution and its relation to the Voltage Fading Behavior in Li-rich Layered $Li_{1.2}Ni_{0.15}Co_{0.1}Mn_{0.55}O_2$ Cathode Material during Cycling: X-ray diffraction and absorption spectroscopy study," presented at the "222th Meeting of the Electrochemical Society, October, 8-12, 2012, Honolulu, Hawaii, USA.
7. Seong-Min Bak, Kyung-Wan Nam, Enyuan Hu, Xiqian Yu, Kyung-Yoon Chung, Sung-Jin Cho, Frederic Bonhomme, Kwang-Bum Kim and Xiao-Qing Yang, "Insight into Thermal Instability of Charged Cathode Materials for Lithium-Ion Batteries: Combined *in situ* Synchrotron X-ray and Mass Spectroscopy Study," presented at the "222th Meeting of the Electrochemical Society, October, 8-12, 2012, Honolulu, Hawaii, USA.
8. Xiqian Yu, Xiao-Qing Yang, Qi Wang, Yongning Zhou, Kyung-Wan Nam, Huiming Wu, Khalil Amine, Yingchuan Lv, Hong Li and Xuejie Huang, Ying Shirley Meng, "The Studies On The Kinetic Behaviors Of Olivine Structured $LiFePO_4$ and Layer Structured $Li_{1.2}(Ni_{0.10}Co_{0.15}Mn_{0.55})O_2$ Cathode Materials Using Time Resolved X-ray Absorption Spectroscopy," presented at the International Battery Association IBA2013, March 11-15, 2013, Barcelona, Spain. **Invited.**
9. Xiqian Yu, Kyung-Wan Nam Xiao-Qing Yang, Yongning Zhou Enyuan Hu, Hung-sui Lee, Daniel Abraham, Huiming Wu, Khalil Amine, and Hong Li "Structure Evolution and its relation to the Voltage Fading Behavior in Li-rich Layered $Li_{1.2}Ni_{0.15}Co_{0.1}Mn_{0.55}O_2$ Cathode Material during Cycling: X-ray diffraction and absorption spectroscopy study," presented at the 2013 MRS Spring Meeting, April 1-5, 2013 San Francisco, USA, **Invited.**
10. Xiqian Yu, Xiao-Qing Yang, Yongning Zhou, Yingchuan Lv, Hong Li, Kyung-Wan Nam, Huiming Wu, and Khalil Amine, "Synchrotron based *in situ* XRD and XAS diagnostic studies on new electrode materials for advanced rechargeable batteries," presented at the 6th International Conference on Advanced Lithium Batteries for Automobile Applications (ABAA6), September 9-11, 2013, Argonne, Illinois, USA 60439, **Invited.**
11. Kyung-Wan Nam, Seong-Min Bak, Enyuan Hu, Xiqian Yu, Youngning Zhou, Lijun Wu, Yimei Zhu, Won-Young Chang, Eric A Stach, Kyung Yoon Chung, Xiao-Qing Yang, "Origin of thermal instability in charged cathode materials for Li-ion batteries: Combined *in situ* synchrotron X-rays and electron microscopy study," presented at the 245th National Meeting of the American-Chemical-Society (ACS) Location: New Orleans, LA Date: APR 07-11, 2013. **Invited.**

V.D.7 Overcharge Protection for PHEV Batteries (LBNL)

Guoying Chen, Principle Investigator

Environmental Energy Technologies Division
Lawrence Berkeley National laboratory
Berkeley, CA 94720
Phone: (510) 486-5843; Fax: (510) 486-5467
E-mail: gchen@lbl.gov

Start Date: October 2009
Projected End Date: September 2013

Objectives

- Develop and implement an inexpensive, long-lasting mechanism that provides self-actuated, reversible and high-rate overcharge protection for high-energy lithium-ion batteries for PHEV applications.

Technical Barriers

- Abuse tolerance.
- Safety.
- Poor cycle life.

Technical Targets

- PHEV40: 96 Wh/kg, 750 W/kg, 5,000 cycles.

Accomplishments

- Developed an inexpensive and scalable electrospinning technique to fabricate novel electroactive fiber separators suitable for overcharge protection in high-energy lithium cells.
- Demonstrated the most stable overcharge protection yet reported in several Li-ion cell chemistries.
- Obtained stable and high-rate overcharge protection in larger-sized pouch cells. Validated scale-up feasibility of the approach.
- Identified an electroactive polymer with good stability at low voltages and demonstrated the use of single-layer separator in providing stable overcharge protection.

✧ ✧ ✧ ✧ ✧

Introduction

Meeting the DOE targets for Li-ion batteries intended for vehicular applications requires the use of high energy density cells and large battery packs. This will no doubt lead to increased importance in addressing the safety hazards associated with cell overcharge and overdischarge. A variety of conditions may be responsible for overcharging in secondary lithium batteries, including charging at normal rates but beyond rated capacity, overvoltage excursions for varying periods, charging at a rate too high for one electrode without exceeding the maximum voltage, and other more complex scenarios. While overcharging is still a major safety issue for lithium batteries, it also has a major impact on battery life. Even slight overcharging reduces the discharge capacity of a cell, potentially causing overdischarging, increased impedance, and local heating.

Battery packs for consumer electronics are protected by electronic controls and by internal shutdown mechanisms like melting separators and pressure or temperature-activated disconnects. In a multicell stack capable of delivering several hundred volts, permanently shutting down a cell reduces the usable capacity of the stack and adds to the burden of the remaining cells in parallel circuit. The electroactive-polymer approach, developed at LBNL, protects cells by forming a reversible resistive shunt between the current collectors during overcharging. The process is self-activated by voltage, and it does not pose interference during normal cell charge and discharge. Unlike the commonly used redox shuttle method, it conducts overcharge current through an electronic rather than a diffusional path, and therefore is capable of high-rate and low-temperature protection. The polymer can be added to cells in a variety of configurations, opening the possibility for cell designs that best accommodate heat transfer during overcharging. Conversely, overheating in internal redox shuttle protected cells can only be avoided by restricting the cell to low cycling rates.

Approach

Electroactive polymers are used for self-actuating and reversible overcharge protection. The redox window and electronic conductivities of the polymers are fine-tuned to avoid interference with a given battery chemistry's normal operation. The morphology of polymer composite membranes and cell configuration of the protection are optimized to achieve the best rate capability and cycle life.

Results

Electroactive Polymer Fiber Separators. The team previously reported that non-woven electroactive-fiber-composite separators with high porosities and an open pore structures can be produced by electrospinning. The presence of the inert polymer phase reduces the concentration of the electroactive polymer in the composite fibers but does not compromise its electronic continuity. In order to expand the protection voltage window for high-energy cells, bilayer fiber membranes consisting of a high-voltage electroactive polymer, poly[(9,9-dioctylfluorenyl-2,7-diyl)] (PFO) on one side, and a low-voltage polymer, poly(3-butylthiophene) (P3BT) on the other were prepared. Chloroform solutions containing either PFO or P3BT were used for electrospinning, with a small amount of polyethylene oxide (PEO) added to adjust solution viscosity and to ensure the formation of polymer fibers during the process. After the initial deposition of PFO/PEO fibers on an aluminum collector, the P3BT/PEO polymer fibers were then directly electrospun onto the surface of the PFO/PEO film. The individual layer thickness is readily adjusted by controlling the amount of each polymer used during electrospinning. Optical images of the membranes show that smooth and uniform coverage were achieved for both layers (Figure V - 153a and Figure V - 153b). The prepared composite membrane was peeled from the Al substrate and the PEO component was removed by sonication in water. Figure V - 154 shows the top-view SEM images of a 50 µm-thick PFO/P3BT (weight ratio 3:1) fiber membrane obtained from the PFO (Figure V - 154a) and P3BT (Figure V - 154b) sides, respectively. It is clear that removal of the PEO had minimal impact on the fiber morphology, and both types of electroactive fibers were intact and well-connected in a highly porous structure.

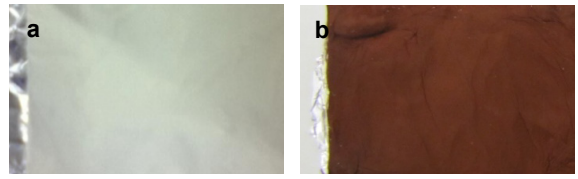

Figure V - 153: Digital images of electrospun-composite membranes on an Al substrate: a) after the deposition of PFO/PEO layer and b) after the deposition of both PFO/PEO and P3BT/PEO layers

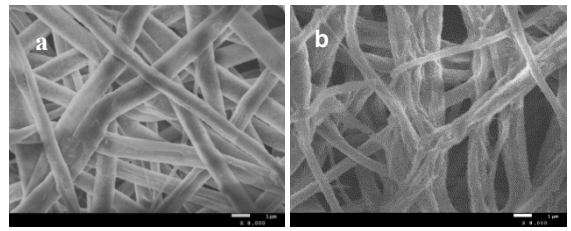

Figure V - 154: Top-view SEM images of an electrospun PFO/P3BT composite membrane: a) PFO side and b) P3BT side

Cells were assembled with the high-voltage PFO side facing the cathode and the low-voltage P3BT side facing the anode. The cycling performance of a spinel $Li_{1.05}Mn_{1.95}O_4$/Li cell protected by such a separator is shown in Figure V - 155a. When cycled at 2/3 C rate and 135% overcharge, the cell repeatedly reached and maintained a steady state potential of 4.2 V. The discharge capacity was retained under the severe overcharge conditions for well over 1,000 cycles in more than 5,000 h or one year of testing time with some rest periods (Figure V - 155b). This is the most stable overcharge protection reported in rechargeable lithium batteries so far, and the results demonstrate the ability of electroactive fiber separators in providing prolonged high-rate overcharge protection.

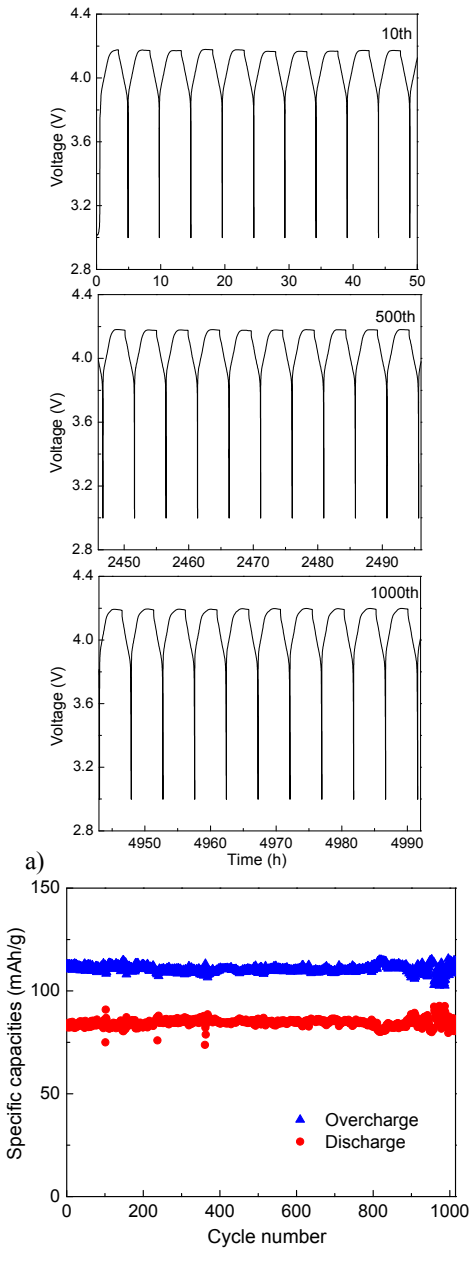

Figure V - 155: a) Charge-discharge cycling profiles and b) specific capacities as a function of the cycle number of a $Li_{1.05}Mn_{1.95}O_4$ half-cell overcharge protected by the electrospun PFO/P3BT composite separator

The performance of a protected $LiNi_{0.8}Co_{0.15}Al_{0.05}O_2$ /Li cell is shown in Figure V - 156. At C/4 rate and 50% overcharge, a constant voltage was reached at 4.2 V and the cell delivered steady performance for more than 160 cycles (Figure V - 156a). The upper limiting voltage is significantly lower compared to that of the previous cells protected by a similar PFO/P3BT composite prepared with either a microporous or glass-fiber membrane. This is likely due to improved polymer distribution and reduced internal resistance in the electrospun fiber separator. The discharge capacity of this cell gradually decayed during cycling (Figure V - 156b), a phenomenon previously observed in $LiNi_{0.8}Co_{0.15}Al_{0.05}O_2$ cells charged to 4.2 V. As a result, the extent of overcharge protection provided by the electroactive separator gradually increased, reaching nearly 100% at 160 cycles.

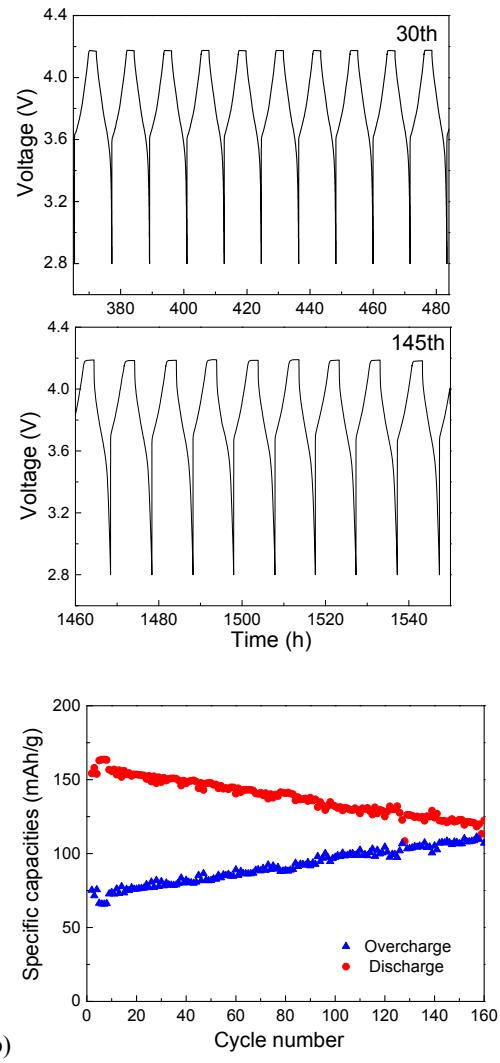

Figure V - 156: a) Charge-discharge cycling profiles and b) specific capacities as a function of the cycle number of a $LiNi_{0.8}Co_{0.15}Al_{0.05}O_2$ half-cell overcharge protected by the electrospun PFO/P3BT composite separator

The scalability of overcharge protection based on electroactive fiber composite separators was also evaluated. A $Li_{1.05}Mn_{1.95}O_4$-Li pouch cell with an electrode area of 3cm x 4cm, which is 15 times larger than that in a typical "Swagelok-type" cell, was equipped with the combination of the PFO/P3BT glass-fiber composites, a configuration previously used in the "Swagelok-type" cell tests. Figure V - 157 shows the

room-temperature voltage profiles of the cell at the various cycling rates. At C/8 rate and 125% overcharge, the cell was reversibly protected at 4.3 V during the first 50 cycles. The steady-state voltage increased with the current density, reaching 4.35 and 4.55 V at C/4 and C rates, respectively. Stable protection was achieved at all rates tested. Compared to the previous protection achieved on the pouch cells equipped with the PFO/P3BT Celgard composites, the upper cell limiting voltage was significantly reduced, further confirming lowered internal resistance and improved performance in the fiber composites.

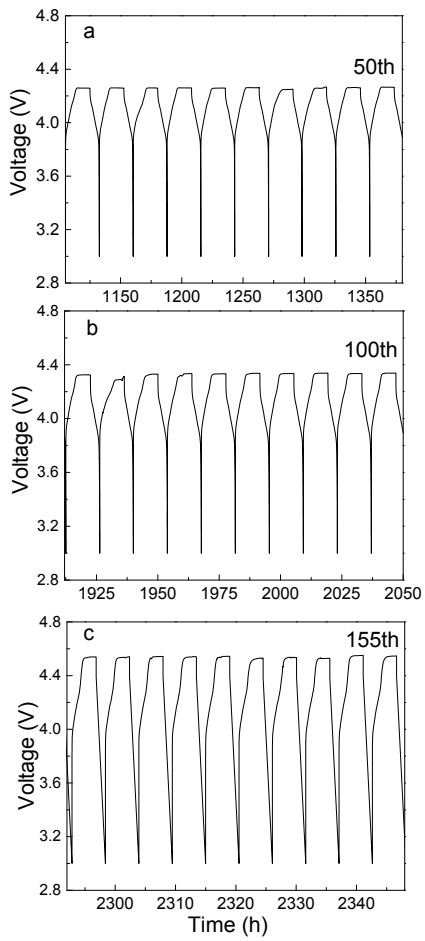

Figure V - 157: Varying-rate cycling profiles of a $Li_{1.05}Mn_{1.95}O_4$ /Li pouch cell overcharge-protected by the PFO/P3BT glass-fiber composites: a) C/8 rate and 125% overcharge, b) C/4 rate and 150% overcharge and c) C rate and 300% overcharge

Alternative electroactive polymers. Poly[(9,9-dioctylfluorenyl-2,7-diyl)-co-(1,4-phenylene)] (PFOP) was found to have an onset oxidation potential of 4.25 V, which is one of the highest values reported so far. When scanning the polymer between 0.1 and 4.5 V vs. Li/Li^+ at 5 mV/s, no obvious degradation was observed on the cyclic voltammogram (Figure V - 158a). This suggests improved low-voltage stability and the possibility of using single-layer polymer composite for overcharge.

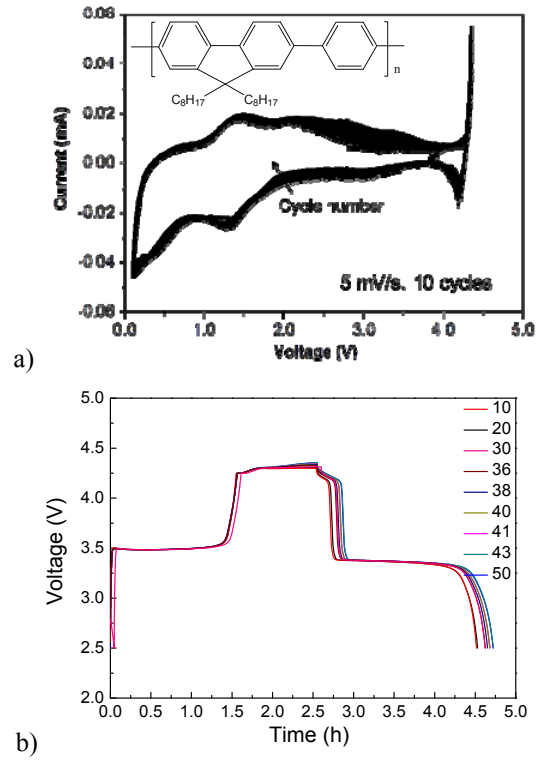

Figure V - 158: a) Cyclic voltammogram of PFOP in 1M $LiPF_6$ in EC: DEC electrolyte and b) cycling profiles of a $LiFePO_4$ half-cell overcharge-protected by the PFOP composite separator

To evaluate this possibility, a PFOP composite membrane was prepared by impregnating a concentrated chloroform solution of the polymer into a microporous Celgard membrane and then used as the separator in a "Swagelok-type" $LiFePO_4$ half-cell with 1M $LiPF_6$ in 1:1 (v/v) EC and DEC electrolyte. The cell was charged and discharged at 0.65 C rate and 80% overcharge. A steady-state potential was reached at 4.3 V which remained nearly constant during the test, suggesting reversible internal shorting established by PFOP (Figure V - 158b). Excellent capacity retention was also observed. The improved low-voltage stability of the polymer allows for stable single-polymer protection, which eliminates the need of the bilayer configuration that was previously adopted to protect the high-voltage polymer from degradation at the anode potential.

Conclusions and Future Directions

Novel electroactive-fiber-composite membranes with a uniform distribution of electroactive polymer were prepared by a simple electrospinning process. When used as battery separators, the membranes provided stable overcharge protection with a significant improvement in cycle life over that achieved with the previous composites prepared by solution impregnation. Electrospinning is a cost-effective and scalable way to produce lithium-ion battery separators with reliable voltage-regulated shunting. An electroactive polymer capable of providing single-layer overcharge protection was also identified and stable cycling performance in protected cells was achieved. Future work will further evaluate the rate capability of the fiber composites, as well as the performance of fiber-composite separators including a supporting polymer that is stable in the cell operating window, such as PVdF and PMMA.

FY 2013 Publications/Presentations

1. B. Wang, T. J. Richardson and G. Chen, "Stable High-Rate Overcharge Protection for Rechargeable Lithium Batteries," Physical Chemistry Chemical Physics, 15 (18), 6849 (2013).
2. G. Chen and T. J. Richardson, "High-Rate Overcharge-Protection Separators for Rechargeable Lithium-Ion Batteries and The Methods of Making The Same," PCT Application based on U.S. Provisional Application 61/647,389, May 2013.
3. G. Chen, "Overcharge Protection for Safer Li-ion Batteries," Energy Storage and Distributed Resources Department Seminar, Berkeley, CA, February 2013.
4. G. Chen, "Overcharge Protection for PHEV Batteries," DOE Hydrogen Program and Vehicle Technologies Program Annual Merit Review and Peer Evaluation Meeting, Washington, DC, May 2013.
5. "Overcharge Protection for Safer and Lasting Rechargeable Lithium Batteries," G. Chen, Berkeley Energy and Resources Collaborative Innovation Expo, Berkeley, CA, October 2013. The poster presentation won the 3rd place award.
6. "Reversible Overcharge Protection for Safer and Lasting Rechargeable Lithium Batteries," G. Chen, the 224th ECS Meeting, San Francisco, CA, October 2013.

V.D.8 Development of Abuse-Resistant Electrolyte Components (SNL)

Christopher J. Orendorff,
Ganesan Nagasubramanian,
Kyle R. Fenton, and Travis M. Anderson

Sandia National Laboratories
P. O. Box 5800, Mail Stop 0614
Albuquerque, NM 87185-0614
Phone: (505) 844-5879; Fax: (505) 844-6972
E-mail: corendo@sandia.gov

Collaborators:
Ram Nagubandi (Binrad Industries)

Start Date: October 2012
Projected End Date: September 2013

Objectives

- Develop and evaluate advanced material components that will lead to more abuse tolerant lithium-ion cell and battery systems.
- Study degradation mechanisms in lithium-ion cells that lead to poor abuse tolerance (runaway thermodynamics, gas evolution, electrolyte combustion).
- Evaluate materials in 18650 cells under abusive conditions to quantify safety performance improvements

Technical Barriers

There are several technical barriers to achieving the goals stated above including:

- Develop lithium-ion cells that are intrinsically abuse tolerant and do not lead to high order catastrophic failures.
- Mitigate the gas evolution and decomposition of the electrolyte.
- Passivation of cathode runaway reactions and interfacial reactions with electrolyte.
- Limited quantities of advanced materials (and numbers of cells with new materials) to evaluate abuse response.

Technical Targets

- Quantify the thermal runaway response of materials at the cell level (18650).
- Determine the effect of advanced material components on the abuse response of lithium-ion cells.
- Evaluate the thermal response of candidate active materials.
- Optimize electrochemical performance of new electrolyte components to meet DOE goals

Accomplishments

- Demonstration of an improvement in thermal runaway free energy for LiF/ABA electrolyte cells compared to $LiPF_6$-based electrolyte cells
- Purification and demonstration of improved performance of electrolyte salt LiF/ABA-1B.
- Synthesis and characterization of LiF/ABA-2 with greater electrochemical stability.

✧ ✧ ✧ ✧ ✧

Introduction

As lithium-ion battery technologies mature, the size and energy of these systems continues to increase (> 50 kWh for EVs); making safety and reliability of these high energy systems increasingly important. While most materials advances for lithium-ion chemistries are directed toward improving cell performance (capacity, energy, cycle life, etc.), there are a variety of materials advancements that can be made to improve lithium-ion battery safety. Specifically, issues related to conventional $LiPF_6$/carbonate electrolyte stability including PF_6^- reactivity, combustion enthalpy, and flammability continue to limit the safety performance of lithium-ion cells. This report highlights work to develop electrolyte components that inherently make lithium-ion cells more resistant to abuse conditions.

Approach

Our approach to developing advanced materials to improve abuse response focuses on redesigning lithium-ion cell electrolytes. This work starts with developing novel two-part electrolyte salts based on inherently stable lithium salts and anion binding agents (ABAs). The ABA components have two important design features: (1) improve the solubility of alternative lithium salts in carbonate solvents by coordinating the salt negative ion at the electron withdrawing coordination site of the ABA and (2) passivate chemical decomposition reactions at electrode interfaces or in the

bulk electrolyte to minimize the consequences and severity of thermal runaway and electrolyte combustion.

The effect of advanced electrolyte components on the thermal response of full cells is determined using several techniques. Full cells will be fabricated in the SNL cell protrotyping facility (2032 coin cells and 18650 cells). Calorimetry techniques will be used to quantifiy imrpovements in heat generation during decomposition reactions. These include accelerating rate calorimetry (ARC), isothermal battery calorimetry (IBC), and differential scanning calorimetry (DSC). Abuse tolerance improvements will be determined by abuse testing full cells which includes thermal, electrical and mechanical abuse conditions.

Results

The use of lithium fluoride (LiF) electrolyte salt has been considered as an alternative to $LiPF_6$ because of its chemical and thermal stability, but early generation anion binding agents (ABAs, used to improve LiF solubility) were large molecules that were inapplicable to lithium-ion cell systems (large molecular weights, low rate capability, low conductivity, voltage instability, etc.). In collaboration with Binrad Industries we have developed LiF/ABA salts for lithium-ion cells to show improved thermal stability and to eliminate some of the shortcomings of using $LiPF_6$ salts.

The primary driver for the development of LiF/ABA-based electrolytes is their ability to stabilize a cell runaway reaction. Figure V - 159 shows DSC on NMC cathodes with $LiPF_6$ and LiF/ABA electrolytes (top) and ARC profiles for 18650 NMC/graphite cells with the same electrolytes (bottom). These results show reduced heat generation not only on the cathode electrodes in DSC, but a significant reduction in the runaway enthalpy and reaction kinetics in 18650 cells. While the mechanism of this behavior is still under investigation, previous results suggest a passivation of the electrode/electrolyte interface by the ABA.

There are a few challenges with the electrochemical performance of the initial LiF/ABA-1A electrolytes. These include (1) 2x lower conductivity than $LiPF_6$ at ambient temperature (~7 mS/cm), (2) capacity fade at the anode electrode because of poor SEI formation, and (3) electrochemical stability (ABA molecule reduction near 0V vs. Li/Li+ and oxidation close to 4.5 V vs. Li/Li+). As prepared, the crystal structure of the initial LiF/ABA-1A shows a DMSO molecule bound to the coordination site of the ABA (Figure V - 160). In spite of its reasonable performance, the bound DMSO limits the ability of ABA to dissolve LiF. The systhesis was improved to prepare the LiF/ABA directly, leading to a replacement of the bound DMSO by afluoride anion (LiF/ABA-1B). The crystal structures for both modules are shown in Figure V - 160 (top). Removal of the DMSO impurity improved the LiF/ABA conductivity by a factor of 2 to 14 mS/cm giving the LiF/ABA comparable conductivity to $LiPF_6$ in EC:EMC shown in Figure V - 160 (bottom).

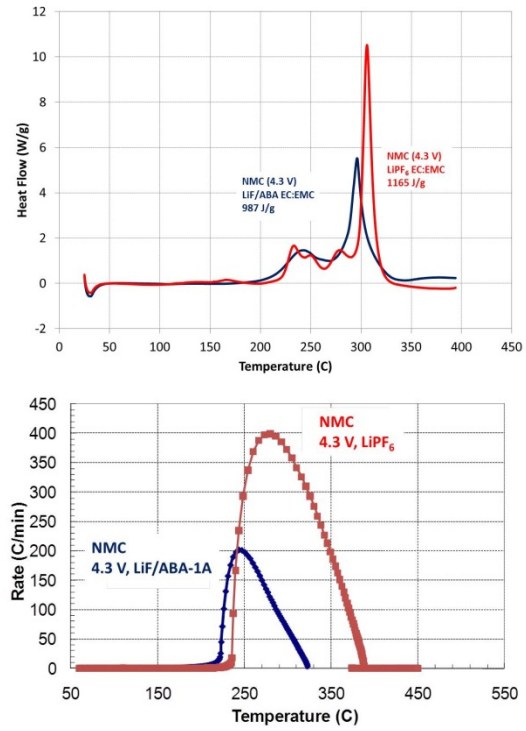

Figure V - 159: (top) DSC of NMC cathodes and (bottom) 18650 cells with in 1 M LiF/ABA-1A in EC:EMC (3:7) and in 1.2 M LiPF6 in EC:EMC (3:7) electrolyte

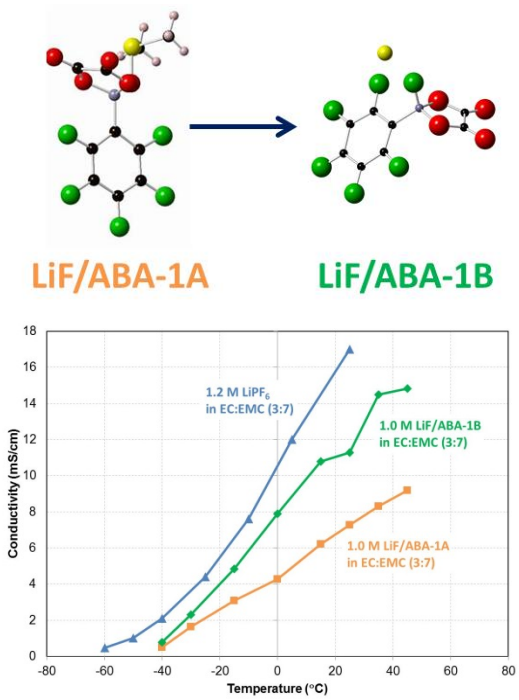

Figure V - 160: Crystal structures of LiF/ABA-1A and -1B and (bottom) conductivity of LiF/ABA-1A, -1B, and $LiPF_6$ in EC:EMC (3:7)

Work to optimize LiF/ABA electrolyte formulations includes improving the capacity fade at the negative electrode. Figure V - 161 shows discharge capacity as a function of cycle number for NMC/graphite cells in 1M LiF/ABA-1A in EC:EMC (3:7). Without any electrolyte additives, the cell shows almost a linear 4% fade/cycle because of poor SEI film formation at the negative electrode. The addition of 2% VC to the electrolyte helps to stabilize the anode interface and significantly reduces the capacity fade during formation. Further improvements to stabilizing the negative electrode interface are made with the addition of 10 mM $LiPF_6$ as an additive to initiate SEI formation. Figure V - 162 shows cyclic voltammetry (CV) data (current density vs. potential) for LiF/ABA cycled from 0-4.5 V (vs. Li/Li+) for 1 M LiF/ABA in EC:EMC and 1 M LiF/ABA + 10 mM $LiPF_6$ in EC:EMC. The addition of 10 mM $LiPF_6$ appears to stabilize the LiF/ABA at negative potentials because of good SEI formation with a current density of -200 $\mu A/cm^2$ at the first cycle (comparable to 1.2 M $LiPF_6$ in EC:EMC electrolyte).

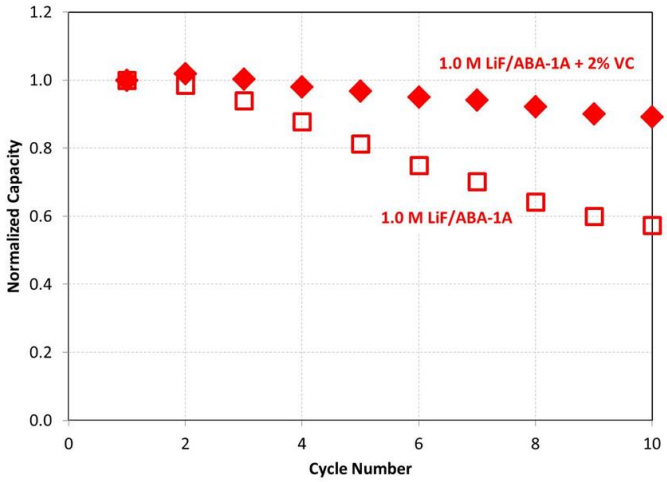

Figure V - 161: Normalized discharge capacity as a function of cycle number for NMC cells in LiF/ABA electrolyte with and without 2% VC (solid and open symbols)

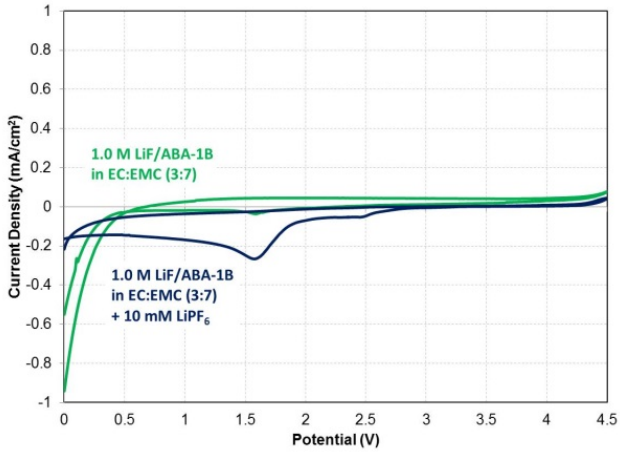

Figure V - 162: Cyclic voltammetry of LiF/ABA electrolyte with and without 10 mM $LiPF_6$ from 0-4.5 V (vs. Li/Li+)

Another task in optimizing the electrolyte performance is to improve the high voltage stability of LiF/ABA for use not only as a conventional cell chemistry but also for use with high voltage electrochemical couples. Figure V - 163 shows the cyclic voltammetry data of LiF/ABA and $LiPF_6$ electrolytes. In the absence of any other electrolyte additives, LiF/ABA-1B has a current density of ~80 µA at 4.5 V vs. Li/Li+, compared to ~20 µA at 4.5 V for $LiPF_6$. The structure of our ABA molecule was modified to improve the voltage stability. The CV of LiF/ABA-2 shows a reduction in the current density at 4.5 V and is comparable to $LiPF_6$ in EC:EMC. It is important to note that the LiF/ABA-2 suffers from the same DMSO impurity as described for LiF/ABA-1 and gives rise to the reduction peak at 2.2 V. This will be purified to improve performance in FY14.

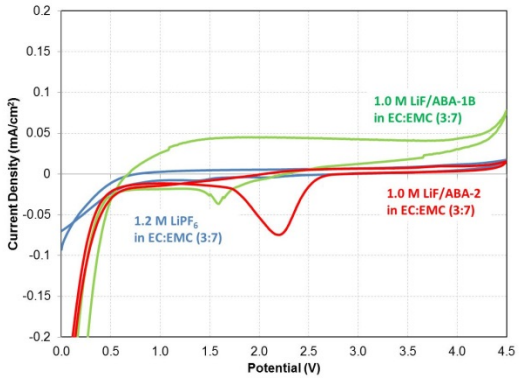

Figure V - 163: Cyclic voltammetry of 1.2 M $LiPF_6$ (blue trace), LiF/ABA-1B (green trace), and -2 (red trace) in EC:EMC (3:7)

Conclusions and Future Directions

LiF/ABA electrolytes are under development with promising results as potential lithium-ion cell components that can be designed to reduce the cell thermal runaway free energy. The challenges associated with electrochemical performance including SEI formation, capacity fade and voltage stability are addressed and improved through molecular design and synthesis of ABAs and optimization of electrolyte formulations. Future directions include demonstration of LiF/ABA electrochemical and safey performance in 18650 cells, continued improvements in observed capacity fade and voltage stability, and characterization of long term stability. We also airm to submit candidate LiF/ABA molecules to the Materials Energineering Research Facility (MERF) at Argonne for the synthesis to be scaled.

FY 2013 Publications/Presentations

1. C. J. Orendorff, J. Lamb, K. R. Fenton, and L. A. M. Steele, "Approaches to Evaluating and Improving Lithium-Ion Battery Safety" AABC February 2013.
2. J. Orendorff, "Approaches to Evaluating and Improving Lithium-Ion Battery Safety" CU-Boulder, February 2013.
3. 2013 DOE Annual Peer Review Meeting Presentation.

V.E Process Development

V.E.1 Manufacturability Study and Scale-Up (ORNL)

Claus Daniel, David Wood III, Jianlin Li, Debasish Mohanty
Oak Ridge National Laboratory
One Bethel Valley Road
P.O. Box 2008, MS-6472
Oak Ridge, TN 37831
Phone: (865) 241-9521; Fax: (865) 241-5531
E-mail: danielc@ornl.gov

Collaborators:
Ashfia Huq (ORNL), Athena Safa-Sefat (ORNL), Andrew Payzant (ORNL), Andy Jansen (ANL), Bryant Polzin (ANL), Chris Orendorff (SNL), Robert Tenent (NREL), Jerry Forbes (Frontier Industrial), John Arnold (Miltec UV), Derek Mainstone (Conquip), Jason Hamilton (Scientific Climate Systems), William Eggers (Bio-logic USA), Ben Schafer (Espec America), multitude of materials suppliers

Start Date: October 1, 2012
Projected End Date: September 30, 2015

Objectives

- Provide a processing and device level scale-up facility and corresponding expertise to the ABR program to scale technology to 1-7 Ah pouch cell demonstration.
- Allow benchmarking of new materials and systems in large scale pouch format.
- Process electrodes for round robin testing and integration in other systems.

Technical Barriers

- Lack of availability of materials processing, reliable cell assembly, and scaling facilities and benchmarking for devices greater than 0.5 Ah.
- Lack of availability for testing new processing and manufacturing routes.

Technical Targets

- Develop processing routes and standards to meet $290/kWh USABC storage goal for PHEVs and <$125/kWh for EVs.
- Lifetime of 10 years and 1,000 cycles at 80% DOD for EVs and 5,000 deep discharge cycles for PHEVs.

Accomplishments

- Successful installation and startup of facility and successful operation well above specified performance (dew point spec: <-30°C, achieved: <-56°C).
- Comparison of tape-cast and slot-die electrode coatings.
- Determined maximum electrode stack number and capacity in 12 mm thick pouch cell with ABR cathode reference NCM 532 and anode reference graphite A10/12 and demonstration of assembly issues with pouches beyond 10 mm thickness.
- Supplied over 100 ft of electrodes to ABR collaborators.

✧ ✧ ✧ ✧ ✧

Introduction

The ABR program's main objective is to solve issues for full electrochemical cells. While many problems can be solved with coin cells, scalability and manufacturability need to be addressed on a full pouch cell basis. Argonne National Laboratory's Cell Fab demonstrates electrochemistry in full pouch cells in devices up to 0.5 Ah. This effort collaborates with Argonne and other collaborators to scale devices beyond 0.5 Ah and further perform manufacturing science to evaluate new materials, develop new manufacturing routes, and enable a domestic supply chain.

Boundary conditions and edge effects need to be adequately addressed. Cell studies need to have a sufficient individual electrode area in order to allow large-scale testing at which further scaling to automotive battery sizes will be "engineering only." Electrode processing and cell assembly studies need to be performed at sufficient scale in order to allow for cost-saving analysis and low-cost processing development for establishing a domestic materials and battery supply chain.

Approach

DOE's open-access Battery Manufacturing R&D Facility (BMF) at the ORNL is specifically designed to take gram-to-kilogram quantities of new materials for performing R&D from slurry processing, through current collector treatment, electrode deposition and processing, and secondary drying studies to full battery pouch cell assembly and testing. Cell dimensions are 66 mm x 99 mm and can range in thickness from single electrode cells to 12 mm thick cells resulting in capacities of up to 6-7 Ah. This facility was set up to integrate new materials, optimize known electrochemical couples in pouch cells, analyze and optimize manufacturing steps individually, and benchmark all materials and processes versus the current state of the art.

The focus of the first year of the BMF was testing of commercially benchmarked electrodes and demonstration of cell performance with ORNL produced cells. Cells are being manufactured for integration into modules and packs for system-level testing. Electrode processing and secondary drying are also being optimized. New materials from our industrial supply chain partners (Vorbeck, Plextronics, FMC, etc.) are being integrated and benchmarked against commercially available technologies. New binder curing technologies are being demonstrated with new cell designs with Miltec UV.

Results

Installation and level of readiness. The 1,400 ft^2 dry room has been installed and is constantly running at 20°C with dew point and relative humidity below -56°C and 0.1%, respectively. A list of equipments (as shown in Table V - 12) have been installed at the BMF and they are currently up and running.

Table V - 12: ORNL BMF equipment list

Equipments	Description
Dry room	For maintaining low humidity environment for battery assembly
Fume hood	For handling chemicals
Balances	For weighing chemicals with various quantities
High shear and planetary mixers	For mixing slurry with various quantities, up to 2 liters and at different shear rates
Corona Treater	For modification of surface energy to improve wetting of wet coating on substrates
Tape caster	For small coating and proof-of-concept
Slot-die-coater	For high quality roll-to-roll electrode manufacturing
Karl-Fischer titration	For evaluation of residual moisture in samples
Vacuum oven	For drying electrodes before cell assembly
Pouch cell assembly line	For pouch cell assembly from forming pouches, punching electrodes, stacking jelly rolls, welding tabs, filling electrolyte to sealing pouch cells
Small assembly line for special pouch cells	For assembling special pouch cells with different dimensions and/or materials sensitive to air, moisture, etc.
Glove boxes	For coin cell and special pouch cell assembly and battery disassembly
Environmental chambers	For temperature control during battery aging and testing
Potentiostats	For testing battery performance
Optical microscope	For observation of electrode morphology and in-process microscopy

Figure V - 164 show a process of cathode coating via a slot-die coater at the BMF. Slurry is supplied by a progressive pump. Coatings are processed continuously and can be up to 10 inches wide. Drying capabilities include a drying furnace with 2 infrared heaters and 7 hot are blowers with independently controlled temperature in each zone. Additional drying capabilities are heating plates, convection heaters, infrared furnaces, and parallel and anti-parallel hot air roll to roll heaters. In the near future, an ultraviolet source will be added. This provides flexibility in studying drying protocols for electrode manufacturing. Figure V - 165 shows a roll of ABR standard A12 graphite anode and $LiNi_{0.5}Mn_{0.3}Co_{0.2}O_2$ cathode (NMC532).

Figure V - 166 shows intermediate products of each step during battery manufacturing: Dispersion/slurry, electrode coating, pouch, punched electrodes, electrode stack or "jelly roll," and finished pouch cell. The dimensions of cathode and anode are 8.44 cm×5.60 cm and 8.64 cm×5.80 cm, respectively. Pouch cell capacity ranges from 100 mAh to 7 Ah on single-side-coating electrodes.

Figure V - 164: Demonstration of electrode coating via slot-die coater

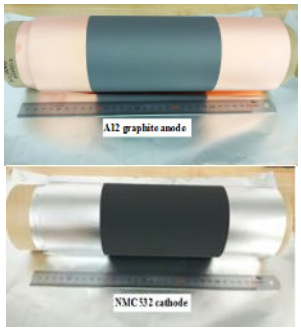

Figure V - 165: A roll of ABR standard A12 graphite anode and NMC532 cathode

Figure V - 166: Intermediate samples in battery manufacturing and finished pouch cell

Areal loading with pump speed and line speed. Coating thickness and areal loading of coating are determined by the pump speed and coating line speed. Figure V - 167 shows areal loading of NMC532 cathodes as a function of coating line speed and pump speed. The areal loading is in linear relation with line speed and pump speed.

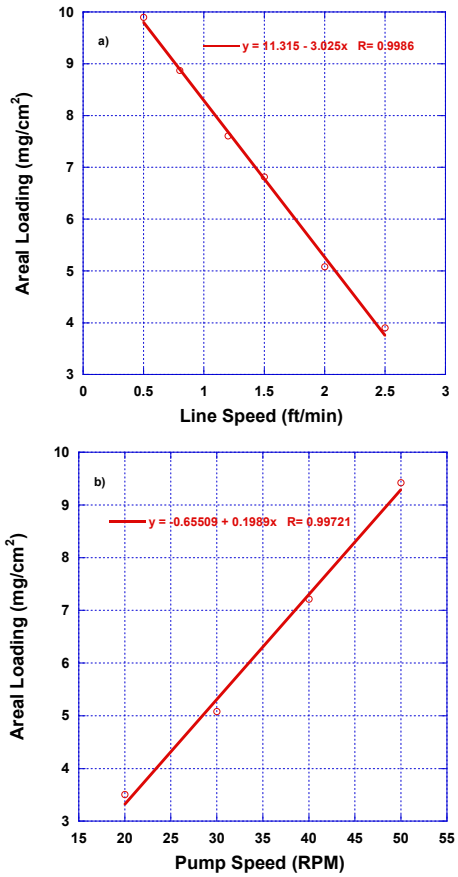

Figure V - 167: Calibration of areal loading of NMC532 cathode with line speed (a, pump speed=40 RPM) and pump speed (b, line speed=1 FPM)

Round robin testing. A roll of ABR standard A12 anode and NMC532 cathode fabricated at BMF was sent to ANL for round robin testing. Detailed information on the electrodes is listed in Table V - 13. The anode to cathode capacity ratio is 1.36. The cross-section of both A12 anode and NMC532 cathode is shown in Figure V - 168.

The electrode performance from full coin cells is plotted in Figure V - 169. The full cells went through four formation cycles at 0.1C between 3.0 and 4.3V before subsequent test. The rate performance shown in Figure V - 169a) was tested at charging and discharging rates of 0.2C, 0.5C, 1C and 2C, respectively, between 3.0 and 4.1 V. The capacity was reduced from 127 mAh/g of NMC532 to 102 mAh/g when the discharging rate increased from 0.2C to 2C. Capacity loss and RPT (reference performance test) capacity vs cycle number was tested between 3.0 and 4.1V, cycling the full cells at 0.2C for the first 19 cycles and 0.5C in subsequent cycles, HPPC (hybrid pulse power characterization) every 50 cycles and RPT (C/24) every 50 cycles. Two of the three cells tested went beyond 500 cycles before capacity dropped to 80% of original capacity. The three cells showed an RPT capacity of 80, 100 and 120 mAh/g after 400 cycles, respectively.

Table V - 13: Electrode information

Electrode	Composition	Areal loading (mg/cm^2)	Porosity (%)
A12	A12/Super P Li/9300 PVDF =92/2/6 wt	7.51	52.2
NMC532	NMC532/Denka carbon black/ 5130 PVDF =90/5/5 wt	12.57	49.0

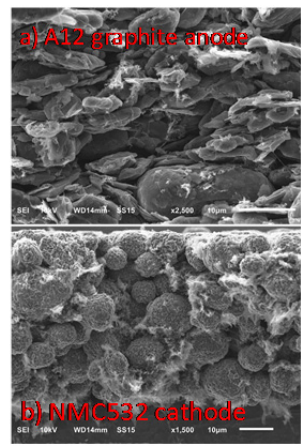

Figure V - 168: Cross-section morphology of A12 graphite anode (a) and NMC532 cathode (b)

Comparison in electrode performance from different coating techniques. NMC532 with TRD202A binder (JSR) was coated with slot-die coater and tape caster through aqueous processing and their performance was compared in Figure V - 170. Figure V - 170 shows the discharge capacity of both cathodes from half coin cells. The one from slot-die coating demonstrated not only much better rate performance, especially at high C-rates, but also cyclic life. There was dramatic capacity degradation after 80 cycles in the one from tape caster and the deviation from cell to cell was also much more substantial compared to that from slot-die coating. Thus, the NMC532 cathode from slot-die coating exhibited much superior electrode performance.

Pouch cell performance. ABR standard A12 anode and NMC532 cathode were assembled into pouch cells with various capacities. Figure V - 171a) shows cyclic performance of one pouch cell with 70 mAh at 0.1C. There was a substantial irreversible capacity loss at the 1st cycle due to formation of solid electrolyte interface (SEI).

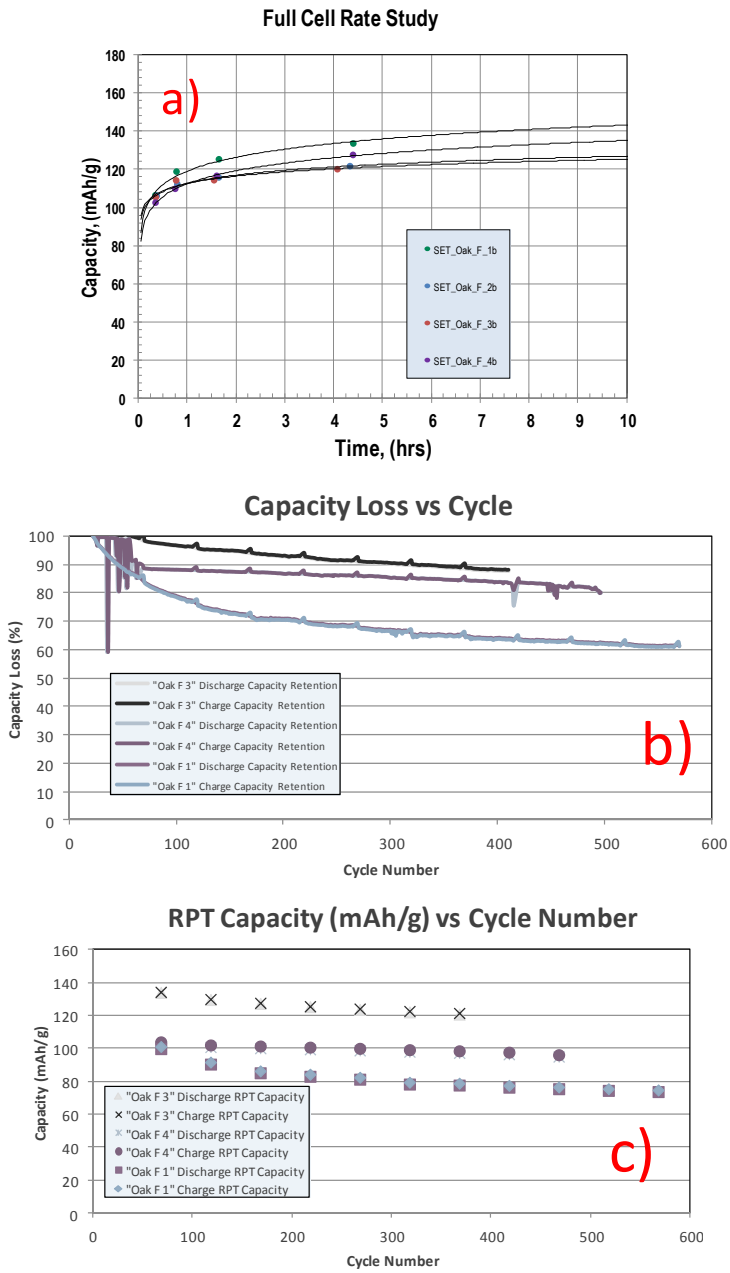

Figure V - 169: Full cell performance of ABR standard A12 anode and NMC532 cathode (a rate performance; b) capacity loss vs cycle number and c) RPT capacity vs cycle number. (Data from ANL)

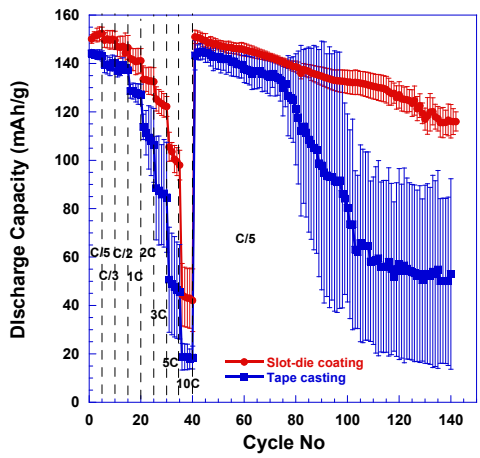

Figure V - 170: Comparison of NMC532 cathode performance through slot-die coating and tape casting

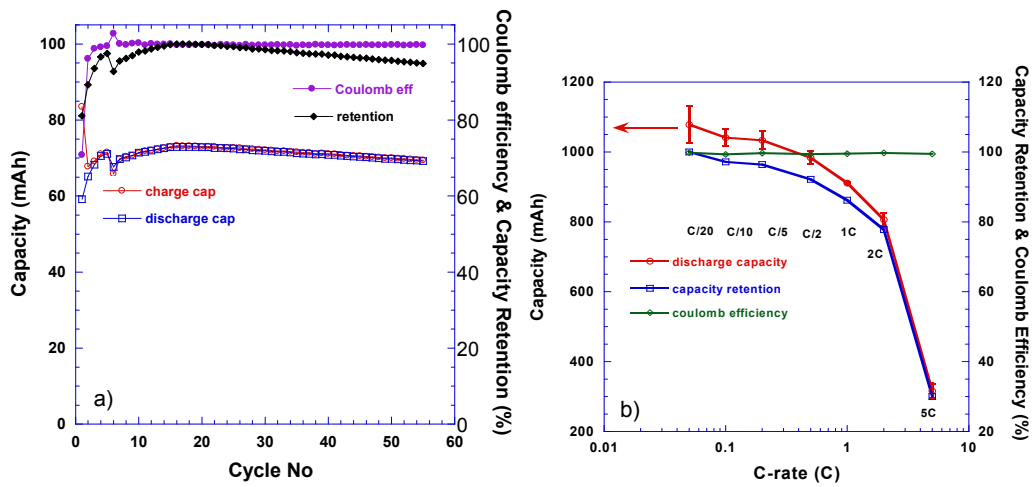

Figure V - 171: Pouch cell performance a) cyclic performance of a 70 mAh pouch cell and b) rate performance of 1Ah pouch cells

Coulombic efficiency increased dramatically and maintained above 99.5% in subsequent cycles. Capacity retention was above 95% after 55 cycles. Figure V - 171b) shows rate performance from nine pouch cells with 1-1.1 Ah. The cells demonstrated excellent repeatability and rate performance.

Construction of pouch cell with maximum capacity. A pouch cell was assembled to estimate maximum capacity with single-side-coated electrodes. The capacity depends on the layers of electrodes, which is limited by the maximum draw depth sustained by the pouch cell packaging material. As shown in Figure V - 172, when the depth exceeded 5.5 mm, mechanical damage to the polymer liner due to stretching started showing a color change along the two long edges. This indicated potential tearing or mechanical failure in the liner material of the packaging laminate. To accommodate more layers of electrodes, a double cup pouch was formed from two pouches with 5.5 mm depth. Also, the jelly roll for the cell with maximum capacity was divided into two separate jelly rolls with 30 layers of NMC532 and A12 in each jelly roll, respectively. This is to overcome misalignment issues in electrode stacking and ease of handling the stacks in the automatic stacker. Each jelly roll was welded with an aluminum and a nickel tab to the cathode and anode, respectively, before the two jelly rolls were welded together. The jelly roll was very thick and posed problems during welding tabs to the jelly roll, which eventually led to poor welding and low capacity as addressed later in this report. The pouch cell was filled with 28 g 1.2M $LiPF_6$ in EC/DEC (3/7 wt), a tab charge was applied, and then the cell was aged at 60°C for 48 h before formation cycle.

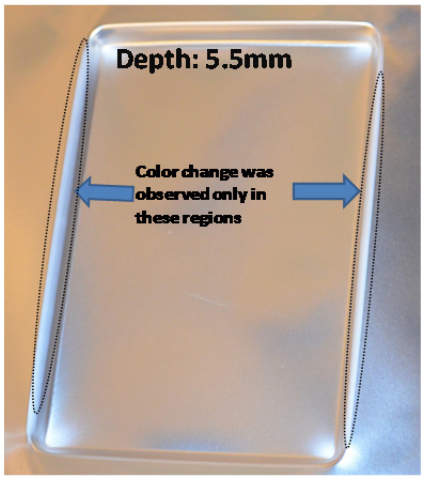

Figure V - 172: Pouch material with 5.5 mm depth showing sign of material tearing at the long edges

Figure V - 173: Pouch cell showing gas generation during aging process

There was substantial gas generation during the aging step as evidenced by the swelling in the pouch cell shown in Figure V - 173. The pouch cell was cut open and resealed in vacuum before testing. The pouch cell was estimated to be 6.5 Ah based on the electrode materials. However, it only delivered 1.52 Ah in capacity after formation cycles. The welding between one Al tab and one jelly roll was disconnected, which means that parts of the jelly roll could not participate in the cell test. This resulted in an immediate drop in capacity by 3.25 Ah. In addition, the strained seals allowed leakage of electrolyte around the tabs. The welding problem is due to short tabs (8 mm) in the BMF electrode design. The problem has been solved by welding the jelly roll at the middle instead of at one end. New cells will be assembled with the improved assembly procedure. It is expected that calendaring and double-side-coating will allow pouch cells to deliver up to 10 Ah.

Development of holders for pouch cell testing. It is critical to maintain stack pressure during testing. The amount of pressure has a significant effect on cell performance. Two types of holders have been developed, one with plastic material and the other with aluminum as shown in Figure V - 174. The plastic holder resulted in low or no significant stack pressure due to bending when tightening the wing screws. As a result, the performance was very poor as shown in Figure V - 175. When replacing the plastic holder with aluminum, the pouch cell performance was substantially improved, especially at high C-rates.

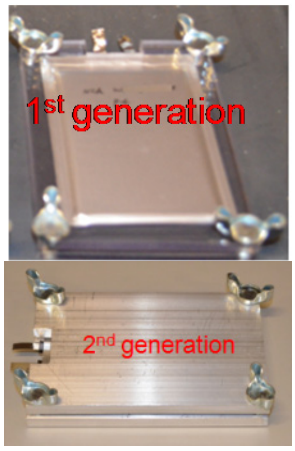

Figure V - 174: Pouch cells with two types of holders

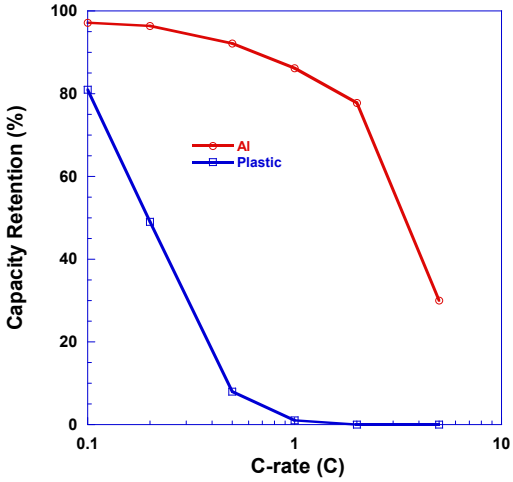

Figure V - 175: Comparison in pouch cell performance with two types of holders

Provide expertise for battery manufacturing and pouch cell assembly to collaborators. While the BMF efforts are funded for ABR activities only, the BMF expertise leverages many other activities funded through other industrial and federal sponsors. The BMF has successfully manufactured pouch cells and provided samples for many collaborators. This includes cells for other ABR work to characterize structure evolution of LMR-NMC cathode by neutron scattering and providing samples for other projects, including DOE's Manufacturing Demonstration Facility (MDF) for projects with FMC Lithium, industrial projects with Plextronics, and DOE's Clean Energy Research Center - Clean Vehicle Center, and others.

Conclusions and Future Directions

The BMF has installed a variety of instruments and has demonstrated successful pouch cell manufacturing. It has delivered pouch cells not only to internal projects but also several external projects, including promoting products for industry partners.

The BMF will continue to develop techniques in battery manufacturing to improve the reproducibility and production rates. Next year, a strong BMF focus will be on double-sided electrode fabrication. Special attention will be paid to edge alignment retrofitting for slot-die coater.

FY 2013 Publications/Presentations

1. D.L. Wood, III, J. Li, D. Mohanty, C. Daniel, B.L. Armstrong, R.B. Dinwiddie, H. Wang, R.M. Trejo, N.C. Gallego, C.I. Contescu, J.Y. Howe, R.A. Meisner, J. Kiggans, and B.D. Brown, "Advanced Materials Processing and Novel Characterization Methods for Low-Cost, High Energy-Density Lithium-Ion Batteries," *Proceedings of the Advanced Automotive Battery Conference* (2013).
2. Claus Daniel, David Wood, Jianlin Li, Debasish Mohanty, Beth Armstrong, and Jim Kiggans, "Cell Materials and Manufacturing," 2013 Cummings Energy Storage Systems Summit, Columbus, IN, October 29-30, 2013 (invited).
3. Claus Daniel, David, Wood, Jianlin Li, Beth Armstrong and Jim Kiggans, "Battery Production Technologies" Energy Storage Solution Industrial Symposium, Oak Ridge, TN, September 4, 2013 (invited).
4. Jianlin Li, Debasish Mohanty, Bradley Brown, David Wood, and Claus Daniel, "Status on electrode fabrication and battery manufacturing at ORNL's Battery Manufacturing R&D Facility," 2013 Clean Energy Research Center-Clean Vehicle Center-seminar Series, Ann Arbor, MI, July 17, 2013 (invited).
5. Claus Daniel, Debasish Mohanty, Jianlin Li, and David Wood, "Overview and progress in cathode materials for lithium ion batteries," 1st International Freiberg Conference on Electrochemical Storage Materials, Freiberg, Germany, June 3-4, 2013 (invited).
6. Claus Daniel, David Wood, Jianlin Li, Beth Armstrong, Jim Kiggans, Debasish Mohanty, and Sergiy Kalnaus, "Electrification of transportation-cost and opportunities," Bridging the Gap Conference 2013, Oak Ridge, TN, March 5-6, 2013 (invited).
7. David Wood, Jianlin Li, Debasish Mohanty, Claus Daniel, Beth Armstrong, Ralph Dinwiddie, Hsin Wang, Rosa Trejo, Nidia Gallego, Cristian Contescu, Jane Howe, Roberta Meisner, Jim Kiggans, and Bradley Brown, "Advanced materials processing and novel characterization methods for low-cost, higher energy-density lithium-ion batteries" Advanced Automotive Battery Conference 2013, Pasadena, CA, February 4-8, 2013 (invited).

V.E.2 Overcoming Processing Cost Barriers of High-Performance Lithium-Ion Battery Electrodes (ORNL)

David L. Wood, III, Jianlin Li, Claus Daniel, and Beth Armstrong
Oak Ridge National Laboratory
One Bethel Valley Road
P.O. Box 2008, MS-6065
Oak Ridge, TN 37831
Phone: (865) 574-1157; Fax: (865) 241-4034
E-mail: wooddl@ornl.gov

Collaborators:
Andy Jansen (ANL), Bryant Polzin (ANL), Chris Orendorff (SNL), David Telep (Dow Kokam), Erin O'Driscoll (Dow Kokam), Mike Wixom (A123 Systems now Navitas Systems), James Banas (JSR Micro), Gregg Lytle (Solvay Specialty Polymers), Mark Ewen (ConocoPhillips)

Start Date: October 1, 2011
Projected End Date: September 30, 2014

Objectives

- Transform lithium ion battery electrode manufacturing by eliminating the costly, toxic organic-solvents while increasing cell energy density through improved electrode architecture (active material utilization), increased electrode thickness, or both.

Technical Barriers

Elimination of Expensive Solvent and Recovery System. Electrode suspensions for lithium ion batteries are currently formulated using expensive polyvinylidine fluoride (PVDF) binder and expensive, toxic, and flammable n-methylpyrrolidone (NMP) solvent. It is desirable to replace these components with water and water-soluble binders, but methods of mass production of these suspensions are currently underdeveloped. The major problems with aqueous electrode dispersions are: 1) agglomeration of active phase particles and conductive carbon additive; 2) poor wetting of the dispersion to the current collector substrate; and 3) cracking of the electrode coating during drying resulting in poor device performance and short life. NMP based processing results in higher performance but has the inherent disadvantages of high solvent cost and the requirement for explosion proof processing equipment and solvent recovery. Initial projections of the minimum cost savings associated with changing to water and water-soluble binder are 70-75% of the electrode manufacturing step, or a reduction from $0.210/Ah to $0.055/Ah. That translates in 15-20% of cost reduction on the pack level. Improvements in this effort are projected to be chemistry-agnostic and with little additional effort adaptable to any electrode chemistry.

Technical Targets

- Low-cost, green manufacturing methodology for lithium ion battery anodes using aqueous suspensions (to meet $290/kWh USABC storage goal for PHEVs).
- Correlation of properties of dispersions and electrode coatings to cell performance and advancement of energy storage manufacturing science.
- Lifetime of 10 years and 1,000 cycles at 80% DOD for EVs and 5,000 deep discharge cycles for PHEVs.

Accomplishments

- Completed half-cell and full coin cell round robin testing with ANL and SNL with CP A10/A12 and TODA NMC 532 electrochemical couple for NMP/PVDF based dispersion chemistry.
- Demonstrated that metal dissolution is of minimal concern for aqueous processing of $LiFePO_4$ and NMC 532 cathode active materials.
- Optimized vacuum drying temperature with dry air at 120°C for ensuring acceptable residual moisture after aqueous electrode processing.
- Matched full coin cell performance through 100 cycles (0.2C/-0.2C) of aqueous suspension and water-soluble binder to NMP/PVDF based suspensions for CP A10/A12 and $LiFePO_4$ electrochemical couple.
- Matched full coin cell performance through 100 cycles (0.2C/-0.2C) of aqueous suspension and water-soluble binder to NMP/PVDF based suspensions for CP A10/A12 and TODA NMC 532 electrochemical couple.

- Match pouch cell (≥3 Ah capacity) performance through 15 cycles (0.1C/-0.1C and 0.2C/-0.2C) of aqueous suspension and water-soluble binder to NMP/PVDF based suspensions for CP A10/A12 and TODA NMC 532 electrochemical couple.

✧ ✧ ✧ ✧ ✧

Introduction

There is growing evidence in the literature that the complex suspensions used during electrode processing, which contain solvent, active graphite, conductive carbon, polymer binder, and perhaps a dispersant (surfactant), must be optimized using colloidal dispersion science. These components have different surface interactions with the solvent and dispersant, and each dispersion must be tailored based on surface charges, rheology, material constituents, order of addition, mixing protocol, coating method, and drying protocol. Whether the suspension is organic or aqueous, there is still much development required to optimize these formulations for uniform coatings, reduce the cost associated with making the electrodes, and correlate suspension properties to electrode performance.

In conventional lithium ion batteries, PVDF is used as the electrode binder because of its electrochemical stability over a large potential window, and NMP is used as the solvent when preparing the suspension. The advantage of using this organic system is that extensive research has been carried out on the resulting electrode microstructure and cell performance. However, there are still areas related to this conventional suspension that are relatively unexplored such as performance effects of solids loading, order of component addition, coating parameters, and drying conditions when materials are varied. The PVDF/NMP system has some disadvantages that make researching replacements attractive, most notably its cost. PVDF also has low flexibility, which can lead to breaking of the physical bond between active graphite and conductive carbon during long-term cycling. It contains fluorine, which is a source of producing stable LiF as a degradation product. The LiF may adversely interact with the otherwise stable solid electrolyte interface (SEI) layers. The use of NMP requires a process of recovery and treatment of the organic vapors for disposal or recycling. Therefore, there is increasing interest in switching the fabrication of composite electrodes from an organic route to an aqueous route. Compared to the organic route, the aqueous route is significantly more economically and environmentally friendly. For example, the cost of NMP in bulk quantities is ~$2.25/L, whereas deionized water is only $0.015/L.

The calendering process, which is critical to balancing energy density and power density demands, is typically done just after electrode casting and drying steps with the goal of improving particle to particle contact and reducing the lithium-ion diffusion distance from the top to the bottom of the electrode. It is also assumed that pressing the electrode improves the adhesion of the active material to the current collector. However the beneficial effects of this step on the overall rate capability have not been studied systematically. Calendering of porous multi-phase materials with porosity gradient through the thickness of the electrode has not been investigated. Moreover, the degree of mechanical damage induced in the particles during the electrode pressing remains unknown.

Apparently, calendering increases the solid volume fraction (SVF) of the electrode material by reducing the thickness of the electrode. This could have a three-fold effect on the subsequent battery performance. Increase in SVF could change permeability of the compressed material. Tangential displacements may shift particles and cause agglomeration of different phases (this is especially relevant when the phases possess properties that differ by orders of magnitude). Finally, normal and shear stresses developed during this process may change the properties of the active material itself.

Approach

Subtask 1. **Aqueous Electrode Processing.** Fabrication of composite electrodes via organic (baseline) and aqueous suspensions will be completed. A focus will be placed on the effect of processing parameters and agglomerate size on the aqueous route cell performance and microstructure of the composite electrode. Several active anode graphite and cathode (NMC, $LiFePO_4$, etc.) materials will be selected with various water-soluble binders. An emphasis will be placed on the ABR baseline anode, ConocoPhillips A10/12, and cathode, Toda NCM 523. The conductive carbon additive will be held constant. Rheological (viscosity) and colloidal (zeta potential) properties of the suspensions with and without dispersant will be measured with a focus on minimization of agglomerate size. These measurements will show the effects of agglomerate size and mixing methodology on suspension rheology and help determine the stability (i.e., ion exchange processes across the surfaces of various crystal structures) of active materials in the presence of water. Composite electrodes will be made by tape casting and slot-die coating, and the drying kinetics of the electrodes will be measured by monitoring the weight loss as a function of time and temperature. Solvent transport during drying will also be monitored as a method to control electrode morphology, porosity, and tortuosity. Electrode microstructure and

surface chemistry will be characterized and correlated with cell performance. Electrochemical performance of electrode coatings made from the various suspensions will be supplied to ORNL's strategic industrial partners for external validation in large cell formats.

Subtask 2. **Electrodes with Tailored Electrode Architecture.** Graded electrode architectures can address the lithium ion mass-transport limitations and will be made by depositing different bilayer coatings using dual-slot die coating. The controlled settling approach (by optimizing dispersion solids loading and viscosity) will be used together with our novel coating method to achieve a two-to-three-layer structure. A detailed calendering study will be conducted to correlate finished electrode structural properties with performance. Different binder types (with a PVDF baseline) at higher loadings will be investigated to increase coating adherence to the current collector substrate and increase electrode pliability around coating line bends.

Subtask 3. **Cell Performance and Process Validation.** Improved cell performance with reduced processing and raw material cost will be demonstrated using pilot-scale coatings. Cells will be tested and evaluated for irreversible capacity loss, AC impedance, capacity vs. charge and discharge rates, and long-term behavior through 100-500 charge-discharge cycles. Half cells, coin cells, and pouch cells will be constructed and evaluated at the ORNL Battery Manufacturing Facility (BMF). The coin cells will be used for screening and coarse evaluation of different suspension chemistries and coating methodologies. A fine tuning of these research areas will be completed using ORNL pouch cells and large format cells with ORNL's industrial partners. Electrode coatings will be produced on the ORNL slot-die coater and supplied in roll form to the industrial partners for assembly into large format cells.

Subtask 4. **Electrode and Active Material Characterization.** Electrode morphology will be characterized by scanning electron microscopy (SEM) and TEM. The bulk microstructure and surface of the active materials will be characterized using XRD and XPS, respectively. In addition, *in situ* TEM will be performed to investigate real-time SEI layer formation as a function of the different suspension chemistries.

Results

Active material solubility in aqueous suspensions. A common question of aqueous lithium ion electrode processing is the solubility of the active-material elemental species in water. To address this issue, saturated $LiFePO_4$ (LFP) and $LiNi_{0.5}Mn_{0.3}Co_{0.2}O_2$ (NMC 532) aqueous suspensions were measured by inductively-coupled-plasma mass spectrometry (ICP-MS) for elemental solubility as a function of suspension age, and the results are shown in Figure V - 176. Lithium-ion solubility for NMC 532 was about 2-3× that of LFP after one hour of exposure to water, whereas the solubility of Ni, Mn and Co for NMC 532 (<0.001 µg/mL) was 1000× lower than that of Fe and P for LFP. In either case, the elemental solubility for all species was low, with no observed concentrations above 20 ppm after one day of aging. From these findings, it can be concluded that if dispersions are mixed, coated, and dried within a day, then exposure to water will not cause active-material solubility problems.

Electrode moisture evaluation and removal. Two additional frequently asked questions are how to remove enough residual moisture from the electrodes after aqueous processing and how any residual moisture would affect electrode performance. An aqueous-processed NMC 532 cathode was dried for two hours at four different temperatures of 80°C, 100°C, 110°C, and 120°C using the air from the ORNL BMF dry room with a dew point between -40°C and -53°C. Prior to drying, each cathode was exposed to the ambient atmosphere outside of the dry room for ~24 h to ensure saturated moisture content. The residual moisture in each cathode after drying was characterized by Karl Fischer titration, and the results are shown in Figure V - 177. The saturated moisture content in the NMC 532 cathode was 625 ppm with no drying, and the residual moisture level decreased with increasing drying temperature down to 45 ppm for 120°C.

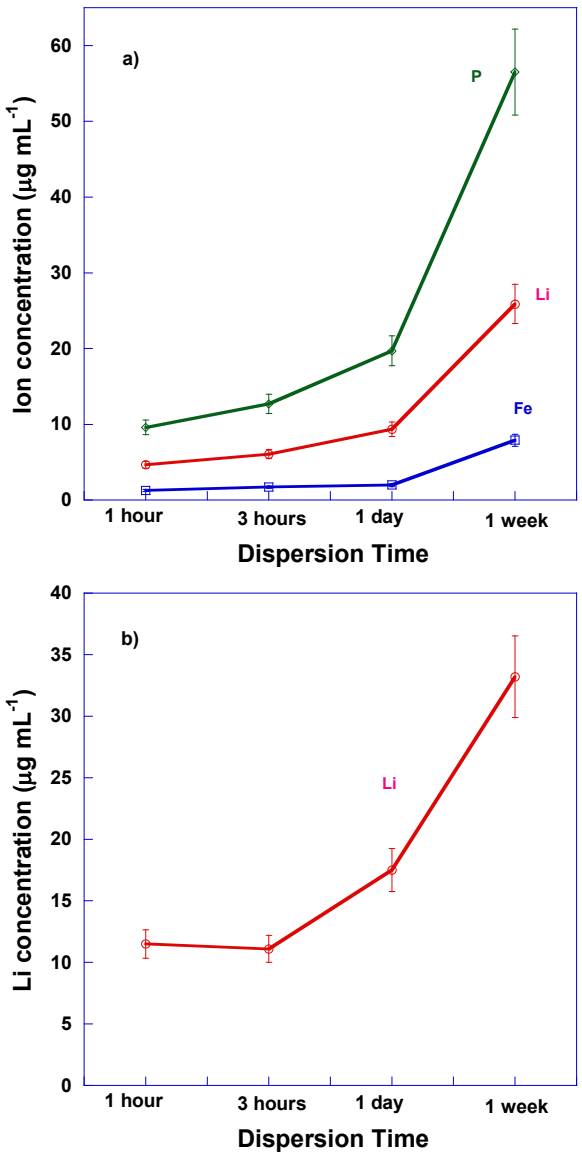

Figure V - 176: Ion solubility in a saturated aqueous suspension a) $LiFePO_4$ aqueous suspension and b) $LiNi_{0.5}Mn_{0.3}Co_{0.2}O_2$ (NMC 532) aqueous suspension

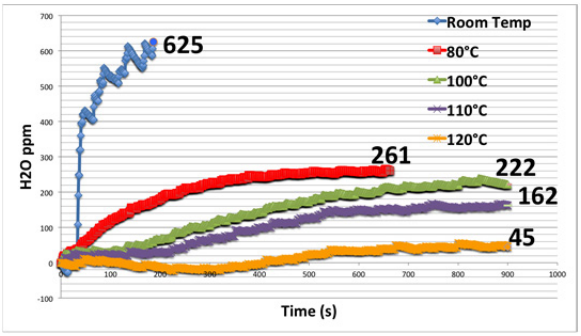

Figure V - 177: Residual moisture in NMC 532 cathodes using various drying temperatures

The effect of residual moisture content for the different drying temperatures on NMC 532 cathode performance was also investigated by evaluating half coin cells. All NMC 532 cathodes in this report had a composition of NMC 532/Denka carbon black/binder/carboxymethyl cellulose (CMC) at a 90/5/4/1 weight ratio. When the binder was PVDF, it was 5 wt% and contained no CMC. Three samples were tested for each condition, discharge capacity was normalized to the NMC 532 mass, and the C-rate was defined as 1C=160 mA/g. All the tests were conducted at 25°C with cutoff voltages between 2.5 V and 4.2 V. As shown in Figure V - 178, discharge capacity of the cathodes dried at 25°C, 80°C, 100°C and 110°C was similar and within 2σ. In contrast, the cathode dried at 120°C demonstrated superior capacity comparable to those processed with NMP (see Figure V - 179 for performance comparison). This finding shows that NMC cathodes made via aqueous processing need to be dried at 120°C or higher to effectively remove excess water and maintain required performance.

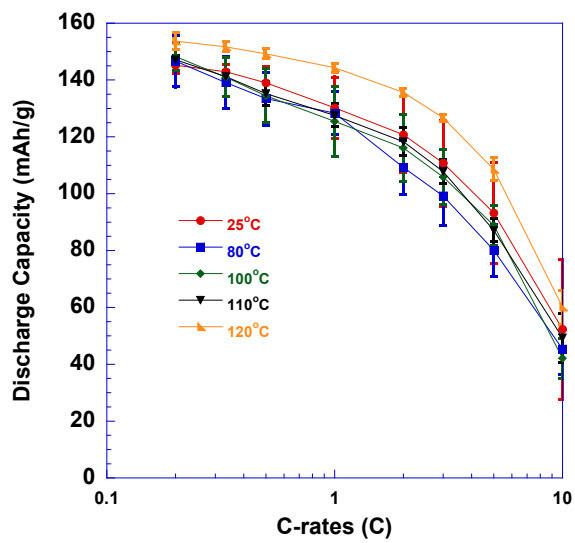

Figure V - 178: Discharge capacity of NMC 532 cathodes after various drying temperatures

Screening of novel water soluble binders for NMC 532 cathodes. Four significantly different water-soluble binders (descriptions are shown in Table V - 14) were investigated using NMC 532 cathodes, and the performance of each aqueous-processed electrode was compared to a PVDF/NMP baseline. At least three NMC 532 half coin cells were tested for each binder, and the average discharge capacity is shown in in Figure V - 179 with 2σ error bars. The tests were begun with rate capability evaluation using a constant charging rate of 0.2C and various discharging rates, followed by 40-100 cycles at 0.2C/-0.2C. All electrodes with water soluble binders demonstrated comparable or better rate performance compared to the one with 5130

PVDF binder and NMP. While the NMC 532 cathodes with water soluble binders exhibited similar capacity at low C-rates, the one with Solvay PVDF latex showed much higher performance at high C-rates. The electrode with PVDF latex also showed nearly identical long-term capacity fade to that with the PVDF/NMP baseline. Based on these findings, the Solvay PVDF latex was selected for full-scale pouch cell evaluation.

Table V - 14: Various binders screened in NMC 532 cathodes

Binder Names	Description	Manufacturer
TRD202A	Fluorine acrylic hybrid latex	JSR Corporation
PVDF Latex	Water soluble PVDF	Solvay Specialty Polymers
Nafion	Perfluorosulfonic acid	DuPont
SBR Latex	Styrene-butadiene copolymer	Targray
5130 PVDF	Polyvinylidene fluoride	Solvay Specialty Polymers

Based on the rate performance and initial 0.2C/-0.2C cycling data (see Figure V - 179), the JSR Micro TRD202A was also selected for full coin cell testing with the VTO ABR baseline ConocoPhillips (CP) A12 natural graphite anode. The A12 graphite was processed using NMP to limit the processing variables associated with the evaluation. Results, shown in Figure V - 180, were compared to the NMC 532/CP A12 full coin cells where both electrodes were processed using NMP. Each full coin cell went through 5 formation cycles at 0.1C/-0.1C. As shown in Figure V - 180 and Figure V - 181, the aqueous-processed cathode with TRD202A binder demonstrated either identical or slightly improved performance, depending on the C-rate, compared to that processed with NMP. Both electrodes also exhibited excellent capacity recovery after the rate capability test, and capacity fade was identical within 2σ error. These observations further confirm that NMC 532 cathodes made via aqueous processing can deliver identical performance to those made via conventional NMP-based processing. Therefore, this manufacturing improvement not only significantly reduces electrode processing cost, but also maintains electrode rate performance and preserves capacity over long-term cycling.

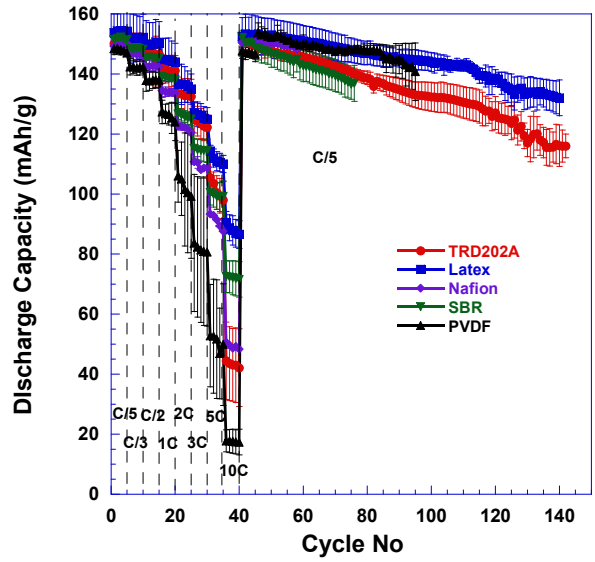

Figure V - 179: Comparison of performance with various water-soluble binders in NMC 532 half cells

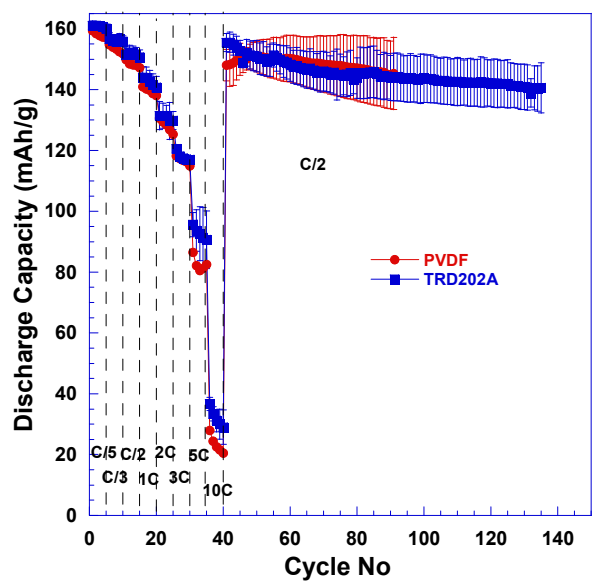

Figure V - 180: Cycling performance comparison of full cells with NMC 532 cathodes using JSR Micro TRD202A (aqueous processing) and baseline 5130 PVDF (NMP processing) binders

Demonstration of large-format pouch cells with NMC 532 cathodes through aqueous processing. Aqueous-processed NMC 532 cathodes with Solvay PVDF Latex as the binder were assembled into a 3-Ah pouch cell with CP A12 graphite anodes (via NMP-based processing). This pouch cell was aged at 60°C for 48 h followed by four formation cycles at 100 mA (0.033C/-0.033C) and exhibited 650 mAh irreversible capacity loss after the first formation cycle (Coulombic efficiency of 82%). As shown in Figure V - 182, the

Coulombic efficiency increased to 98% after the second formation cycle and continued to improve to >99% after subsequent cycles. This cell demonstrated a capacity of 3 Ah at 0.1C discharge rate and 2.8 Ah at 0.2C. The rate capability and long-term cycling (capacity fade) tests are still ongoing.

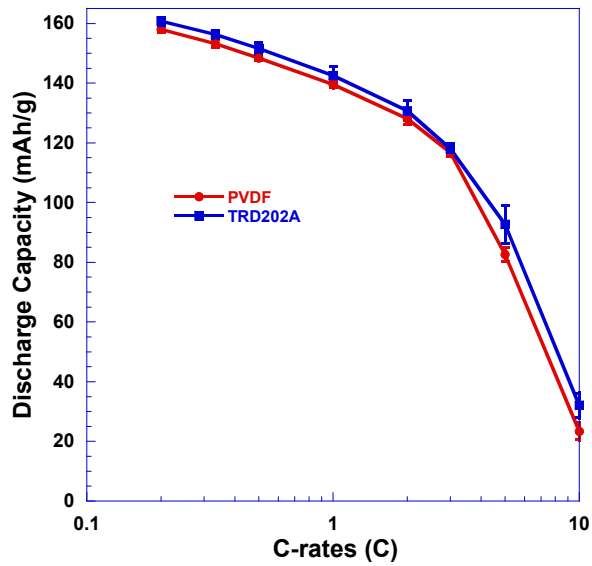

Figure V - 181: Rate performance comparison of full cells with NMC 532 cathodes using JSR Micro TRD202A (aqueous processing) and baseline 5130 PVDF (NMP processing) binders

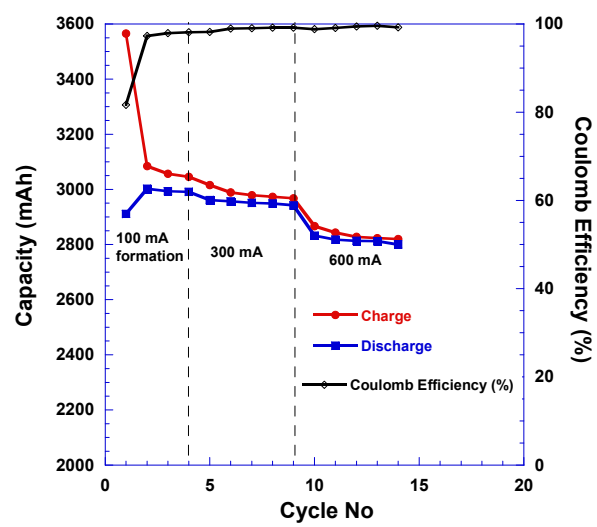

Figure V - 182: Successful scale-up and rate performance of a 3-Ah full pouch cell with a NMC 532 cathode and Solvay PVDF Latex binder via aqueous processing

Conclusions and Future Directions

It was demonstrated that if the exposure of the active material, such as NMC 532 or LFP, to water is less than ~1 day, solubility of the various elemental species is negligible. NMC 532 cathodes were successfully fabricated with four water soluble binders via aqueous processing. Residual moisture in these cathodes can be easily removed by oven drying with dehumidified air for 2 h. In addition, NMC 532 cathodes made through aqueous processing demonstrated comparable or better performance compared to those cathodes made with NMP, as demonstrated with half coin cells, full coin cells, and full-scale pouch cells.

ORNL will continue to optimize water-soluble binder content, particle size, molecular weight, and mechanical properties for NMC 532 cathodes, including applying a lithium-ion conductive binder, such as Li-exchanged Nafion®. Thick, high-energy electrodes will also be developed by incorporating novel design features such as a porosity gradient through dual-slot-die coating, calendering optimization, and inclusion of higher-conductivity additives such as multilayer graphene. Manufacturing of composite anodes and cathodes through aqueous processing will be further refined and commercialization partners will be sought.

FY 2013 Publications/Presentations/Patents

1. Aqueous Processing of Composite Lithium Ion Electrode Material, J. Li, B.L. Armstrong, C. Daniel, and D.L. Wood, III, U.S. Patent Application 13/651,270 (2013).
2. Jianlin Li, Beth Armstrong, Jim Kiggans, Claus Daniel, and David Wood, "Optimal polyethyleneimine concentration and mixing sequence for $LiFePO_4$ aqueous nanoparticle dispersions," *Journal of Colloid Interface Science*, **405** (1), 118-124 (2013).
3. Jianlin Li, Beth L. Armstrong, Jim Kiggans, Claus Daniel, David L. Wood, III, Lithium Ion Cell Performance Enhancement Using Aqueous LiFePO4 Cathode Dispersions and Polyethyleneimine Dispersant, *J Electrochem. Soc.*, **160** (2), A201-A206 (2013).
4. D.L. Wood, III, J. Li, D. Mohanty, C. Daniel, B.L. Armstrong, R.B. Dinwiddie, H. Wang, R.M. Trejo, N.C. Gallego, C.I. Contescu, J.Y. Howe, R.A. Meisner, J. Kiggans, and B.D. Brown, "Advanced Materials Processing and Novel Characterization Methods for Low-Cost, High Energy-Density Lithium-Ion Batteries," *Proceedings of the Advanced Automotive Battery Conference* (2013).
5. Claus Daniel, David Wood, Jianlin Li, Debasish Mohanty, Beth Armstrong, and Jim Kiggans, "Cell Materials and Manufacturing," 2013 Cummings Energy Storage Systems Summit, Columbus, IN, October 29-30, 2013 (invited).

6. Claus Daniel, David, Wood, Jianlin Li, Beth Armstrong and Jim Kiggans, "Battery Production Technologies" Energy Storage Solution Industrial Symposium, Oak Ridge, TN, September 4, 2013 (invited).
7. David L. Wood, III, Claus Daniel, Jianlin Li, Debasish Mohanty, and Bradley Brown, "Cutting Edge Lithium-Ion Cell Research at the Oak Ridge National Laboratory Battery Manufacturing Facility (BMF)," 2013 CERC-CVC Annual Technology Forum, Beijing, China, August 19-20, 2013.
8. Jianlin Li, Debasish Mohanty, Bradley Brown, David Wood, and Claus Daniel, "Status on electrode fabrication and battery manufacturing at ORNL's Battery Manufacturing R&D Facility," 2013 Clean Energy Research Center-Clean Vehicle Center-seminar Series, Ann Arbor, MI, July 17, 2013 (invited).
9. Claus Daniel, Debasish Mohanty, Jianlin Li, and David Wood, "Overview and progress in cathode materials for lithium ion batteries," 1st International Freiberg Conference on Electrochemical Storage Materials, Freiberg, Germany, June 3-4, 2013 (invited).
10. Claus Daniel, David Wood, Jianlin Li, Beth Armstrong, Jim Kiggans, Debasish Mohanty, and Sergiy Kalnaus, "Electrification of transportation-cost and opportunities," Bridging the Gap Conference 2013, Oak Ridge, TN, March 5-6, 2013 (invited).
11. David Wood, Jianlin Li, Debasish Mohanty, Claus Daniel, Beth Armstrong, Ralph Dinwiddie, Hsin Wang, Rosa Trejo, Nidia Gallego, Cristian Contescu, Jane Howe, Roberta Meisner, Jim Kiggans, and Bradley Brown, "Advanced materials processing and novel characterization methods for low-cost, higher energy-density lithium-ion batteries" Advanced Automotive Battery Conference 2013, Pasadena, CA, February 4-8, 2013 (invited).

V.E.3 Development of Industrially Viable Electrode Coatings (NREL)

Robert Tenent

National Renewable Energy Laboratory
16253 Denver West Parkway
Golden, CO 80401
Phone: (303) 384-6775
E-mail: Robert.tenent@nrel.gov

Subcontractor:
University of Colorado at Boulder

Start Date: January 2012
End Date: September 2013

Objectives

- The ABR program is focused on improving cycle life, abuse tolerance and reducing cost for PHEV battery technologies.
- Previous work conducted by NREL and the University of Colorado at Boulder has demonstrated that thin, conformal coatings of lithium ion battery electrodes formed by atomic layer deposition (ALD) can dramatically improve abuse tolerance and cycle life which in turn reduces ultimate cost.
- Current technology for performing ALD is not amenable to high throughput manufacturing methods and thus represents a high priced bottleneck in the implementation of ultrathin electrode coatings at a commercial scale.
- The objective of this current work is the development of a system for deposition of thin protective electrode coatings using a novel "in-line" atmospheric pressure ALD (AP-ALD) reactor design that can be integrated into manufacturing to address needs for improvement in rate capability, cycle life, and abuse tolerance in a cost effective manner.

Technical Barriers

- Limited calendar and cycle life.
- Abuse tolerance.
- High cost.

Technical Targets

- Design and construction of prototype in-line ALD coater for deposition on porous substrates

✧ ✧ ✧ ✧ ✧

Introduction

In previous work, NREL, in partnership with the University of Colorado, has shown that extremely thin, conformal coatings deposited with the ALD technique are capable of dramatically improving cycleability of lithium-ion cells. This project seeks to convert the common ALD processing format into a new reactor geometry that is compatible with battery electrode manufacturing.

As part of this effort for FY13, NREL and the CU-Boulder team has successfully completed design and construction of a new in-line ALD reactor. Work in this area has focused on modification of previous reactor designs to build a system capable of assessing the ability to obtain ALD-type coating processes in an in-line format and under acceptable battery manufacturing conditions. Earlier reactors were constructed to conduct initial feasibility testing of the ALD process when converted to an in-line format and with deposition occurring at atmospheric pressure; however, these early designs focused on planar substrates. More recent work has focused on creating a system that is capable of deposition onto moving coated battery electrode foils, as used in present manufacturing. Special emphasis was placed on designing a system to understand the impact of coating on porous substrates.

Approach

ALD coating methods are conducted by sequential and separate exposure of a sample substrate surface to gas phase precursors that react to form a film. Deposition is typically performed in a closed reactor system at mild vacuum as is shown in Figure V - 183. Precursor exposure steps are conducted in a single chamber and are separated in time. In a typical exposure "cycle", a sample is exposed to one precursor and the chamber is then purged with inert gas prior to exposure to the second precursor that completes the coating reaction. The "cycle" ends with another extensive inert

gas purging step before the process can be started again. Film growth takes place by repeating this cycling precursor exposure process multiple times. The sequential and separate exposures are key to achieving the excellent conformal film deposition on highly textured substrates for which the ALD technique is known.

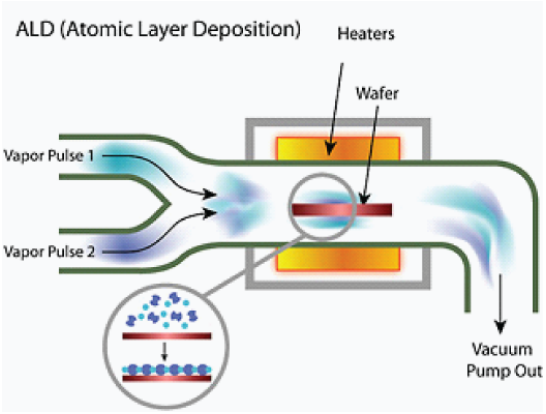

Figure V - 183: A typical ALD chamber with sequentially separated precursor exposures that draws out overall processing time

As an alternative to the temporal separation of precursor exposure in the same reaction chamber, our work proposes a ***spatial*** separation of precursor exposure steps that is more consistent with "in-line" processing techniques. Figure V - 184 shows a simplified conceptual schematic of our proposed apparatus.

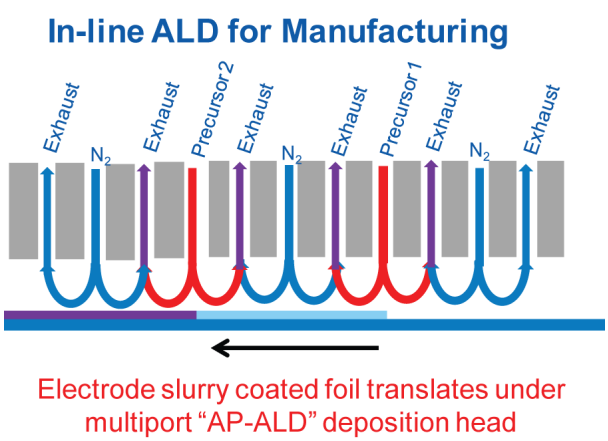

Figure V - 184: A simplified schematic demonstrating the in-line spatial ALD concept

Our "spatial" ALD approach employs a multichannel gas manifold deposition "head" that performs sequential exposure of precursor materials as an electrode foil transits beneath it. It is important to note that similarly designed deposition heads are currently employed by glass manufacturers for production of a variety of coated glass products using high-volume, in-line atmospheric pressure chemical vapor deposition (AP-CVD). Our approach leverages this existing knowledge base as well as our ALD expertise in order to enable in-line ALD coating that will allow the transfer of our previously demonstrated ALD-based performance improvements to larger format devices.

Results

Push-Pull Reactor Design. A crucial factor for successful coating of battery electrodes using in-line ALD technique is the ability to coat *porous* substrates. Coating of a porous substrate presents a specific technical challenge, as precursor materials must be able to fully penetrate as well as be removed from the porous film as rapidly as possible to enable high processing line speeds. This requires that the porous film be exposed to alternating high and low gas pressure regimes at different stages of the deposition process. At high local pressures (viscous flow conditions), a high number of gas phase collisions drive penetration of precursor gases into the film, while low local pressures (molecular flow conditions) allow rapid removal of unreacted precursor prior to the next precursor exposure step. We have termed the rapid progression through alternating high and low local pressure regimes the "push-pull" reactor design. A fundamental schematic of the "push-pull" reactor concept is shown in Figure V - 185. In addition to precursor introduction and exhaust channels, the system is also designed with a nitrogen gas window that is pressured higher than the dosing precursors in between the precursor ports. This nitrogen gas purge will ensure that there is no cross talk between the different reactants that would lead to bulk film deposition.

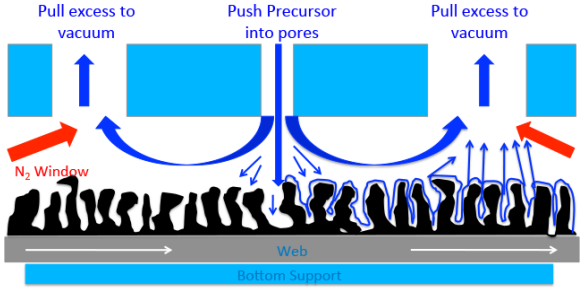

Figure V - 185: A simple schematic demonstrating the alternate high and low pressure regimes present in the "push-pull" reactor concept

Digital Modular Roll-to-Roll (R2R) System Design. As shown schematically earlier, a linear translational roll-to-roll design was initially considered for our "push-pull" deposition system. However, it was determined through earlier results and discussions with

additional R2R processing experts that a linear design would not be capable of maintaining adequate tension on the web substrate during the "push-pull" deposition process. An improved format is a rotating drum-in-drum design as shown in Figure V - 186. In the drum-in-drum system, a rotating inner drum on which substrates are mounted is set inside a fixed outer drum that contains all gas sources as well as purge and exhaust lines. The inner drum rotates the web radially while maintaining sufficient tension on the line to ensure accurate gas head to substrate spacing.

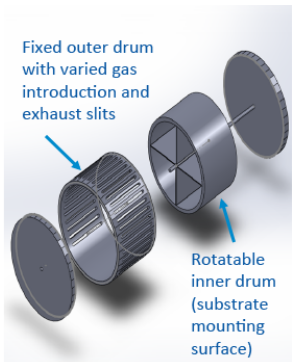

Figure V - 186: Diagram of drum-in-drum reactor format

In order to maximize reactor flexibility and enable extensive deposition condition optimization work, we have adopted what we term a "digital modular" system design. Figure V - 187 shows a more detailed schematic of the drum-in-drum reactor design and demonstrates the digital modular design. To implement the "digital modular" design, the fixed outer drum of the reactor is faceted and has slots drilled every 2.5 cm. Precursor introduction as well as reactant exhaust occurs through the attachment of specific "modules" to these slots. Precursor dosing and vacuum exhaust modules have been fabricated that are able to fit to any of the slots in the external drum. This design will allow the modules to be moved interchangeably on the external drum to allow the maximum amount of variability in dosing and vacuum modules spacing. This enables extensive experimentation across a broad range of deposition conditions in order to optimize performance.

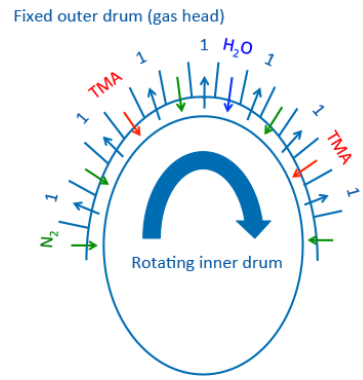

Figure V - 187: Schematic representation of the "digital modular" design concept

Module Design. Computational flow dynamics simulations were conducted to optimize the precursor introduction module design in order to ensure uniform precursor exposure to the moving substrate across the sample surface. As an example, Figure V - 188 shows output from CFD calculations as well as the final constructed precursor introduction module. Our simulations showed that under expected deposition conditions, a minimum height of 2" was required for the precursor concentration to become uniform across the entire width of the module. Modules were constructed at a height of 5" in order to allow sufficient time and space for the precursor concentration to become uniform.

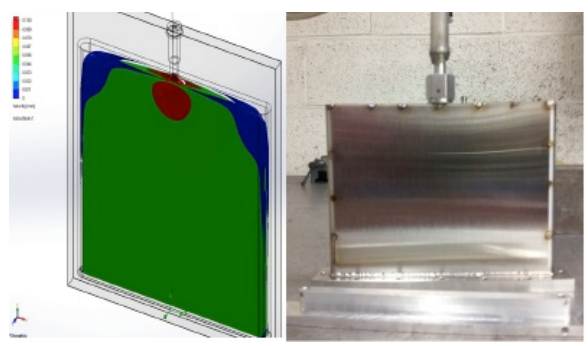

Figure V - 188: Fabricated and final assembly of the drum-in-drum in-line reactor

As discussed previously, another benefit of using the modular slot design is that blank modules can be added to modify channel spacing, furthermore, new modules can be added in the future without having to modify the main deposition head. As an example additional modules are being designed that will allow for the use of *in situ* diagnostics including pressure sensing and mass spectrometry as well as a module that will enable in-line plasma assisted deposition.

Reactor Construction and Assembly. Following the design phase, reactor parts were fabricated, assembled and are currently under test. Figure V - 189 shows the final fabricated internal and external drum units including the faceted slits for process module

interfacing as well as the full reactor at different stages of completion. Note that a portion of the external drum has been left intact. This was left unmodified to enable later integration of the unit within existing R2R processing units as will be briefly described below.

Figure V - 189: Compulational flow dynamic simulation of gas flow through the precursor introduction module and final construction

Conclusions and Future Directions

In FY13 the NREL/CU team designed and completed construction of a new in-line ALD based electrode coating reactor. Initital testing of the unit is currently underway. If additional funding can be obtained for a continuation of this effort into FY14, experiments will be conducted to determine optimal parameters for conformal coating on porous substrates. This work will entail detailed Design of Experiment methods used to determine optimal conditions to ensure conformal coating of a moving porous substrate. The output from this work will identify acceptable conditions for conformal coating of materials in an in-line format. Experiments will initially be conducted with model porous substrates with well-known geometries that will enable detailed measurements of coating quality. Following this initial optimization work, the NREL/CU team will partner with other ABR collaborators to coat larger format battery electrodes. Larger format electrodes will be fabricated into cells for testing at the NREL/CU laboratories within collaborating labs.

It is anticipated that in a later stage, the NREL/CU team will partner with battery manufacturers and other laboratories to integrate the new reactor design into a battery electrode coating process. Toward that end, the existing reactor was intentionally designed to enable integration with further R2R processing capabilities. Figure V - 190 shows an early stage schematic for integration of the digital modular reactor design into a R2R system. The unmodified sidewall of the outer drum of the reactor will be modified to include roller designs to bring an electrode foil into the reactor and into contact with the inner drum. The roller integration is shown on the left side of the Figure V - 190 schematic.

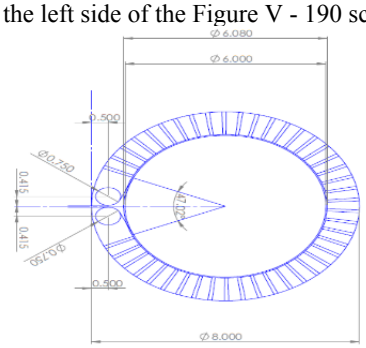

Figure V - 190: Initial schematic of roller integration within the drum-in-drum reactor design

FY 2013 Publications/Presentations

1. 2013 DOE Annual Peer Review Meeting Present.

V.E.4 Roll-to-Roll Electrode Processing NDE and Materials Characterization for Advanced Lithium Secondary Batteries (ORNL)

David Wood III, Debasish Mohanty, Jianlin Li, Curt Maxey, Ralph Dinwiddie, and Claus Daniel
Oak Ridge National Laboratory
One Bethel Valley Road
P.O. Box 2008, MS 6065
Oak Ridge, TN 37831
Phone : (865) 574-1157; Fax: (865) 241 4034
E-mail: wooddl@ornl.gov

Collaborators:
Daniel Abraham (ANL), Kevin Gallagher (ANL), Jason Croy (ANL), Guido Bender (NREL), Michael Ulsh (NREL), Mike Wixom (A123 Systems and Navitas Systems), Frank Reilly (Ceres Technologies), Mark Ewen (ConocoPhillips), Erin O'Driscoll (Dow Kokam), David Telep (Dow Kokam), Jerry Forbes (Frontier Industrial Technology)

Start Date: October 11, 2011
Projected End Date: September 30, 2014

Objectives

- Raise the production yield of lithium secondary battery electrodes from 80-90% and the associated cell acceptance rate by utilizing in-line measurement and *ex situ* diagnostic tools for electrode structural characterization to improve the performance.
- Reduce electrode and cell cost by investigating and implementing in-line X-ray fluorescence (XRF), laser scanning, infrared (IR) thermography, and thermal diffusivity as non-destructive evaluation (NDE) and quality control (QC) tools for coating areal weight, thickness, composition, and defect location:
  - Identify the nature of defects/flaws generated during electrode coating and their impact on battery performance.

Technical Barriers

- Material processing cost and electrode quality control.
- Cell acceptance rate, calendar life, and performance.

Technical Targets

- Low-cost manufacturing methodology with minimized scrap rate for lithium ion battery electrodes using both organic and aqueous suspensions (to meet $290/kWh USABC storage goal for PHEVs and <$125/kWh for EVs).
- Lifetime of 10 years and 1,000 cycles at 80% DOD for EVs and 5,000 deep discharge cycles for PHEVs.
- Correlation of electrode defects with performance to meet calendar life and long-term cycling needs.

Accomplishments

- In-line laser thickness measurement enabled data precision of less than ±2% for electrode wet thickness measurement. The high thickness precision was critical to evaluating thickness variation across electrodes at different regions.
- IR thermography was successfully implemented to identify pinholes, blisters, divots, and agglomerates in dried electrodes. Temperature variation in IR thermographs was critical for locating these different defects. An increase in the temperature profile suggested the presence of agglomerates, and a decrease in the temperature profile indicated divots, pinholes, and blisters.
- Off-line XRF was used to successfully measure the concentration of Cu contamination in electrodes. In addition, excellent off-line measurements of cathode transition-metal stoichiometry were obtained. However, this technique was de-selected as a viable in-line method due to the insufficient accuracy of areal weight measurement and low required line speed.

✧ ✧ ✧ ✧ ✧

Introduction

In-line XRF is a valuable, non-destructive QC tool that determines chemical composition uniformity and presence of contaminants in a variety of industries including geological analysis, plastics, textiles,

pharmaceuticals, fertilizers, foodstuffs, forensics, mining feeds and refineries, cement production, catalysts, glass, ceramics, heat resistant coatings, thin films, semiconductors, photovoltaics, multilayer films, etc. The measurement may be executed with an energy dispersive X-ray fluorescence detector (EDXRF) for high throughput and low cost or a wavelength dispersive detector (WDXRF) for high resolution and low detection levels. The technique is highly compatible with roll-to-roll manufacturing and film processing and is independent of coating technique. Other advantages are that a large sample area can be accommodated, 2-D (x-y) scanning over a coating surface can be implemented, and coating thicknesses can be measured. These many features make the technique highly compatible with lithium secondary battery electrode production. However, issues such as compatibility of XRF detection rate with desired coating line speeds (20-60 ft/min is the current state-of-the-art) and detection of trace, isolated metal contaminants (such as Fe, Al, and Cu) present considerable technical challenges. Compositional and thickness uniformity achieved via in-line XRF could be correlated with X-ray computed tomography (XCT) information regarding electrode morphological and microstructural changes during drying to provide additional insight.

Currently, the independent measurement of lithium secondary battery electrode loading via dual-side (slot-die) coating is achieved by pulling a sample from the master roll product, and removing the coated material from each side to measure the relative coating distribution. Total material loading is determined by Beta Gauge measurement of the total dried electrode mass. From this output, adjustments to the total loading are made by reducing or increasing the amount of electrode dispersion applied to both sides of the current collector. Output from a Beta Gauge does not capture the loading on each side of the electrode substrate; thus, potential imbalances may result in applying too much (or too little) coating to one side of the current collector. Extreme levels of imbalance may lead to localized lithium plating or excessive resistance growth in the operating cell due to relative over/under utilization of the electrode. Traditional thickness measurements of moving webs using laser displacement have been prone to inaccurate results due to vibration of the current collector substrate. Methods to directly monitor the applied coating for dual-side application would be beneficial for providing real time measurement to ensure the quality of production electrodes. The desired effect would be to provide feedback to the individual pumping device used to apply electrode dispersion to each side and meter the dispersion flow rate to either increase or decrease accordingly. This needed QC improvement would reduce the amount of total electrode dispersion required and finished electrode roll scrap discarded.

Recent advances in laser thickness measurement may provide a better opportunity to accurately measure the wet layer applied to each side of the current collector substrate. By positioning measuring devices after both the first and second slot dies (i.e., in a production setting) in discrete locations to measure across the entire width, the dispersion distribution across an individual lane could be monitored and feedback for adjustments to the applied wet layer on each side could be provided. Comparing the distribution profile of the wet coating layer to that achieved with the final dry layer (determined by inline EDXRF) could also provide insight into how the electrode coating settles during the drying process. The state-of-the-art is to operate the pump metering devices based on a relative pump speed, which dispenses a given amount of dispersion to either side of the current collector. Measurement of the applied wet layer for each side may better allow for adjustments needed as the dispersion properties change over the duration of a coating batch.

IR imaging, or thermography, will be used to determine the location and frequency of electrode coating defects such as pinholes, blisters, and particle agglomerates, as well as uniformity of coating thickness and quantification of areal weight. An IR camera will be installed on the dry coating end of our slot-die coater to obtain this data.

Approach

Determining defects in dried electrodes by IR thermography. An IR camera detects the IR energy emitted from an object and simultaneously displays the image as a function of temperature. Any defect or flaw in the object will appear as a temperature variation at that point. Therefore, IR thermography is essential to examine the dry electrode homogeneity exiting the slot-die coater oven and to detect any flaws, or defects (e.g., pinholes, divots, blisters, large agglomerates, or contaminants) present on the electrode surface. The IR imaging QC will be correlated with the battery performance data to determine any further systematic flaw formation mechanism and its impact on electrochemical performances.

Determining feasibility of in-line laser thickness measurement with equipment supplier. Recent advances in laser thickness measurement may provide a better opportunity to accurately measure the wet layer applied to each side of the current collector substrate. By positioning measuring devices after both the first and second slot dies (i.e., in a production setting) in discrete locations to measure across the entire width, the dispersion distribution across an individual lane could

be monitored and feedback for adjustments to the applied wet layer on each side could be provided. Comparing the distribution profile of the wet coating layer to that achieved with the final dry layer (determined by inline EDXRF) could also provide insight into how the electrode coating sets during the drying process. The state-of-the-art is to operate the pump metering devices based on a relative pump speed, which dispenses a given amount of dispersion to either side of the current collector. Measurement of the applied wet layer for each side may better allow for adjustments needed as the dispersion properties change over the duration of a coating batch. Keyence was selected as the partner for developing a laser thickness senor, or set of sensors, for lithium secondary battery electrode production. ORNL has a single-sided slot-die coating system, so only single-sided electrode coatings will be evaluated. ORNL will rent the sensors from Keyence and integrate them directly into ORNL's slot-die coating line for the proof-of-concept experiments.

Determining feasibility of in-line XRF with equipment supplier. In-line XRF is a valuable, non-destructive QC tool that determines chemical composition uniformity and presence of contaminants in a variety of industries. The measurement may be executed with an energy dispersive detector (EDXRF) for high throughput and low cost or a wavelength dispersive detector (WDXRF) for high resolution and low detection levels. The technique is highly compatible with roll-to-roll manufacturing and film processing and is independent of coating technique. Other advantages are that a large sample area can be accommodated, 2-D (x-y) scanning over a coating surface can be implemented, and coating thicknesses can be measured. These many features make the technique highly compatible with lithium secondary battery electrode production. However, issues such as compatibility of XRF detection rate with desired coating line speeds (20-60 ft/min is the current state-of-the-art) and detection of trace, isolated metal contaminants (such as Co, Al, and Cu) present considerable technical challenges. Compositional and thickness uniformity achieved via in-line XRF could be correlated with X-ray computed tomography (XCT) information regarding electrode morphological and microstructural changes during drying to provide additional insight. Ceres Technologies was selected as the equipment partner based on their commercial success with performing in-line XRF on PV panels.

Results

Successful alignment of two-laser-caliper system on ORNL slot-die coater and wet-electrode thickness data collection. The two-laser-caliper system (Keyence) was successfully mounted and aligned on the ORNL slot-die coater (Figure V - 191a). The schematic of the thickness measurement by this laser caliper system is shown in Figure V - 191b. The thickness of a sample "t" can be determined by adding the two output voltages from the lasers (Figure V - 191c) and then dividing by the slope, which is given as in the formula:

$$V_1 = m\left(\frac{t}{2}\right)$$

$$V_2 = m\left(\frac{t}{2}\right)$$

$$V_1 + V_2 = m(t)$$

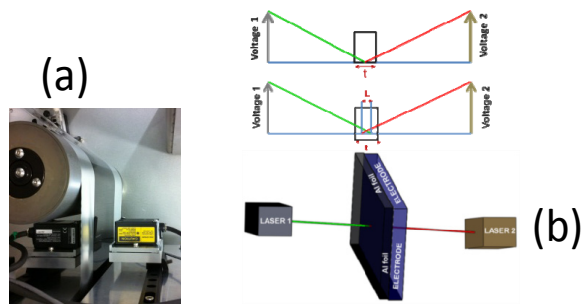

Figure V - 191: Mounted lasers (a); alignment of a two-laser-caliper system to measure the thickness of the electrode coating (b); determining sample thickness with a perfectly aligned system (c); determining sample thickness with calibration constant while measuring the thickness of the coating (d)

However, it is difficult to align two lasers perfectly and between the two lasers' focal points, an overlap of one thickness should be added to the equation above (Figure V - 191d) to represent the lack of coincidence of the two focal points. Rearranging the components, both "t" (sample thickness) and "l" (calibration constant) can be isolated, enabling the expression to be easily used for both calibrating the system with a known thickness and measuring thickness with a calibration constant. The equation can be rewritten as

$$V_1 + V_2 = m(t + l)$$

The various sources of errors such as physical and data acquisition errors were systematically studied particularly applicable to ORNL slot-die coater and summarized in the Table V - 15. The laser caliper system was utilized to measure the wet-thickness of TODA HE5050 cathode and ConocoPhillips graphite A12 anode. Before measuring the thickness of the TODA HE5050 the system was re calibrated with the current collector which is bare Al foil with a thickness of 15 µm and the thickness data was collected at a speed of 1ft/minute for 5 minutes. In Figure V - 192a, the Δd/d (Where d represents the thickness value and Δd is the difference between two adjacent data) vs. time with a confidence interval of 95% is presented. The data collected over the five minutes run were averaged to obtain the thickness of the Al foil. The average

thickness of the bare Al foil was calculated as 15.67 µm with a standard deviation of 0.23 µm (T=19°C). This value is in agreement with the expected thickness of a bare Al foil and shows the capability of our laser system to obtain an accurate thickness measurement. In the next step, the wet-thickness data of the TODA HE5050 coating was collected for a 20 minutes run at a speed of 1ft/minute. In Figure V - 192b, thickness data the Δd/d vs. time with a confidence interval of 95% is presented. The data obtained for 20 minutes were averaged and the thickness value was obtained as 118.51µm (T= 20°C) with a standard deviation of 2.75 µm. This indicates that the slurry coating is homogeneous across the measurement line, which was also confirmed from the Δd/d values that did not change over the time during coating is in agreement with this result.

The laser caliper system was also used to obtain the thickness of the ConocoPhillips A12 graphite anode. Before collecting the thickness of the anode coating, the system was recalibrated with the bare Cu foil (current collector) of thickness 20µm. The data was collected for 5 minutes at a speed of 1ft/min and the plotted as Δd/d vs. time (Figure V - 192c). The average thickness data was calculated as 19.97 µm (T =20°C) with a standard deviation of 0.76 µm. This value is in agreement with the expected thickness value for the bare Cu foil. After recalibration, the wet-thickness data for the A12 graphite coating was collected for 20 minutes at a speed of 1 ft/min and the data was plotted as Δd/d vs. time (Figure V - 192d). The average wet-thickness was calculated to be 89.96 µm with a standard deviation of 1.27 µm. Comparing the thickness variation of the cathode (Figure V - 192b) and anode (Figure V - 192d), Figure V - 192d shows a higher standard deviation than that in Figure V - 192b, which verifies that the laser sensors can effectively detect the thickness variation in an LIB electrode. Here the standard deviation can be taken as an indication of uniformity of the thickness.

Identification of nature of coating defects and flaws by IR thermography. The schematic of IR-setup for monitoring flaws in the dried electrodes coming out from the slot-die coater is given in Figure V - 193a. For experimental set-up, FLIR SC-8200 IR camera with a 25 mm lens (no filters or extender rings) and a 6,000 J Hensel flash system at ~60% flash power was used. The IR camera has 1,024 by 1,024 pixels and the wavelength range is 3 to 5 microns. The images were reordered during entire coating, and data were processed to detect any flaws in the electrode.

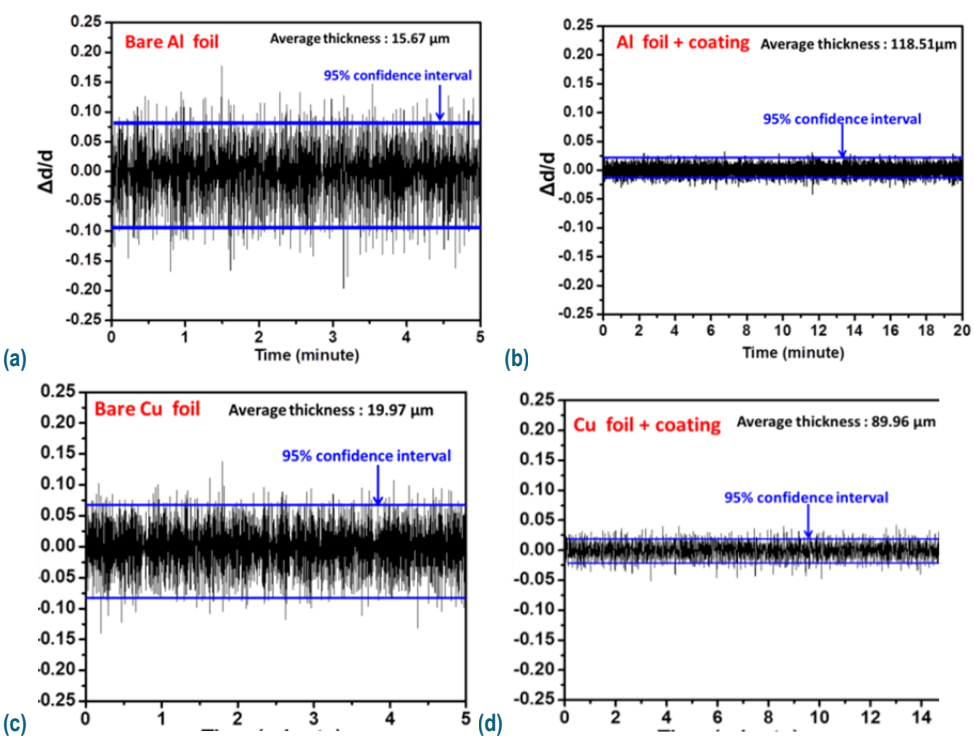

Figure V - 192: Thickness measurement data (Δd/d) from (a) bare Al foil, (b) TODA HE5050 cathode material, (c) bare Cu foil, and (d) ConocoPhillips A12 graphite anode with 95% confidence interval, where d represents the thickness value and Δd is the difference between two contiguous data

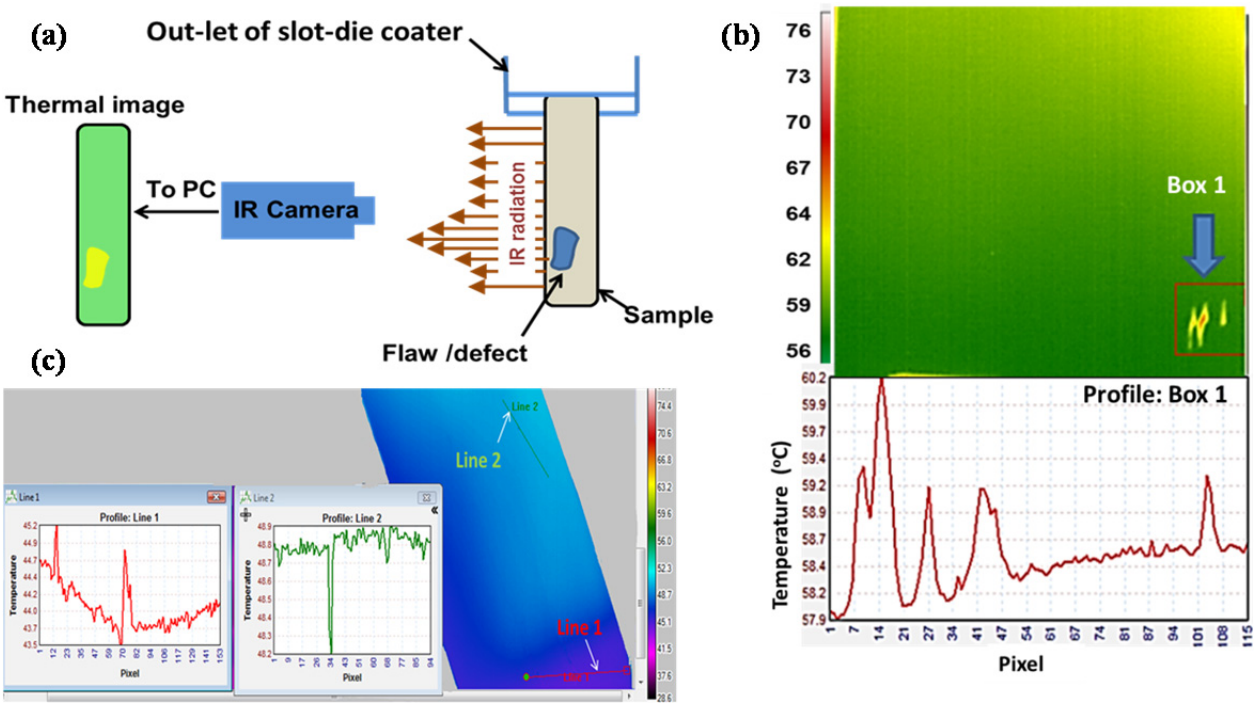

Figure V - 193: (a) Schematic of IR thermography experimental setup. The IR camera is set in front of the dried electrode exiting the slot-die coater, and the subsequent thermal image is digitally processed. (b) Scan along the TODA HE5050 cathode showing the temperature variation, which indicates the presence of defects in the electrode. (c) IR thermography from dried anode shows the increase (line 1) and decrease (line 2) in temperature profile indicating the blister and pinholes in the electrode which could not be visible optically

Table V - 15: Expected errors that may originate during thickness measurement by the laser caliper system mounted on the ORNL slot-die coater

Error Sources	Expected Error Range	Type	Remarks
Laser Alignment	0–10 µm	Lateral/ Thickness	Perfectly aligned laser triangulation sensors will result in perfect thickness measurements; misalignment will result in either lateral or cosine errors in thickness measurement.
Surface Reflectivity	Minimal	Reliability	Automatic gain control in sensors tends to negate these concerns. Sensors should be verified to be usable over the range of expected reflectivity.
Angle of Measured Surface	~1% thickness based on 8 degree tilt	Thickness	Any deviation from orthogonality results in a cosine error in the measurement.
Temperature	0–15 µm	Thickness	This error source is based on the thermomechanical properties of the mounting structure and the range of temperatures over which the system must operate.
Vibration	± 3 µm	Thickness	For a well-aligned caliper, this error range is the result of sampling error and the degree of vibration.
Dynamic Range	0.6 µm	Resolution	The laser displacement sensor controller output has less resolution than the computer's data acquisition system, and thus is the limiting factor in dynamic range.
Sampling Error	2 µm[b] With a speed of 5m/min	Lateral	This error source is greatly dependent on the speed at which a sample passes through the laser caliper.

A representative IR thermograph from a region of TODA HE5050 electrode with defect is shown in Figure V - 193b. The temperature scan from that area shows an increase in the temperature profile confirming the presence of defects in the electrode. This technique was also applied for the graphite A12 anode coating, and the results are given in Figure V - 193c. The observed increase in the temperature profile along the line-1 scan

and the decrease in the temperature profile along the line-2 scan may be due to (1) temperature increase across the defect region corresponding to a blister or agglomerate where heat cannot be released more quickly and (2) temperature decreases corresponding to pinholes and divots where heat is released from the coating surface more quickly.

XRF as a NDE technique to measure cathode transition-metal stoichiometry and electrode areal weight and to identify metal particle contaminants in the electrode. ORNL has contributed to designing an in-line XRF measurement system with Ceres Technologies specifically designed for lithium ion battery cathode coatings. The XRF desktop unit (Figure V - 194) was used to measure the cathode transition-metal stoichiometry and cathode areal weight and to identify deliberately introduced metal particle contamination in the electrode while coating. Only preliminary off-line data was obtained, as it was determined that this technique was not appropriate for production scaling due to insufficient areal-weight accuracy and incompatibility with coating line speeds.

The instrument was used to monitor the TM composition at different coating positions for two different cathode types: a traditional TODA NMC 532 coating and a TODA LMR-NMC HE5050 coating. The Mn to Co ratio and Ni to Co ratio for the NMC 532 cathode was found to be ~2.5 and 1.5 respectively. These results demonstrate excellent compositional uniformity across the electrode coating. The same compositional analysis was also completed on a LMR-NMC cathode (TODA HE5050), and the ratios between Mn to Co and Ni to Co in four different regions were found to be the nominal values of 1.5 and 5.5, respectively. However, the areal weight values measured by XRF were 20-25% too low as compared to the actual values measured with a balance. The actual areal weights of the NMC 532 and HE5050 were 11.9 mg/cm^2 and 10.2 mg/cm^2, respectively, as compared to 9.4 mg/cm^2 and 7.7 mg/cm^2, respectively, when analyzed by the desktop XRF unit.

Two different sample types were prepared for measuring metal particle contaminants:

Sample 1: Co and Cu metal powder were mixed into a TODA NMC 532 slurry, and then the electrode was prepared by tape casting (designated as NMC532-Co-Cu).

Sample 2a: Cu metal powder was sprinkled over the wet electrode after tape casting (NMC532-Cu).

Sample 2b: Co metal powder was sprinkled over the wet electrode after tape casting (NMC532-Co).

Figure V - 195 shows the relative TM ion composition collected from Sample 1 (NMC532-Co-Cu) in region R1 and R2. From the XRF data, it is evident that the Co concentration is higher because excess Co was added in the slurry before tape casting. It was also observed that the wt% of Cu in the region R1 is 5.378% and R2 is 7.213%, which demonstrates the ability of XRF technique for detecting metal-particle contamination of different concentration that might be present in the cathode slurry while mixing. Figure V - 195 shows the composition spectrum acquired from region R1, confirming the presence of Co and Cu impurities in the electrode.

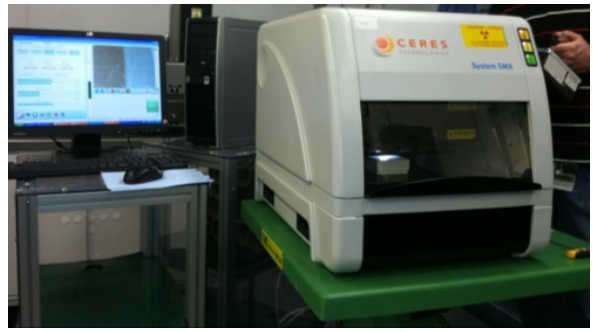

Figure V - 194: Desktop Ceres Technologies XRF unit

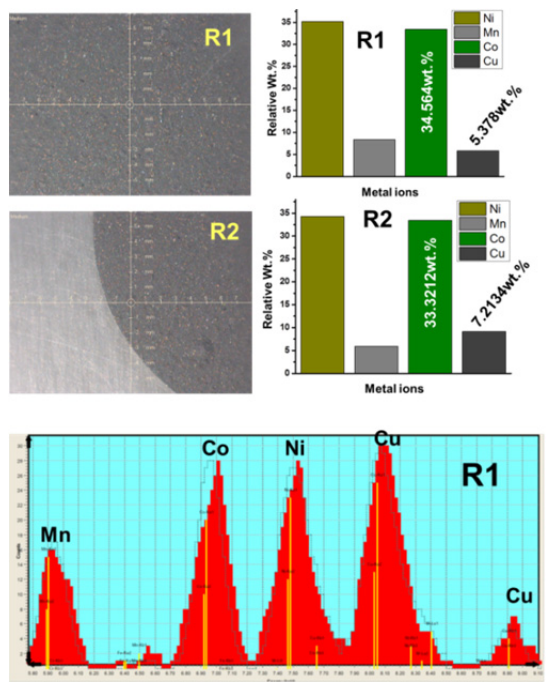

Figure V - 195: Optical images (top left), XRF data (top right), and composition spectrum (bottom) from two different regions of NMC 532 electrode contaminated with Co and Cu. The spectrum shows the presence of Cu in the electrode

Figure V - 196 shows the relative TM ion composition collected from Sample 2a (NMC532-Cu) in region R1 and R2. It was observed that the wt% of Cu in region R1 was 0.0071% and R2 was 0.0429%, showing that the XRF method can also trace very small amount of metal contamination from the Cu foil slitting process. The digital images also show a higher amount of Cu in

region R2 compared to R1. Figure V - 197 shows the relative transition metal ion composition collected from Sample 3 (NMC532-Co) in region R1 and R2. It was observed that the wt% of Co in region R1 was 22.77% and R2 was 29.45%, demonstrating that the R2 region had more Co contamination than R1 and that both regions had an excess of Co. In this electrode, a negligible amount of Cu (~0.003%) was detected).

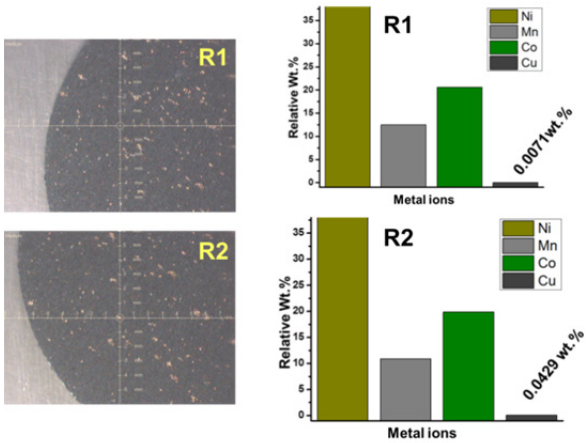

Figure V - 196: XRF data from sample 2a (NMC532-Cu). Optical image (left) and relative wt% of transition metal composition with Cu impurity from area R1 and R2 (right)

Figure V - 197 shows the relative transition metal ion composition collected from Sample 2b (NMC532-Co) in region R1 and R2. It was observed that the wt% of Co in region R1 was 22.77% and R2 was 29.45%, demonstrating that the R2 region had more Co contamination than R1 and that both regions had an excess of Co. In this electrode, a negligible amount of Cu (~0.003%) was detected.

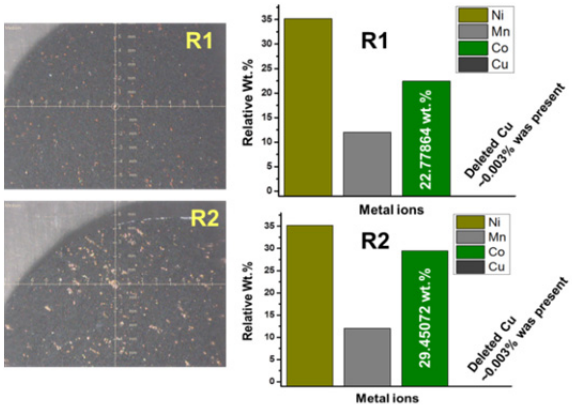

Figure V - 197: XRF data from Sample 2b (NMC532-Co). Optical image (left) and relative wt% of transition metal composition with Co impurity (right) from region R1 and R2 (right)

Conclusions and Future Directions

- The laser-caliper method was developed specifically for use as a LIB electrode NDE and QC tool on the ORNL slot-die coating line. Possible errors and uncertainties of the laser caliper system were provided. Thickness precision of less than ±2% for in-line laser thickness measurement was achieved. The thickness deviation of the cathodes was typically ± 2.0-2.3%, and for anodes, it was typically ± 2.2-2.6%. Differences in standard deviation values were taken as references for the thickness of the electrode at different regions. In the next step, the technique will be transferred to industry partner (TBD) pilot/production line.
- The XRF method yielded the concentration of deliberately added metal contaminants in the electrode; however, this technique could not provide the reliable areal weight accuracies (no-go decision).
- IR thermography successfully detected the defects in dried electrodes. An increase in the temperature profile suggests the presence of agglomerates, and a decrease in the temperature profile indicates divots, pinholes, and blisters that were not observed optically. In the next step:
  - Method(s) will be developed to generate different electrode coating defects such as pinholes, blisters, large agglomerates, divots, and metal particle contaminants for evaluation in full coin cell test matrix.
  - Comprehensive, statistically representative full coin cell data on different types of electrode coating defects will be obtained to determine which type of defects cause cell failures or substandard performance and correlate IR thermography electrode QC data with full coin cell statistical data quantifying capacity/voltage fade.
  - Pass/fail criteria will be developed for lithium-ion electrode coating defects such as metal particles, pinholes, blisters, divots, large agglomerates, etc.
  - Automatic flaw detection during the electrode coating will be developed.
- In-line electrode porosity measurement will be developed with NREL using thermal diffusivity.

FY 2013 Publications/Presentations

1. D. Mohanty, J. Li, L.C. Maxey, R.B. Dinwiddie, C. Daniel, and D.L. Wood, "Improved QC of Slot-Die Coated Lithium Ion Battery Electrodes by IR Thermography and Laser Thickness Techniques," *Analytical Methods*, Revised, 2013.
2. 2013 DOE Annual Peer Review Meeting Presentation.
3. Mohanty, J. Li, C. L. Maxey, R. B. Dinwiddie, C. Daniel and D. L. Wood, "In-Line Non-destructive testing of a lithium-ion Battery Electrode by Laser Caliper and Thermography" MRS Fall meeting Boston, Massachusetts, December 1-6, (2013) (accepted)
4. D.L. Wood, III, J. Li, D. Mohanty, C. Daniel, B.L. Armstrong, R.B. Dinwiddie, H. Wang, R.M. Trejo, N.C. Gallego, C.I. Contescu, J.Y. Howe, R.A. Meisner, J. Kiggans, and B.D. Brown, "Advanced Materials Processing and Novel Characterization Methods for Low-Cost, High Energy-Density Lithium-Ion Batteries," *Proceedings of the Advanced Automotive Battery Conference* (2013).
5. Claus Daniel, David Wood, Jianlin Li, Debasish Mohanty, Beth Armstrong, and Jim Kiggans, "Cell Materials and Manufacturing," 2013 Cummings Energy Storage Systems Summit, Columbus, IN, October 29-30, 2013 (invited).
6. Claus Daniel, David, Wood, Jianlin Li, Beth Armstrong and Jim Kiggans, "Battery Production Technologies" Energy Storage Solution Industrial Symposium, Oak Ridge, TN, September 4, 2013 (invited).
7. David L. Wood, III, Claus Daniel, Jianlin Li, Debasish Mohanty, and Bradley Brown, "Cutting Edge Lithium-Ion Cell Research at the Oak Ridge National Laboratory Battery Manufacturing Facility (BMF)," 2013 CERC-CVC Annual Technology Forum, Beijing, China, August 19-20, 2013.
8. Claus Daniel, Debasish Mohanty, Jianlin Li, and David Wood, "Overview and progress in cathode materials for lithium ion batteries," 1st International Freiberg Conference on Electrochemical Storage Materials, Freiberg, Germany, June 3-4, 2013 (invited).
9. Claus Daniel, David Wood, Jianlin Li, Beth Armstrong, Jim Kiggans, Debasish Mohanty, and Sergiy Kalnaus, "Electrification of transportation-cost and opportunities," Bridging the Gap Conference 2013, Oak Ridge, TN, March 5-6, 2013 (invited).
10. David Wood, Jianlin Li, Debasish Mohanty, Claus Daniel, Beth Armstrong, Ralph Dinwiddie, Hsin Wang, Rosa Trejo, Nidia Gallego, Cristian Contescu, Jane Howe, Roberta Meisner, Jim Kiggans, and Bradley Brown, "Advanced materials processing and novel characterization methods for low-cost, higher energy-density lithium-ion batteries" Advanced Automotive Battery Conference 2013, Pasadena, CA, February 4-8, 2013 (invited).